

UNCLASSIFIED

AD NUMBER

AD863990

LIMITATION CHANGES

TO:

Approved for public release; distribution is unlimited.

FROM:

Distribution authorized to U.S. Gov't. agencies and their contractors; Critical Technology; JAN 1970. Other requests shall be referred to Air Force Arnold Engineering Development Center, AETS, Arnold AFB, TN 37389. This document contains export-controlled technical data.

AUTHORITY

AEDC, USAF ltr dtd 26 Mar 1975

THIS PAGE IS UNCLASSIFIED

AEDC-TR-70-14

FEB 2 1970

FEB 26 1970

SEP 26 1973

DEC 24 1973

FEB 26 1982

toluene p 36

Qy 20



# RESEARCH STUDIES AND THE DEVELOPMENT OF MHD GENERATORS AND ACCELERATORS

MAR 24 1989

## TECHNICAL REPORTS FILE COPY

SEP 24 1993

J. Teno, T. R. Brogan, S. W. Petty, et al.

AVCO Everett Research Laboratory

January 1970

This document is subject to special export controls and each transmittal to foreign governments or foreign nationals may be made only with prior approval of Arnold Engineering Development Center (AETS), Arnold Air Force Station, Tennessee 37389.

This document has been approved for public release  
its distribution is unlimited.

per AF letter  
dtd 26 March 75  
signed CWO, Col. STINFO

**ARNOLD ENGINEERING DEVELOPMENT CENTER  
AIR FORCE SYSTEMS COMMAND  
ARNOLD AIR FORCE STATION, TENNESSEE**

PROPERTY OF U. S. AIR FORCE  
AEDC LIBRARY  
F40600-69-C-0001

# ***NOTICES***

When U. S. Government drawings specifications, or other data are used for any purpose other than a definitely related Government procurement operation, the Government thereby incurs no responsibility nor any obligation whatsoever, and the fact that the Government may have formulated, furnished, or in any way supplied the said drawings, specifications, or other data, is not to be regarded by implication or otherwise, or in any manner licensing the holder or any other person or corporation, or conveying any rights or permission to manufacture, use, or sell any patented invention that may in any way be related thereto.

Qualified users may obtain copies of this report from the Defense Documentation Center.

References to named commercial products in this report are not to be considered in any sense as an endorsement of the product by the United States Air Force or the Government.

RESEARCH STUDIES AND THE DEVELOPMENT OF  
MHD GENERATORS AND ACCELERATORS

J. Teno, T. R. Brogan\*, S. W. Petty, et al.  
AVCO Everett Research Laboratory

This document is subject to special export controls and each transmittal to foreign governments or foreign nationals may be made only with prior approval of Arnold Engineering Development Center (AEDC), Arnold Air Force Station, Tennessee 37389.

This document has been approved for public release  
its distribution is unlimited.

Per AF letter dtd 26 March 75  
signed W.O. Cole, STINFO

---

\*Consultant



## FOREWORD

This is the final report on the LORHO Pilot Program conducted to evaluate the potential of MHD generator-accelerator units for hypersonic wind tunnel drive. The work was conducted by AVCO Everett Research Laboratory, a Division of AVCO Corporation, Everett, Massachusetts, from August 21, 1963, to December 1969 under Contract AF40(600)-1043 with the Arnold Engineering Development Center (AEDC), Air Force Systems Command (AFSC), Arnold Air Force Station, Tennessee, under Program Element 62410034, Project 7778, Task 11. The manuscript was submitted for publication on December 17, 1969.

The authors of this report appreciate the invaluable assistance by the many members of the staff of Arnold Engineering Development Center and ARO, Inc., who have participated in the LORHO program. The authors would like to recognize the significant contributions to this study and to the preparation of this report by J. W. Lothrop and O. K. Sonju.

Information in this report is embargoed under the Department of State International Traffic in Arms Regulations. This report may be released to foreign governments by departments or agencies of the U. S. Government subject to approval of the Arnold Engineering Development Center (AEDC), or higher authority within the Department of the Air Force. Private individuals or firms require a Department of State export license.

The reproducibles used to reproduce this report were supplied by the authors.

This technical report has been reviewed and is approved.

Robert C. Straub, Jr.  
1st Lt, USAF  
Technical Facility  
Development Division  
Directorate of Plans  
and Technology

Harry L. Maynard  
Colonel, USAF  
Director of Plans  
and Technology

## ABSTRACT

This report presents the results of the LORHO Pilot Program undertaken to evaluate the potentiality of MHD generator-accelerator units for hypersonic wind tunnel drive. The use of MHD is considered because it can lead to tunnel conditions which cannot be achieved by other means and at the same time a facility of reasonable cost and operational simplicity. Basic features governing the design of matched MHD generator-accelerators are discussed with particular reference to the important parameters of operating voltage as related to gas conductivity, electric and magnetic field strength, and accelerator discharge stagnation pressure. These conditions lead to the choice of a high-voltage single-circuit output Hall configuration MHD generator coupled to a diagonally connected MHD accelerator fed with gas from a separately driven arc heater. A power level of 20,000 KW was chosen for the LORHO Pilot. Design details of the generator and accelerator are given, along with a detailed description of generator performance and the comparison of that performance with the analysis. The generator delivered a maximum output of 18,000 KW and provided a convincing demonstration of the utility of MHD for the present application. The accelerator has not been operated. Methods of uprating the performance of the MHD generator to levels as high as 100,000 KW output are discussed. For completeness a brief description of the over-all LORHO Pilot facility is provided.

This document is subject to special export controls and each transmittal to foreign governments or foreign nationals may be made only with prior approval of Arnold Engineering Development Center (AETS), Arnold Air Force Station, Tennessee 37389.

## TABLE OF CONTENTS

<u>Section</u>		<u>Page</u>
I	INTRODUCTION AND SUMMARY	1
	1. Background	1
	2. Program Objectives and Scope	4
	3. Summary and Conclusions	6
II	SYSTEM CONSIDERATIONS	17
	1. Basic Principles of Matched MHD Accelerator-Generator Units	17
III	DESIGN, CONSTRUCTION, PERFORMANCE AND UP-RATING OF THE MHD POWER SUPPLY	25
	1. Introduction	25
	2. Analysis of the MHD Channel Flow	32
	3. Mechanical Design of the MHD Power Supply	44
	4. Description of the Performance Evaluation Program	76
	5. Comparison of Observed and Expected Performance	110
	6. Upgrading the LORHO MHD Power Supply	119
IV	DESIGN AND CONSTRUCTION OF THE HIGH POWER MHD ACCELERATOR	130
	1. Introduction	130
	2. Theoretical Considerations	131
	3. The "As Built" High Power LORHO MHD Accelerator	141
	4. Mechanical Design of the High Power Accelerator	152
V	BRIEF DESCRIPTION OF THE LORHO PILOT FACILITY	172

<u>Section</u>	<u>Page</u>
APPENDIX I    BOUNDARY LAYERS IN MHD GENERATORS	185
APPENDIX II    END EFFECTS IN HALL CONFIGURATION MHD GENERATORS	201
APPENDIX III   FLOW INSTABILITY IN HALL CONFIGURATION MHD GENERATOR	227
APPENDIX IV    EXPLORATORY STUDIES WITH A LOW POWER MHD ACCELERATOR	253
APPENDIX V    ELECTRODE DEVELOPMENT EXPERIMENTS	261
REFERENCES	271

## LIST OF ILLUSTRATIONS

<u>Figure</u>		<u>Page</u>
1	1500 kilowatt Mark II Experimental MHD Power Generator	3
2	Mark V 20,000 kilowatt (net) Self Excited, Rocket Driven MHD Power Generator	5
3	Schematic of the 20,000 kilowatt LORHO Pilot MHD Accelerator-Generator System	7
4	LORHO Pilot 20,000 kilowatt MHD Accelerator	9
5	LORHO Pilot MHD Power Supply	10
6	LORHO Pilot Power Supply MHD Channel	11
7	Cutaway Sketch of LORHO Pilot Facility	12
8	External View of LORHO Pilot Facility	13
9	Schematic Illustrating Multiple Arc Plasma Generator Drive with MHD Generator	15
10	Coordinate System for MHD Channel Flow	18
11	Schematic of the 20,000 kilowatt LORHO Pilot MHD Accelerator-Generator System	22
12	MHD Hall Generator Efficiency ( $\eta$ ) and Electric Field, $E$ as a Function of Loading Parameter ( $\alpha$ ) for Various Values of the Hall Coefficient	27
13	Calculation Variation of Flow Parameters with Channel Axial Station for Original MHD Power Supply Design	37
14	Loft of Original and Modified MHD Generator Channel-Diffuser Configurations	38
15	"As Built" Configuration of the MHD Generator	40
16	Plan View of "As Built" Configuration Showing Location of Major Components	41
17	Diffuser Recovery at an Inlet Mach Number of 2.88	42

<u>Figure</u>		<u>Page</u>
18	Diffuser Recovery at an Inlet Mach Number of 1.75	43
19	Ten Electrode Test Section Used for Evaluation of Electrode Configurations for MHD Generator	45
20	Long Duration Test Facility (LDTF) Operation for Generator Electrode Evaluation	46
21	Some Typical Test Results for the Selected Electrode Configuration	47
22	Original and Modified Generator Electrode Configurations	49
23	Assembled MHD Generator Channel Subsection of Thirty (30) Rings	51
24	Assembled MHD Generator Channel Major Section of Ninety (90) Rings	52
25	MHD Generator Channel Assembly Details	53
26	Completed LORHO Pilot MHD Generator Channel	54
27	LORHO Pilot Modified MHD Generator Configuration	56
28	Predicted and Measured Combustion Chamber Wall Heat Flux at Various Locations	59
29	Some Details of the Combustion Chamber	60
30	Details of the Propellant Injector Assembly	61
31	Combustion Chamber Injector Assembly	62
32	Combustion Chamber Liner Assembly	63
33	Combustion Chamber Liner Housing	64
34	Assembled Combustion Chamber	65
35	MHD Channel Inlet Nozzle Configuration	66
36	Supersonic Nozzle Setup for Final Contour Machining	67
37	Operating Stresses in the Combustion Chamber	69
38	Nozzle Stresses at 10 atmospheres Combustion Pressure	70

<u>Figure</u>		<u>Page</u>
39	Diffuser During Final Fabrication	71
40	Modified Diffuser Configuration	73
41	Final Coil for Generator Magnet	75
42	Generator Magnet Field Coil Thermal Transient Characteristics	77
43	Iron Yoke Assembly for Generator Magnet	78
44	Measured Centerline Field Strength for Generator Magnet	79
45	Generator Magnet Magnetization Curve	80
46	Schematic Showing Locations of Which Temperatures and Pressures are Measured in Generator System	83/84
47a	Control Temperature and Pressure Instrumentation used to Establish Flow, Temperature and Pressure of Cooling Water for Generator	85
47b	Electrical Instrumentation of Generator	86
47c	Schematic of Load Resistor Bank	87
48	Typical Pressure Distribution for Group I & Group II Runs Compared	98
49	Some Test Results of Run #21, First Series	100
50	Chamber Pressure, Power and Exit Static Pressure for Run 19 as a Function of Time	106
51	Selected Data from Runs 19, 20 and 21 (Modified Channel)	107
52	Configuration of Modified Channel	112
53	Unloaded Static Pressure Distribution in MHD Channel	113
54	Loaded Static Pressure Distribution in MHD Channel	114
55	Transverse Current Distribution in MHD Channel	116
56	Voltage Distribution on the Channel	117
57	Voltage-Current Characteristics at Various Seed Concentrations	118
58	Calculated Voltage Distributions for First Series Run of Three Seed Concentrations, and measured Distribution	120

<u>Figure</u>		<u>Page</u>
59	Calculated Incompressible Shape Factor Distribution for First Series Run at Three Seed Concentrations	121
60	Mark V SSF Channel	125
61	Mark V SSF Channel Insulator Wall	126
62	Mark V SSF Channel Electrode Wall Before Filling Grooves with Zirconia Electrode Material	127
63	Critical Loading Coefficient vs Interaction Parameter Based on Diameter and Mach Number	135
64	Electrical Conductivity and Hall Coefficient as a Function of Temperature for Air at Various Seed Concentrations at a Pressure of 0.1 Atmospheres	137
65	Some Characteristics of an Early Constant Area Accelerator Design	140
66	Variation of Some Flow and Electrical Parameters with Length for the Center Point of the "As Built" Accelerator Design, Three Terminal Connection	142
67	Total Current and Axial Electric Field for the Three Terminal Connection at the Design Point	145
68	Matching Characteristics for Accelerator and Generator, Three Terminal	146
69	Matching Characteristics for Accelerator and Generator, Two Terminal	147
70	Electric Field and Current Vectors for Two Terminal Design at Calculated Velocity of 6800 meters/second	149
71	Current Vectors for Various Total Currents and Magnetic Fields, Two Terminal	150
72	Accelerator Diffuser Requirements for Three Critical Operating Points	151
73	Summary of Diffuser Test Results	152
74	Diffuser Configuration for High Power Accelerator	153
75	Maximum Design Velocity as a Function of Hall Coefficient for "As Built" Accelerator in Two (Channel 1) and Three (Channel 2) Terminal Configurations	154



<u>Figure</u>		<u>Page</u>
76	Schematic of High Power Accelerator System	155
77	Plenum Chamber Inlet Diffuser and Plenum Chamber	157
78	Supersonic Expansion Nozzle Before Welding	159
79	Completed Nozzle After Welding	160
80	Accelerator Channel Module	161
81	Channel Subassembly Partially Completed	163
82	Completed High Power Accelerator Channel	164
83	Supersonic Exit Diffuser for Accelerator	166
84	Piping Schematic for Accelerator System	167
85	Accelerator Seeder System	168
86	Magnet for High Power Accelerator	169
87	Field Distribution High Power Accelerator Magnet	171
88	External View of LORHO Pilot Facility	173
89	Sectional View of LORHO Pilot Facility Identifying Major Equipment Items	174
90	Fluid System Schematic	176
91	Fluid System Schematic Continued	177
92	MHD Generator Load and Ballast Arrangement	179/180
93	LORHO Pilot Operators' Control Station	181
94	MHD Accelerator Air Supply System	183
95	Boundary Layer Shape Factor as a Function of Mach Number $M$ and Velocity Profile Parameter $n$ for $h_w/h_i = 0.5$ , and $r = 1.12$	195
96	Channel Static Pressure Distribution	198
97	Voltage, Current and Power Output as a Function of Time	199
98	Calculated Incompressible Shape Factor and Velocity Distribution in MHD Channel	200

<u>Figure</u>		<u>Page</u>
99	Mappings Representing Solution of Idealized Problem: a) Channel in Physical Space, b) Channel Mapped to Potential Space, c) Intermediate Mapping	206
100	Electric Potential Distribution in Power Section and Integrated Net Wall Current in Diffuser due to End Effect	207
101	Axial Electric Field Enhancement in Power Section and End Effect Wall Current Density in Diffusers.	209
102	Typical electric fields associated with the sudden termination of the magnetic field in a shorted Hall generator.	214
103	Typical electrical fields associated with the sudden termination of the magnetic field in a shorted Hall generator.	217
104	Equivalent length and field scaling factor as a function of the wall parameter.	219
105	Distribution of net current into electrode segments near the end of a Hall generator that results in con- stant axial electric field at the wall.	222
106	Distribution of bleeder resistors from segment (at -x from channel end) to diffuser to produce the current distribution of Fig. 105 and hence a constant axial field at the wall.	223
107	Total power dissipated in the bleeder resistor system of Fig. 106.	224
108	Complex perturbation impedance for idealized Hall generator.	241
109	Absolute stability map for idealized generator: fraction of energy flux converted vs load parameter	242
110	Absolute stability map for idealized generator: critical interaction parameter vs load parameter	244
111	Complex perturbation impedance for the "Mark II" combustion driven Hall generator at three loads	247
112	Complex perturbation impedance for the "high interaction" Hall generator at five loads	249

<u>Figure</u>		<u>Page</u>
113	Test Modules for Low Power Accelerator Channel	255
114	Design of Low Power Accelerator	256
115	Nozzle Assembly for Low Power Accelerator	258
116	Low Power Accelerator Nozzle Assembly on Combustion Chamber Test	259
117	Low Power Accelerator on Combustion Chamber Heat Transistor Test	260
118	300 Kilowatt Arc Heater Used for Early Electrode Development Tests	264
119	"Brick Rig" Test Channel for 300 Kilowatt Arc Heater	265
120	DC Excitation Circuit for Brick Rig	266
121	300 Kilowatt Arc Heater in Operation	267
122	Schematic of Thermal Dynamics 2000 Kilowatt Arc Heater Utilized for Electrode Development	268
123	2000 Kilowatt Arc Heater Test Setup	269
124	2000 Kilowatt Arc Heater in Operation	270
125	Typical Electrode Characteristics as Determined in 2000 Kilowatt Arc Heater Test Rig	271

## LIST OF TABLES

<u>Table</u>		<u>Page</u>
I	Methods of Interconnection for MHD Generator and Accelerator	20
II	LORHO Generator Burner Specifications	57
III	Group I Runs--Tests with Original Channel	88
IV	Group II Runs--Tests with Modified Generator Channel	92
V	Diameter of Each Ring of Original Channel	102
VI	Correspondence Between Ring Numbers in New and Old Channels	103
VII	New Rings for Modified Channel	104
VIII	LORHO Three Terminal MHD Accelerator	143

## LIST OF SYMBOLS

p	- pressure, newtons/m <sup>2</sup> , or atm
h	- enthalpy, cal/gm
R	- gas constant, cal/gm°K
T	- temperature
$\dot{m}$	- mass flow, Kg/sec
u	- velocity, m/sec
M	- Mach number
j	- current density, amp/cm <sup>2</sup>
E	- electric field, volts/cm
B	- magnetic field, tesla
x, y, z	- coordinates, meters
e	- electron charge, coulombs
V	- voltage, volts
I	- current, amperes
W	- power output, watts
A	- area, m <sup>2</sup>
H	- shape factor, $\delta^*/\theta$
$\bar{H}$	- equivalent incompressible shape factor
$C_f$	- wall friction coefficient
St	- Stanton number
D	- hydraulic diameter - meters
q	- heat transfer rate, watts/m <sup>2</sup>
s	- interaction parameter
L	- length
t	- transformed coordinate
$\rho$	- density, Kg/m <sup>3</sup>
$\sigma$	- electrical conductivity, mho/m
$\omega$	- electron cyclotron angular frequency, sec <sup>-1</sup>
$\tau$	- electron mean collision time, sec
$\Omega = \omega\tau$	- Hall parameter

$\alpha$	- loading coefficient (non-dimensional)
$\phi$	- $E_y/E_x$
$\eta$	- MHD process efficiency
$\Delta$	- change in
$n$	- electron density, meters <sup>-3</sup>
$\beta$	- degree of ionization
$\Theta$	- boundary layer momentum thickness, m
$\delta$	- boundary layer thickness, m
$\delta^*$	- boundary layer displacement thickness, m
$r$	- specific heat ratio
$\mu$	- viscosity, Kg/m sec

#### SUBSCRIPTS

$o$	- reference
$s$	- stagnation
$x$	- in the direction of the x coordinate
$y$	- in the direction of the y coordinate
$e$	- electron
$l$	- core
$w$	- wall
$\langle \rangle$	- average
$c$	- coil
$T$	- total

## SECTION I

### INTRODUCTION AND SUMMARY

#### 1. BACKGROUND

Initial discussions concerning the LORHO Pilot program began as early as 1961. At that time, Major D. J. Harney and Lt. Leon E. Ring of the Arnold Engineering Development Center (AEDC) were investigating the feasibility of "steady flow" test facilities for simulation of conditions encountered over the full range of hypersonic flight conditions of interest to the Air Force. It was quickly evident that to simulate flight energies encountered when the flight Mach number is greater than seven, some form of direct electric energy input to the wind tunnel working gas must be employed in order to achieve the appropriate tunnel enthalpy. Further, when the requirement for electric energy for the simulation of enthalpy is combined with a mass flow requirement for some degree of Reynolds number simulation, it was also evident that very large electric power levels are involved. Finally, it was clear that the test requirements can be met with a facility that has a relatively limited duty cycle; typically, one with only several minutes of operation per day.

Further consideration involved the method of adding the electrical energy to the gas. At the time that initial studies of the LORHO were first undertaken, the plasmajet-driven wind tunnel was the usual method of accomplishing the electrical input. However, although very high enthalpy levels could be achieved in these devices, they could not be achieved at pressure levels which would yield interesting conditions after expansion to a high Mach number. Roughly speaking:

$$P \left( \frac{h}{RT_0} \right) \leq 10^4$$

$$200 \times 4000 = 160 \times 10^4$$

could be achieved, where  $P$  is the arc chamber pressure in atmospheres, and  $\left( \frac{h}{RT_0} \right)$  is the stagnation enthalpy ratio.<sup>(1)</sup> Thus, the arc jet was found not to be a suitable gas generator.

The development of an adequate gas generator depends on devising a method of adding energy and momentum to a high Mach number flow. Ring<sup>(2)</sup> and Harney here recognized the potential use of magnetohydrodynamic (MHD) acceleration for the application. With MHD, the addition of energy and acceleration of the gas can occur simultaneously at high Mach numbers, so that very large increases in effective stagnation pressure can result at acceptable heat loads on the accelerator components.

Indicated power requirements for the MHD accelerator and the plasma jet, which supplies gas to the accelerator inlet, were several hundred megawatts divided roughly between the arc and MHD accelerator. A very rapid increase from no load to full power is desirable for both arc and accelerator. The indicated duty cycle was from one to a few runs per day, each of which would be approximately three minutes in duration. As initially conceived, the arc was to be driven by AC and the MHD accelerator by DC with negative ground, in order that the test section be at ground potential.

The power requirements described above are difficult to meet in an economic and convenient way with conventional equipment, particularly for the MHD accelerator. First cost of the equipment, kilowatt demand charges, operational restrictions on time and loading rate, and switchgear and control requirements all combine to produce a difficult situation which can be handled only at excessive cost. It was for this reason that an MHD generator power supply was considered for the drive of the MHD accelerator, and became the source of the "all MHD" system.

At the time of the initial discussions in 1961, MHD generator technology was very much in its infancy. At the Avco Everett Research Laboratory (AERL), a program jointly sponsored by Avco Corporation and a group of private utility companies led by the American Electric Power Company, then headed by Mr. Philip Sporn, had been underway since November 1959. The purpose of this program was to investigate the use of MHD for central station power generation, where the ability of the MHD generator to handle extremely hot gases promised power plants of unprecedented efficiency, even as high as 60%. The program included experimental studies of MHD generator fluid dynamic and electrical characteristics, MHD component development under the environment to be experienced in a utility plant, other experimental studies directly related to the central station use and system analysis.

As part of the above program, a large (for the time, that is) experimental MHD generator called the Mark II and shown in Fig. 1, had been constructed for the purpose of obtaining a detailed understanding of MHD generator flow and electrical characteristics. The generator channel was of sufficient cross-section so that the MHD effects dominated heat transfer and friction losses, while the channel length was such that the generator operated through a substantial pressure ratio ( $\approx 3/1$ ). The equipment was designed for operating times of one minute or less, limited only by heat sink capability of the components. The generator was placed in operation in December 1960. By mid-1961 when initial discussions of the LORHO began, the Mark II had achieved an output of approximately 600 kw, and was eventually to achieve a maximum output of about 1500 kw in September 1962. (3)

Although constructed in connection with the utility program, the Mark II also provided the first dramatic demonstration of the unique capability of a rocket engine-MHD generator combination to produce huge amounts of electric power for a limited duration, with relatively simple



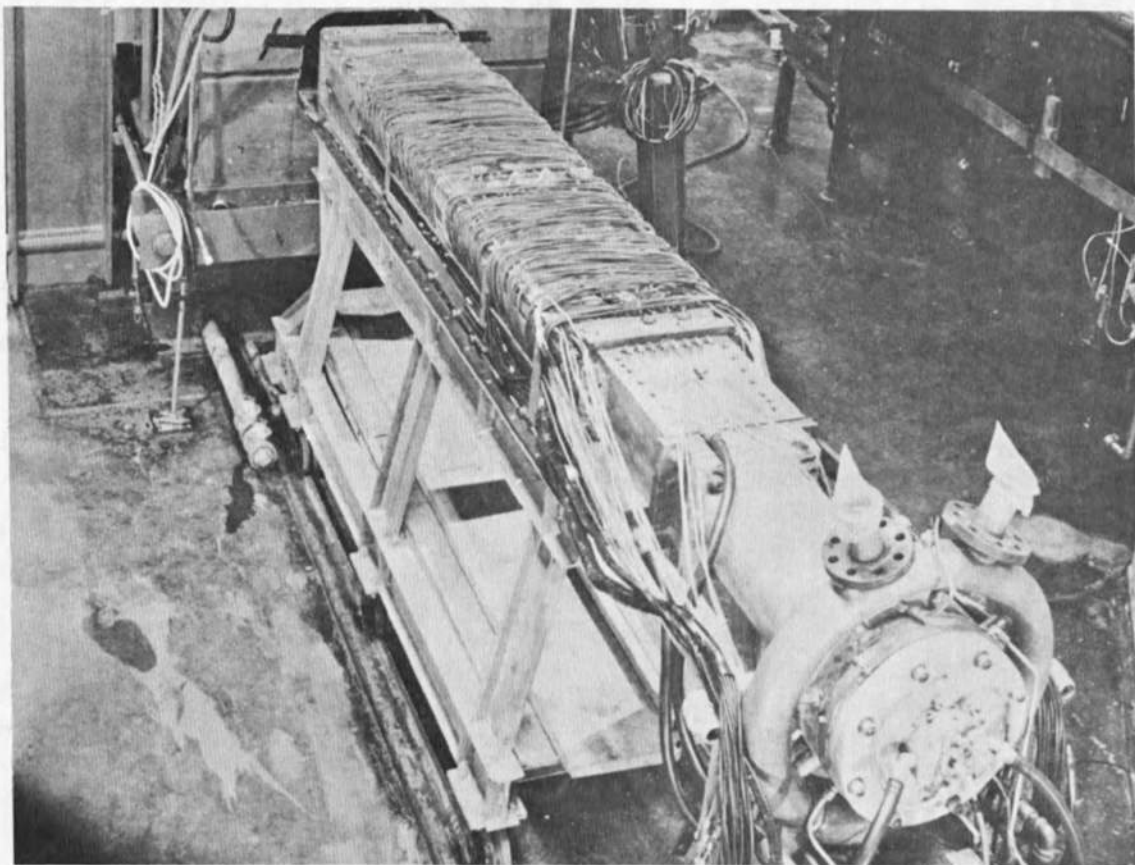


Fig. 1 1500 kilowatt Mark II Experimental MHD Power Generator

and inexpensive equipment. Thus, early operation of the Mark II coincided with initial LORHO considerations, and led the AEDC personnel to consider the all-MHD system for the tunnel.

Other government agencies were also interested in the potential of the rocket driven generator (RDG) and, in April 1962, with support of the Advanced Research Projects Agency, a program to design, construct and test a 20,000 kw RDG was begun. This generator, called the Mark V and shown in Fig. 2, was placed in initial operation in December 1963, and eventually delivered a maximum net output of 23,000 kw, providing a conclusive demonstration of RDG capability. (4, 5)

The LORHO Pilot program was initiated in July (or Aug.) 1963. It called for a 20,000 kw RDG driving an MHD accelerator. The goal was to achieve an accelerator discharge velocity of 25,000 ft/sec. An AC plasma jet operated off the power line was to deliver hot air to the MHD accelerator inlet via a settling chamber. At the time the LORHO Pilot program was initiated, the design output of the MHD generator greatly exceeded the 1500 kw maximum output which had been achieved by the Mark II, and was comparable to the 20,000 kw design net output of the nearly completed but not yet operated Mark V. The accelerator performance goal was much beyond anything that had been achieved or that was even underway at the time.

## 2. PROGRAM OBJECTIVES AND SCOPE

The initial objective of the LORHO Pilot program was the design, development, construction and performance evaluation of a matched 20,000 kw MHD accelerator-generator unit. An air exit velocity of 25,000 ft/sec. was the design goal of the MHD accelerator. The MHD generator was to be driven by seeded combustion gases. Air at 3000-4000°K for the accelerator inlet was to be provided from an AC arc heater driven off the main power line. As accomplishment of the design goals necessitated advances in the state-of-the-art of MHD devices, research studies were to be conducted as a part of the program. A major part of these research studies was concerned with obtaining an efficient, high current density, rugged electrode configuration for the MHD accelerator. A second facet of the research program involved construction and hot gas test of a small channel which simulated the constructional features of the 20,000 kw MHD accelerator.

The performance evaluation of the 20,000 kw MHD accelerator-generator unit and some of the hot gas tests on the small channel were to be carried out at AEDC. For this phase of the program, AERL provided data analysis and technical support to the AEDC contract operator.

Items of research equipment provided under this Contract have included a 20,000 kw MHD generator and accelerator channels, a low power accelerator channel, and other closely associated equipment. The design for the combustion chamber for the MHD generator was carried out as a part of the program, but the actual hardware was provided under

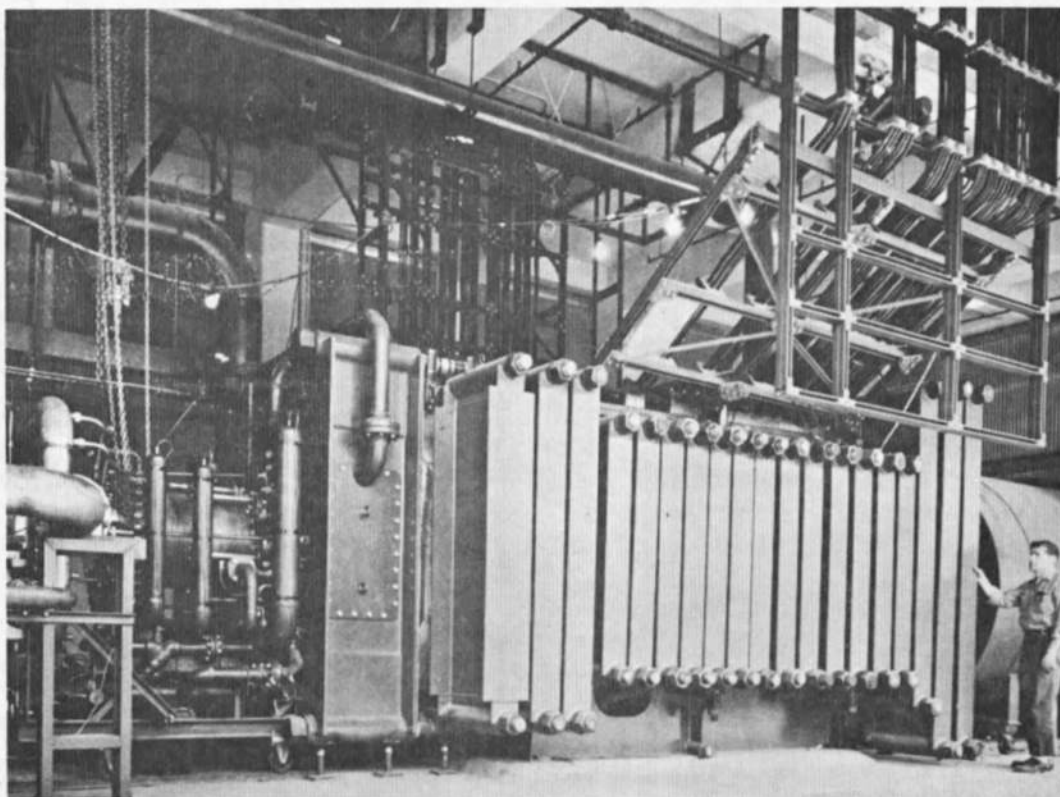


Fig. 2      Mark V 20,000 kilowatt (net) Self Excited, Rocket Driven  
MHD Power Generator

separate Contract AF 40(600)-1116. Finally, AERL was the design contractor for the LORHO Pilot facility under Contract AF 40(600)-1077; the Anderson-Nichols Company of Boston assisted AERL in this latter effort.

### 3. SUMMARY AND CONCLUSIONS

Section II is concerned with over-all system considerations which finally led to selection of the specific system which is described. The selected LORHO Pilot system is shown in Fig. 3. Heated air at a pressure of ten atmospheres and a temperature of approximately 5100°K is supplied to a settling chamber from a three-phase AC arc heater supplied to the government under a separate procurement by the Westinghouse Electric Company. From the settling chamber where seed is injected, the air is expanded to the MHD accelerator inlet where the flow conditions are approximately

$$P\left(\frac{h}{RT_0}\right) = 1.25 \times 10^3$$

$$\begin{aligned} P_0 &= \text{stagnation pressure} = 10 \text{ atm} \\ \dot{m} &= 0.5 \text{ kg/sec} \\ T &= 3,000^\circ\text{K} \\ \rho &= 0.4 \text{ atm abs} \\ u &= 2,600 \text{ meters/sec} \\ M &= 2.5 \\ \frac{h_s}{RT_0} &= 125 \end{aligned}$$

$$\frac{P_i}{P_0} = \frac{970}{10} = 97$$

$$\left(\frac{u_i}{u_0}\right)^2 = \left(\frac{7800}{2600}\right)^2 = 9$$

A two (-or three-) terminal diagonally connected MHD accelerator configuration is employed and is directly connected to the MHD generator power supply which develops 10,000 volts at 2000 amperes in single circuit output. Neither switchgear nor ballast resistance are employed between accelerator and generator; the generator seed flow control serves as the switch while the inherent constant current characteristic of the MHD generator output provides more than adequate short circuit protection for the accelerator. The design conditions of the accelerator exit are:

$$97 \text{ or } 970 \rightarrow P_0 = \text{stagnation pressure} = 970 \text{ atm}$$

$$T = 3,000^\circ\text{K} = 5400 \text{ R}$$

$$\rho = 0.05 \text{ atm abs}$$

$$u = 7,800 \text{ m/sec} = 25,584 \text{ ft/s}$$

$$M = 7.5$$

$$\frac{h_s}{RT_0} = 450$$

$$P\left(\frac{h}{RT_0}\right) = 4.4 \times 10^5$$

$$= 4.4 \times 10^4 \rightarrow 10^4$$

$$\text{if } P = 97$$

$$\frac{P_i}{P_0} = 8$$

The potential advantages of the MHD acceleration process are vividly illustrated by Fig. 3. To obtain these discharge conditions from an arc heater, the heater would need to deliver air at  $h_s/RT_0 = 450$  and a stagnation pressure of 970 atm; no such arc heater can even be

$$C = \sqrt{gRT} \cdot \sqrt{1.32(1)^2} \cdot 53(5400) = 3471 \text{ ft/s}$$

$$M = \frac{u}{C} = \frac{25584}{3471} = 7.4$$

## LORHO PILOT FACILITY

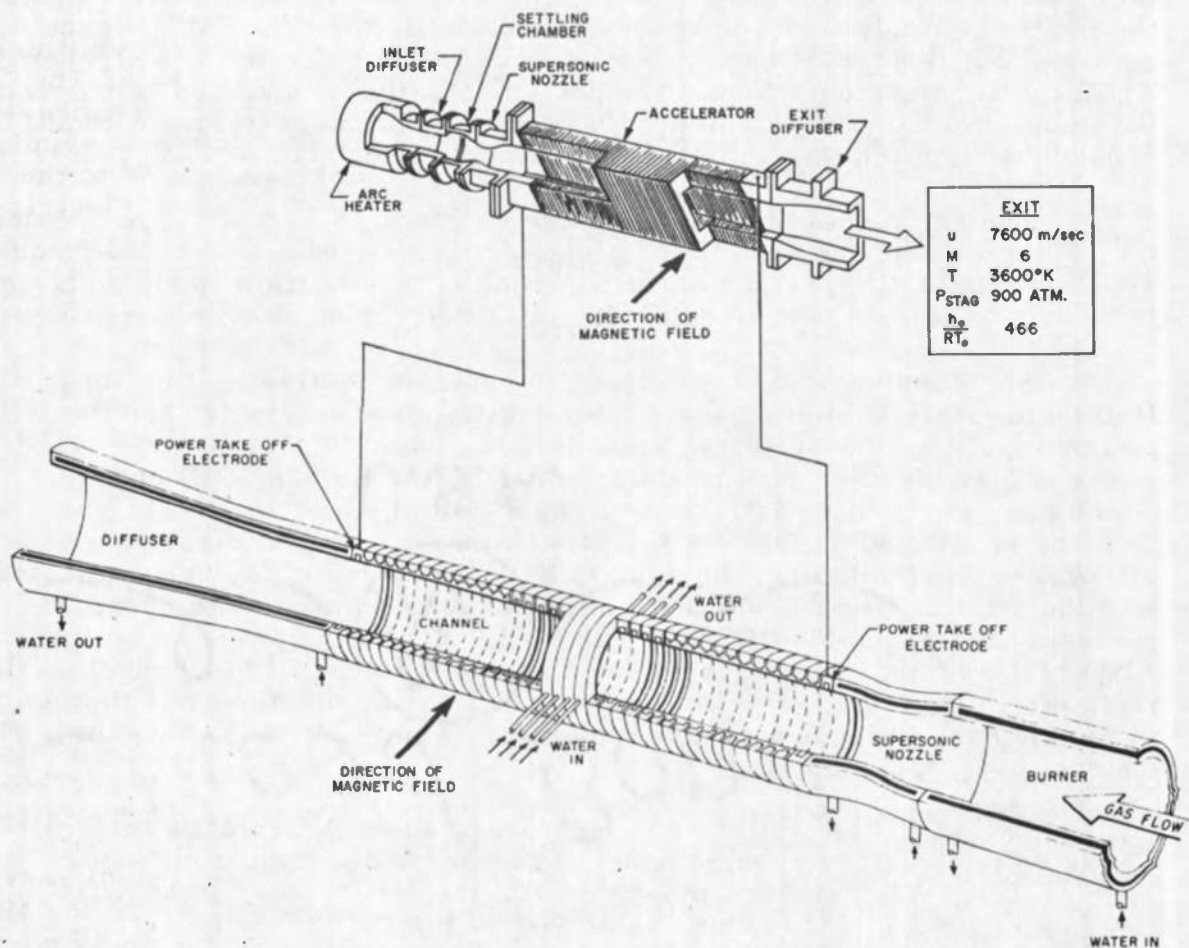


Fig. 3 Schematic of the 20,000 kilowatt LORHO Pilot MHD Accelerator-Generator System

$$\frac{h_2}{RT_0} = 450$$

$$h_2 = 450 \left( \frac{0.0684}{R} \right) 519 = 16021 \text{ BTU/lb} \quad !$$

$$\frac{h_2}{RT_0} = 125 \quad h_2 = 4500 \text{ BTU/lb} \quad \text{reasonable for arc heater}$$

contemplated, except one employing a MARC which itself utilizes an MHD acceleration.

In spite of these impressive figures, the calculated design performance falls short of what would really be desired for a hypersonic flow facility in terms of Reynolds number per foot, albeit essentially achieving the desired enthalpy. As is shown in Section II, the achievable Reynolds number/foot is approximately proportional to the electric field strength,  $E$ , in the accelerator channel; the design actually constructed represents the maximum value of  $E$  which, it was felt, could be sustained without breakdown with the then existing technology.

The completed MHD accelerator is shown in Fig. 4. The accelerator, together with the associated plenum chamber, supersonic inlet nozzle and supersonic diffuser has all water-cooled construction, and, so far as is known, is the largest modular diagonal MHD channel ever constructed.

For considerations described in detail in Section II, the linear Hall configuration with separate field excitation was selected for the MHD power supply. This selection permitted the use of a simple and rugged water cooled circular ring modular construction for the MHD channel which has proven very satisfactory under actual operating conditions. Toluene is utilized as fuel for the generator while the oxidizer is a gaseous nitrogen-oxygen mixture; the seed is KOH dissolved in methanol injected into the toluene feed line. Maximum generator mass flow is 60 Kg/sec. A view of the assembled LORHO Pilot MHD power supply is shown in Fig. 5; the combustion chamber is in the foreground. The channel itself is shown in Fig. 6. It is 4.5 meters in length and one meter in diameter at the channel exit. In terms of generator volume, it is the largest MHD channel ever constructed.

The LORHO Pilot has not been operated as a complete system. Changing test facility requirements, have prevented operation of the accelerator. As described in Section III, the MHD power supply delivers an output of 18,000 kw, some 90% of the 20,000 kw objective. With the exception of the low voltage single circuit Faraday Mark V at 24,000 kw, the 18,000 kw output is the largest achieved on a single output with an MHD generator. In addition, the 9,000 volt output has not been exceeded. The performance of the LORHO Pilot MHD Power Supply has provided a convincing demonstration of the utility of the rocket driven MHD generator (RDG) in providing very large blocks of power for limited durations with simple and inexpensive equipment.

Figures 7 and 8 show a cutaway of the LORHO Pilot facility and an external view of the completed installation. The generator exhausts through the large stack, while the accelerator and another plasma generator exhaust through the smaller ducts.



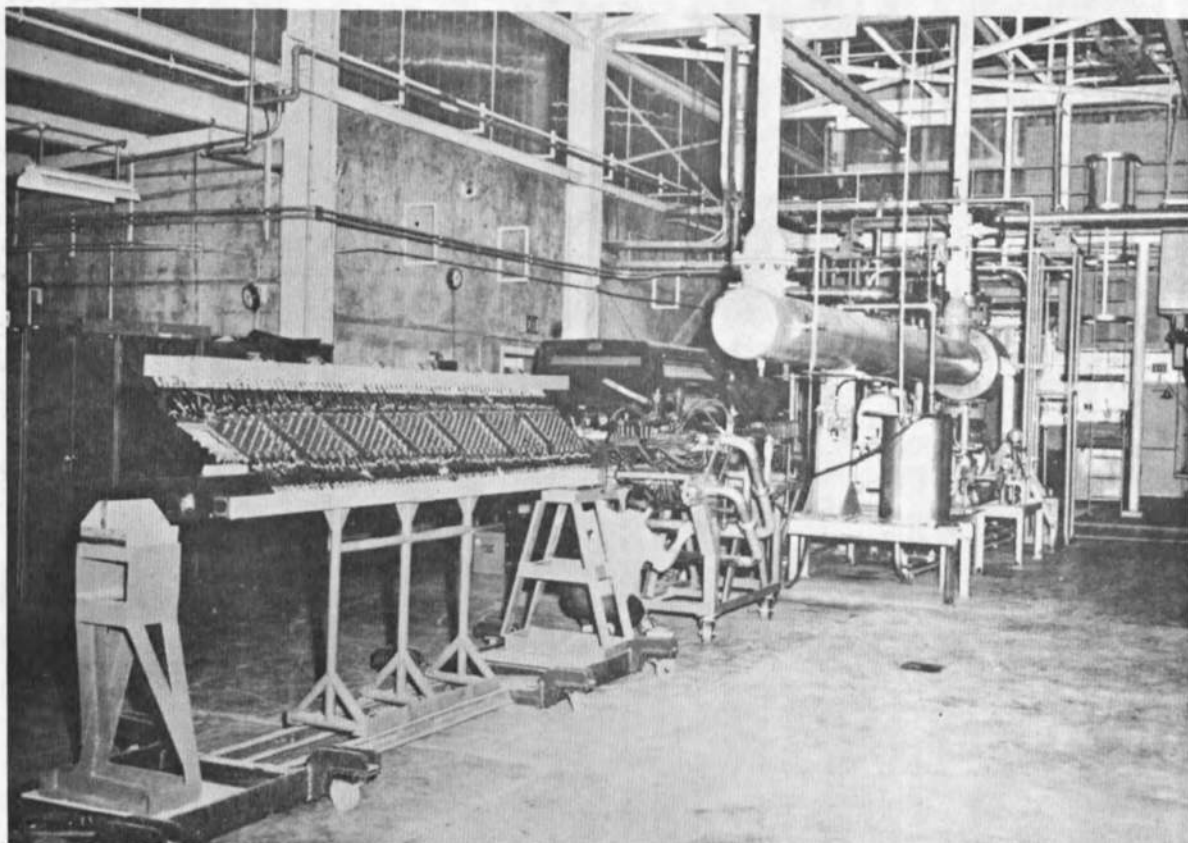


Fig. 4 LORHO Pilot 20,000 kilowatt MHD Accelerator

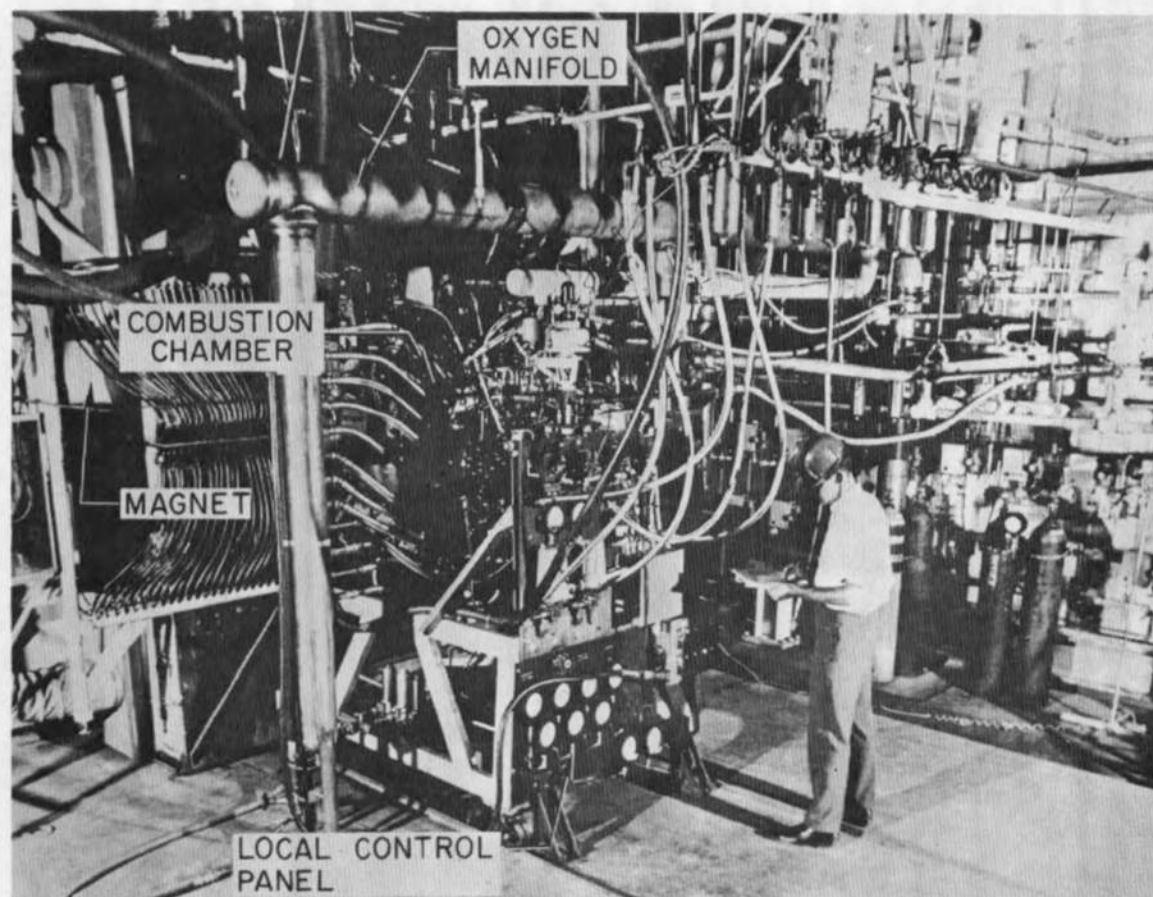


Fig. 5 LORHO Pilot MHD Power Supply



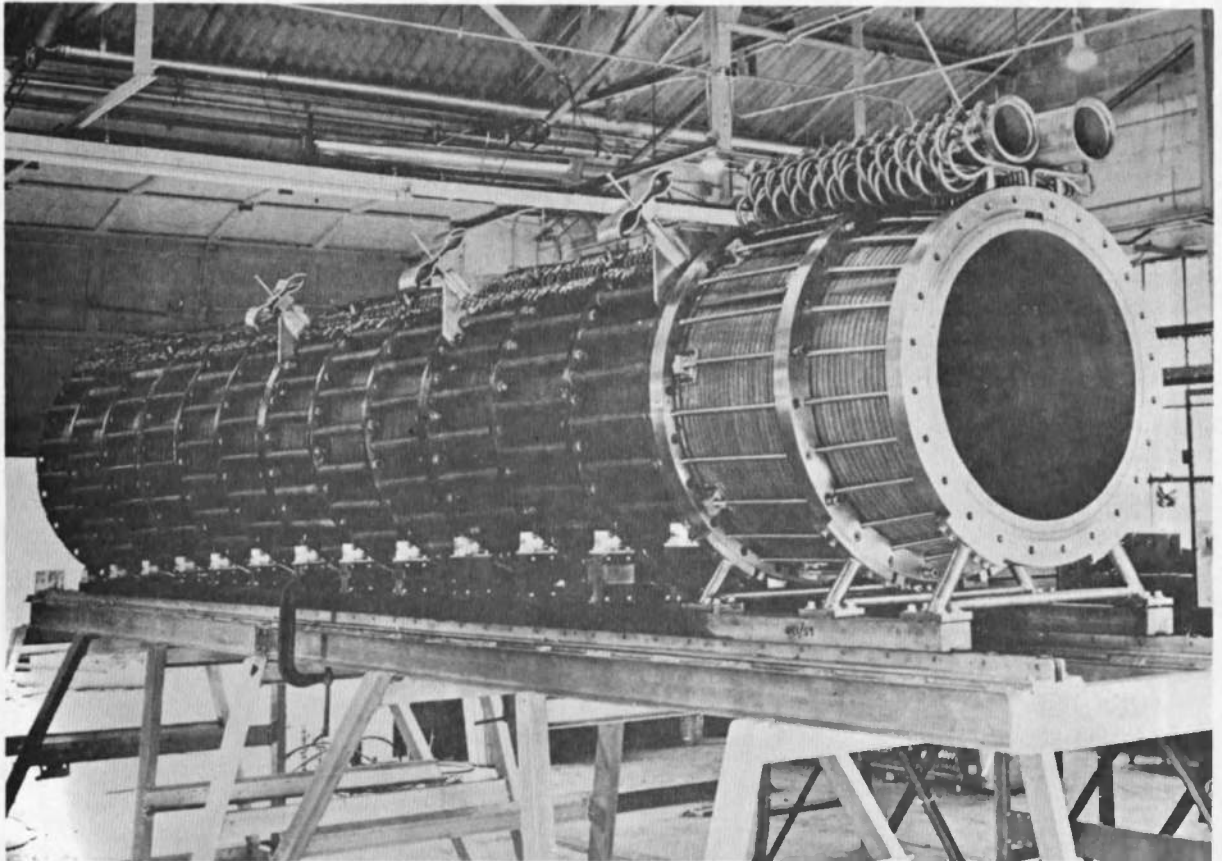


Fig. 6 LORHO Pilot Power Supply MHD Channel

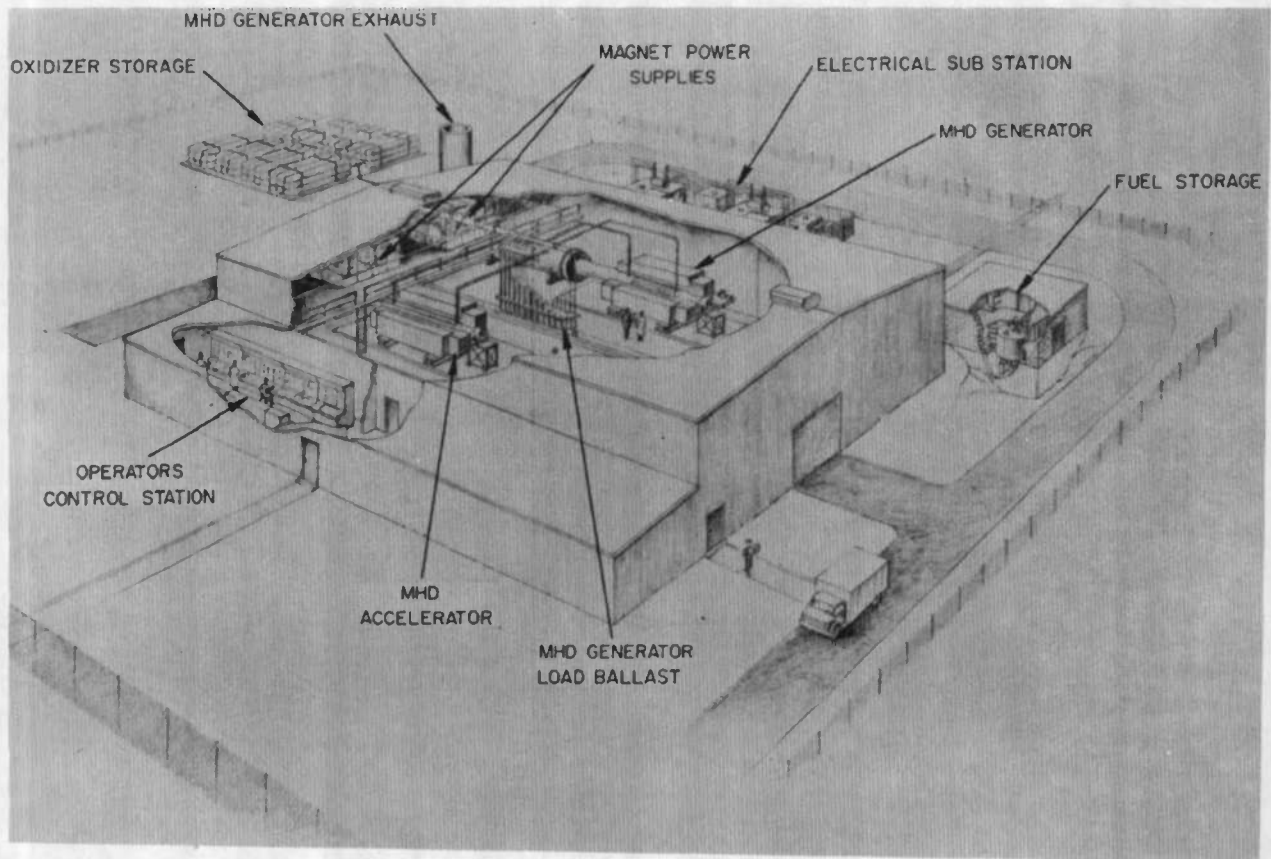


Fig. 7 Cutaway Sketch of LORHO Pilot Facility

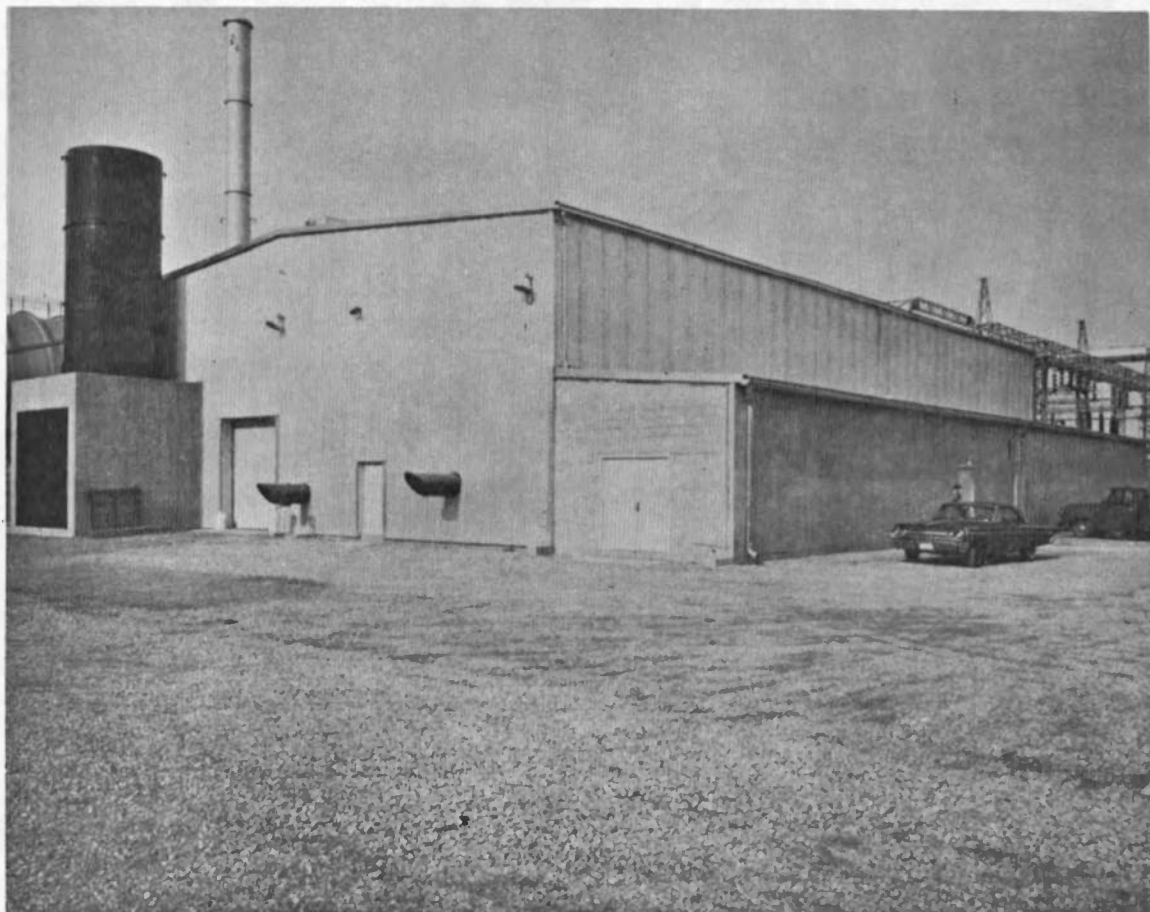


Fig. 8 External View of LORHO Pilot Facility

In a further program under separate contract with AEDC, AERL has investigated the application of LORHO Pilot MHD type power supplies to multiple arc heater drive using the one megawatt AERL Mark II Hall generator<sup>(6)</sup>. This program is discussed in AEDC TR 68-180. This program demonstrated that the characteristics of the rapid start, independent of the power system, lack of switchgear, and inherent short circuit protection make MHD an ideal choice for this application. The multiple arc drive system is shown in Fig. 9.

The MHD generator and accelerator are discussed in detail in Sections III and IV respectively. Section V presents some very preliminary considerations for upgrading the MHD power supply, and it is shown that power levels of up to seventy-five megawatts may be achieved with modification. Appendices and References complete this report.

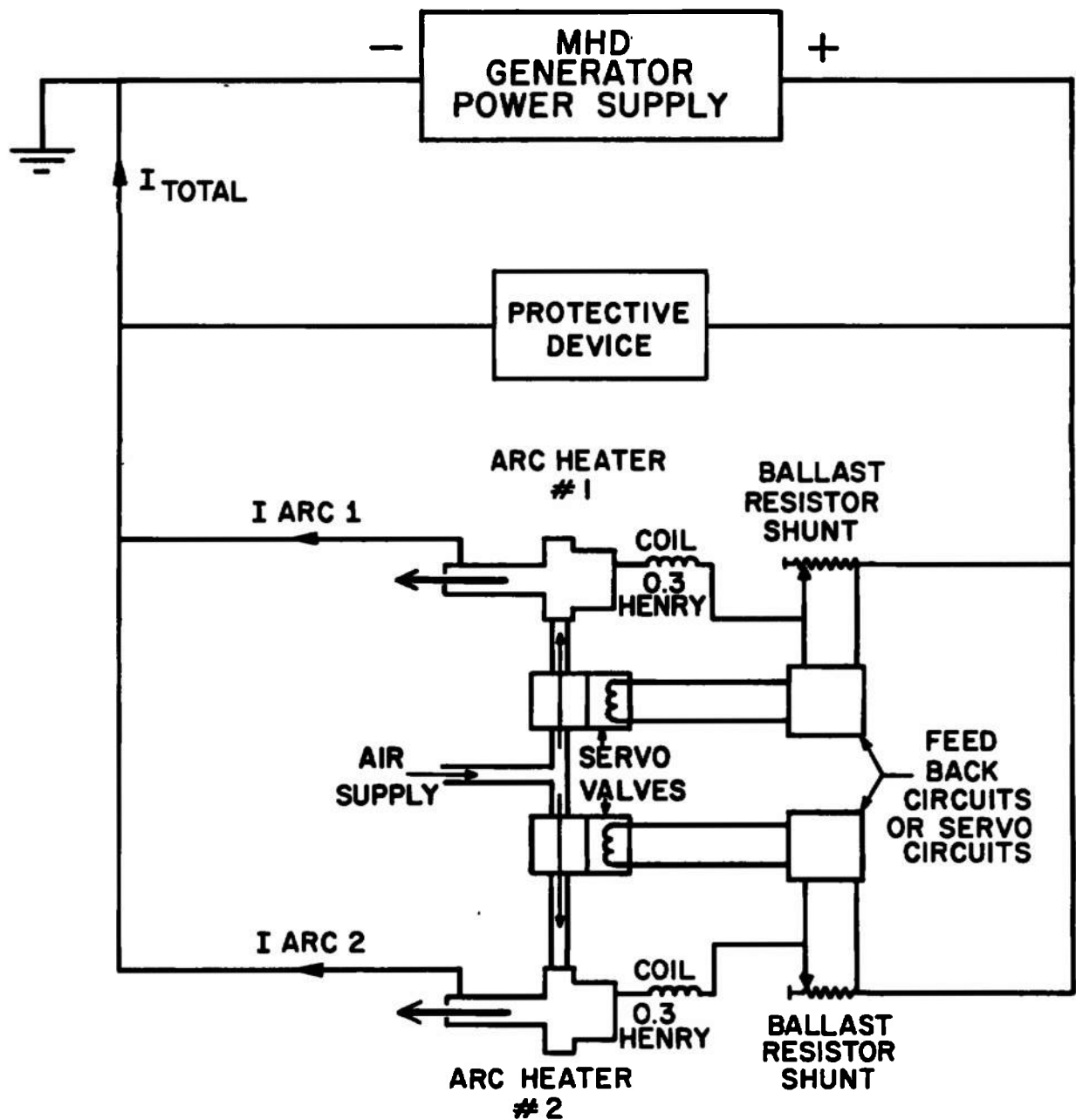


Fig. 9 Schematic Illustrating Multiple Arc Plasma Generator Drive with MHD Generator

## SECTION II

### SYSTEM CONSIDERATIONS

#### A. BASIC PRINCIPLES OF MATCHED MHD ACCELERATOR-GENERATOR UNITS

Referring to the coordinate system of Fig. 10, the Ohm's law for the one-dimensional flow in the x-direction, with velocity  $u$ , including electron Hall effects, but excluding ion slip may be written:

$$j_x = \frac{\sigma}{1 + \Omega^2} \left[ - (E_y - uB) \Omega + E_x \right] \quad (1-a)$$

$$j_y = \frac{\sigma}{1 + \Omega^2} \left[ E_y - uB + \Omega E_x \right] \quad (1-b)$$

where  $j_x$  and  $j_y$  and  $E_x$  and  $E_y$  are the components of the current and electric fields respectively,  $\sigma$  is the scalar electrical conductivity and  $\Omega$  the Hall coefficient for electrons. Two modes of operation are generally considered. In the first, the normal, conduction, or Faraday mode,  $j_x$ , the Hall current is zero so that:

$$E_x = (E_y - uB) \Omega \quad (2)$$

and

$$j_y = \sigma (E_y - uB) = \sigma uB (a_1 - 1) \quad (3)$$

where  $a_1 = E_y/uB$  is the loading coefficient and  $a_1 > 1$  for an accelerator while  $1 > a_1 > 0$  for a generator. In order for  $j_x$  to be zero, it is necessary that the generator channel be built with electrical insulation both along and perpendicular to the flow direction. The segmented electrode<sup>(7)</sup> geometry is appropriate here (as it is also for the second mode of operation).

The second mode is the Hall mode. Here,  $E_y = 0$  and the energy transfer is due to the product  $j_x E_x$ . We have:

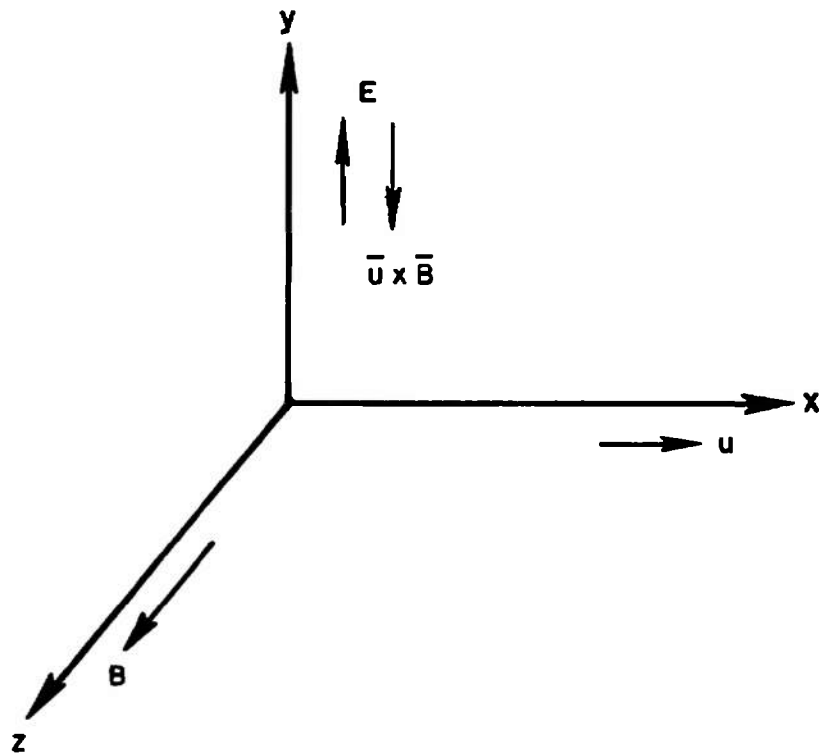


Fig. 10 Coordinate System for MHD Channel Flow

$$j_x = \frac{\sigma}{1 + \Omega^2} \left[ + \Omega uB + E_x \right] \quad (4)$$

$$j_y = \frac{\sigma}{1 + \Omega^2} \left[ \Omega E_x - uB \right] \quad (5)$$

$$j_y = \sigma uB (1 - a_2) \quad (6)$$

where  $a_2 = \frac{\Omega j_x}{\sigma uB}$  is the loading coefficient for a Hall MHD device, and  $0 < a_2 < 1$  for a generator, while  $a_2 > 1$  for an accelerator.

The magnitude of the electric field is a very important consideration in the design of steady flow MHD devices. The electrode wall must generally be run hot in order to make contact with the body of the gas, so that electrons can be emitted from the cathode. Since these hot electrode surfaces can lead to voltage breakdown which could short out the Hall potential, there is generally a maximum value of  $E_x$  which can be tolerated before voltage breakdown occurs. The magnitude of the field depends on the gas that is being used. However, it is found that, as a general rule, the voltage between adjacent electrodes in the axial direction should not exceed the minimum arc burning voltage for the gas. For polyatomic gases such as combustion products or air, it appears that 40 volts/segment is a reasonable maximum value. When water cooling is introduced, the pitch between adjacent segments is of the order of 1 cm, although this can probably be reduced. At the present state of the art, however, it appears that the electric field along the flow axis should be limited to 4 kv/meter, and we have attempted to do this in our designs. In the case of the accelerator, this has not been possible without excessive sacrifice in operating pressure level, and the design of the accelerator has taken some liberties with the axial field. In the generator, the field does not exceed 4 kv/meter.

In principle, both the generator and accelerator may be operated in the normal or Hall mode. Thus there are several possibilities for interconnection of accelerator and generator:



TABLE I

METHODS OF INTERCONNECTION FOR MHD  
GENERATOR AND ACCELERATOR

<u>Accelerator</u>	<u>Generator</u>
1 Normal	Normal (coupled in detail, segmented electrode pair on accelerator to a pair on the generator)
2 Normal (diagonally connected)	Normal (diagonally connected)
3 Hall	Normal (diagonally connected)
4 Hall	Hall
5 Normal (diagonally connected)	Hall

Let us consider the first possibility in which each segmented electrode pair on the MHD generator is connected to a similar pair on the accelerator. If no ballast resistance is employed, the voltages appearing across both devices are equal. However, not only must the voltage of electrode pairs connected together be equal, but also the voltage between adjacent pairs on both the generator and accelerator must be equal and, desirably, such that no Hall current flows. When the program first began it was our intention to utilize this approach. However, when calculations were undertaken it was found that it would be extremely difficult, if not impossible, to make both the transverse and axial fields equal on both the accelerator and generator in such a way that no Hall current would flow. The reasons for this are the large differences in flow velocity, gas density, electrical conductivity, and magnetic field strength in the generator as opposed to the accelerator. Also it was realized that such a method of hook-up would in all likelihood have very little flexibility in that it would probably be well suited only to one mode of operation of the accelerator and that operation at off-design conditions would lead to inefficient operation. These considerations, which will not be gone into in detail here, led us to discontinue this approach.

Before proceeding to discuss the other approaches, we need to consider the influence of the Hall effect on the potential distribution in the MHD channel flow devices. Because of the Hall effect the electric field is not normal to the flow direction, but at an angle such that

$$\phi = \frac{E_y}{E_x} = \frac{a_1}{\Omega (a_1 - 1)}$$

for the normal current mode of operation. Lines perpendicular to the field lines are equipotential lines. Thus, for example, in the case of an accelerator a point on the anode is at the same potential as a point on the

cathode further downstream while the situation in the generator is reversed. The equipotentials make an angle  $\beta = \cot^{-1} \phi$  with the flow direction. As described in Section IV, the channel may be built of a stack of modules inclined at the angle  $\beta$  with the flow direction. The requirement that the transverse voltages match at each station has been eliminated. If the currents per electrode at inlet and outlet of both generator and accelerator can be made equal, then it is possible to connect only across the inlet and outlet electrodes. As it is, intermediate connections may be required in order to effect some current balancing. The main voltage requirement is that the overall voltage developed along the axis of the two devices be approximately equal. There are, however, two difficulties with this device. First, it appears that this type of operation could lead to inefficient MHD generator operation at off-design conditions. Second, the number of connections at either end of the accelerator and generator is different. The number of connections on each device is equal to  $D\phi/\ell$  where  $D$  is the typical channel dimension, and  $\ell$  the pitch between adjacent electrodes on the same side of the duct. Since generally the size of the generator channel is much larger than that of the accelerator, while  $\phi$  and  $\ell$  are roughly equal, it is clear that a considerable amount of power would have to be wasted in order to couple the generator and accelerator together.

The third and fourth modes of operation of the MHD accelerator-generator unit involve Hall accelerators. The MHD accelerator is extremely sensitive to internal dissipation at the high Mach numbers which are desirable. In a Hall type device, the presence of both an axial and transverse current leads to increased dissipation over that of a comparable normal current device with the exact dissipation being dependent on the value of the Hall parameter. We therefore made the decision not to proceed with either of these two modes of operation. A Hall accelerator might be considered for reduced outlet velocity or incremental upgrading of an arc plasmajet.

The last possibility, a diagonally connected MHD accelerator coupled to an MHD generator operating in the Hall mode, has seemed most attractive to us. The second choice would probably have been to operate both devices in the diagonally connected condition. After a good deal of consideration, it was decided to proceed with the last possibility, and the MHD accelerator-generator unit which was employed in the LORHO pilot is shown schematically in Fig. 11. The MHD generator is operated in the Hall mode with supersonic flow at Mach numbers varying between 2.5 and 2.0. The generator static pressure is of the order of 0.40 atmospheres. The generator is driven by combustion gases seeded with potassium salt to provide ionization and conductivity. The voltage required by the accelerator is of the order of 10,000 volts at 2000 amperes, as will be described in Section IV. With the MHD generator combustion chamber pressure limited to a value considered reasonable and proper for long life, it is necessary to reduce the electrical conductivity of the combustion gases below that obtainable using pure oxygen as the oxidizer. Therefore, some nitrogen diluent is used in the generator combustion chamber and this leads to reduced heat

## LORHO PILOT FACILITY

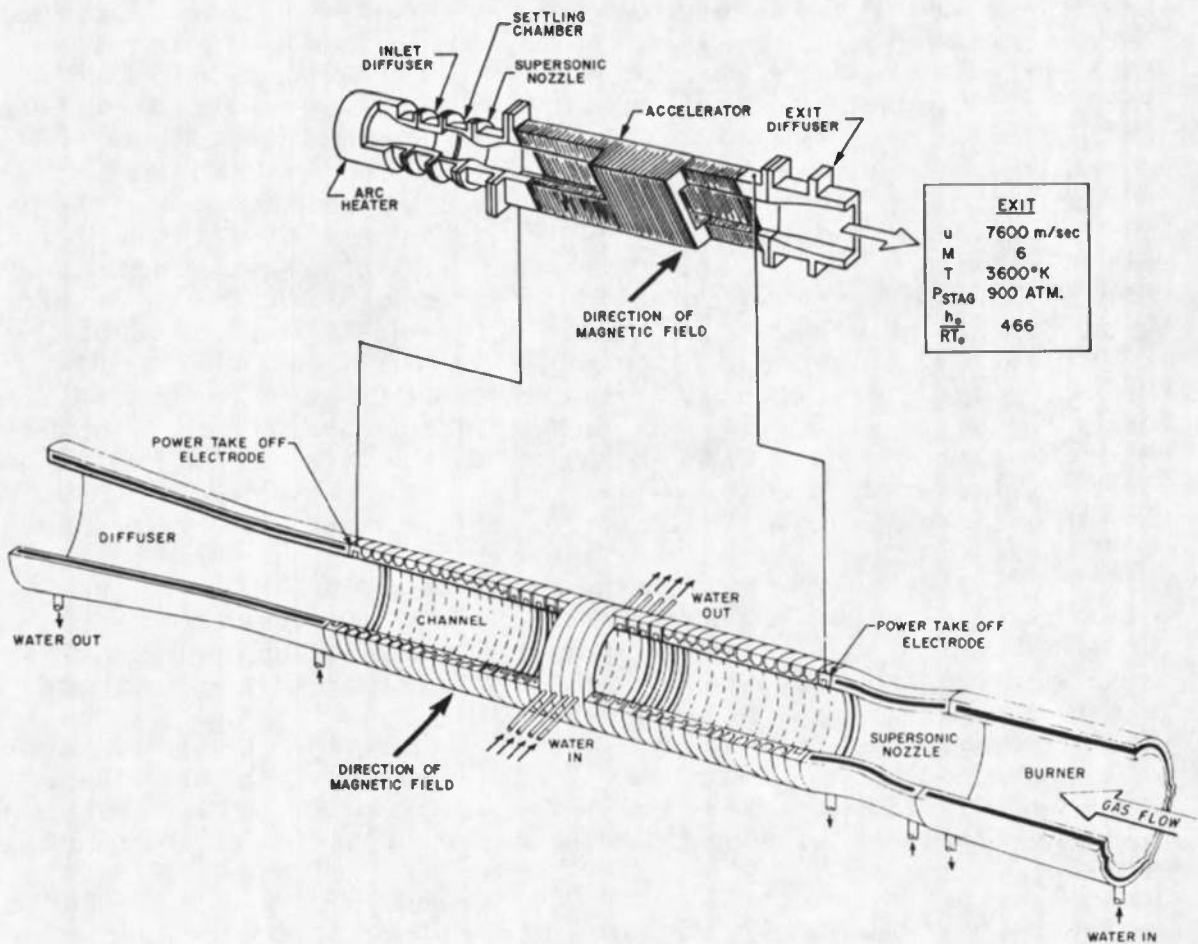


Fig. 11 Schematic of the 20,000 kilowatt LORHO Pilot MHD Accelerator-Generator System

transfer rates and more economic operation. Considerations of the maximum tolerable electric field in the generator lead to the use of an iron core electromagnet. The manner in which the generator is connected to the accelerator is shown in the figure. The single-circuit output of the generator must be applied to the accelerator in such a way that the voltage between adjacent equipotentials on the accelerator is a proper value.

We should here comment on the voltage developed along the axis of importance in both the generator and accelerator. In both the devices, the acceleration, or, in the case of the generator, deceleration, are carried out at nearly constant thermodynamic conditions. That is to say, most of the energy input goes into changing the kinetic energy of the working fluid. In the interest of simplicity, we will neglect any internal dissipation. The gas conductivity is primarily due to the movement of the light electrons under the influence of induced and applied fields. The electrons in turn exert forces on the ions electrostatically. The ions are coupled to the gas by collisions with the neutral particles. If the ions are completely in contact with the gas, that is to say there is no ion slip, then each ion will give up its energy  $1/\eta$  during the MHD process times, where  $\eta$  is the degree of ionization. Thus, each ion can go through a potential difference  $V_x$  given by:

$$e V_x \eta = \frac{1}{2} m \Delta u^2$$

where  $m$  is the mass of a neutral particle,  $e$  is the electron charge,  $V_x$  is the voltage developed along the axis of the device, and  $\Delta u^2$  is the change in kinetic energy. In actual practice it may be possible to achieve variations in axial voltage of the order, say of a factor of two, by adjusting the seed concentration, operating temperature, etc., but basically the above relation gives a fundamental value of the Hall voltage which must be developed in either a Hall or normal current device.

Now on both generator and accelerator the molecular weights of the gases are approximately the same. However, the change in kinetic energy in the accelerator will be roughly eight to ten times that in the MHD generator. On the other hand, we have seen that they must develop equal axial voltages. Therefore it is evident that the degree of ionization in the MHD generator must be of the order of one-tenth that in the MHD accelerator if they are to develop equal voltages. It is this consideration that leads to the introduction of nitrogen diluent in the generator. As we will see, it also leads to operation at high supersonic speed and relatively low seed concentration. Since the electrical conductivity is roughly proportional to the degree of ionization, particularly in the generator working fluid, we see that the low degree of ionization is equivalent to low conductivity. We should also mention here that the low conductivity working fluid to be used in the MHD generator makes it more attractive to consider separate excitation of an iron core magnet rather than

self-excitation of the magnet by the generator itself, as has been the case with the Mark V generator which will be discussed briefly in Section IV.

The choice of a normal mode diagonally connected accelerator and a single circuit output Hall generator has somewhat separated the design problems and made it possible to design the two devices with relative independence. It is also believed that this will lead to very considerable flexibility in utilization of the two devices.

## SECTION III

DESIGN, CONSTRUCTION, PERFORMANCE and UPRATING  
OF THE MHD POWER SUPPLY

## 1. INTRODUCTION

The decision to employ a separately excited, single-circuit output high voltage Hall configuration MHD generator as the power supply for the LORHO Pilot was taken in early July 1964. (8) As was described in Section II, this decision to go to a generator configuration with which there was no experience at any significant power level was made necessary by the practical difficulties associated with matching the accelerator with other configurations of the MHD generator; the desirability of single-circuit output; and singularly attractive constructional features of the Hall configuration. The generator design was finalized in December 1964, and the equipment shipped to AEDC in August 1965. More than one year then elapsed between shipment and initial operation in early October 1966.

The methods utilized to calculate the flow in heavily loaded MHD channels in July 1964 were substantially less sophisticated (and hence easier to survey) than those which could be employed today. There were considerable uncertainties in the electrical properties, conductivity and Hall parameter, for generator working fluids. Wall friction and heat transfer losses in the relatively short ( $L/D < 10$ ) channels were averaged across the channel cross-section. This permitted use of one-dimensional methods of flow analysis (3, 9). A simple, after the fact, correction was applied to adjust the channel area profile for boundary layer displacement thickness. Other details could be factored in by assigning gross "degradation factors" to the ideal calculations. This approach seemed to yield fairly good results, particularly for the 1.5 megawatt segmented electrode Faraday Mark II generator which was the largest that had been operated (3, 9). In Reference 3 the overall performance of a heavily loaded segmented electrode generator with favorable pressure gradient was found to be accurately predictable. In Reference 4, the occurrence, location and strength of shock waves in a heavily loaded MHD supersonic flow ( $M \approx 1.4$ ) were explained under the assumption of essentially inviscid flow choking due to the MHD body forces; an assumption which was correct for the operating conditions of the Mark II corresponding to low Mach number supersonic flow and little flow deceleration. It is believed that these procedures, although not complete, would still be quite satisfactory for generators of the segmented electrode or diagonally connected Faraday configuration operating with good favorable pressure gradient. Thus, the design of the Hall configuration LORHO Pilot MHD power supply was approached with confidence even though the understanding of details of the flow were not complete. //

There were four constraints which were originally imposed on the design of the power supply:

- 1) The channel must discharge to the atmosphere with a diffuser if desirable.
- 2) The magnetic field is limited to 19,000 gauss which could easily be produced in a large gap iron window frame electro-magnet.
- 3) The minimum practical Hall coefficient was 2.0; later this value was increased to 2.5.
- 4) To obtain adequate conductivity, the minimum static temperature of the gas in the generator channel was about 2,400°K, the temperature below which KOH formation "steals" the seed from the gas.

The first two and the fourth of these constraints are quite obvious. Figure 12 illustrates the reasons for the third constraint. Here are shown for the Hall configuration ( $E_y = 0$ ) the axial electric field strength,  $E_x$ , and the efficiency,  $\eta$ , where:

$$\eta = \frac{\text{work output}}{\text{work done by gas against field}} = \frac{j_x E_x}{j_x B u}$$

where  $j_x$  and  $j_y$  are the axial and transverse current densities,  $B$  the magnetic field strength, and  $u$  the gas velocity. It will be appreciated that a fraction  $(1 - \eta)$  of the work done by the gas appears as Joule dissipation in the gas and increases the entropy. In addition, as will be seen for the particular case of the Hall generator at low  $\omega\tau$ , the heating interacts with the flow in such a way that its effect must be carefully considered in the design of the generator.

Note that for a segmented electrode or perfect diagonally connected generator,  $\eta = \alpha$ , where  $\alpha = E_y/UB$ , so that, ideally,  $\alpha$  can be increased arbitrarily close to unity, but, in practice, must differ from unity in order to obtain acceptable power density. For the Hall generator:

$$\eta = \alpha - \frac{\alpha^2}{(\omega\tau)^2 (1-\alpha)}$$

where now:

$$\alpha = \frac{(\omega\tau) j_x}{\sigma u B} = \left( \frac{\rho \omega\tau}{B} \right) \left( \frac{I}{\dot{m}} \right) \frac{1}{\sigma}$$

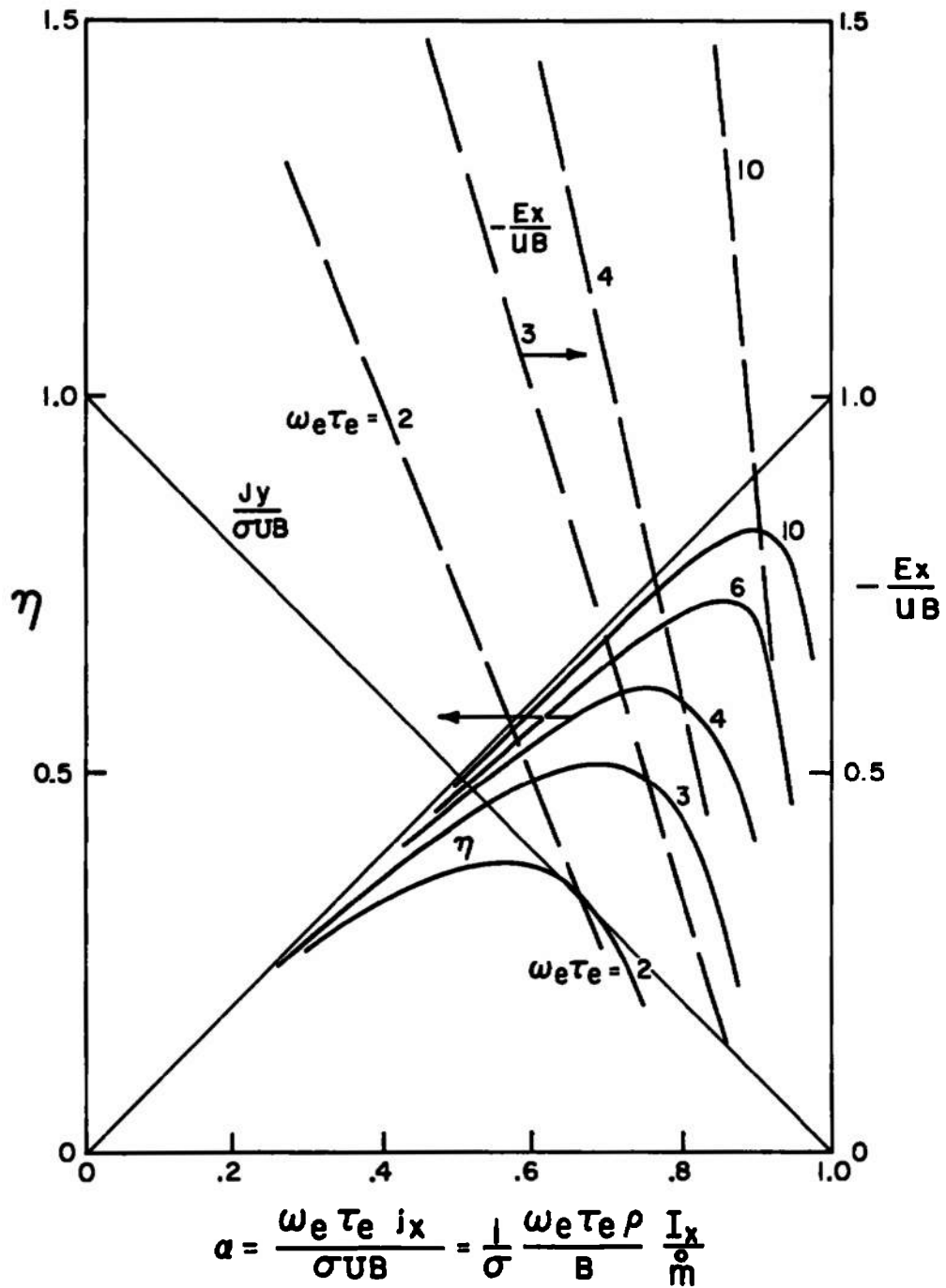


Fig. 12 MHD Hall Generator Efficiency ( $\eta$ ) and Electric Field,  $E$  as a Function of Loading Parameter ( $\alpha$ ) for Various Values of the Hall Coefficient



where  $\rho$  is the gas density,  $I$  the output current, and  $\dot{m}$  the mass flow. The parameter  $\alpha$  is most useful. This is true because using  $\alpha$  as defined above, the one-dimensional momentum equation governing the flow is

$$\rho u \frac{du}{dx} + \frac{dp}{dx} = -\sigma u B^2 (1 - \alpha)$$

The equation reads the same for both segmented Faraday and Hall configurations.

We see from Fig. 12 that the efficiency becomes quite unacceptable at Hall coefficients much below 2. Thus  $\omega\tau > 2$ . Now, for a given temperature and gas composition, we have, approximately:

$$\omega\tau = A \left( \frac{B}{p} \right)$$

where  $A$  is a constant with dimensions, say atm/tesla, and  $p$  is the gas pressure in atmospheres. Initially the design contemplated the use of medium fuel oil ( $H/C = 1.44$ ) as the generator fuel, and, for reasons to be explained, a nitrogen-oxygen mixture with molar ratio ( $N_2/O_2$ ) of unity as the oxidizer. For such a mixture, and a temperature of 2,500°K,  $A = 0.45$  atm/tesla. Thus, with  $B$  limited to 1.9 tesla, the static pressure at the channel inlet was limited to about 0.45 atm absolute (6.3 psia) in order to achieve an acceptable value of the Hall coefficient.

Now in the definition of the loading coefficient,  $\alpha$ ,  $(\rho\omega\tau/B)$  may be taken as constant for small temperature variation. The ratio  $I/\dot{m}$  is constant. Thus,  $\alpha \sim \sigma^{-1}$ . So, ideally, to "ride" the peak efficiency at a given value of the Hall coefficient implies that  $\sigma = \text{constant}$ , that is, that the gas temperature and pressure remain relatively constant throughout the flow. Thus, for the LORHO Pilot power supply power extraction comes about by flow deceleration at relatively constant pressure and temperature corresponding to the familiar "impulse mode" operation of conventional turbines. And, as in a turbine, this has important consequences as will be seen. In any case, with the inlet static pressure limited to 0.45 atm abs by constraints 2 and 3, constraint 1 leaves little option but to use an essentially impulse design.

The generator specifications called for an output of 10,000 volts at 2000 amperes. We now show that both the diagonally connected Faraday and Hall configurations display characteristic voltages and current, which will now be desired. The momentum equation may be put in the form:

$$\rho u \frac{du}{dx} + \frac{dp}{dx} = \frac{\sigma E_x B}{\omega\tau} - \frac{j_x B}{\omega\tau} \quad (7)$$

where  $x$  is the axial direction,  $\rho$  the gas density,  $p$  the pressure,  $\sigma$  the conductivity,  $\omega\tau$  the Hall coefficient,  $E_x$  the axial electric field, and  $j_x$  the axial current. For the perfect diagonal generator, the last term

in Eq. (7) is zero, while for a Hall generator, it is small except when the generator is virtually short-circuited. For the purpose of this discussion, it will be neglected. Using the fact that:

$$\frac{\sigma B}{\omega \tau} = n_e e \quad (8)$$

where  $n_e$  is the electron density, and  $e$  the electron charge, we have from Eq. (7).

$$\rho u \frac{du}{dx} + \frac{dp}{dx} = n_e e E_x \quad (9)$$

which states that the rate of change of fluid momentum is equal to the force required to force the total charge of one sign through the electric field. The effect is as if the electrons were trapped in the generator while the ions and neutral particles flow through; (this, in fact, is precisely what occurs in a Hall generator, which is really a space charge neutralized electrogasdynamic generator) thus, either configuration displays a "characteristic current"  $I_c$  given by:

$$I_c = n_e e u A = \beta \left( \frac{e}{m} \right) \dot{m} \quad (10)$$

where  $\beta$  is the degree of ionization,  $\left( \frac{e}{m} \right)$  the ion charge to gas particle

mass ( $m$ ) ratio, and  $\dot{m}$  the mass flow. Now to return to the characteristic voltage. Let us compare a number of generators in which the total change in fluid momentum through the generator is the same for each, while the variation  $u = u(\rho, p)$  is also identical. For all of these generators, the integrals of the right side of Eq. (9) will also be equal. The result is particularly simple if the "impulse" configuration is employed where the thermodynamic properties (and hence  $\eta_e$ ) are nearly constant while the output is extracted from the kinetic energy of the flow. The impulse configuration is particularly suitable for the Hall generator as we have seen. In this approximation:

$$\frac{\eta}{\beta} \frac{u_1^2 - u_2^2}{2} = \frac{n_e e V_c}{\rho} \quad (11)$$

or

$$V_c = \frac{\frac{1}{2} m (u_1^2 - u_2^2)}{e} \frac{\eta}{\beta} \quad (12)$$

$\beta = n_e/N$ , where  $N$  is the neutral particle number density and  $\beta \ll 1$ ,  $u_1$  and  $u_2$  are the initial and final gas velocities and  $\eta$  the thermodynamic efficiency. Equation (12) states that each ion can be "kicked" against the field  $1/\beta$  times before the momentum of the gas as a whole has been expended. We see that  $V_c \sim \beta^{-1}$ . Since  $\beta \sim n_e \sim \sigma$ , high output voltage requires that  $\sigma$  be small.

The value of  $V_c$  appropriate to the potassium seeded kerosene oxygen combustion products used in the Mark V is approximately 4000 volts. Thus, it is necessary to effect a substantial reduction in electron density below that of the Mark V in order to achieve the high voltage output. Since  $\sigma \sim n_e$ , this also implies a substantial reduction in  $\sigma$  compared to the pure oxygen used in the Mark V.

Since the negative output terminal of the generator is required to be at ground potential, the combustion chamber, expansion nozzle, all fuel, oxidizer and seed feed lines, and all combustion controls can be at ground potential, which is convenient. The diffuser must float at the full generator potential, which is inconvenient and caused some difficulty, as will be described. The reverse situation would also have experience some inconveniences.

It now remains to select the generator mass flow. This can be estimated as follows: The "impulse" configuration is appropriate for the Hall generator operation being employed. For the impulse case we can write approximately:

$$\frac{1}{2} \dot{m} (u_1^2 - u_2^2) \eta = W \quad (13)$$

where  $\dot{m}$  is the mass flow and  $W$  the power output. Now  $u = Ma$  where  $M$  is the Mach number and  $a$  the sound speed, and  $a_2 \approx a_1$  with impulse operation. The generator must discharge to the atmosphere from the exit Mach number. Because the boundary layer is relatively thick and unstable at the generator exit, a simple diffuser composed of a straight section followed by a conical section was deemed appropriate. Such a diffuser can discharge to a pressure of about  $\gamma p_2 M_2^2 = 1$  atmosphere, where  $\gamma$  is the effective specific heat ratio, and  $p_2$  the exit static pressure. In the generator itself, with but a small static gradient at high load, the flow velocity can be decelerated to about 75% of the inlet velocity before boundary layer separation on the electrode wall<sup>(10)</sup> therefore,  $M_1/M_2 = 4/3$  and Eq. (13) becomes

$$\dot{m} = \frac{2W}{\frac{7}{9} \cdot \frac{\eta}{p_2} a_1^2} \quad (14)$$

With the working fluid being employed, Hall coefficients between 2 and 3 are achieved with a field of 20,000 gauss at pressures of the order of 0.4 atm absolute. Values of  $\eta = 0.4$  to 0.5 are appropriate to these values of  $\omega\tau$ . The speed of sound is about 850 m/sec. Thus, a mass flow of 60 kg/sec (132 lbs/sec) is indicated. At a discharge pressure of 0.4 atmospheres the channel exit diameter is 0.9 meters. The channel length required to achieve a flow deceleration to 75% of the initial velocity is approximately 4 meters using  $N_2/O_2 = 1$  for the oxidizer, and a seed concentration of 0.5% K by weight. The indicated combustion pressure is 10 atm.

The basic operating parameters for the original LORHO Pilot power supply design were selected on the basis of the above analysis. These parameters are summarized in the Table below:

Design Operating Conditions for 20,000 kilovolt  
LORHO Pilot MHD Power Supply

Fuel	Medium Fuel Oil
Oxidizer	$N_2/O_2 = 1$ (gas) *
Seed	0.5% K, KOH in methanol or water
Total Mass Flow	60 kg/sec
Magnetic Field	19,000 gauss
Combustion Pressure	10 atm absolute
Output Voltage	10,000 volts
Output Current	2,000 amperes
Channel Inlet Mach Number	2.5
Channel Inlet Pressure	0.5 atm absolute
Channel Inlet Velocity	2100 m/sec
Channel Inlet Temperature	2450°K

The following considers the detailed aerodynamic design of the generator channel.

$$* \text{ air } N_2/O_2 = \frac{80\%}{20\%} = 4$$

i.e.  $O_2$  from 20% by vol. to 50% by vol.

## 2. ANALYSIS OF THE MHD CHANNEL FLOW

A number of iterations in the methods of channel flow analysis have taken place since the beginning of the LORHO program. It seems pointless to describe all of these here. Rather, the method of analysis presently used is given here, and detailed comparison with experiments is described after relating particulars of channel construction. Two channel-diffuser configurations were employed; the second configuration evolved as the result of experience gained on the first series of approximately twenty three performance tests.

Comparisons of detailed analytical performance calculations and experimental data for large scale MHD generators with one megawatt or more in electrical power output and operating in the segmented Faraday electrode mode have been reported.<sup>(3, 4)</sup> Good agreement between experimental and analytical results was achieved. Discussion of Hall generator results for a 1 MW machine has been published previously.<sup>(11)</sup>

The analysis in this application is different than was previously applied to the Faraday generator.<sup>(3, 4)</sup> It is assumed that the flow is developing rather than fully developed. The flow is divided into an inviscid core occupying most of the channel area and a boundary layer confined to the immediate vicinity of the channel walls. Boundary-layer displacement thicknesses are calculated from momentum integral equations for both electrode and insulator walls, taking into consideration shape factor, compressibility and wall cooling effects. Wall-roughness effects on the skin friction are also included. The energy equation for the boundary layer is not solved. In the present application, the electrical dissipation in the boundary layer is relatively small compared to the wall heat transfer rate and, the usual (no MHD) compressible flow relation between velocity and enthalpy should be sufficiently accurate. A detailed discussion of the boundary layer calculations are given in Appendix I.

The performance characteristics, in particular the Hall voltage, of the Hall generator are more sensitive to nonuniformities in the flow than the Faraday generator characteristics. In the present work, approximate nonuniformity effects are included. Nonuniformities in velocity, electrical conductivity, and Hall parameter in the vicinity of both the electrode and insulator walls are treated. Performance degradation due to finite segmentation and  $\vec{j}_x \times \vec{B}$  forces<sup>(12)</sup> are also considered.

The plasma is assumed to be in chemical equilibrium at the local conditions at all points in the flow field. Since the plasma consists of combustion products, the electron density is assumed to be in Saha equilibrium at the translation temperature of the plasma. In the analysis, both the thermodynamic and the transport properties of the gas mixture are required. The thermodynamic equilibrium properties of the combustion products, considering the fifty most important species, were calculated as a function of temperature and pressure by the method outlined in Ref. 13. The electrical conductivity  $\sigma$  and the Hall parameter  $\omega\tau$  were evaluated as a function of temperature and pressure using Frost's

approximation<sup>(14)</sup> with the effects of electron attachment to OH and other species included and accounting for magnetic field strength effects.<sup>(15, 16)</sup> The viscosity  $\mu$  was evaluated using Wilke's mixture rule and the first approximation of the Chapman-Enskog expansion with Lennard-Jones' potentials for the individual species except for H<sub>2</sub>O where an experimental correlation was used.<sup>(17)</sup>

The governing equations for the inviscid core flow can be written as:

Continuity

$$\dot{m} = \rho_1 u_1 A_1 \quad (15)$$

Momentum

$$\rho_1 u_1 \frac{du_1}{dx} + \frac{dp_1}{dx} = j_{y1} B \quad (16)$$

Energy

$$\rho_1 u_1 \left( \frac{dh_1}{dx} + u_1 \frac{du_1}{dx} \right) = j_{x1} E_{x1} + j_{y1} E_{y1} \quad (17)$$

where  $x$  = axial distance,  $y$  = transverse distance in the  $\vec{u} \times \vec{B}$  direction,  $\dot{m}$  = mass flow,  $\rho$  = gas density,  $u$  = gas velocity,  $A$  = area,  $p$  = static pressure,  $h$  = enthalpy,  $B$  = applied transverse magnetic field strength,  $j$  = current density, and  $E$  = electric field strength. The subscript 1 means inviscid core values, and the subscripts  $x$  and  $y$  indicate vector components.

The momentum integral equation for compressible flow applicable to MHD generator problems becomes,

$$\frac{d\theta}{dx} + (2+H) \frac{\theta}{u_1} \frac{du_1}{dx} + \frac{\theta}{\rho_1} \frac{d\rho_1}{dx} = \frac{c_f}{2} - \int_0^\delta \frac{(j_{y1} - j_y)B}{\rho_1 u_1} d\ell \quad (18)$$

where  $\theta$  = momentum thickness,  $H$  = compressible shape factor,  $\delta$  = boundary-layer thickness,  $\ell$  = distance from surface, and  $c_f$  = friction factor. Rough-wall friction factors are used, and the level of roughness chosen depends on the condition and construction of the channel walls. The last term on the right in Eq. (18) is the only term where the MHD effects appear explicitly. Since  $j_y$  on the average is constant through the electrode boundary layer, the MHD term vanished in that case. However, for the insulator wall this term gives rise to the Hartmann effect.<sup>(17)</sup>

In Eq. (18), a solution for the shape factor in terms of the other parameters is required. For compressible turbulent boundary layers, no really useful method for determining the shape factor are available.

However, for incompressible flows several empirical correlations are in use as for instance Garner's equation. No correlations account for MHD effects. In lack of established formulations, the following procedure has been applied. The incompressible shape factor  $\bar{H}$  was calculated as a function of the momentum thickness and core properties in accordance with Garner's equation. Garner's equation is

$$\left(\frac{\rho_1 u_1 \theta}{\mu_1}\right)^{1/6} \theta \frac{d\bar{H}}{dx} = e^{5(\bar{H}-1.4)} \left[ - \left(\frac{\rho_1 u_1 \theta}{\mu_1}\right)^{1/6} \frac{\theta}{u_1} \frac{du_1}{dx} - 0.0135 (\bar{H}-1.4) \right] \quad (19)$$

As in incompressible (no MHD) boundary-layer theory,  $\bar{H}$  is here used both as an approximate separation criteria ( $\bar{H} < 1.8$ ) and as a means of establishing approximate velocity profiles,  $u/u_1 = (\ell/\delta)^{2/\bar{H}-1}$ . To evaluate  $H$ , the density profile is also required. Crocco's relation for a compressible flow with zero pressure gradient and with a Prandtl number of one gives

$$\frac{h}{h_1} = \frac{h_w}{h_1} + \left(1 - \frac{h_w}{h_1} + \frac{u_1^2}{2h_1}\right) \frac{u}{u_1} - \frac{u_1^2}{2h_1} \left(\frac{u}{u_1}\right)^2 \quad (20)$$

With this  $h$ -distribution and with constant pressure through the boundary layer, the density profile is then determined from the chemical equilibrium calculations. The usual integrations can now be performed to obtain the value of  $H$ . Since no detailed boundary layer measurements exist for this flow, the accuracy of this technique cannot be assessed at this time. However, it appears to be adequate for the prediction of performance in the present application as well as in earlier work.<sup>(11)</sup> A more detailed discussion of the boundary layer calculations appears in Appendix I.

The treatment of the nonuniformity effects will be discussed next. The effects of the boundary layer profiles are accounted for by using appropriate average values in Ohm's law. It is assumed that  $E_x$  is uniform across the channel and that  $j_y$  is constant through the electrode boundary layer and that  $E_y$  does not vary through the insulator boundary layer. Treating the two boundary layers separately and defining the loading parameter as

$$a = \frac{\langle \omega \tau \rangle \langle j_x \rangle}{\langle \sigma \rangle u_1 B} \quad ,$$

one obtains for the electrode boundary layer

$$\frac{E_x}{u_1 B} = - \frac{\langle \omega \tau \rangle}{G} \left[ \frac{\langle u \rangle}{u_\infty} - a - \frac{a G}{\langle \omega \tau \rangle^2} - \frac{E_{y \text{ el. d.}}}{u_1 B} \right] \quad (21)$$

and

$$\frac{j_y}{\langle \sigma u_1 B \rangle} = - \frac{1}{G + \langle \omega \tau \rangle^2} \left[ \frac{\langle u \rangle}{u_1} - \frac{\langle \omega \tau \rangle E_x}{u_1 B} - \frac{E_{y \text{ el. d.}}}{u_1 B} \right] \quad (22)$$

where

$$G = \langle \sigma \rangle \left\langle \frac{1 + \omega \tau^2}{\sigma} \right\rangle - \langle \omega \tau \rangle^2 \quad (23)$$

and for the insulator boundary layer

$$\frac{E_x}{u_1 B} = - \frac{\left\langle \frac{\sigma \omega \tau}{1 + \omega \tau^2} \right\rangle}{\left\langle \frac{\sigma}{1 + \omega \tau^2} \right\rangle} \left[ \frac{\left\langle \frac{\sigma \omega \tau u}{1 + \omega \tau^2} \right\rangle}{\left\langle \frac{\sigma \omega \tau}{1 + \omega \tau^2} \right\rangle u_1} - \frac{\langle \sigma \rangle a}{\langle \omega \tau \rangle \left\langle \frac{\sigma \omega \tau}{1 + \omega \tau^2} \right\rangle} - \frac{E_{y \text{ el. d.}}}{u_1 B} \right] \quad (24)$$

and

$$\frac{\langle j_y \rangle}{\langle \sigma \rangle u_1 B} = - \frac{\left\langle \frac{\sigma}{1 + \omega \tau^2} \right\rangle}{\langle \sigma \rangle} \left[ \frac{\left\langle \frac{\sigma u}{1 + \omega \tau^2} \right\rangle}{\left\langle \frac{\sigma}{1 + \omega \tau^2} \right\rangle u_1} - \frac{\left\langle \frac{\sigma \omega \tau}{1 + \omega \tau^2} \right\rangle}{\left\langle \frac{\sigma}{1 + \omega \tau^2} \right\rangle} \frac{E_x}{u_1 B} - \frac{E_{y \text{ el. d.}}}{u_1 B} \right] \quad (25)$$

The  $\langle \rangle$  sign stands for average values across the channel in either the direction across the electrode or insulator boundary-layers. The same velocity and enthalpy distributions as discussed previously are used in these integrations. The profiles of  $\sigma$  and  $\omega \tau$  were obtained from the equilibrium calculations. The effects of transverse pressure gradients set up by the  $\vec{j}_x \times \vec{B}$  force in the inviscid core are calculated in a similar fashion as discussed in Ref. 12. However, both conductivity and Hall parameter variations are included. The effect of finite segmentation has been estimated from previous work (4, 18) indicating that this effect is small in the present application. It is observed that this effect is equivalent to  $G = 1 + \omega \tau \cdot s/h$  and  $u/u_1 = 1$  for the situation where the electrode width is small compared to the electrode pitch  $s$ .  $h$  is the channel dimension in the  $\vec{u} \times \vec{B}$  direction. The combined effect of these nonuniformities is approximated by considering the "effective leakage resistances" in the  $x$  and  $y$  directions of the different nonuniformities to be in a parallel connection shorting out the channel core. No acoustic instability phenomena<sup>(19)</sup> have been included since the observed generator outputs were stable under normal operating conditions.



The conservation of electricity is satisfied by requiring that  $I_x = \langle j_x \rangle A$ , where  $I_x$  = total Hall current and  $A$  = actual channel area. The electrical power output is equal to  $-I_x \int_0^L E_x dL$ , where  $L$  = channel length.

To solve this problem, the differential equations are expressed in terms of derivatives in  $x$  and solved by a four point Runge-Kutta integration procedure on a digital computer.

A number of Hall channel configurations were analyzed in detail in order to arrive at what was believed to be an optimum loft for the channel area profile so as to operate within the four restrictions discussed in III.A and still achieve the desired output. The initial calculations were based on the use of fuel oil with a hydrogen carbon atomic ratio (H/C) of 1.44 as the fuel, a magnetic field of 17,000 gauss and assuming for pressure recovery a simple cylinder as the supersonic diffuser with a  $3^\circ$  diverging subsonic diffuser at the downstream end. These initial calculations indicated that the operating conditions described in Section III.1 would lead to about a 10 percent performance margin over the design goal with boundary layer still limiting the design. However, as more details were considered in the analysis, and as data from the Mark II Hall generator experiments began to come in, it became clear that the design with heavy fuel oil was, at best, marginal, and very sensitive to the precise properties of the gas which were probably only known to 15-20%. The performance was particularly sensitive to errors in Hall parameter. Some indication of the difficulty is seen from Fig. 13 which shows the rapid rise in shape factor  $\bar{H}$ , temperature and boundary layer thickness near the end of the channel. Note particularly how the electric field (slope of the voltage) is much reduced at the channel inlet. It can be shown that if the real  $\omega\tau$  is 10% less than the calculated value at a calculated value of 2.2, the generator will be at short circuited at the channel inlet. The design also seemed sensitive to wall friction coefficient. Accordingly, it was deemed necessary to change to a fuel with a lower value of H/C in order to increase the Hall coefficient. This is the source of the choice of toluene,  $C_7H_8$ ,  $H/C = 1.14$ . With the toluene, it was again possible to arrive at a channel design with an indicated performance equal to the design goals.

As will be seen, this "as built" channel actually produced 16,000 kw at 80% of the design mass flow, and was then modified after the initial series of performance evaluation runs. The actual loft of both the original and modified nozzle-channel-diffuser combinations is indicated in Fig. 14. Both versions utilized the same nozzle, with an exit diameter of 28" equal to the channel inlet diameter. The original channel had a length of 157" and an exit diameter of 36" while the modified channel utilized a length of 185", and an exit diameter of 40", the maximum permitted by the magnet aperture. The original diffuser is discussed above. The modified diffuser employed a converging section so as to mate up with the original diffuser with the 36" inlet. However, due to a water jacket failure at the beginning of the test program with the modified channel, the original diffuser was shortened to the length indicated.

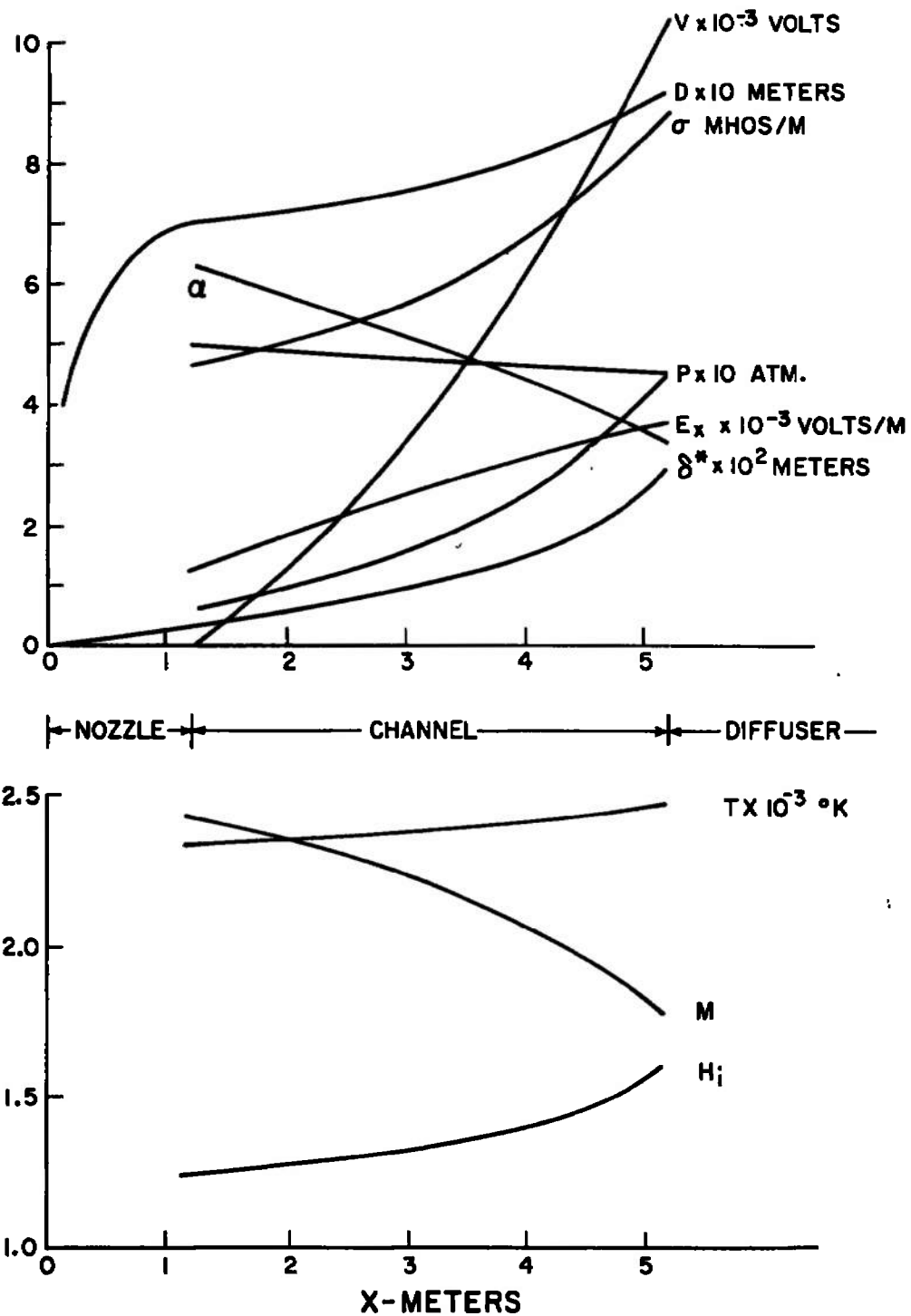


Fig. 13 Calculation Variation of Flow Parameters with Channel Axial Station for Original MHD Power Supply Design

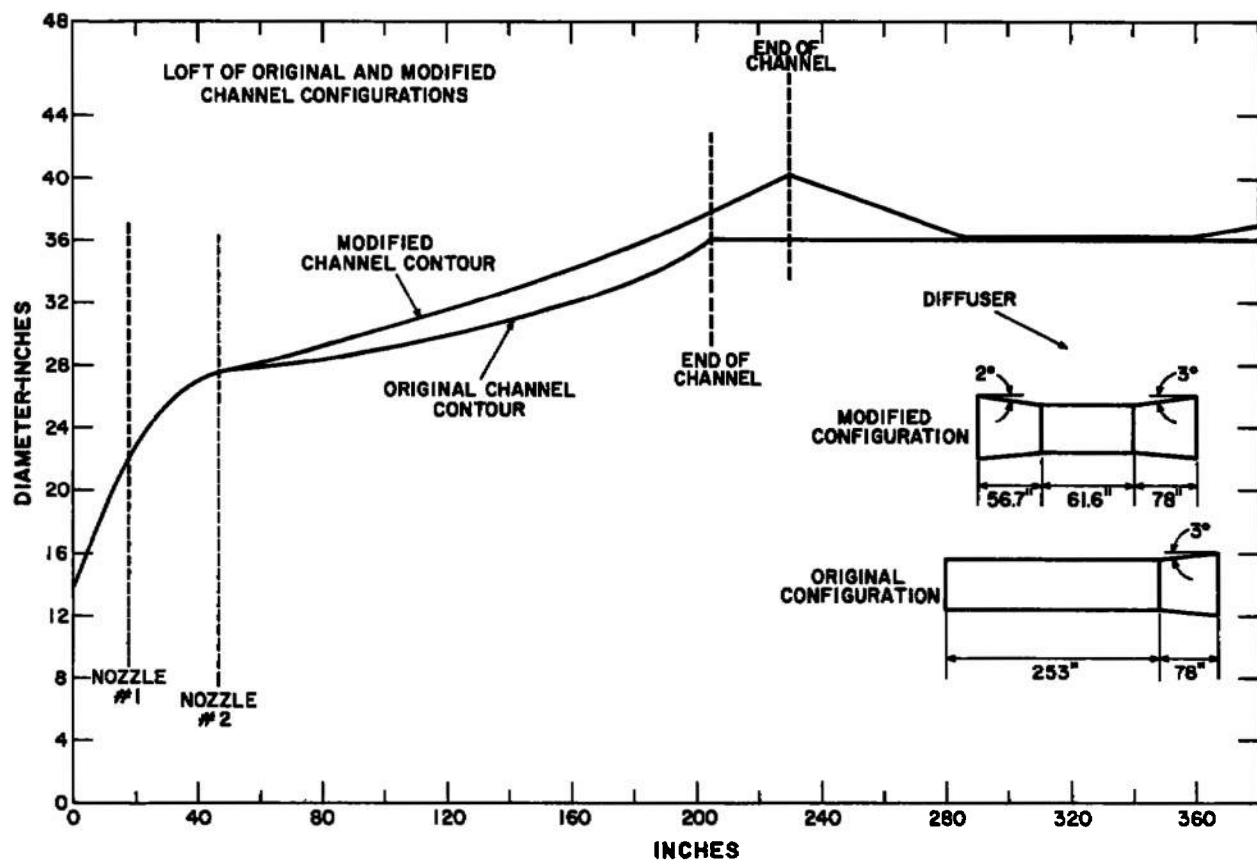


Fig. 14 Loft of Original and Modified MHD Generator Channel-Diffuser Configurations

Such a length is marginal for a supersonic diffuser. In addition, due probably to the thick, unstable boundary layer at the channel exit, the convergence from 40" to 36" is excessive since the expected boundary layer contraction due to the cold diffuser wall apparently was not fully achieved. As we will see, these two factors rather than boundary layer stall in the channel itself caused some difficulty during evaluation of the modified configuration.

Further calculations considered the off design performance of the MHD channels. The results of these calculations are described in Section IV in connection with the discussion of the match up of generator and accelerator. It will be seen there that the unique constant current characteristics of the Hall MHD generator are especially suited to loads such as MHD accelerators and arcs.

An overall sketch showing the complete original configuration from burner through diffuser is shown in Fig. 15 and an overall plan view of the equipment showing magnet configuration and exhaust breeching in relation to the channel in Fig. 16. Although engineering details of the LORHO generator construction will be presented shortly, these figures are shown here to indicate the result of translation of MHD channel flow analysis into actual hardware. In terms of generating volume, the unit is the largest MHD generator ever constructed.

#### A. Supporting tests

Certain experimental tests were conducted to support the analytical work described above. These were to evaluate a) diffuser pressure recovery and b) electrode configuration.

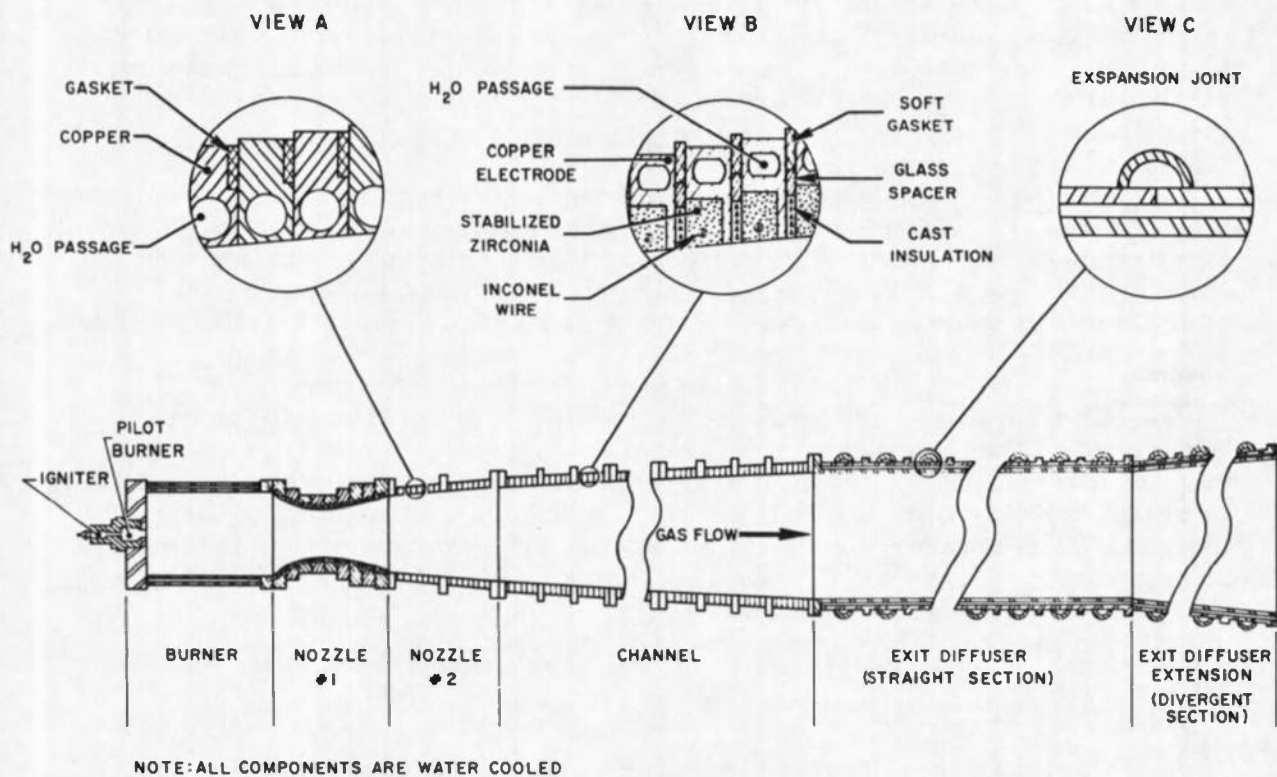
##### 1. Diffuser Pressure Recovery

The diffuser pressure recovery tests were conducted using room temperature compressed air and were designed to evaluate both starting conditions where the diffuser inlet Mach number would be 2.88, and the running conditions where the inlet Mach number is lower. Results for the original configuration are shown in Figs. 17 and 18, and indicated adequate recovery, although it must be noted that the highly cooled wall and adverse shape factor of the actual generator flow could lead to more difficult inlet conditions than those studied in these tests.

##### 2. Electrode Configuration

The AERL Long Duration Test Facility (LDTF) was utilized both for tests to estimate electrode drop for the performance analysis, and to evaluate the durability of electrode configurations in the working environment.

Test configurations of the LORHO Generator electrodes were fabricated using a small scale 4" diameter model. A number of tests were performed with these configurations to evaluate electrode performance and endurance in a long duration combustion gas environment at the appropriate



CROSS SECTION OF LORHO PILOT GENERATOR

Fig. 15 "As Built " Configuration of the MHD Generator

LORHO PILOT MHD GENERATOR

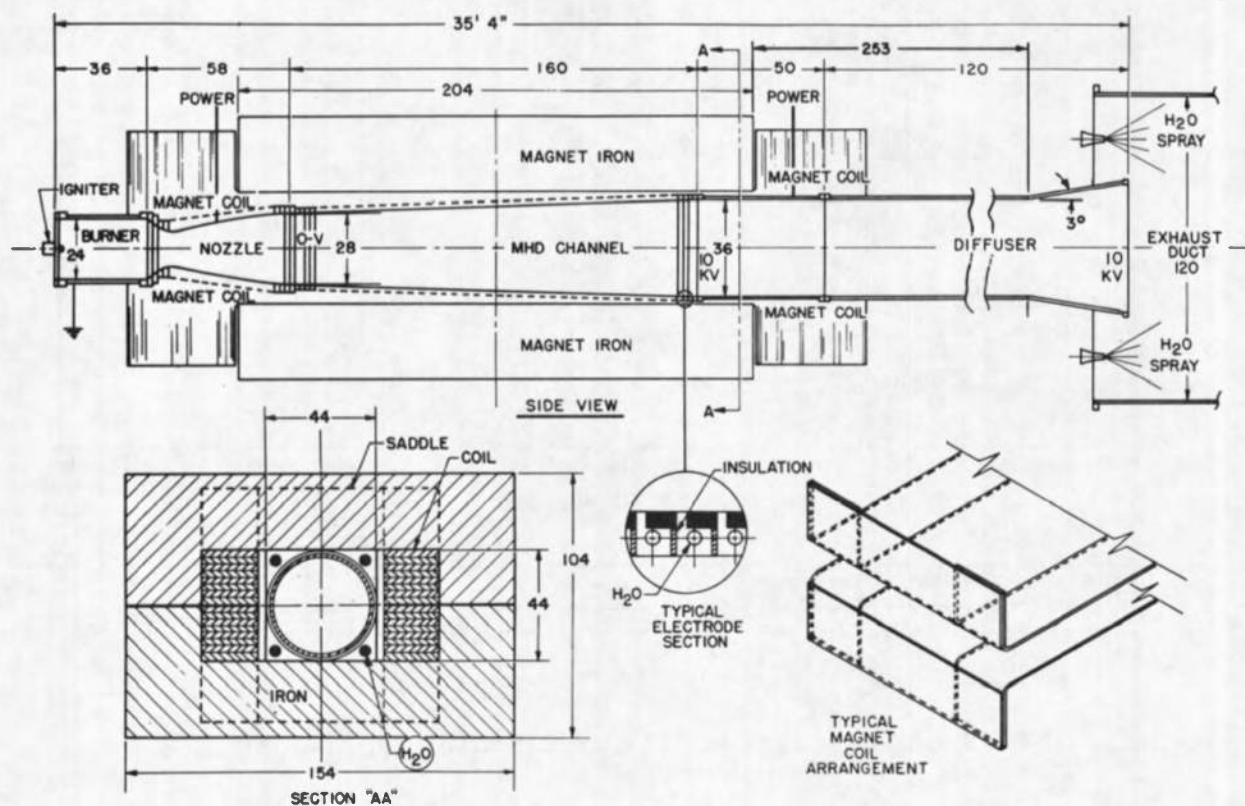


Fig. 16 Plan View of "As Built" Configuration Showing Location of Major Components

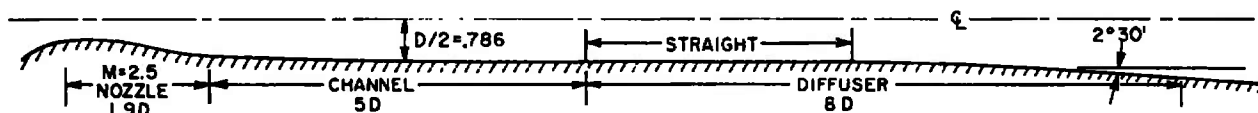
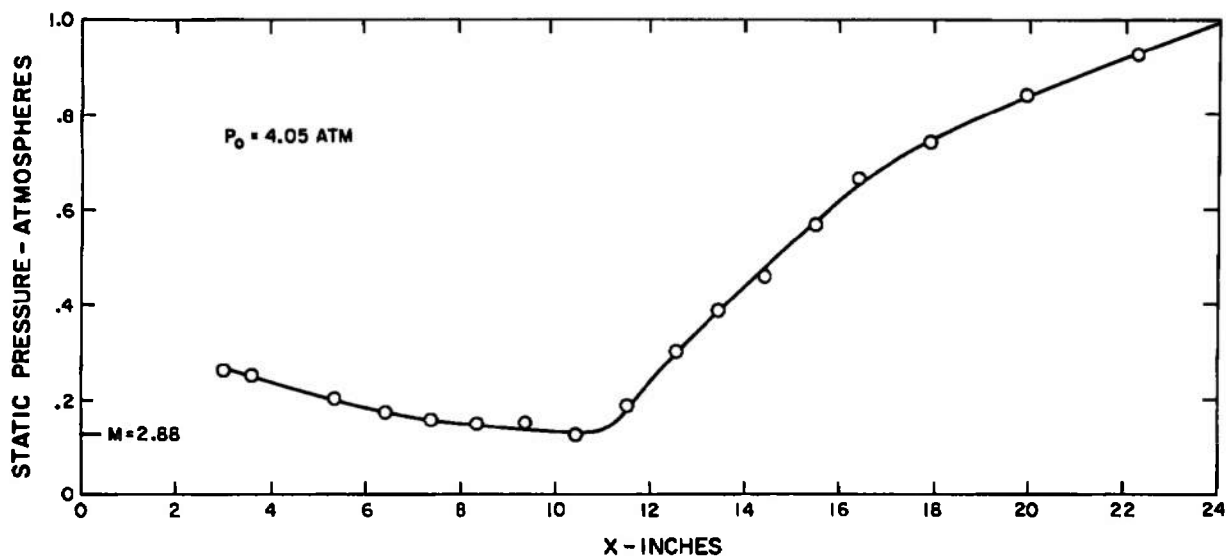


Fig. 17 Diffuser Recovery at an Inlet Mach Number of 2.88

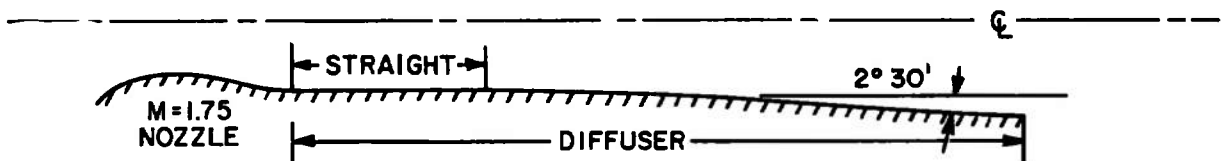
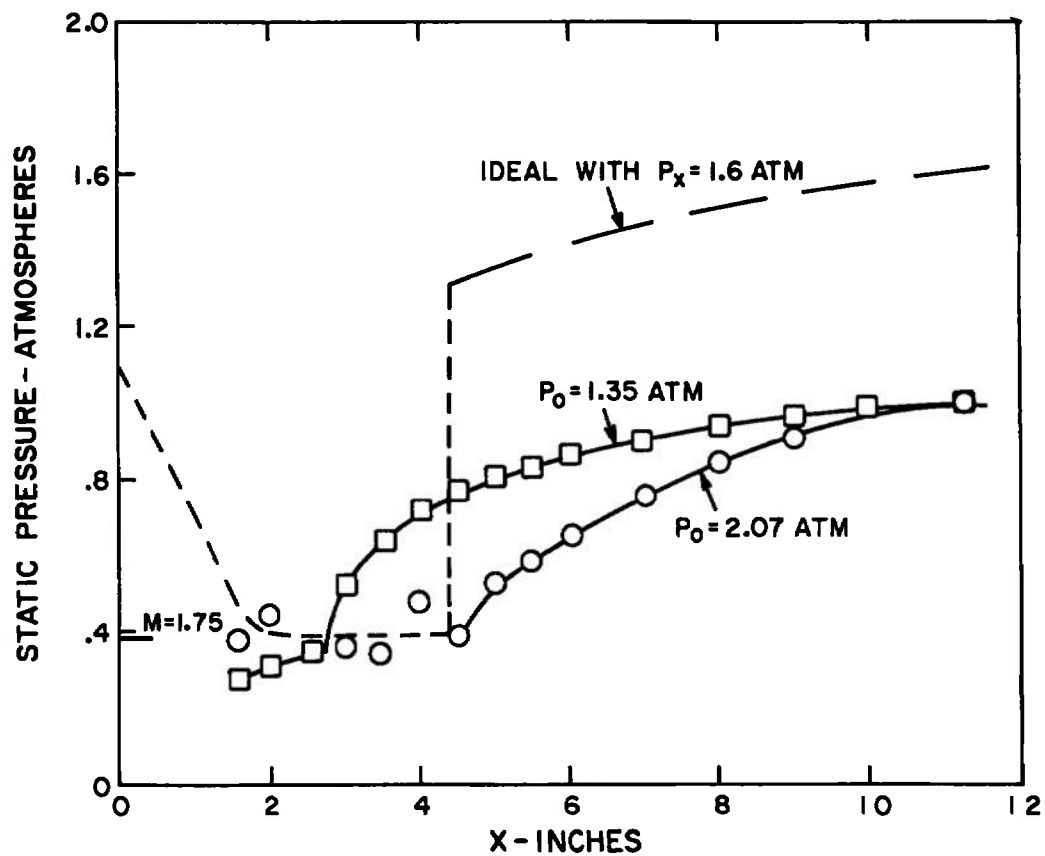


Fig. 18 Diffuser Recovery at an Inlet Mach Number of 1.75



heat transfer rates. The photograph of a typical section tested is shown in Fig. 19 and shows only slight attrition of the electrode surfaces after 4.4 hours exposure to the hot test gas. This electrode section consists of 10 copper rings which are assembled in the center of a Hall channel configuration having a total of 42 rings. A magnetic field of 18 Kilogauss is imposed and the  $N_2/O_2$  ratio of the burner can be varied to produce heat transfer rates from about  $1/4$  to  $1/2$  million Btu/Hr/Ft<sup>2</sup>, the inlet and outlet heat transfer rates respectively for the LORHO generator channel. The LDTF is shown in operation in Fig. 20 with the channel installed.

Test results for the original design configuration chosen are shown in Fig. 21. The axial voltage gradient measured during the test defines the performance of the electrode as regards its capacity to circulate the transverse current. The circulation of the transverse current is augmented by insertion of a .060" thick stainless steel wire imbedded circumferentially in the zirconia electrode material. Maximum voltage gradient was 3400 volts/meter. A number of runs were made to evaluate prefired sintered zirconia versus castable type, strip wire versus wire inserts, and welded versus silver-soldered or riveted attachments. The prefired ceramic did not appear to have any advantage over the castable type which can be troweled into the grooves easily. A number of runs of extended duration were directed towards establishing the most optimum position of the electrical conduction piece imbedded circumferentially in the zirconia electrode material. Stainless steel wires of different diameters at various depths below the surface were tested to determine the best performance regarding axial voltage sustained and lifetime. A .060" wire size seems the most suitable, imbedded approximately .050" below the surface. A number of cyclic runs were performed on this configuration to establish durability. These runs in general have been about three minutes of hot operation, about five minutes of shutdown, with the cycle repeated for about 20 cycles. Performance runs at 3300 to 3400 volts/meter axial voltage gradient were obtained and performance on some tests displayed gradients up to 4000 volts/meter. A discussion of the electrode configuration used in the modified channel is discussed below.

### 3. MECHANICAL DESIGN OF THE MHD POWER SUPPLY

One of the advantages of a Hall current MHD channel is the relative simplicity of the structural design. This advantage is further reflected in construction, assembly, and maintenance operations that are easier and quicker than on either a Faraday or diagonal-type channel.

The circular ring type construction chosen for the LORHO channel offers the following advantages:

1. Circular geometry is compatible with the more conventional burner, nozzle, and diffuser designs thus eliminating complicated and costly transition sections.
2. A circular structure offers optimum buckling resistance to the cooling water and gas pressure loads.

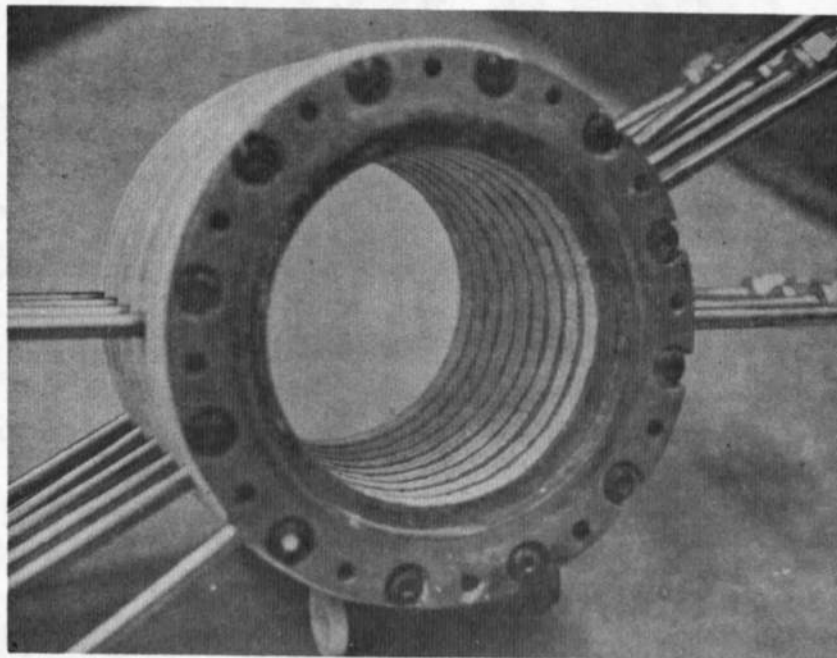


**Fig. 19**    **Ten Electrode Test Section Used for Evaluation of Electrode Configurations for MHD Generator**

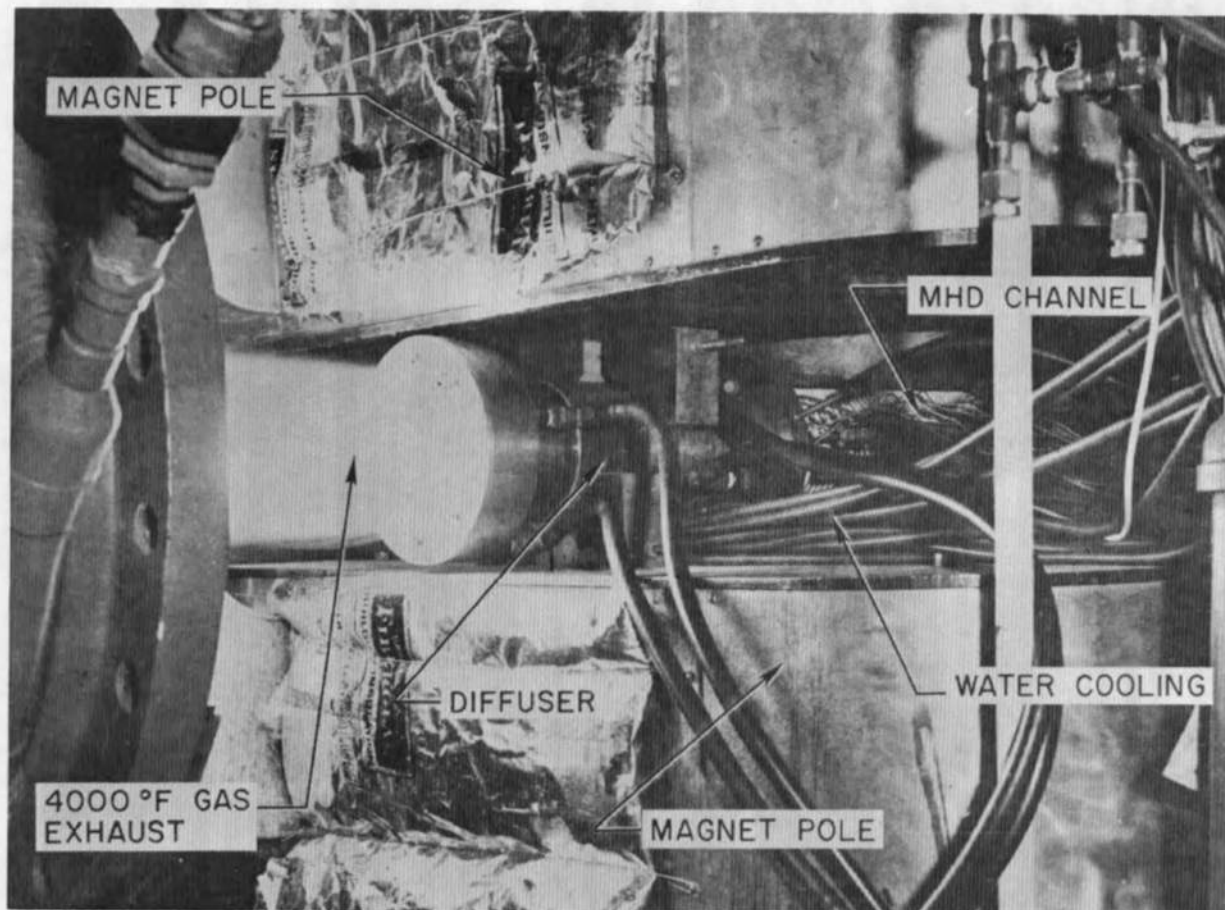


Fig. 20 Long Duration Test Facility (LDTF) Operation for Generator Electrode Evaluation

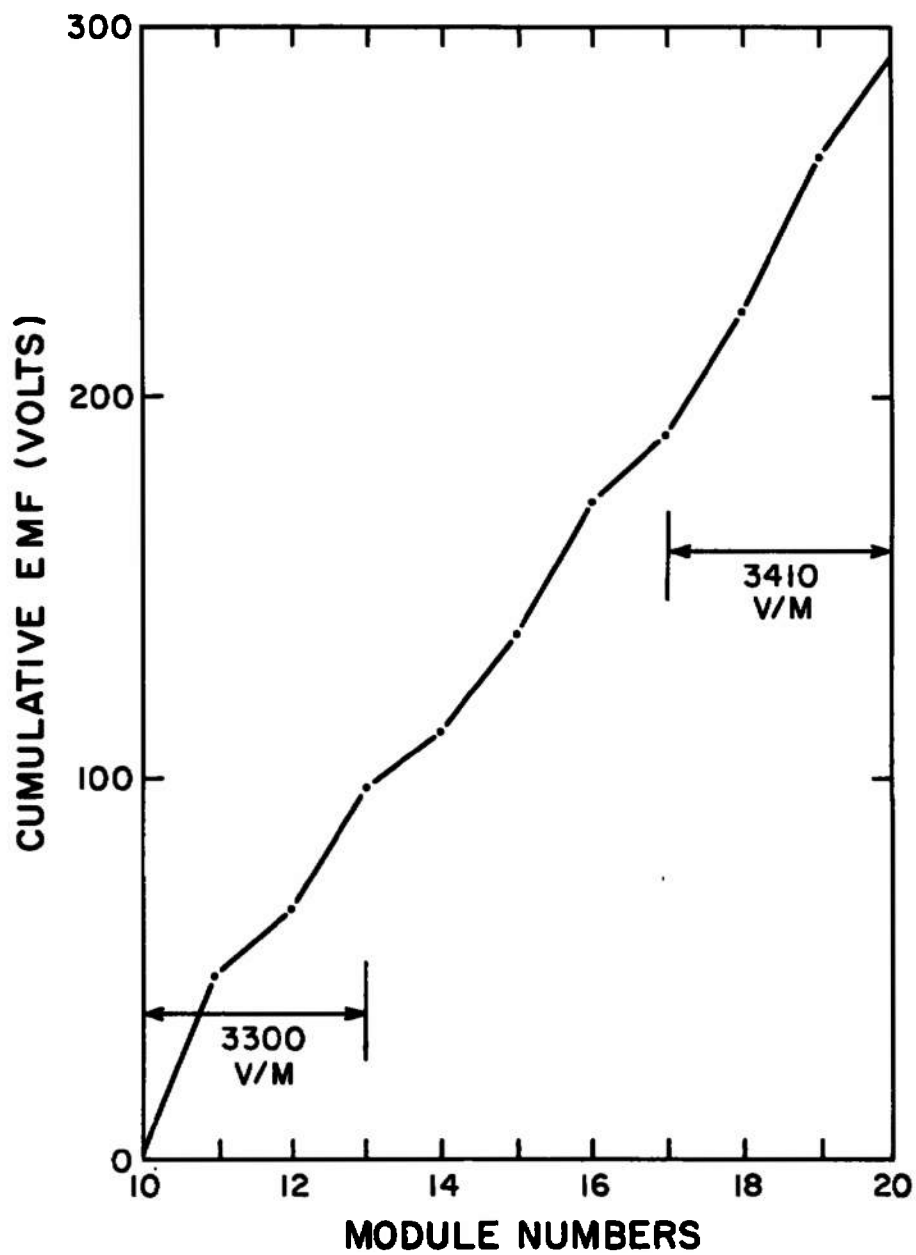


Fig. 21 Some Typical Test Results for the Selected Electrode Configuration

3. The individual rings provide a natural short circuit path for the  $I_y$  currents.
4. The rings can be separately water cooled eliminating risky water seals.
5. All gas seals are circular gaskets with no requirement for sealing the three dimensional corners of a box structure.
6. Individual rings are conducive to modular type construction where the channel can be subdivided into self-contained sections, any one of which can be disassembled without disturbing the others.

Now these advantages are not gained without the necessity of some trade-off compromises -- for example:

1. A circular channel does not make the most effective use of a rectangular field volume. A circular magnet window would increase the generator cost noticeably. However, the unoccupied portion of the aperture provides space for the water cooling manifold.
2. Each ring must be fabricated to a different diameter to accommodate the required area change.
3. The upper limit on segmentation will be reached slightly sooner in a ring-type as opposed to a flat-wall type channel.

The LORHO channel is constructed from OFHC copper extrusions of  $3/8'' \times 3/4''$  cross-section with a  $3/16''$  diameter centrally located cooling passage. Figure 22 gives dimensioned section details with material specifications for a typical electrode pair assembly. A  $1/4''$  deep electrode groove is milled into each bar prior to rolling and silver brazing into a complete ring. The electrode material is a mixture of 15% zirconium diboride and 85% zirconium oxide. The  $ZrO_2$  is stabilized with 5% calcium oxide. This ceramic mixture is manually troweled into the electrode groove and then oven cured at  $200^\circ F$  for two hours.

The optimum groove depth was approximated both theoretically and experimentally for various gas conditions as described previously. At a LORHO channel heat flux of  $0.2 \times 10^6$  Btu/hr/ft<sup>2</sup> the surface temperature of the zirconia electrode is expected to be above  $3000^\circ F$ . An inconel wire is positioned below the ceramic surface to a depth where its temperature will be approximately  $2000^\circ F$  -- safely below its melting point but still in the relatively low resistivity area of the zirconia. Inconel was chosen for its excellent high temperature oxidation resistance. It has been estimated that when the LORHO channel operates at its average current density of 0.5 amps/cm<sup>2</sup> the cathode temperature will be approximately  $150^\circ F$  less than the anode due to the cooling effect from electron emission. The inconel wires were short sections with a single center attachment to the copper ring. The free ends however, tended to move under the thermal stress and this differential expansion would lift out the zirconia above the wire.

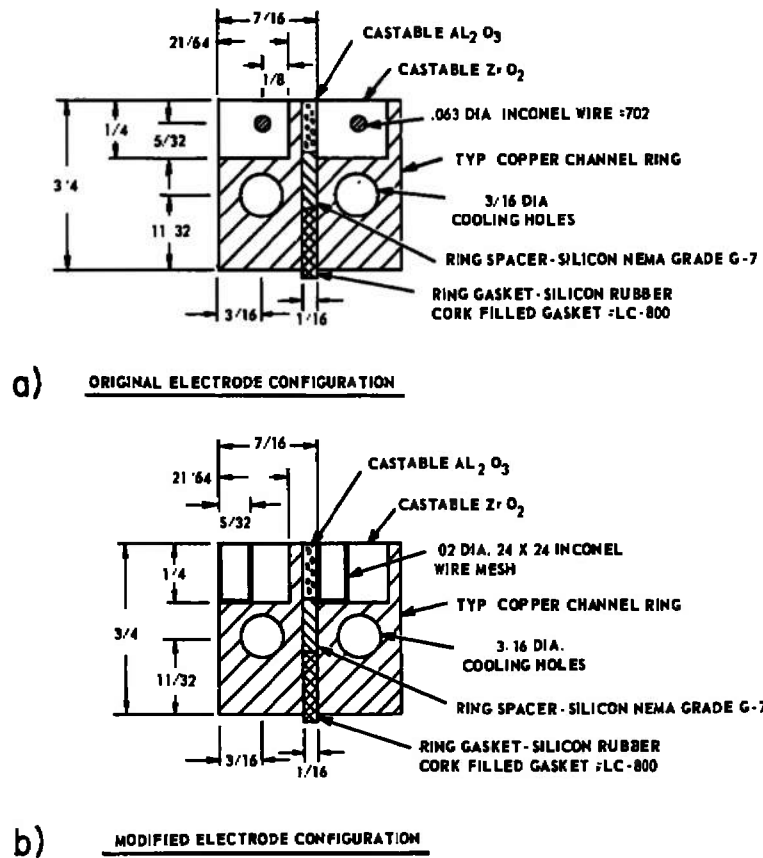


Fig. 22 Original and Modified Generator Electrode Configurations

Continued loss of electrode material during each test run and the subsequent repacking became such an inconvenience that a modification (see Fig. 22 ) was tested and proved very successful. The wires were replaced with "U" shaped rings of inconel wire mesh brazed to the bottom of the electrode groove. This construction provides a tenacious retaining surface for both the zirconia electrode and alumina insulator ceramics and also effectively doubles the L/D of the electrode groove while still retaining the low resistance current transfer point between the zirconia and the metal.

The rigid silicon spacers between rings are required to keep a constant electrode pitch and to insure the proper compression of the rubber-cork gaskets which provide the gas seal.

The 4 meter channel length of the original configuration is divided into 360 rings with a pitch of  $7/16$ ". The segmentation is chosen to keep the voltage between adjacent electrodes at 40 or less. The rings are assembled into flanged subsections of 30 each. Figure 23 is a photo of an assembled subsection being aligned with the rings of the adjoining subsection prior to their assembly. Three such subsections constitute a major section (90 rings) of which there are four in the channel. Figure 24 is a photo of an assembled major section showing a technician troweling in aluminum oxide insulating refractory between electrodes (see Fig. 3 ). The electrode surfaces have been covered with masking tape prior to this operation. Non-conductive glass epoxy tie bolts and spacer sleeves are used to hold the minor subsections together as well as to each other. The resultant major sections are joined to each other by a simple bolt flange. Details of this method of construction are shown as a sketch in Fig. 25 , while Fig. 26 , is a photograph of the completed channel and expansion section of the supersonic nozzle. This photo also shows the details of the channel mounting base and rollertrack transfer cart for conveying the generator in and out of the magnet which is equipped with a similar rollertrack base. The nozzle expansion section, visible in Fig. 26 , is of the similar construction as the channel except the extruded copper rings are somewhat larger cross section and are in metal to metal contact with one another. This insures a smooth and accurately contoured surface for the accelerating gas and also serves as the grounded power take-off terminal for the generator. The high voltage (10 kV) terminal is located in the inlet flange of the exit diffuser.

In addition to the modifications made to the electrodes and described above, operating experience on the MHD generator led to the decision to utilize this rebuild time to also incorporate the following improvements into the channel:

1. The outlet/inlet area ration was less than optimum due to underestimation of the boundary layer thickness. Also, the area profile was not optimum and needed to be opened up in mid channel as shown in Fig. 14 .

These corrections were accomplished by replacing approximately 10% of the channel rings and redistributing the remainder.



Fig. 23      Assembled MHD Generator Channel Subsection of Thirty (30) Ring



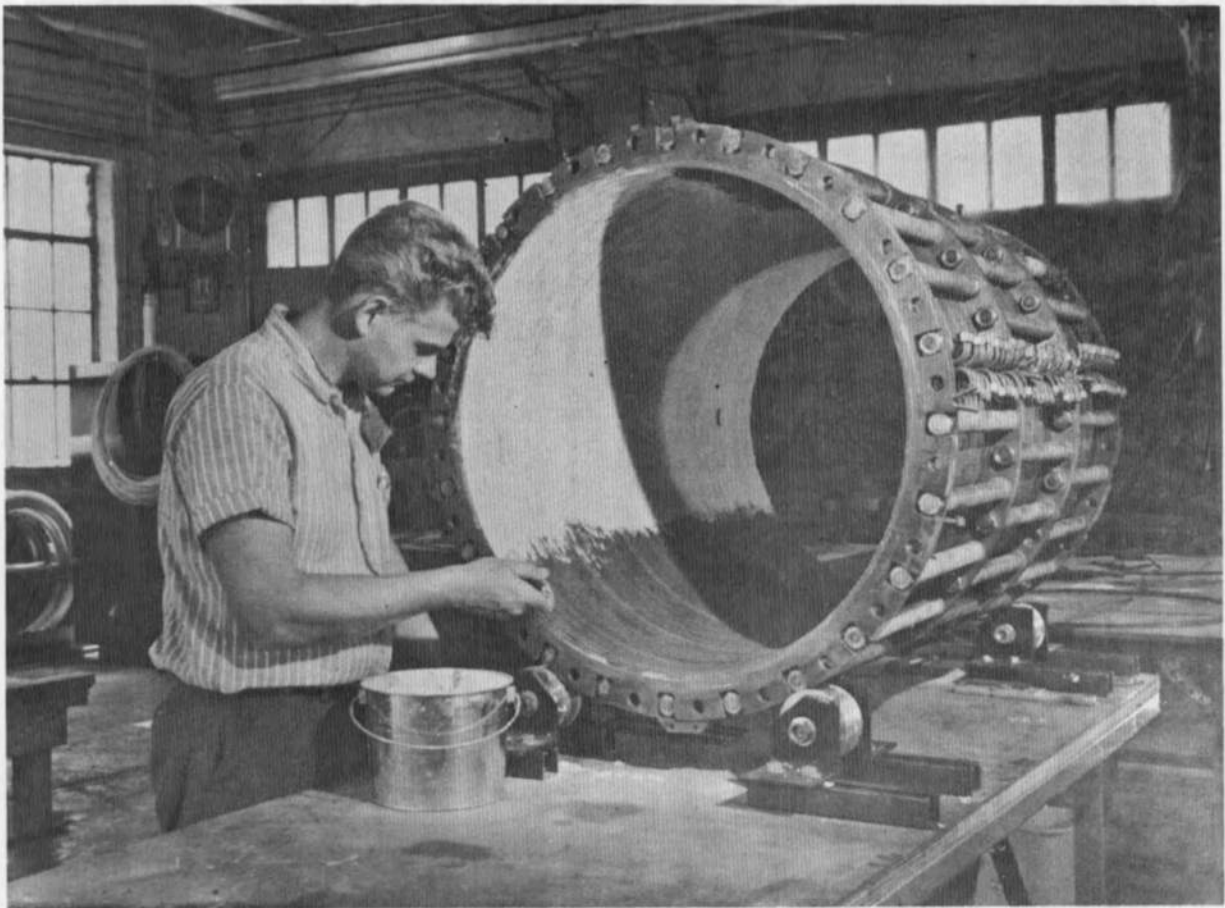


Fig. 24      Assembled MHD Generator Channel Major Section of Ninety (90) Rings

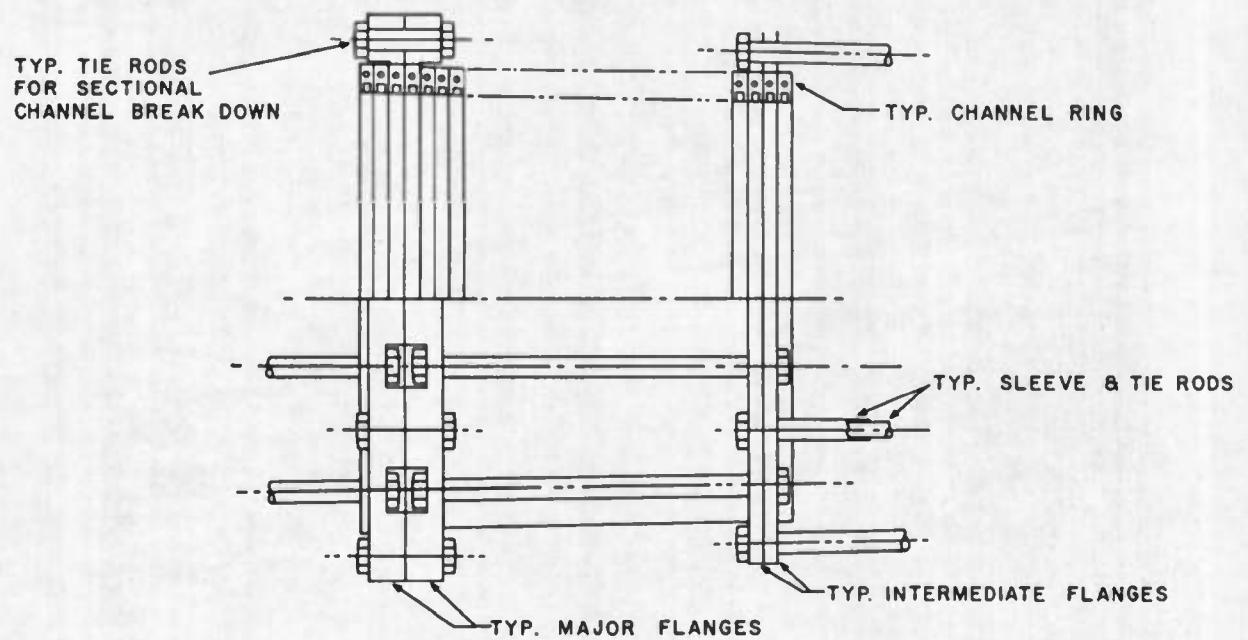


Fig. 25 MHD Generator Channel Assembly Details

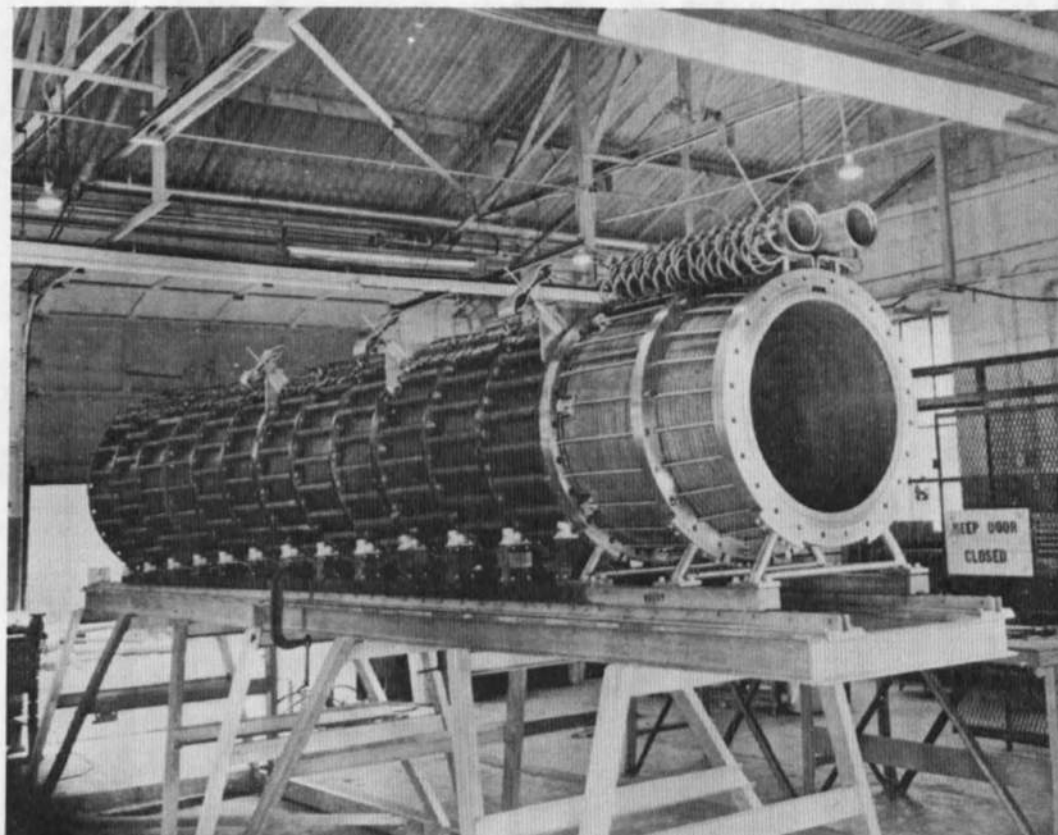


Fig. 26      Completed LORHO Pilot MHD Generator Channel

2. Arcing at both the inlet and exit power take-off areas of the the channel frequently caused local damage to the adjacent modules. Further, there was a performance degradation particularly noticeable from the pressure increase at the inlet end of the channel due to having effectively a short-circuited Hall generator, i.e., the inlet nozzle. To offset both these effects the channel has been lengthened from 4 to 4.68 meters by the addition of a fifth modular section and at least at the downstream edge power can be extracted where the axial electric field is near zero. No difficulty was experienced at the inlet as the electric field there was always quite low due to overestimation of  $\Omega$ .

A dimensioned layout showing the relationship of the modified generator components is shown in Fig. 27.

#### A. Combustion Chamber, Construction and Operating Experience

The design of the rocket-engine type combustion chamber for the RDG has evolved from other experimental MHD programs. In particular, much of the operating experience obtained with the Mark V burner was directly applicable to the LORHO design. The design reflects the two important differences compared with an ordinary rocket engine, high thermal cyclic fatigue capability, and one of a kind "hogged" construction. The design included:

1. Use of a spark ignited continuously operating pilot burner for main chamber ignition. Continuous operation insures against large accumulations of combustible mixtures in the generator in the event of a burner flameout.
2. Use of copper alloys for the highly stressed burner parts. Ductile alloys with high thermal conductivity offer the best choice for good life under the thermal cycling and may be utilized when weight is not an important consideration in the design.
3. All "hot" parts are convectively cooled with back side water pressures always kept higher than combustion pressures to minimize damage from a metal failure.

The design operating conditions with pertinent dimensions and characteristics for the LORHO burner are listed in Table II. Stoichiometric operation with toluene fuel ( $C_7H_8$ ) and a nitrogen-oxygen molar ratio of one ( $N_2/O_2 = 1$ ) at 10 atmospheres stagnation pressure produces a theoretical flame temperature of  $3170^\circ K$ . Actual operation close to this condition corresponded to a theoretical flame temperature of  $3130^\circ K$  with a measured heat loss to the cooling water of approximately 10,000 Btu/sec or 3% of the burner heat release.

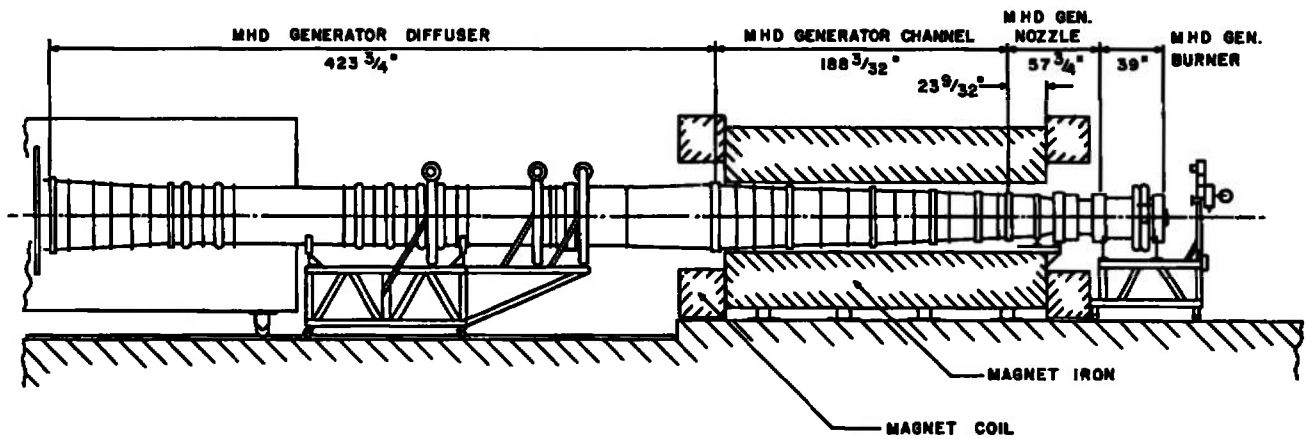


Fig. 27 LORHO Pilot Modified MHD Generator Configuration

**TABLE II**  
**LORHO GENERATOR BURNER**  
**SPECIFICATIONS**

	Main Burner	Pilot Burner	Igniter Burner
Total Mass Flow Rate (lb/s)	132 (60 Kg/s)	0.69	0.015
Fuel	Toluene	Ethane	Ethane
Oxidizer	Gaseous nitrogen/ oxygen mixture	Gaseous oxygen	Gaseous oxygen
Seed	KOH dissolved in methyl alcohol	None	None
Fuel Flow Rate (lb/s)	18.4	0.086	0.0023
Oxygen Flow Rate (lb/s)	58.7	0.322	0.0069
Nitrogen Flow Rate (lb/s)	51.4	0.282	0.0060
Seed Flow Rate (lb/s)	1.32	-----	-----
Methyl Alcohol Flow Rate (lb/s)	2.14	-----	-----
Seed Ratio	1/2 mole % K	-----	-----
Nitrogen/Oxygen Ratio (mole/ mole)	1.0	1.0	1.0
Oxygen/Fuel Ratio (lb/lb)	3.12 (stoic.)	3.74(stoic.)	3.0 (fuel rich)
Chamber Pressure (psig)	147.0(10atm)	252.0	237.0(pilot bur. off) 300.0(pilot bur. lit)
Fuel Pressure (psig)	400.0	500.0	500.0
Oxidizer Pressure (psig)	400.0	500.0	500.0
Chamber Diameter (in.)	24.0	1.5	0.5
Throat Diameter (in.)	13.5	0.75	0.125
Chamber Length (in.)	36.0	2.6	1.5
Contraction Ratio (Chamber area/ throat area)	3.17	4.0	16.0
L*(in.)- Chamber vol./throat area	132.0	12.6	24.0

Original burner design parameters were based on heat flux values calculated for fully developed flow conditions utilizing turbulent boundary layer methods. Resulting values are summarized in Fig. 28 for the igniter, pilot and main chamber liners, and nozzle throats. For comparison purposes typical measured values are indicated for the pilot and main burner during a 100% mass flow run.

Figure 29 is a conceptual drawing of the LORHO burner and nozzle showing to scale pertinent details of construction including material call-outs, cooling water configuration, and backplate propellant injection. The backplate overlaps the upstream end of the burner liner to provide protection in the corner against gas recirculation. In addition, gaseous nitrogen ( $\sim 2\%$  of total flow) is injected at this location to provide cooling action. The backplate proper is a two piece construction, an external stainless steel closure plate and the inner welded construction copper face plate which has a built-in water cooling passage. The intermediate space serves as the oxygen manifold. A series of staybolts are used to provide structural reinforcement between the two plates. The fuel is injected separately from an external manifold through 60 fuel injectors centered in the nitrogen-oxygen sonic orifice ports which are evenly distributed over the area of the backplate (see Fig. 30). A photograph of the backplate injector assembly is shown in Fig. 31.

The burner liner is a fluted cylinder of beryllium copper reinforced with seven welded support rings. In order to maintain adequate cooling water velocity, circumferential aluminum filler blocks are installed between the support rings prior to assembly into an outer stainless steel housing. The liner is free to expand in the axial direction so that the only thermal stress is due to the temperature difference across the liner thickness. Photographs of the liner assembly and burner housing are Figs. 32 and 33 respectively. The completed burner and nozzle assembly mounted on its mobile cart is depicted in Fig. 34.

The contour for the generator nozzle, which is a supersonic axisymmetric shape, must be designed by the method of characteristics for the desired gas conditions. The contour was obtained through the use of an existing three dimensional characteristic computer program available at AEDC. As shown in Fig. 35, this nozzle is mated to the generator channel at a point on the nozzle contour where the wall slope matches the inlet angle of the generator channel power section. A photo of the supersonic section of the nozzle set up for final contour machining is shown in Fig. 36. For convenience of seal design, the mating flange between the burner and channel was chosen at the atmospheric pressure point of the supersonic nozzle. The high pressure side of the nozzle (integrally mounted to the burner housing) is constructed of heavy forged rings of silver bearing copper. The addition of small amounts of silver increases the elevated temperature yield strength of copper by as much as 25%. The individual rings are bolted together and the gas seals are located on the cold side of the cooling water passages. Each ring is individually cooled via slots milled parallel to the gas surface (see Fig. 29).

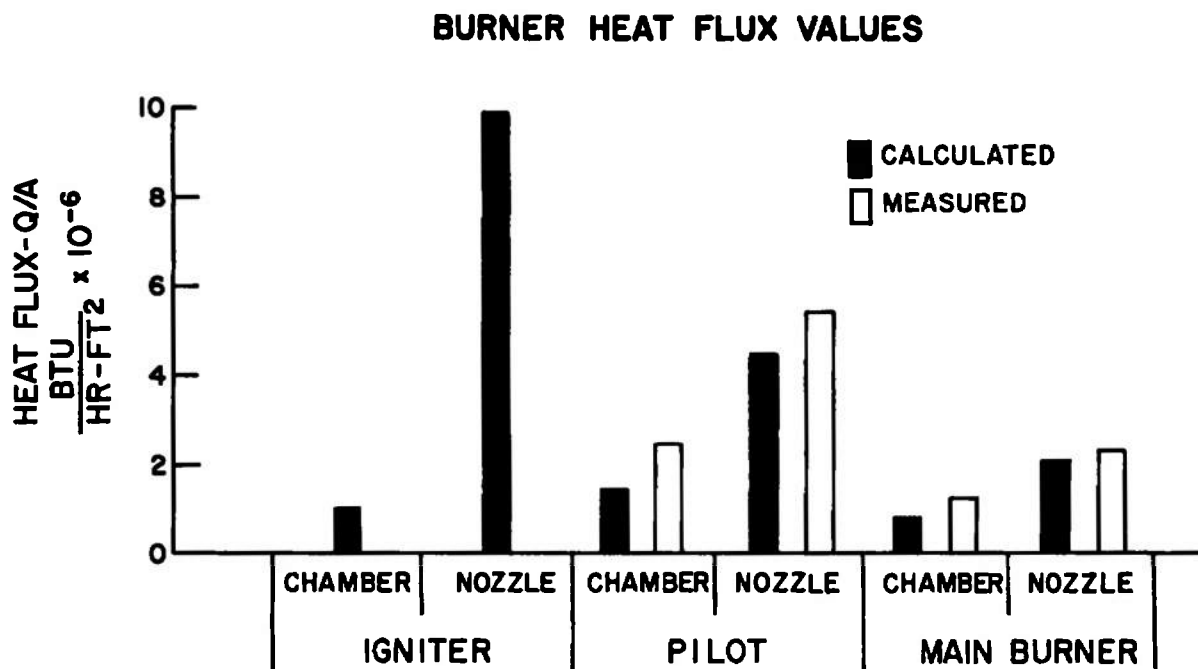


Fig. 28 Predicted and Measured Combustion Chamber Wall Heat Flux at Various Locations



## LORHO MHD GENERATOR BURNER DESIGN

$P_{\text{CHAMBER}} = 10 \text{ ATM}$   
 $\text{TOTAL FLOW} = 60 \text{ kg/sec}$   
 $P_{\text{H}_2\text{O}} = 400 \text{ PSI}$

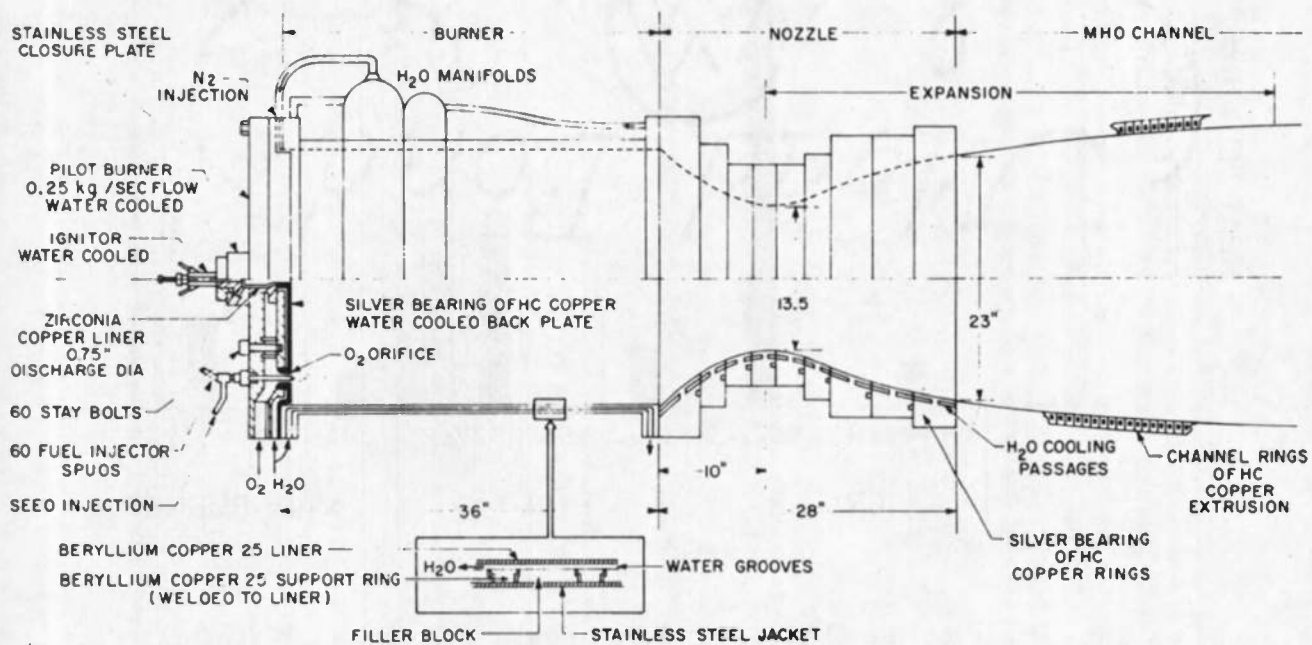


Fig. 29 Some Details of the Combustion Chamber

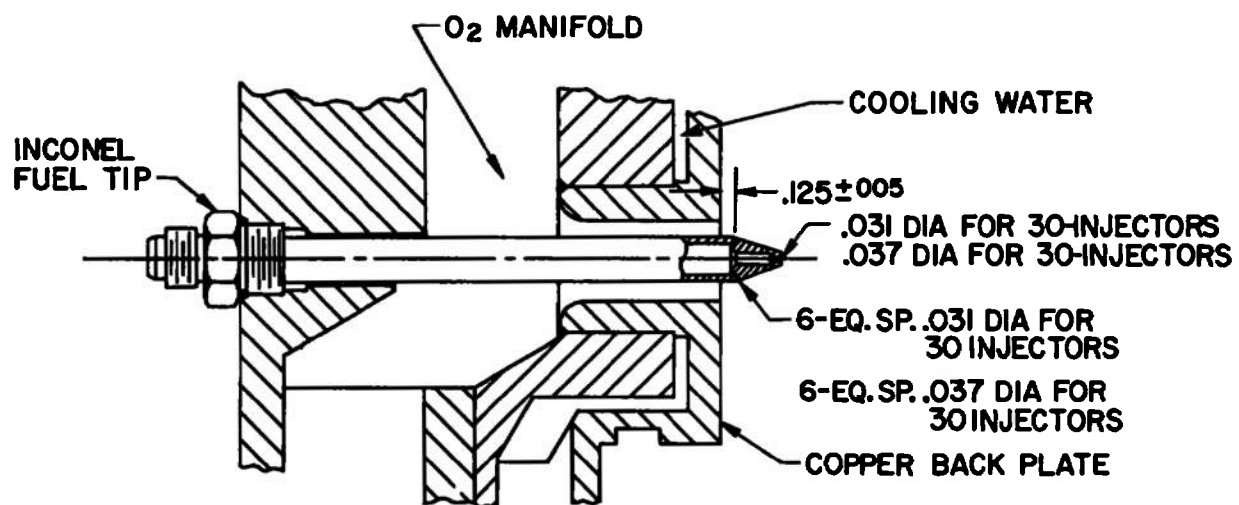


Fig. 30 Details of the Propellant Injector Assembly

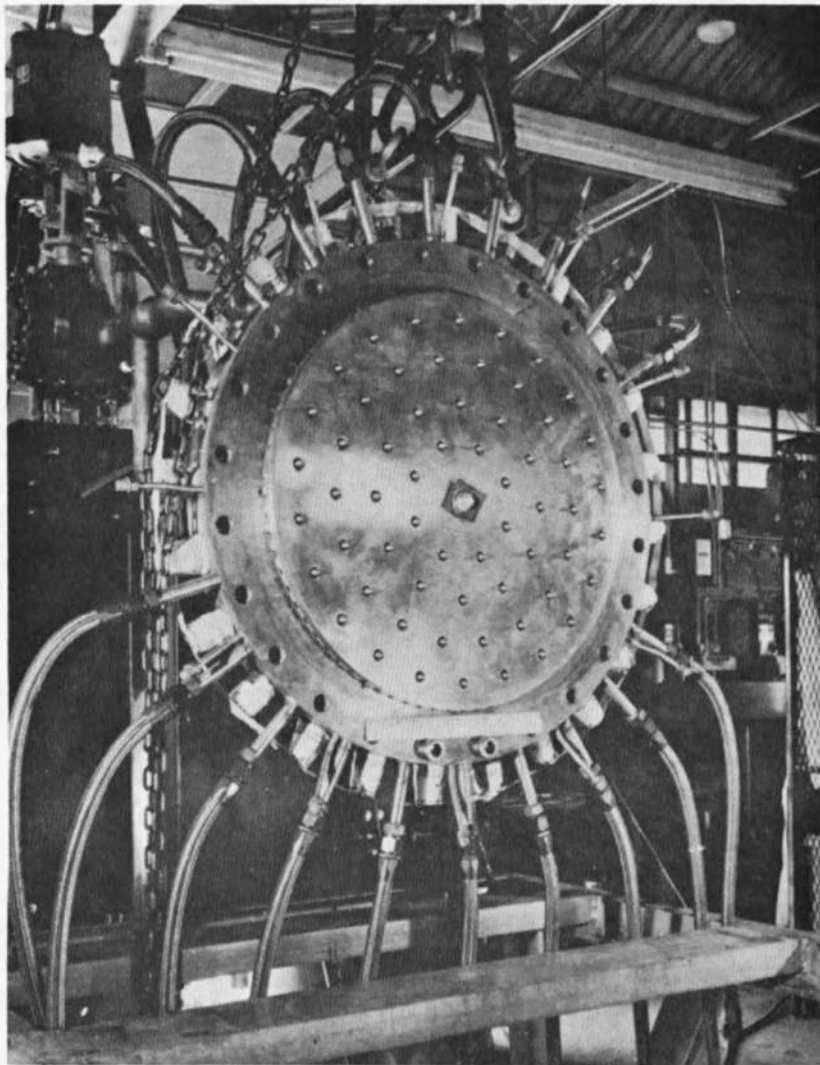
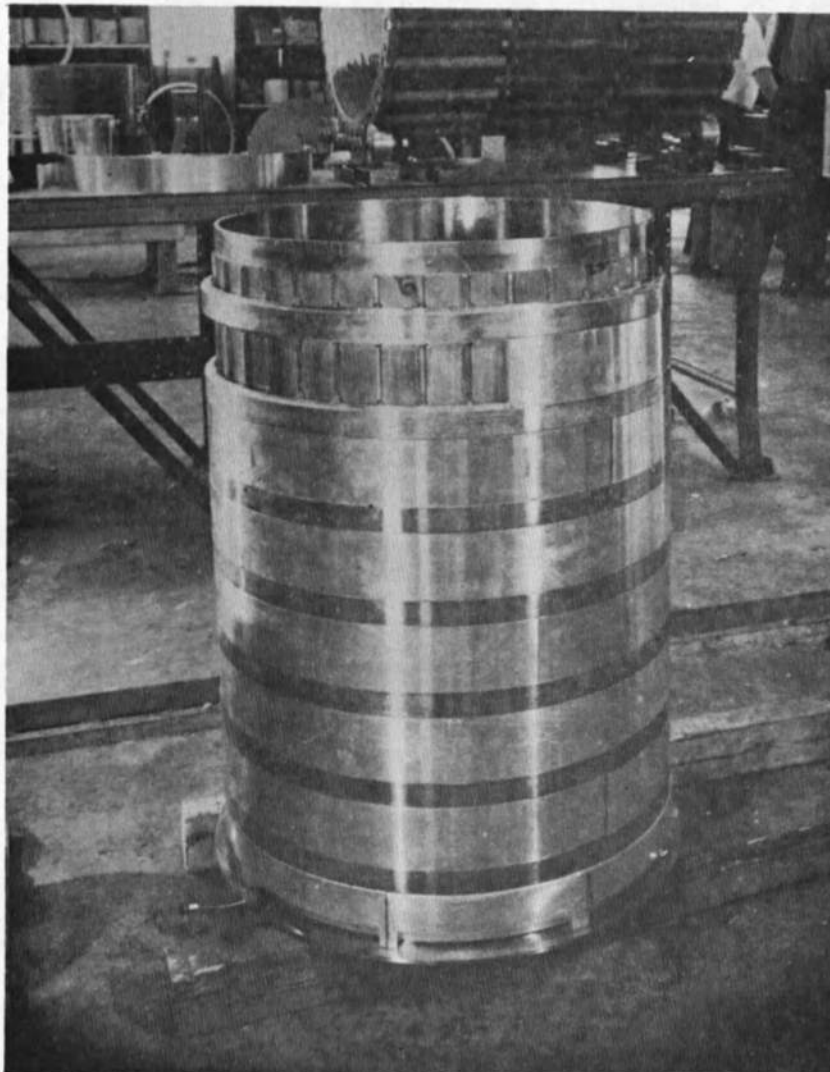


Fig. 31      Combustion Chamber Injector Assembly



**Fig. 32**      **Combustion Chamber Liner Assembly**

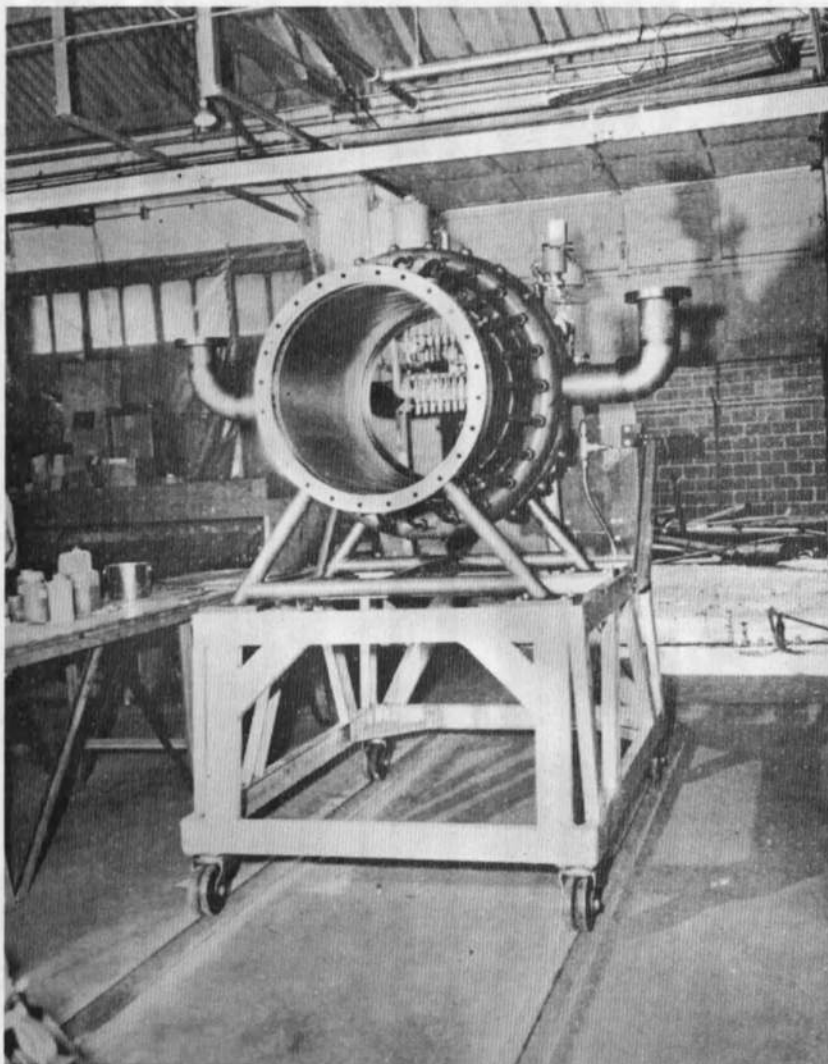


Fig. 33    Combustion Chamber Liner Housing

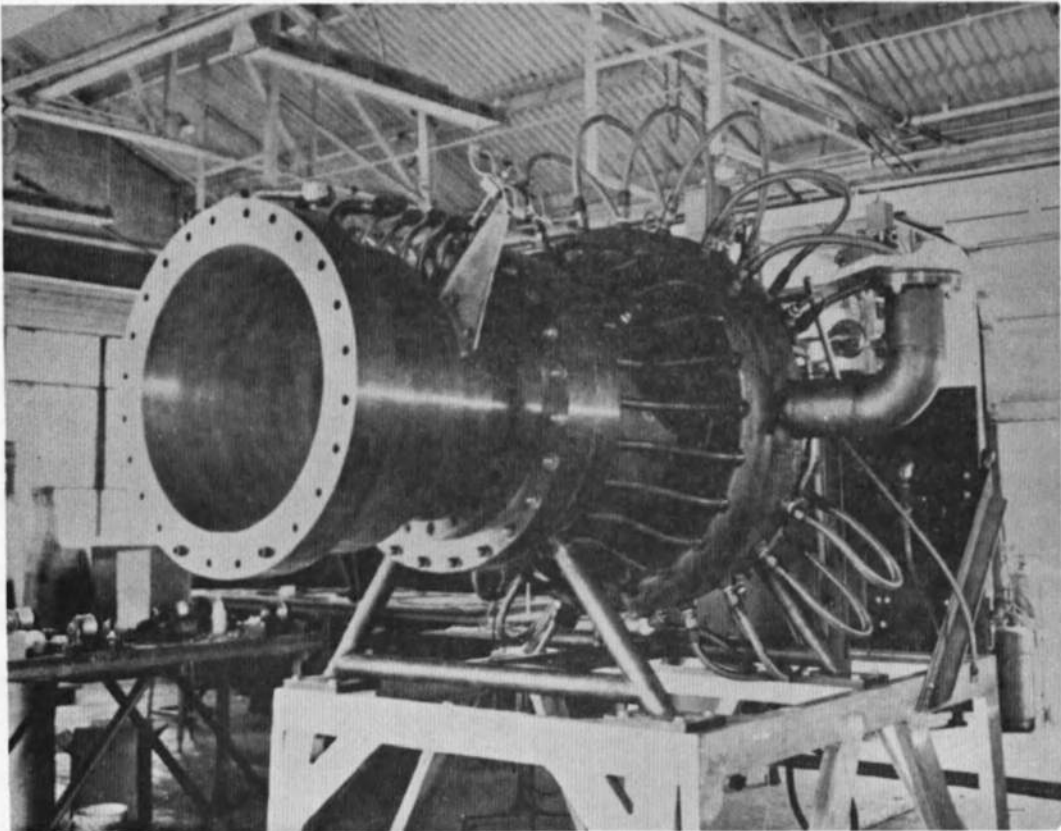


Fig. 34 Assembled Combustion Chamber

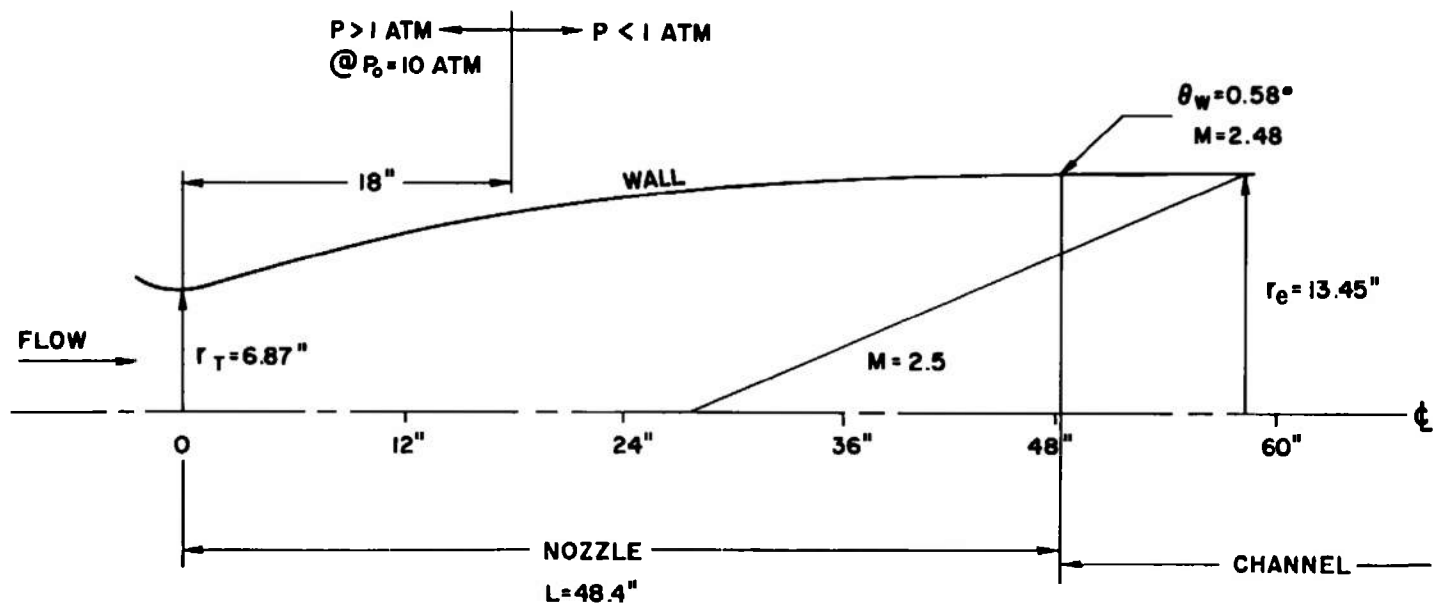


Fig. 35 MHD Channel Inlet Nozzle Configuration



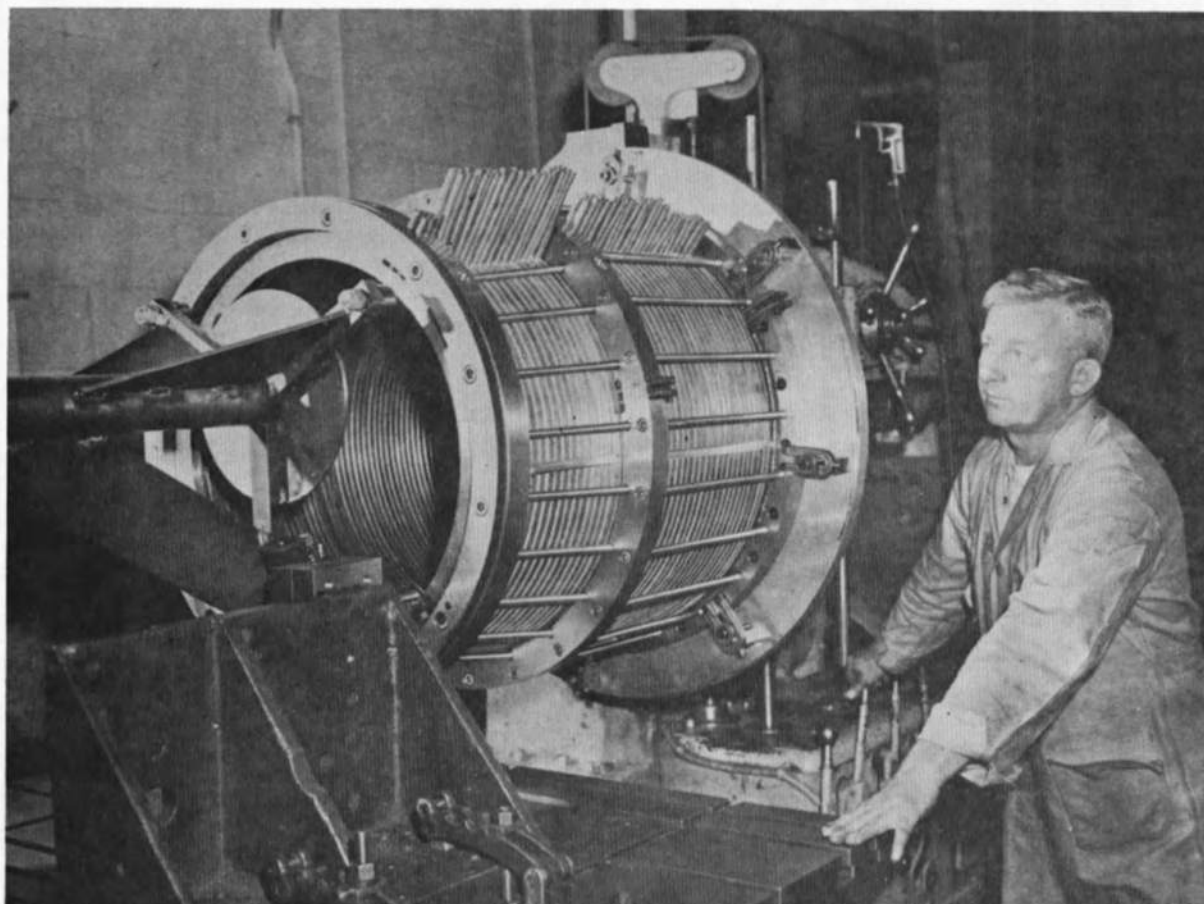


Fig. 36      Supersonic Nozzle Setup for Final Contour Machining



Calculated stress summaries for critical areas of the burner and nozzle are included as Figs. 37 and 38, respectively in pictorial schematic form.

During initial operational checks of the MHD generator-burner the following modifications to the original design were necessary:

1. Combustion difficulties in the pilot and igniter chambers were attributed to liquification of the ethane fuel as the pressure and temperature dropped in the feed system from the storage bottle to the burner. A change to methane cured the liquification problem, but necessitated an oxidizer change in the igniter from  $N_2/O_2 = 1$  to  $N_2/O_2 = 0$ . The resultant increased effluent temperature is required because of the higher ignition temperature and lower combustion rate of methane.
2. Unexpectedly high operating temperatures of the burner liner were attributed to excessive recirculation partially due to the high contraction ratio. This situation was corrected by selectively increasing the size of the inner rows of oxidizer and fuel injection ports to increase the mass flow in the central portion of the chamber.
3. Originally the seed mixture was introduced under pressure directly into each of the 60 fuel lines just prior to entering the combustion chamber. Random variations in gas conductivity from run to run were attributed to inadequate mixing and distribution of the seed. This problem was alleviated by introducing the seed solution in the main fuel line considerably upstream of the burner which allowed for proper mixing prior to entering the combustion chamber.

The combustion chamber has been operated at rated mass flow and below on many occasions, and performance is satisfactory.

#### B. Diffuser Construction and Operating Experience

As already discussed, the LORHO MHD generator was designed to operate under supersonic conditions. The Mach number varies from approximately 2.5 during no load to approximately 1.8 at peak load. The maximum available stagnation pressure is 10 atm without load. The static pressure in the channel was designed to be approximately 0.5 atm or less. To operate with these conditions existing in the channel, a diffuser must be used to permit exhausting the flow to the atmosphere. Based on the prior experience and also the experience with the Mark II Hall generator the diffuser designed for the original LORHO facility consists of a constant area inlet section 253" long with a 36" diameter followed by a subsonic section 78" long with a 30° half angle divergence. A photo of the diffuser in the final phase of fabrication is shown in Fig. 39.

LORHO BURNER - STRESS DIAGRAM (10 ATM. CONDITION)

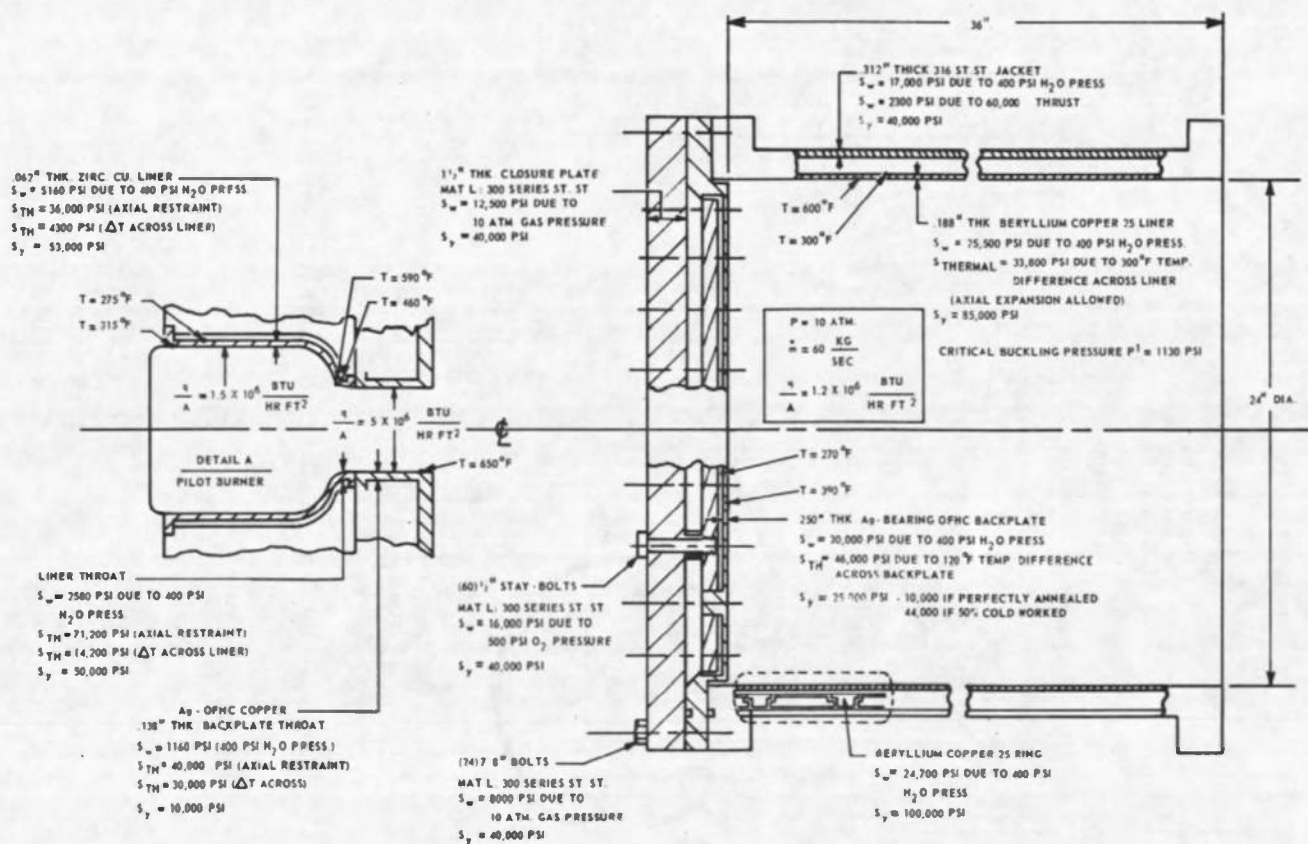


Fig. 37 Operating Stresses in the Combustion Chamber

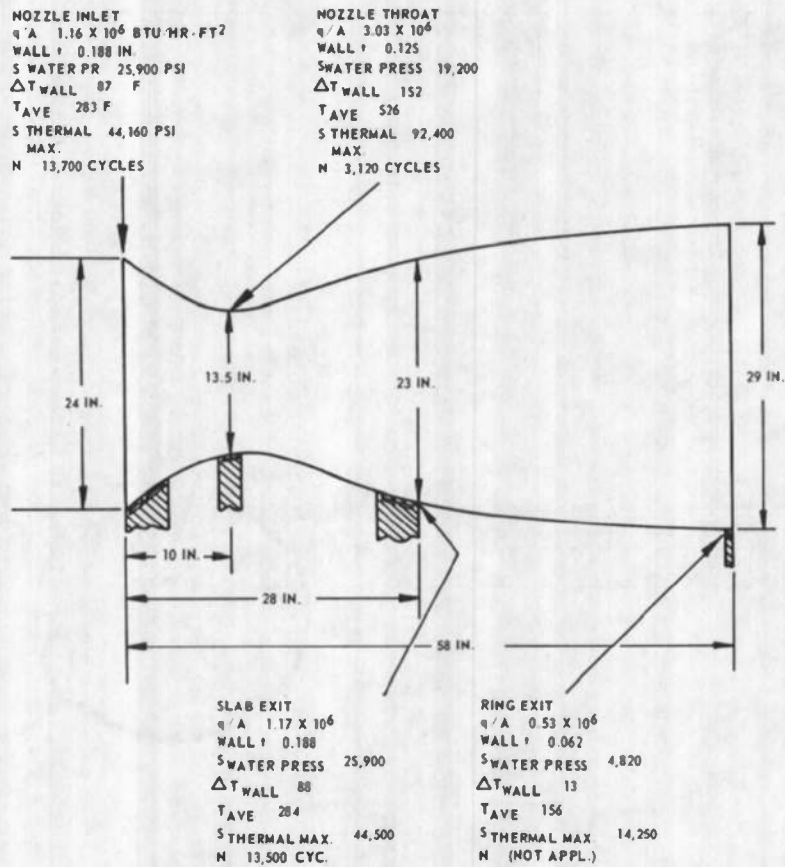


Fig. 38 Nozzle Stresses at 10 atmospheres Combustion Pressure

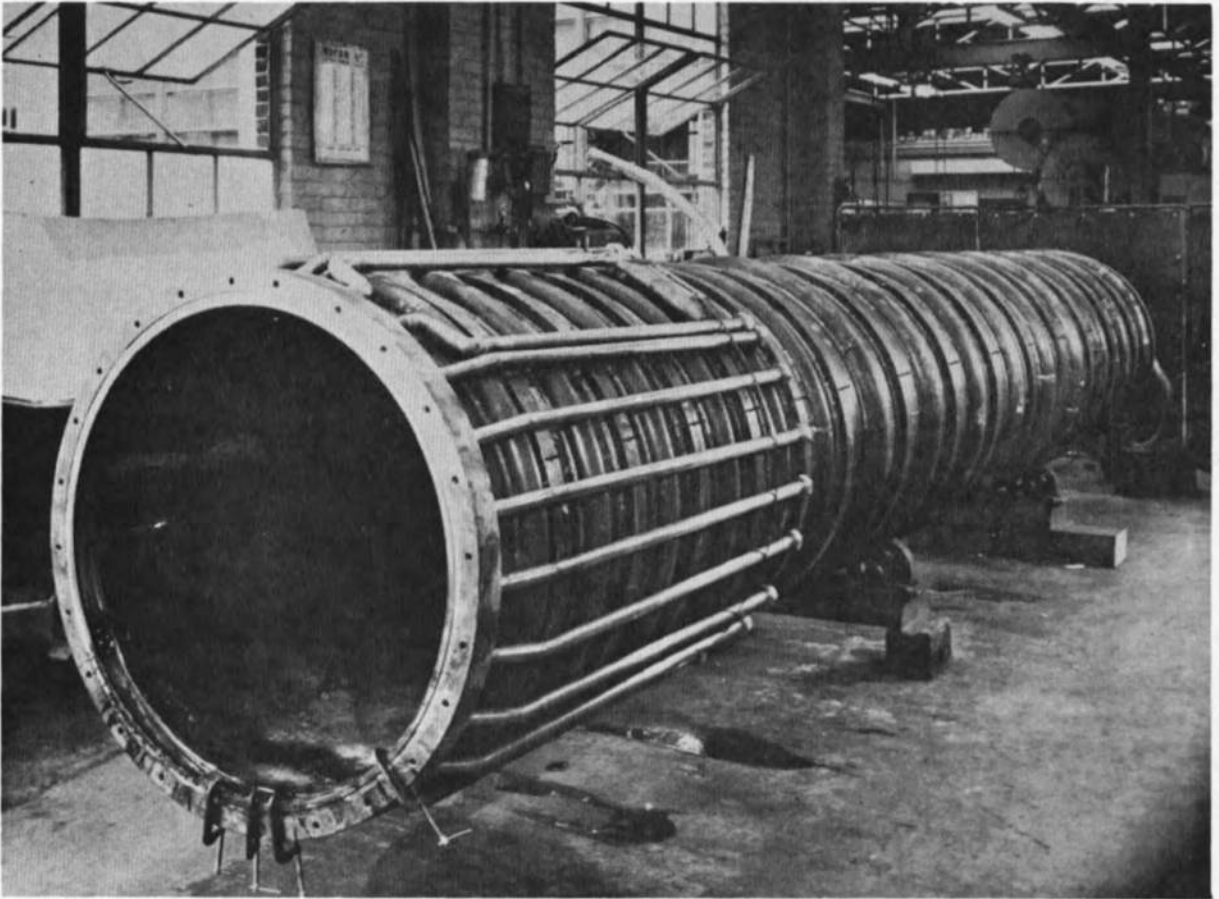


Fig. 39      Diffuser During Final Fabrication

The modifications to the MHD generator discussed earlier increased the channel exit diameter from approximately 36 to 40 inches. This, of course, necessitated changes in the diffuser. Originally, a constant area diffuser followed by a subsonic diffuser scaled up from the present diffuser was considered. A study of the test results of the LORHO Pilot channel and diffuser showed, however, that because of the cooling effect of the cold walls, the flow expanded to a higher Mach number in the diffuser and consequently required a higher stagnation pressure at the diffuser inlet to recover, thus making the recovery less efficient. In a typical example, the static pressure dropped from 0.517 atm to 0.342 atm in 160" of the diffuser. Because of this situation, it was decided to use a convergent inlet section which would at the least counteract the expansion due to boundary layer cooling. Using Rayleigh Line data it was determined that the appropriate convergence angle to overcome the expansion caused by cooling was  $4^\circ$  (total angle). This convergence angle is also appropriate for those cases where a convergent section is used at low Mach numbers in the typical applications referred to previously.

By adding a convergent inlet section which necks down to the previous channel exit diameter it was possible to use the original diffuser. Two items which must be considered are starting, and the length of the constant area section. With reference to starting, the maximum allowable diffuser contraction ratio for a specific heat ratio of 1.1 is 1.67. The modified diffuser has a contraction ratio of 1.245 and should be within the limit so that no starting problem should be encountered. The literature indicates that the length of the shock region in the constant area section of a diffuser is between 8 and 12 diameters. (The length of the shock region is defined as the distance between the point where pressure starts to rise to the point where pressure is a maximum.) Because a length less than this degrades performance it was decided to make the straight section in the modified diffuser 8 diameters long. In addition, if the convergent section just compensates for any expansion due to cooling, then the equivalent straight section length of the proposed diffuser will be 9.5 diameters. The final proposed configuration is shown in Fig. 40.

The two section views show the types of construction employed in the original and modified diffuser, both of which were made of carbon steel. In the earlier design the outer jacket was equipped with semi-toroidal expansion joints located between the reinforcing rings. This design was necessary to relieve the axial thermal stresses calculated for the assumed heat flux. Operating experience showed the heat flux was conservative by almost a factor of two, therefore permitting the new diffuser extension section to be designed to withstand the combination of thermal and buckling stresses without expansion provision. This resulted in welded plug type reinforcing pins between the inner and outer liners and effected a considerable cost savings in the fabrication.

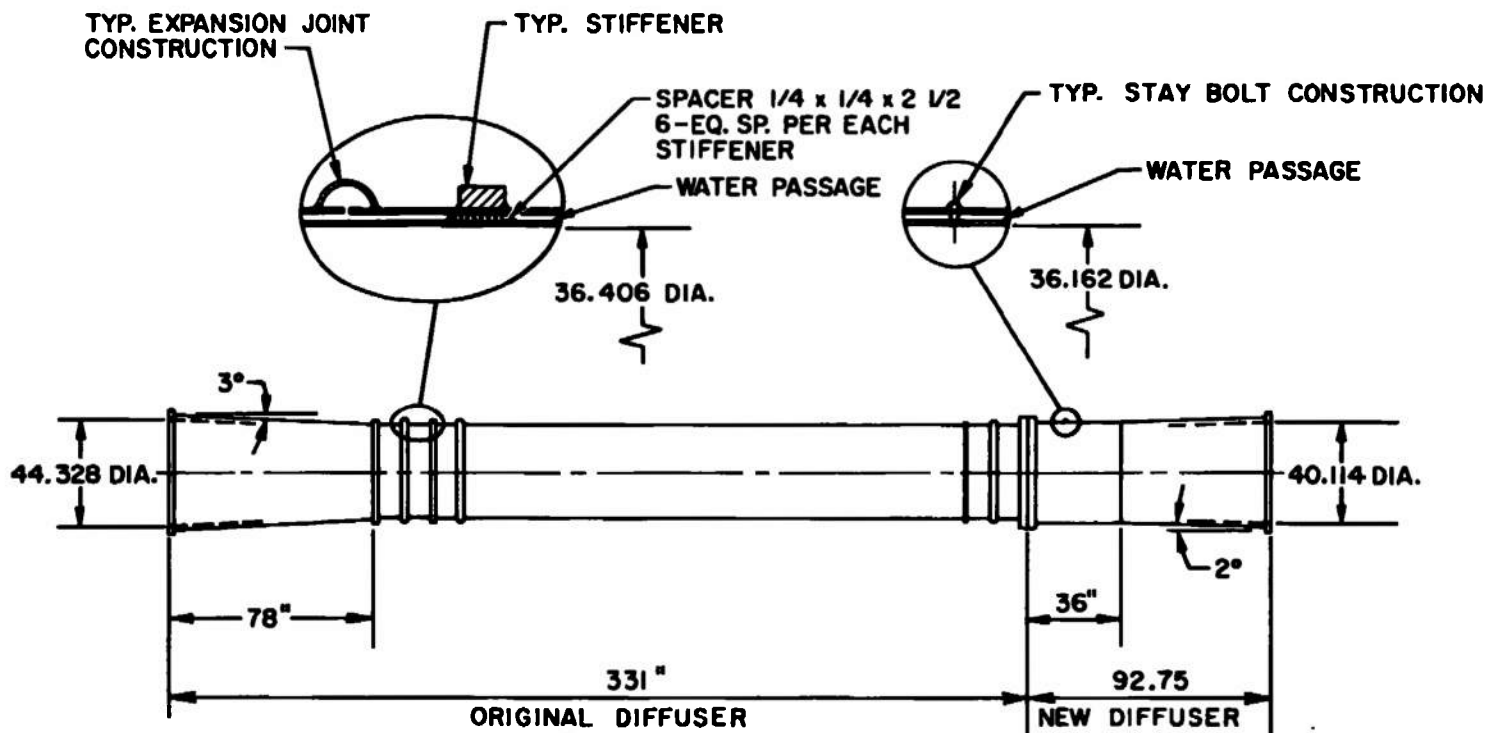


Fig. 40 Modified Diffuser Configuration

## 1. Magnet

The generator magnet is a solid iron-core electromagnet with aluminum energizing windings. It produces a uniform field of 19 kilogauss in an aperture which is 44" x 44" x 204" long (field in the vertical 44" direction). Operating time at maximum field (3 mw input power) is thermal inertia limited to 5 minutes. The total magnet weight is approximately 1 million pounds.

The overall system is optimized for minimum installed cost. Actual operating time may be less than 1 hour per week. Long term electric power costs were therefore not considered in the optimization.

Design studies included construction and testing of a model magnet. The modular construction of the model permitted testing a variety of magnetic geometries.

## 2. Design Features

### a) Energizing Coils

The cost optimization indicated that although an aluminum coil magnet would be somewhat larger than a copper coil magnet, its installed cost would be less. The aluminum coil has the additional advantage of having a much higher thermal mass (based on comparison of minimum cost systems).

The following argument should clarify the cost advantage for aluminum windings in large magnet systems.

The scaling factors for magnet systems are such that as apertures increase the current density and the windings decrease. This leads to the fact that the "window frame" configuration is not only magnetically optimum but also gives minimum cost. With this configuration one can determine a minimum cost coil build for any operating field (independent of aperture dimensions). Thus, as the apertures become very large the coil dimensions become small by comparison. For a given conductance, aluminum is substantially cheaper than copper and is therefore the choice for large aperture magnet systems.

Each of the two magnet coil assemblies has 85 turns and weighs 19 tons. Referring to Fig. 41, each turn is comprised of two long plates and 4 short bent plates, all 1/4" thick. Each long plate has a bent plate welded to its upper edge and both ends. The bent plates are lap welded to a matching bent plate rising from the other long plate in the turn. There is 12 mil polyester glass insulation between turns.

Every other long plate is water cooled via an aluminum cooling tube which is bonded to the plates with aluminum fiber filled epoxy. The bent plates (saddle section) are cooled by air which blows through the winding section. There are approximately 1/16" passages for air cooling between the plates in this region.



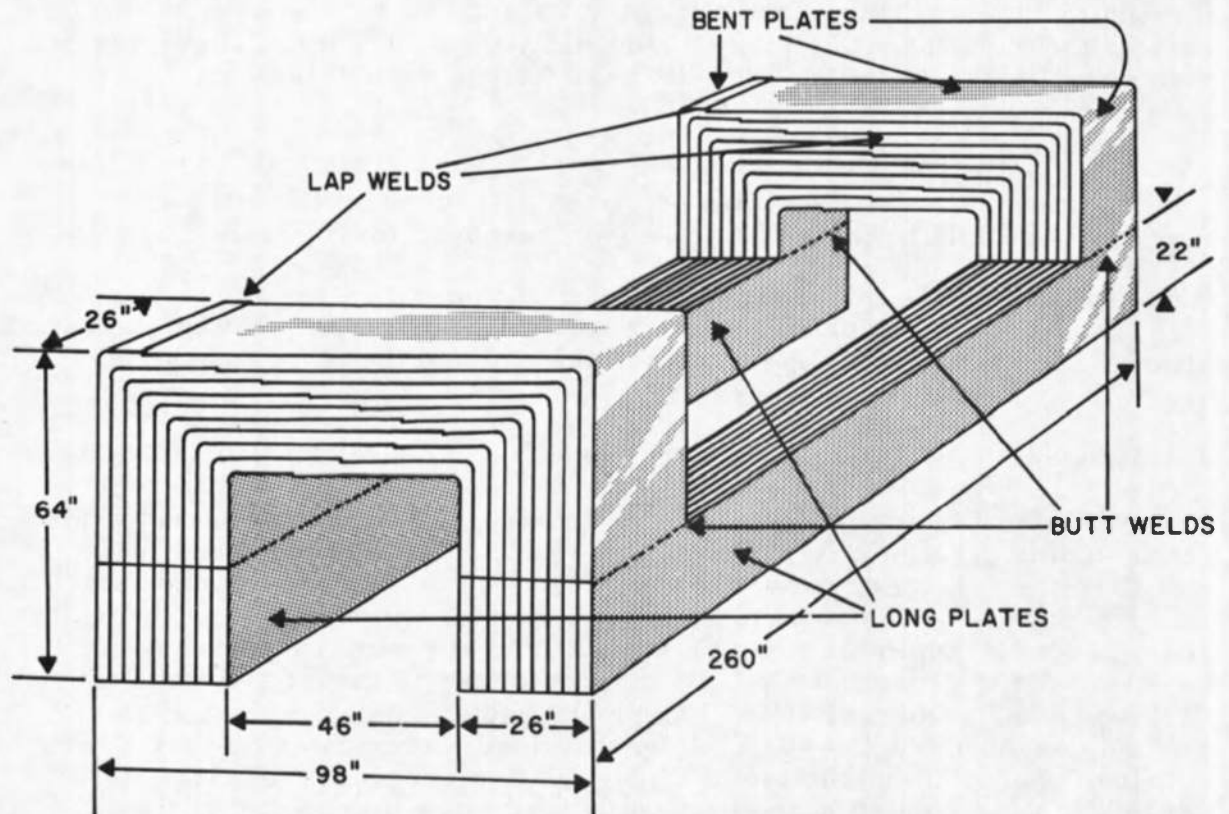


Fig. 41 Field Coil for Generator Magnet



The cool down time required after each 5 minute field run is one hour. The thermal response characteristics are shown in Fig. 42 .

b) Magnet Steel

The magnet frame consists of six low carbon steel forgings, referring to Fig. 43 , there are two top yoke and two bottom yoke sections, each of these is 35" x 165" x 204" and weighs 340,000 lbs. There are two side yokes, each is 35" x 44" x 204" and weighs 91,000 lbs.

c) Field Plots (Figs. 44 and 45)

The axial field plot (Fig. 44) is as measured on the completed magnet. The MHD channel location is superposed for reference.

Figure 45 is the predicted magnetization curve and shows the very high magnetic utilization factor for a window frame configuration (essentially all of the ampere turns appear across the gap and the field strength is nearly linear with current).

#### 4. DESCRIPTION OF THE PERFORMANCE EVALUATION PROGRAM

In all, the evaluation program consisted of some 46 generator tests not including preliminary burner tests with a dummy channel and individual ignitor and pilot burner tests. These 46 tests were divided into two groups; one group of 24 tests using the original generator channel, and a second group of 22 tests on a modified generator channel. As will be discussed the maximum power generated was 18 mw at a voltage of 9213 volts and a current of 1950 amperes--obtained during Run 19 performed on February 25, 1969. It was decided after achieving the 18 mw output to change the direction of the evaluative program from tests to optimize the generated power per se to performance mapping of the generator characteristics. There is every reason to believe that if the generator operation had been trimmed more in terms of seeding, fuel-oxygen ratio, etc., that 20 mw or more could easily have been achieved (at the conditions of Run 19 the voltage was only off some 700 volts and the current, 50 amperes!)

The general philosophy adopted in the LORHO performance evaluation program was to follow a systematic step-by-step checkout of all systems beginning first with the ignitor, then the ignitor and pilot, followed by burner testing and finally tests with power generation beginning at low power levels and proceeding to high output powers. As will be discussed, delays in the program were caused by 1) combinations of the control system, interlock system, and individual system components malfunctioning and 2) insulation failure particularly around the generator exhaust.

To assess the performance of the MHD Generator system including the ignitor, pilot and main burners, nozzle, generator channel and diffuser,

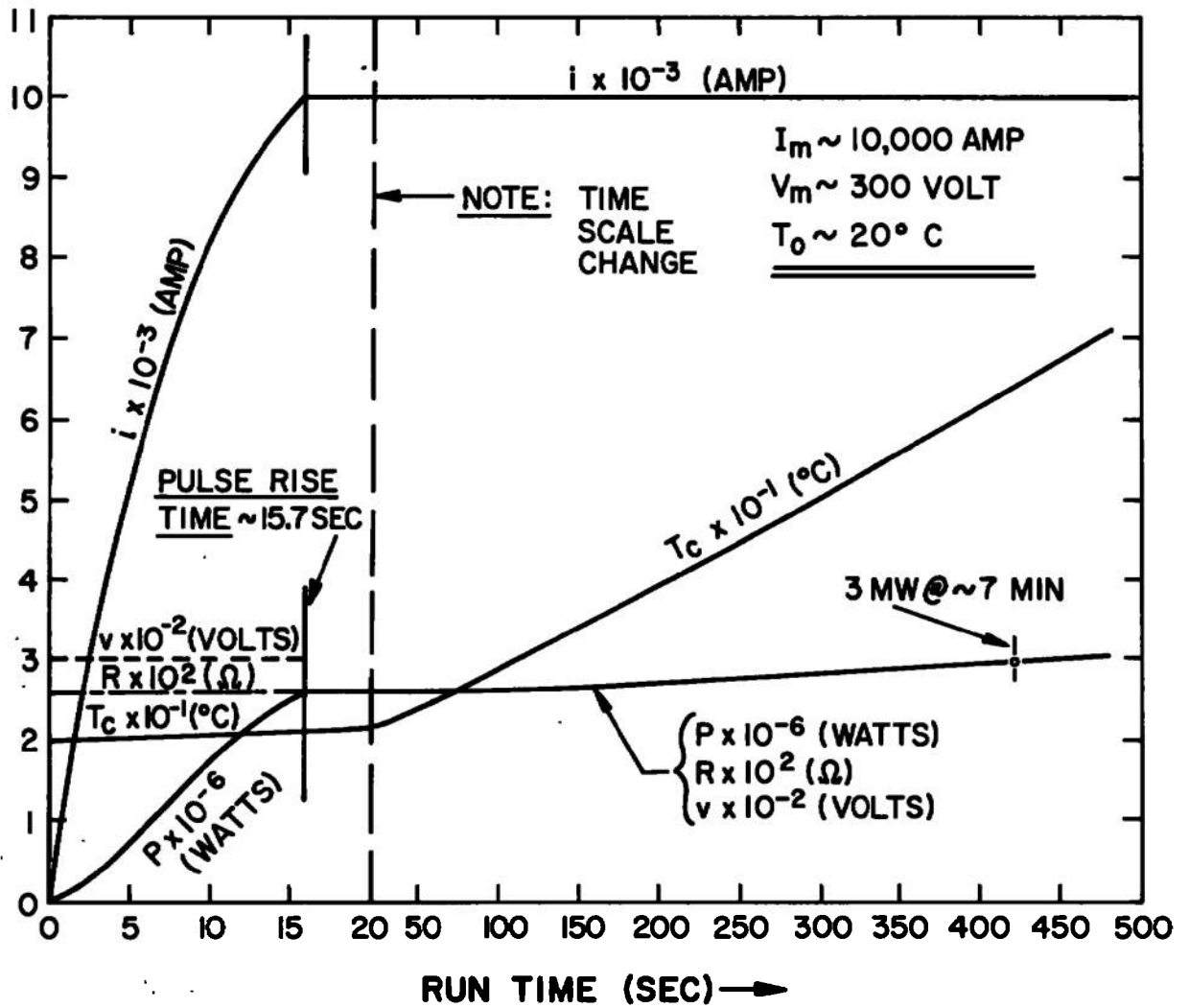


Fig. 42 Generator Magnet Field Coil Thermal Transient Characteristics

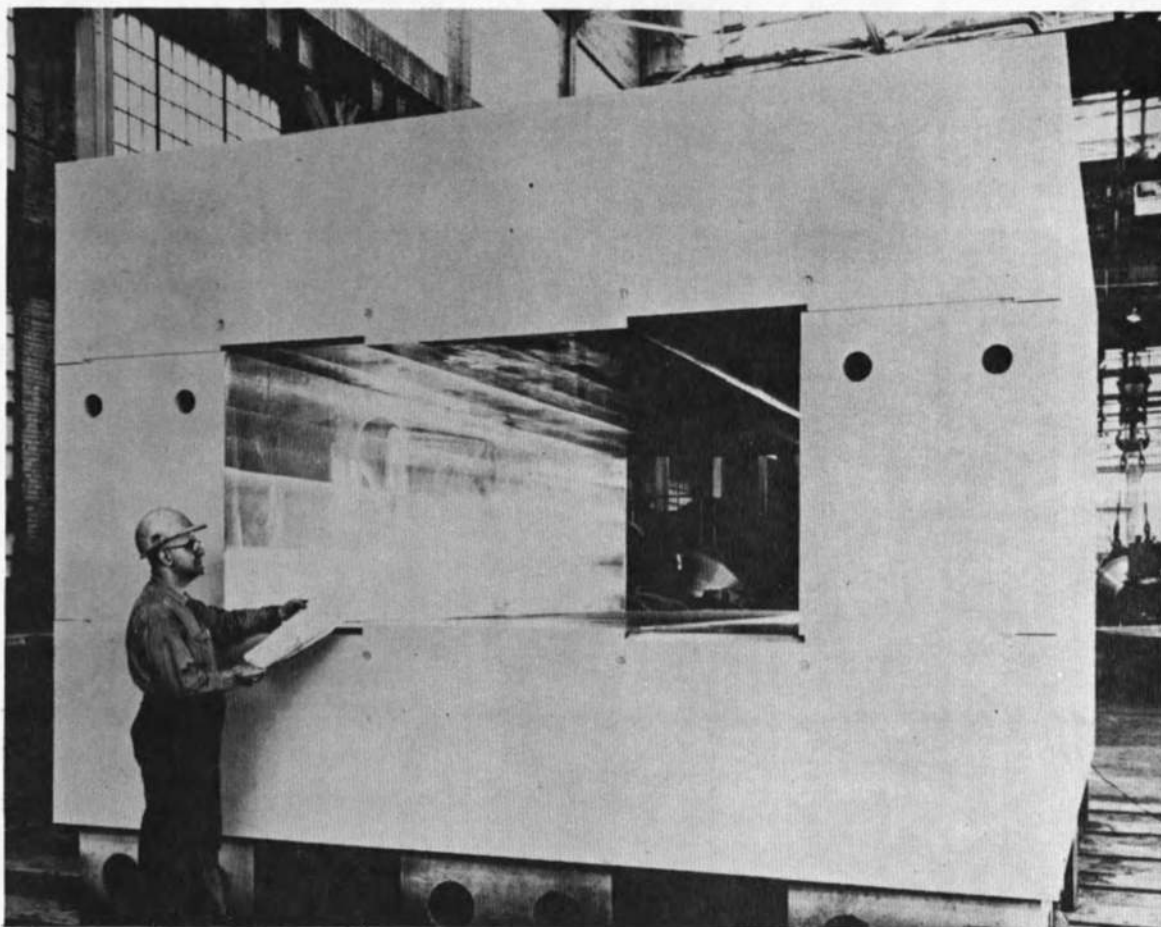


Fig. 43 Iron Yoke Assembly for Generator Magnet

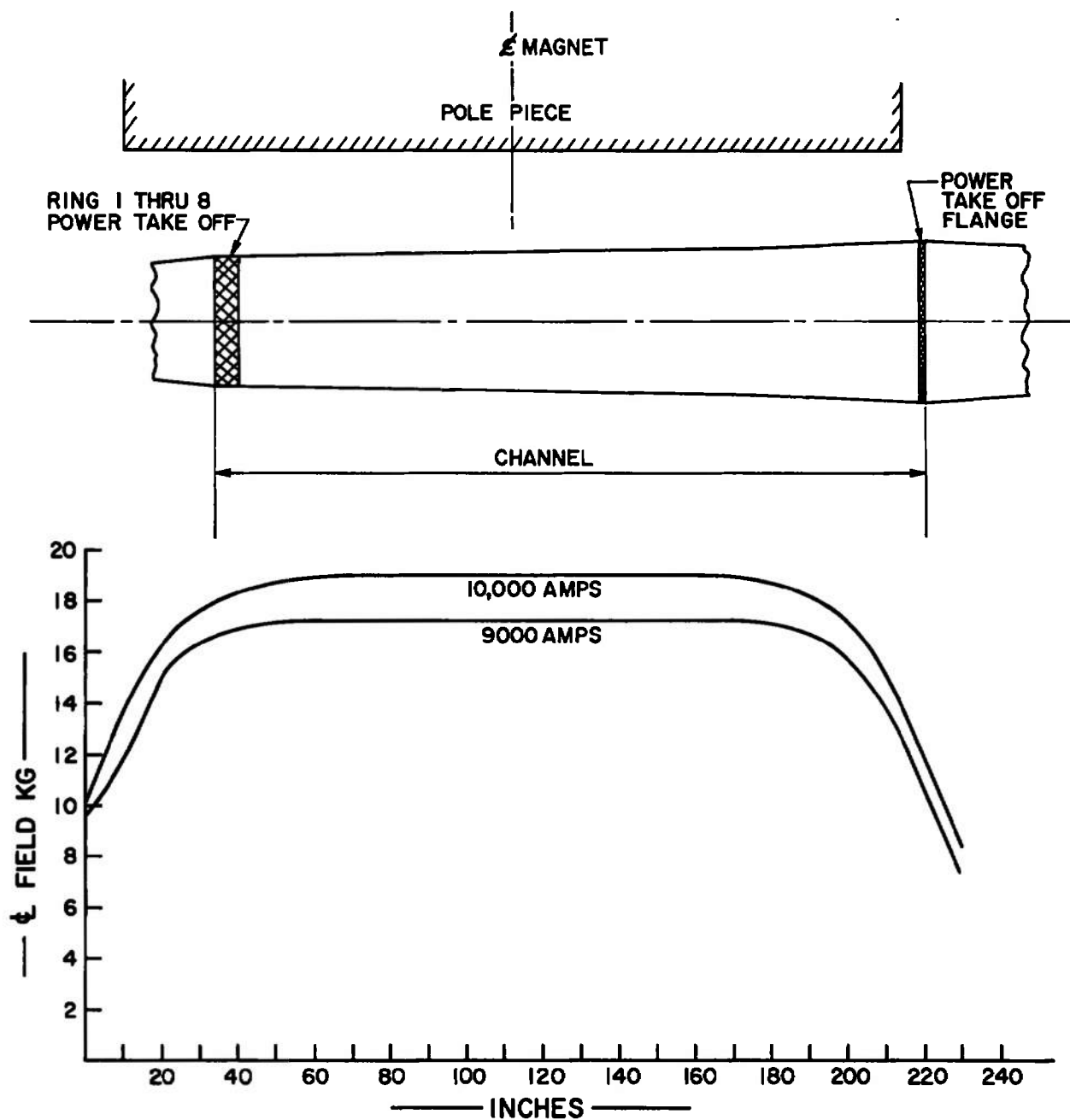


Fig. 44 Measured Centerline Field Strength for Generator Magnet

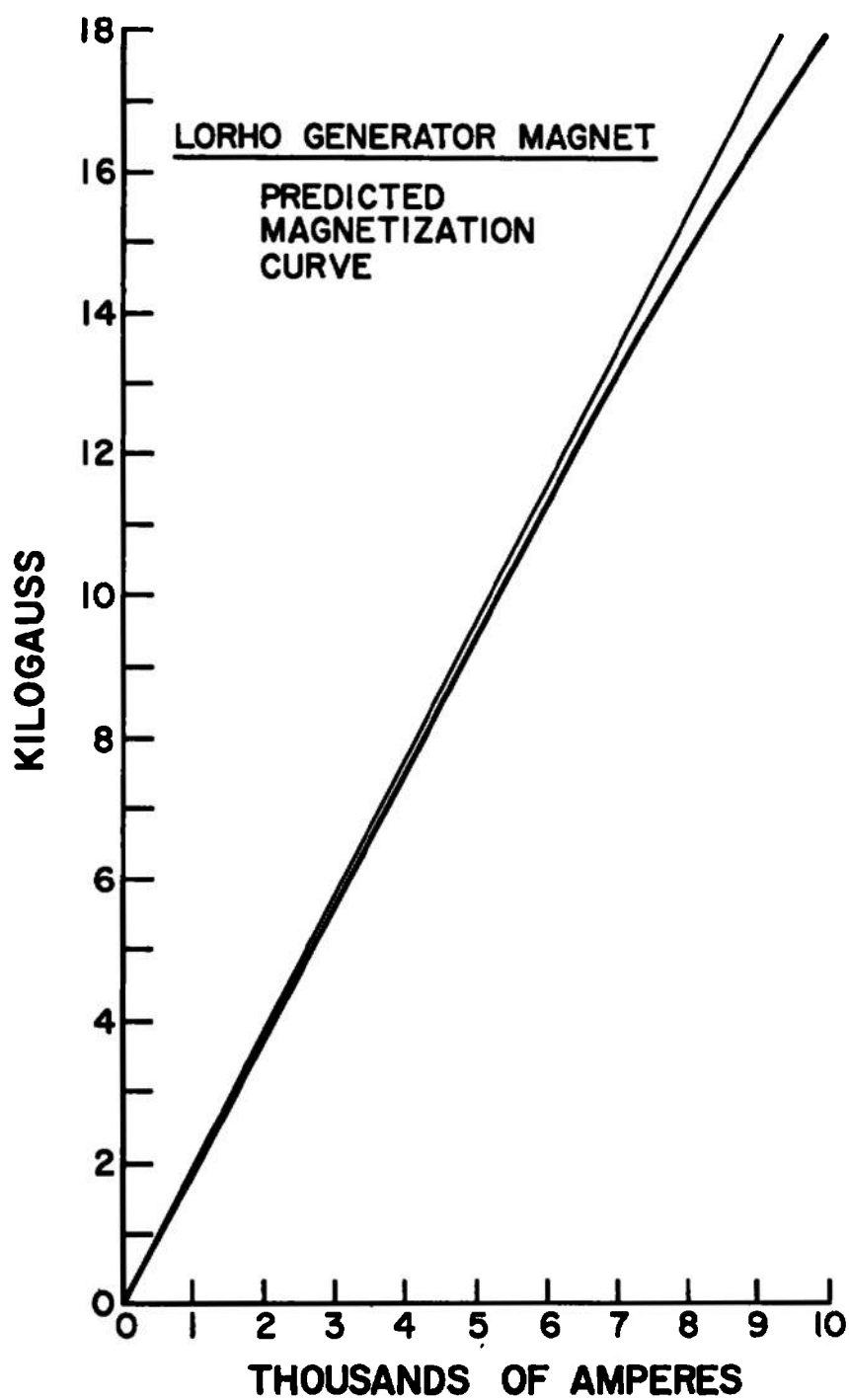


Fig. 45 Generator Magnet Magnetization Curve

extensive instrumentation was used to monitor temperatures, pressures, flows, voltages and currents during the tests. Special care was required to electrically isolate much of the instrumentations since the generator, diffuser and breech operated at voltages up to 10,000 volts.

Figure 46 is a schematic showing the locations at which temperatures and pressures were measured in the MHD generator system. As the diagram shows, exit water temperatures were measured in the pilot burner, main burner, nozzle, several individual channel rings and the diffuser. Most of the temperature data were recorded using either a recording temperature potentiometer or photographing temperature gages at a rate of every two seconds. The numbers along the generator channel in the diagram refer to particular ring numbers. Pressures were measured either with transducers (electrical readout) or by means of a manometer (visual readout). The two horizontal bars at the lower edge of the diagram show those pressures which were measured with a manometer (marked "manometer tube no. ") and those measured with transducer and electrically or visually read out (marked "Beckman"). All manometer pressure variations were recorded photographically while the other pressures were either recorded on an oscillograph or read on tape which was later processed by AEDC's Beckman and accompanying computer facilities and then digitally printed out as a function of time. Static pressures were measured at different angles with respect to the magnetic field direction as shown by the inset in Fig. 46.

Figure 47a shows the control and temperature and pressure instrumentation used to establish the flow, temperature and pressure of the cooling water for the components of the MHD generator system. Approximate water flow rates used during most of the test program are shown. All of this information was recorded either manually (visual observation of gages) at the beginning of the test or photographically at every two seconds during the test.

Figure 47(b) shows the electrical instrumentations used in the performance evaluation program. To isolate control room instrumentation from the 10,000 volt MHD generator, Norbatrol transducers or Hall Effect devices were employed. The Norbatrol units are in reality DC to AC signal transformers which use a transformer insulated for 10,000 volts between the input and output signal. The Hall Effect devices can be operated at low voltage if the primary leads are adequately insulated as they were in this instance. Ring transverse currents ( $J_y$  currents) at ten locations, as shown, were observed. The transverse currents were measured by using split rings and connecting the split rings together through an external ammeter shunt. Ring-to-ground voltages as well as the voltages between groups of rings were also observed. The ring-to-ring voltages were recorded photographically while the ring-to-ground voltages were recorded electrically (using both oscillographs and tape). The total current in the generator as well as in each part of the load was also observed. The vertical lines marked 0, 36, etc., are an indication of distance (measured in inches) from the burner back plate.

Figure 47 (c) is a schematic of the load used in the performance evaluation program. As shown, there were five different load resistors, each consisting of a varying number of different sized stainless steel water cooled tubing (in series) as indicated in Fig. 47(c). Individual resistor currents as well as the total current could be measured directly. Since one of the electrical connections to each of the stainless steel tubes could be moved so as to vary the resistance between terminals, any resistance value from zero up to 7.8 ohms at 2200 amperes could be obtained by making the appropriate series-parallel combination of individual resistors.

As already mentioned, two groups of tests were conducted, one group, Group I Runs--see Table III, was performed with the original MHD generator channel while the second group, Group II Runs--see Table IV, was performed after the original generator channel was modified as will presently be discussed. The first group of tests, Group I Runs, commenced on September 8, 1966, after the LORHO Pilot facility had been completed and the instrumentation, controls, and protective systems checked out. Essentially, Runs 1, 2, 3, and 4 were made for the purpose of an overall system checkout. As indicated in Table III, the tests were made without magnet field at 60% mass flow (100% mass flow = 132 #/sec). Considerable time was spent in these early tests in an effort to get the ignitor and pilot burners to start and operate reliably. The conclusions reached as a result of this effort were:

- 1) Methane was a better fuel for both the ignitor and pilot burners rather than ethane since the latter had a tendency to liquefy at the operating conditions encountered.
- 2) The oxidizer for the ignitor had to be changed to pure oxygen to obtain a sufficiently high flame temperature in the ignitor to make starting the pilot reliable.
- 3) The ignitor and pilot could be reliably operated with only 40% and 60% of the design mass flow, respectively.

Run 4 was a successful test of the MHD generator system for sixty seconds with seed but without field.

The next several runs, Runs 5 through 8, were short-circuit tests at 80% mass flow. During the performance of this group, seed feeding difficulties were encountered; seed feeding and achieving uniform distribution of the seed continued to present difficulties throughout the total evaluation program. Several other things were discovered during the tests:

- 1) A considerable number of water taps in the water cooling manifold were clogged, thus stopping water flow to a number of channel rings. These taps were replaced immediately.

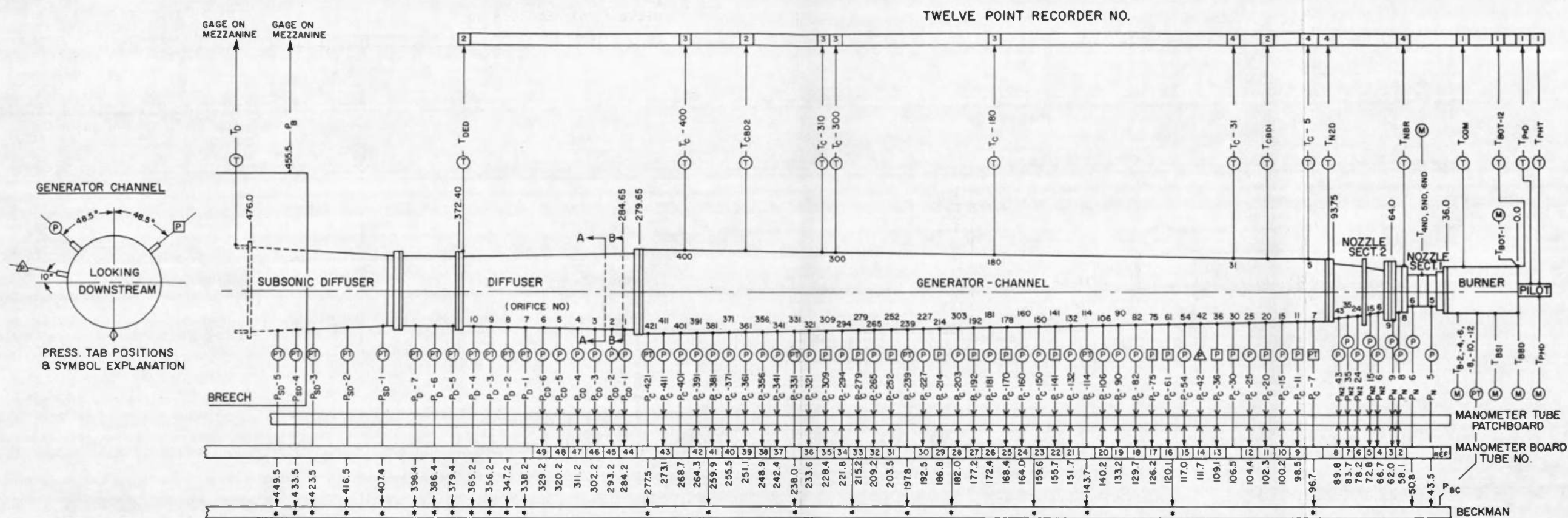


Fig. 46 Schematic Showing Locations of Which Temperatures and Pressures are Measured in Generator System



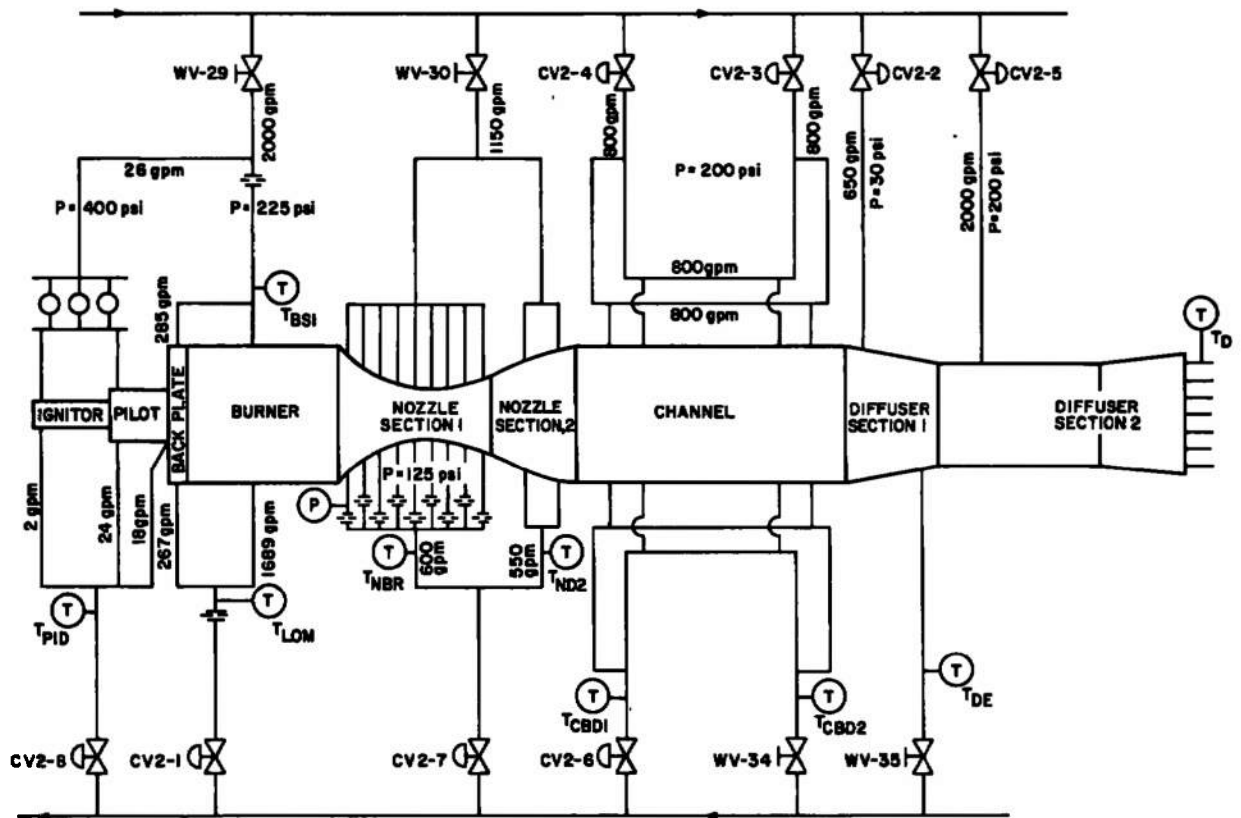


Fig. 47a Control Temperature and Pressure Instrumentation used to Establish Flow, Temperature and Pressure of Cooling Water for Generator

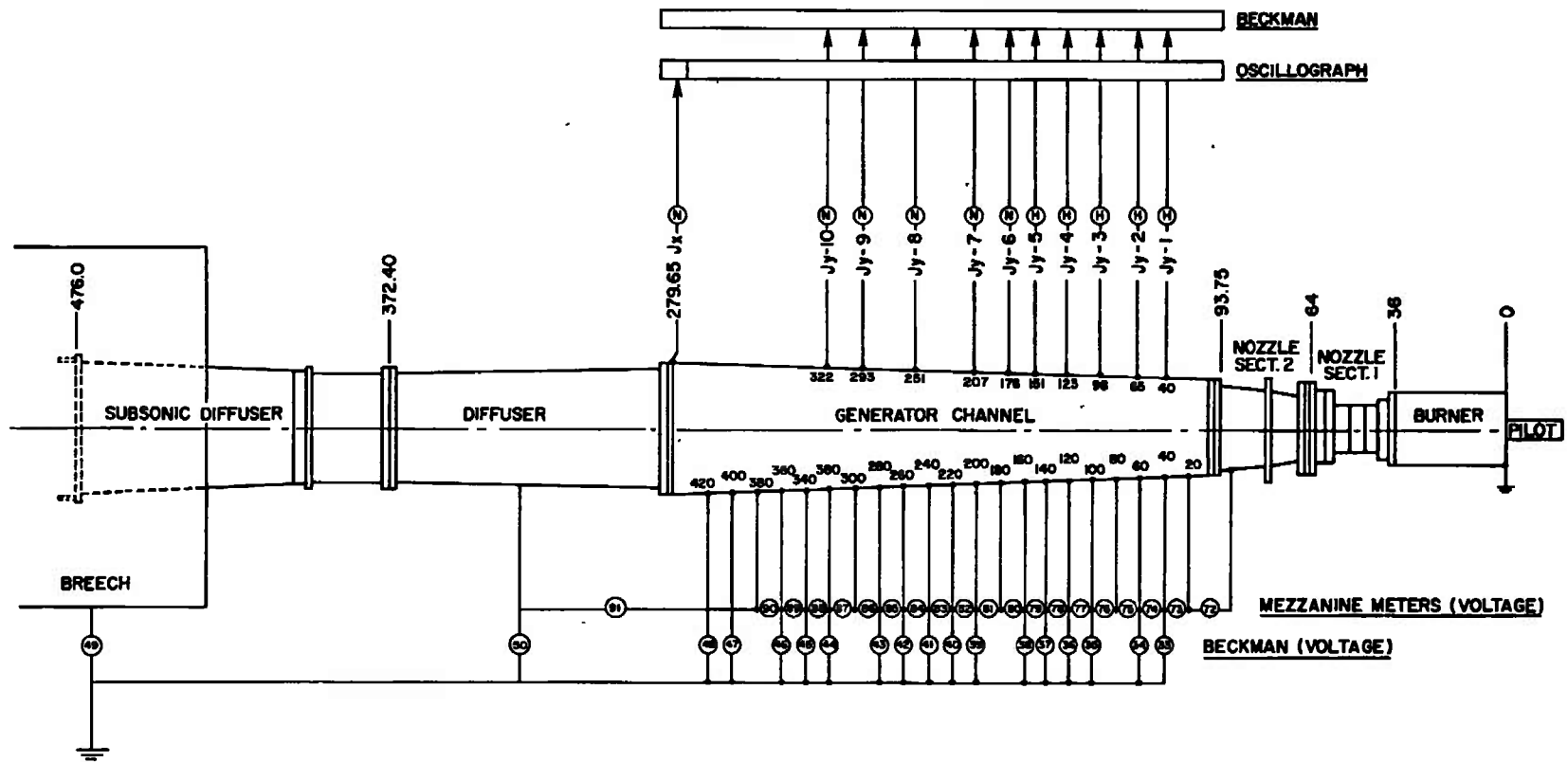
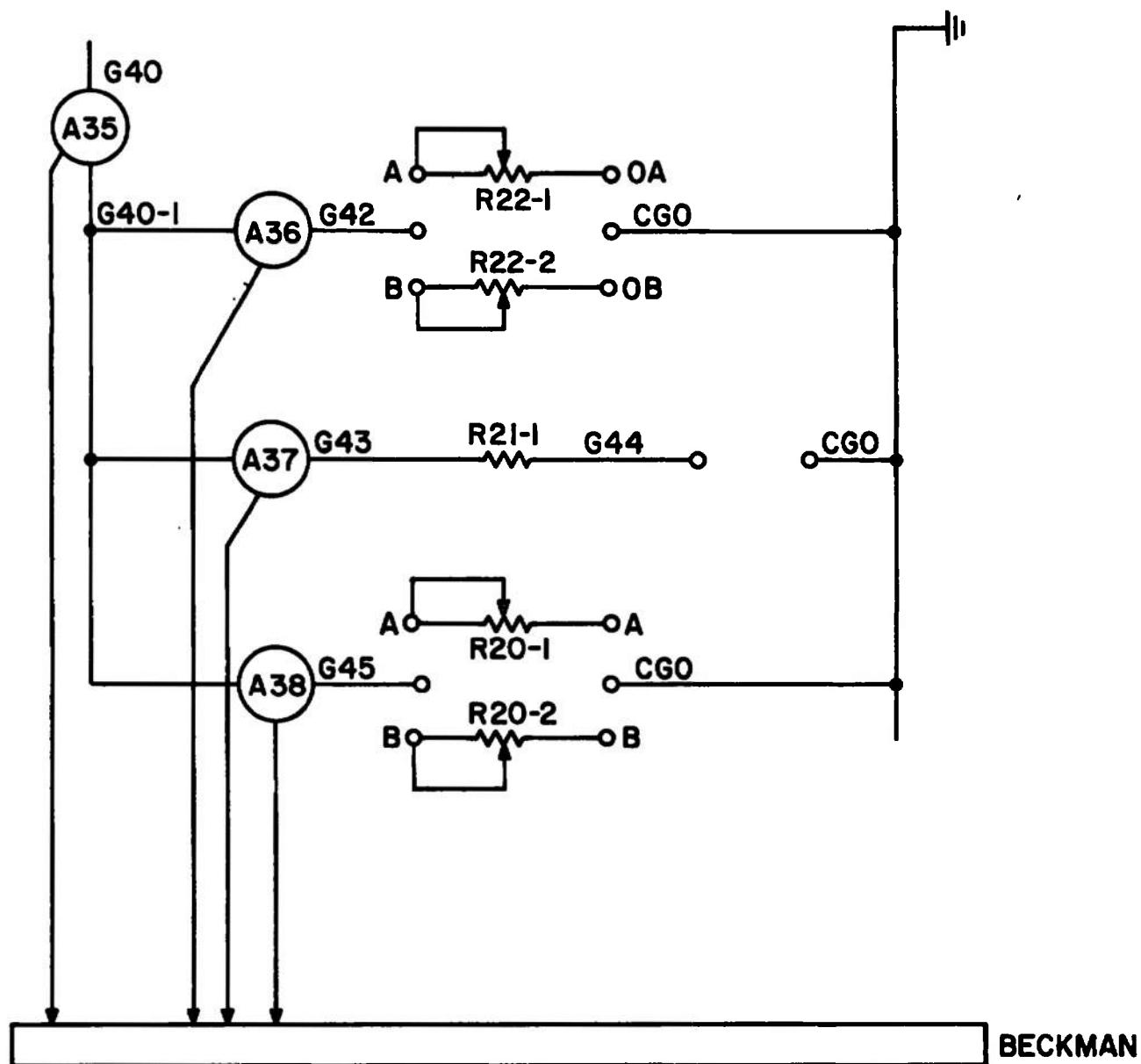


Fig. 47b Electrical Instrumentation of Generator



RESISTOR NO.	RESISTANCE	NO OF TUBES	TUBE DIA	CURRENT RATING
20 - 1	3.57 OHMS	12	5/8"	1600 AMPS
20 - 2	3.60 OHMS	12	5/8"	1600 AMPS
21 - 1	5.98 OHMS	20	5/8"	1600 AMPS
22 - 1	9.64 OHMS	18	3/8"	640 AMPS
22 - 2	9.97 OHMS	18	3/8"	640 AMPS

**Fig. 47c Schematic of Load Resistor Bank**

TABLE III  
GROUP I RUNS--TESTS WITH ORIGINAL CHANNEL

Run No.	Date of Test	$\dot{m}$ % of Full Mass Flow (132 #/sec)	Load ohms	Maximum Power Current Voltage	Comments
1	9-8-66	60	----	----	Both the ignitor and pilot burner failed to operate because of malfunctioning protective interlocking relays.
2	9-13-66	60	----	----	Ignitor and pilot burner fuel changed to methane. Ignitor oxidizer changed to pure oxygen. Changes made to obtain most repeatable and reliable starting of ignitor and pilot burner.
3	9-28-66	60	----	----	Test of 10 second duration made to checkout MHD generator system without magnetic field or seed.
4	9-29-66	60	----	----	Test of 60 second duration made as a longer checkout of the MHD generator system with seed but without magnetic field.
5	10-3-66	80	0 (s-c)	----	This attempt at a short circuit test failed because of a seed control relay malfunction.
6	10-5-66	80	0 (s-c)	---- 800 amps ----	This test was a second attempt at a short circuit test during which a short circuit current of 800 amperes was achieved. The seed readout instrumentation failed during the test. Also, it was discovered that many taps in the water manifold were completely blocked with sealant; this resulted in the extreme heating of several generator rings and popping of intermodular gaskets.
7	11-14-66	80	0 (s-c)	----	This run was the third in a series of short-circuit tests. Attempts to turn on the seed failed so that little or no short-circuit current was generated. Discovered a large variation in the outlet water temperatures from the burner

TABLE III (Continued)

Run No.	Date of Test	m % of Full Mass Flow (132 #/sec)	Load Ohms	Maximum Power Current Voltage	Comments
7 (cont.)					indicating the possibility of a liner hotspot. Traced to instrumentation error.
8	12-1-66	80	0 (s-c)	---- 1200 amps ----	The run was the last of the short-circuit-tests. A short circuit current of 1200 amperes was obtained. It was impossible to turn the seed "full on".
9	12-2-66	80	2.5	----	During this run, burnout of the pilot liner and throat occurred because of the cooling water freezing.
10	12-7-66	80	2.5	5.12 mw 1414 amps 3660 volts	Operation of the over voltage protective unit terminated the test prematurely. This action was initiated by arcing.
11	12-9-66	85	3.27	4.57 mw 1163 amps 3920 volts	Operation of the over voltage protective unit terminated the test prematurely. This action was initiated by arcing.
12	12-12-66	85	3.27	----	A malfunction of spray bank control relay prevented the test from being completed.
13	12-19-66	85	3.27	6.1 mw 1355 amps 4530 volts	The test was terminated prematurely because of an arc over from the diffuser to the exhaust duct to ground.
14	12-30-66	85	3.27	----	Run aborted because of malfunction of fuel feed system to pilot.
15	1-3-67	85	3.27	----	Run aborted because of building-to-exhaust duct seal failure.
16	1-6-67	85	3.27	8.0 mw 1545 amps 5162 volts	Traced seeding difficulties to the use of wrong seed valve signal spring.

TABLE III (Continued)

Run No.	Date of Test	in % of Full Mass Flow (132 #/sec)	Load Ohms	Maximum Power Current Voltage	Comments
17	1-13-67	85	3.27	12 mw 1875 amps 6362 volts	Limited power generated because of low seeding rate due to too high a fuel manifold injection pressure. Arcing at the rear of the channel damaged several channel rings.
18	2-3-67	85	4.7	16.1 mw 1840 amps 8700 volts	Premature shutdown of the test was the result of arcing to ground at the generator output cable.
19	2-8-67	85	4.7	13.8 mw 1713 amps 8082 volts	The MHD generator flow stalled during this test. After conclusion of the test the pilot burner was found to be leaking water.
20	2-16-67	90	4.7	13.0 mw 1708 amps 8064 volts	The MHD generator flow stalled during this test because of poor loading. To improve performance in the next several runs it was planned to decrease the nitrogen-to-oxygen ratio and to evaluate the performance using cesium carbonate as a seeding material with a water carrier.
21	2-23-67	80 at $N_2/O_2 =$ 75	4.7	16.1 mw 1840 amps 8711 volts	As noted, the nitrogen-to oxygen ratio was changed from 1.0 to 0.75. The mass flow was reduced to 80%. The generator channel flow stalled during this test. After the test, it was discovered that rings # 1 and 2 of the generator were damaged as a result of current concentration and subsequent arcing.
22	3-17-67	90%	4.7	13.6 mw 1687 amps 8049 volts	Cesium used as seed. Diffuser ruptured at front seam
23	3-31-67	100%	4.7	6.19 mw 1152 amps 5371 volts	Cesium used as seed. As a result of using too much water which caused the seed mixture to be wrong, the generator power output was relatively low.

TABLE III (Concluded)

Run No.	Date of Test	m % of Full Mass Flow (132 #/sec)	Load Ohms	Maximum Power Current Voltage	Comments
24	4-5-67	100%	4.7	14.7 mw 1755 amps 8382 volts	Cesium used as seed. Steady run at a power level greater than 14.2 mw, however, leak developed in test rings containing advanced design electrodes.

TABLE IV  
GROUP II RUNS--TESTS WITH MODIFIED GENERATOR CHANNEL

Run No.	Date of Test	Nominal Mass Flow # / sec.	Approx. N <sub>2</sub> /O <sub>2</sub>	Load Resistance	Maximum Power Current Voltage	Comments
1	6-4-68	112	0.75	No load No seed No magnet	----	Run #1 was a 15-second test to check out the facility and generator system.
2	6-6-68	112	0.75	0 Short circuit test	No current	Run aborted because of oxidizer oscillation before seed was turned on.
3	6-11-68	112	0.75	0 Short circuit test	No record of current	Short circuit test with same condition as for Run #2. Because of an instrumentation failure, there was no record of performance obtained.
4	7-3-68	112	0.75	0 Short circuit test	0 3000 amps 0	The current in some instances exceeded the range of the instrumentation.  Burner oscillations at high seed rates caused pressure and current fluctuations. These were corrected in later runs by resetting the valving in the fuel and seed systems.
5	7-10-68	112	0.75	2.367 ohms	11.84 mw 2199 amps 5384 volts	The test was normal in all respects except that the current level did not correspond to or follow the seeding rate. Plans were made to examine the oxidizer mixture, seed mixture, fuel and oxidizer feeding control, and other possible causes in future tests to determine the cause of this situation.
6	7-12-68	112	0.75	3.22 ohms	11 mw 1817 amps 6050 volts	The seeding rate was held constant at 0.8 wt%K for approximately 30 seconds to check the correlation of the seeding rate versus current. Some of the effect noted in Run #5 still persisted, but by and large, the current and seeding rate correlated well.



TABLE IV (Continued)

Run No.	Date of Test	Nominal Mass Flow # / sec.	Approx. N <sub>2</sub> /O <sub>2</sub>	Load Resistance	Maximum Power Current Voltage	Comments
7	7-16-68	112	0.75	4.485 ohms	16.3 mw 1872 amps 8700 volts	The generator produced approximately 16 mw for some time at approximately 85% of rated mass flow. An attempt to increase the power output beyond this value caused the flow to stall.
8	8-13-68	112	0.75	4.485 ohms	11.5 mw 1528 amps 7511 volts	Test was aborted because of severe arcing between the diffuser and ground. Shutdown was initiated by operation of the over-voltage protective device which responded to the high rate of change of voltage. A film of the diffuser exterior showed considerable arcing between the diffuser and the diffuser cart some of which occurred before what was apparently a dead short circuit to ground at one point in the test.
9	8-16-68	112	0.75	4.485 ohms	14.4 mw 1736 amps 8297 volts	Between this run and Run #8 insulation was replaced between the exhaust breech and the diffuser. Although the power generated in this case was higher, arcing was responsible for a premature shutdown. After the run it was discovered that some of the insulation had been dislodged. Also, a water leak was discovered in nozzle ring #8.
10	11-5-68	112	0.75	4.485 ohms	No electrical output	Run aborted because of malfunctioning control system.
11	11-5-68	112	0.75	4.485 ohms	No electrical output	Attempted several times to get burner started, trouble finally traced to malfunctioning water flow relays in the breech spray bank.

TABLE IV (Continued)

Run No.	Date of Test	Nominal Mass Flow # / sec.	Approx. $N_2/O_2$	Load Resistance	Maximum Power Current Voltage	Comments
12	11-6-68	112	0.75	4.485 ohms	16.7 mw 1870 amps 8936 volts	Test was terminated prematurely because of erratic behavior of control system. Power was generated without stalling which indicates an improvement over past performance as in Run #7. Power output limited because seed flow limit was reached.
13	11-12-68	112	0.75	4.485 ohms	No electrical output	Test aborted because of failure of oxygen flow controls. Trouble traced to pressure-to-current transducer in oxygen flow control.
14	11-13-68	112	0.75	4.485 ohms	15.4 mw 1805 amps 8526 volts	Experienced erratic fuel flow because of seed mixture-fuel interaction. Also, arcing occurred at the diffuser. There was a normal shutdown of the test.
15	1-29-69	132	----	4.46 ohms	-----	$N_2/O_2 = 0.93$ . Water carrier used to inject seed. Run aborted due to magnet power supply failure and ignitor start failure.
16	1-31-69	132	----	4.46 ohms	9.94 mw 1615 amps 6696 volts From diffuser to breech.	This test made under same operating conditions as Run #15. The test revealed that the flame temperature obtained was low so that conduction gas had reduced conductivity and therefore the generator could not be heavily loaded.
17	2-4-69	119	----	4.46 ohms	8.89 mw -typical (15.02 mw-momentary) 1392 amps-typical (1784 amps-momentary) 6392 volts-typical (8420 volts-momentary)	Only difference between this test and the two previous tests was that the O/f ratio was set at 3.08. The results of this test were comparable to the results of Run #16. Power output momentarily jumped up as the seed flow was stopped at the end of the run.

TABLE IV (Concluded)

Run No.	Date of Test	Nominal Mass Flow # /sec.	Approx. N <sub>2</sub> /O <sub>2</sub>	Load Resistance	Maximum Power Current Voltage	Comments
18	2-24-69	115	----	4.46 ohms	----	The seed carrier changed from water to methanol. Test aborted before data collected.
19	2-25-69	115	----	4.46 ohms	17.97 mw 1950 amps 9213 volts	The oxidizer nitrogen to oxygen ratio for this run was 0.7 with an oxygen-to-fuel ratio of 2.93. Generated the maximum power output for the whole series of 18 mw. Normal startup and shutdown.
20	2-27-69	115	----	2.17 ohms	No attempt to maximize power.	Same nitrogen to oxygen ratio as for Run #19. Load resistance of 2.17 ohms connected to the generator. For this and following runs the seeding rate was increased in steps and held at each step until steady state operating conditions were obtained; then, seeding rate changed to obtain data for the next step. This process was continued to full load at which time generator was short-circuited. Seeding rate was then backed off to zero to obtain the short-circuit characteristic as a function of seeding rate.
21	3-4-69	115	----	3.38 ohms	No attempt to maximize power.	Used the same nitrogen to oxygen ratio as for Run #20. The oxygen to fuel ratio was changed to 3.12. Load resistance of 3.38 ohms connected to the generator.
22	3-13-69	115	----	4.46 ohms	No attempt to maximize power.	Normal startup. As the generator loading was increased and at about 1000 amperes load current, burner backplate severely damaged as the consequence of losing cooling or burning in the oxygen manifold. This run concluded this series of tests.

- 2) An apparent nonuniform heating of the burner liner was discovered which was ultimately traced to poor temperature instrumentation.
- 3) The original brazed two piece fuel injectors were found to be defective due to diffusion of silver braze material into the structure metal, nickel, which led to stress corrosion, cracking and even complete failure of one of the fuel injectors. All the injectors were replaced with one piece units,

and

- 4) Relatively low gas conductivity was observed. In an attempt to bring about better distribution of the seed and to reduce some of the heat load on the burner liner, the flow rate of fuel, seed and oxidizer was redistributed with respect to the back plate, i. e., the fuel, seed and oxidizer flows were reduced for the outermost and innermost injector rows on the back plate while the flows were increased for the middle two injector rows. Also, the seed was injected directly into the burner with the fuel upstream of the fuel manifold as opposed to using a separate seeding manifold. The effort here was directed to concentrating more flow in the core as opposed to near the boundary.

Power generation tests were initiated with Run 9 and continued to the end of this first test series. Several tests were made at low resistance (2.5 ohms), followed by tests with a load resistance of 3.27 ohms and ending with tests with a load resistance of 4.7 ohms. As Table III indicates, one of the major difficulties encountered was electrically isolating the downstream of the MHD generator system to be capable of successfully withstanding or holding off 10,000 volts from the generator output terminal to ground without allowing appreciable leakage currents. Arcing to ground and insulation failure was the primary cause of premature shutdown of tests. The problem became worse as higher voltages were generated at higher values of load resistance.

In each test the burner was started and after steady flow had been established, the seed concentration was increased. Operation with high power output (13 mw and more) was accompanied by stalling in the channel as evidenced by a rise in the channel exit pressure accompanied by reduction in output voltage. In each case the power maximized before stall. The seeding system was a continuing source of difficulty. The performance of a Hall generator is closely related to the Hall coefficient which in turn depends to a large extent on the percentage water in the combustion products. Therefore, it is extremely important for good performance to keep the water content as low as possible. As it turned out, the seed carrier, methanol, contains water and also has a relatively high H/C ratio. Since the operating temperature was lower than anticipated, to achieve a reasonable working value of conductivity required adding more seed which had a self-cancelling affect on any improvement

of the performance since the addition of seed resulted in a larger generated power output while the addition of the seed carrier degraded the Hall coefficient and hence the performance. Based on the Group I Runs, certain conclusions were made concerning the design and performance of the original generator channel. These conclusions are enumerated below. They formed the basis for modifying the channel as will be discussed shortly.

- 1) Durability problems were experienced with the electrode design originally used. The electrode design used in the original channel was over two years old at the time of test. It was concluded that more recent electrode designs were needed to achieve reasonable electrode durability.
- 2) The outlet/inlet area ratio for the original channel was found to be less than optimum as indicated by the adverse pressure distribution which developed from mid-channel downstream. This is shown in Fig. 48 which compares the pressure distributions from typical Group I and Group II Runs (the static pressure measurement at the channel inlet is not to be taken too seriously since the very thin boundary layer there combined with the rough wall makes the pressure reading very sensitive to pressure point alignment at this location). The original channel was designed to have a slight favorable static pressure gradient in order to assist with boundary layer stability. The unfavorable gradient both compromises the boundary layer stability and increases the growth rate (see Eqs. (18) and (19)). The difficulty is further compounded by increased boundary layer growth due to the higher than expected wall drag coefficient for this type of channel as determined by extensive concurrent testing with the 1.5 megawatt Mark II generator. (11) The high drag coefficient seems to be due to the peculiar form of the roughness which consists of ordered ribs perpendicular to the flow. (33) Since we are dealing with a closed channel, the higher than expected boundary layer growth chokes off the inviscid core flow area and thus increases the adverse pressure gradient so that the effect is self compounding. Although there is some uncertainty, it seems that the basic starting point for the difficulty is the increased wall roughness with the other effects following. A further effect of the adverse pressure gradient is increased current density at the downstream end of the channel due to higher than expected temperature. Thus the Group I results indicated that it was imperative to open up the channel profile to obtain some favorable static pressure gradient, and the success of this modification is evident on Fig. 48.
- 3) The use of methanol in large quantities to carry the seed into the burner was found to cause a decrease in the burner temperature because of the lower heating value of methanol, as opposed to toluene, and also was responsible for a higher water concentration in the exhaust products because of the higher hydrogen content of methanol. This results in a reduction in performance of between ten and fifteen percent. Dry seed injection would certainly result in improved performance.

COMPARISON OF THE PERFORMANCE OBTAINED IN RUN # 21 USING THE ORIGINAL CHANNEL AND RUN # 7 USING THE MODIFIED CHANNEL

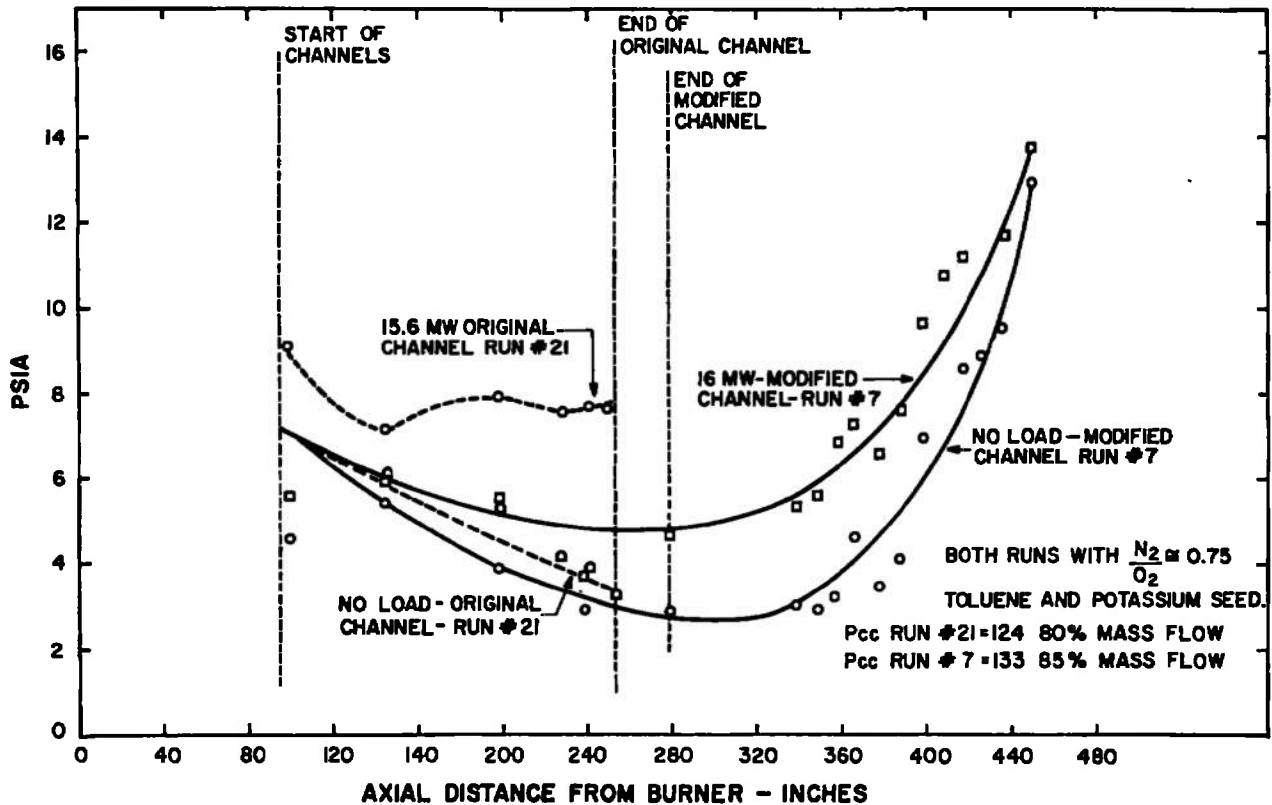


Fig. 48 Typical Pressure Distribution for Group I & Group II Runs Compared

- 4) Arcing at both the inlet and exit of the channel at the power take-off electrodes occurred in some cases with damage to the modules involved. Further, there was a performance degradation particularly noticeable from the pressure increase at the inlet end of the channel due to having effectively a short-circuited Hall generator, i.e., the inlet nozzle. Both of these effects could be eliminated by extending the channel at the inlet and exit so that power would be extracted where the axial electric field is near zero. This has the additional advantage of better utilization of the magnetic field.
- 5) Three difficulties were experienced with the exhaust system which discharges the spent combustion gases at high potential to the atmosphere:
  - a) Electrical contact between exhaust gases and metal exhaust breech.
  - b) Shorts or low resistance paths between breech and ground.
  - c) Leakage currents to ground through the breech spray cooling water which runs off the bottom of the breech, and is somewhat conducting due to dissolved seed.

Item a) above was probably largely responsible for whatever unsteadiness appeared on the output in the unstalled condition (unsteady output is expected when stalled), since the contact between gas and breech is of a highly transitory character. Actual arcing between the metal breech itself and ground was reduced by attention to the insulation. To avoid arcing, it was concluded that every effort should be made to raise the impedance to as high a value as possible between the hot gas and diffuser and the breech.

Test results of Run 21, which is typical of the tests in this group, are shown in Fig. 49. This figure shows the variation of the combustion chamber pressure, ( $P_{BC}$ ), the weight percent seeding rate, ( $S_W$ ), the load current, ( $A_{35}$ ), and the load or terminal voltage ( $V-50$ ), as functions of time. During the run the seed rate was varied three times from a low value up to the value where the downstream static pressure of the channel had appreciably increased. A maximum power of 16.0 mw was achieved at time, 50.77 seconds after the test was started. Evidence of channel stalling is apparent upon examination of the variation of downstream static pressure, ( $P_{C 355}$ ), measured at Ring No. 355. Note that as the generated power increases this exit static pressure rises almost to atmospheric pressure in some cases.

In spite of the difficulties encountered, it is important to note that the generator, the first Hall generator of any size ever built did achieve 16 MW power output or 80% of the design value at 80% of the design mass flow, i.e., the design value of power output per unit mass flow was achieved.

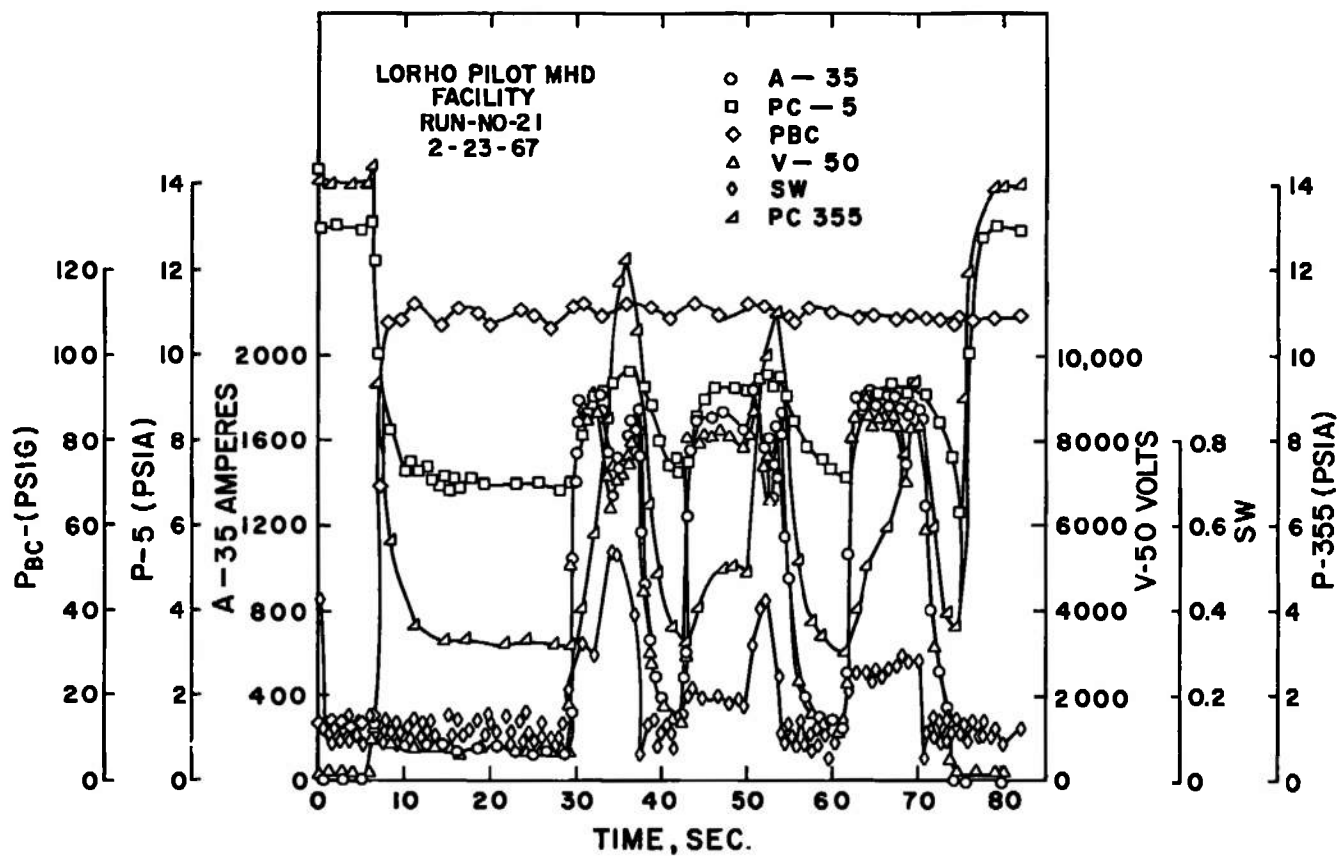


Fig. 49 Some Test Results of Run #21, First Series



On the basis of the Group I Runs and the conclusions drawn from this series of tests, recommendations for modification to the MHD generator system were made to the Air Force and accepted; the objective of the proposed changes was to improve system performance. The changes made to the system included.

- 1) For the purpose of improving electrode performance and durability, the electrode design was changed to correspond to the latest optimum design. Whereas wires were used as current collectors in the original electrodes, a U-shaped inconel screen insert was soldered in the electrode groove of the rings as shown in Fig. 22 to serve as a current collector and in addition to provide a ceramic retaining structure which was lacking in the first design.
- 2) The channel area ratio was enlarged and at the same time the channel profile was changed to conform more closely to the theoretical optimum. As a result of both the LORHO Pilot tests and Avco Everett Research Laboratory's Mark II Hall Generator tests, design programs had been upgraded and more closely checked against experiment to verify the validity of the programs. Tables V, VI and VII are included here to indicate the exact modifications in terms of ring internal diameters which were made to the original channel. Table V give the diameter of each ring of the original channel. Table VI lists the correspondence between ring numbers in the new channel and the old channel. Finally, Table VII lists the new rings which were made for the modified channel. Figure 14 shows the final contour of the modified MHD Generator system.
- 3) A comparison of the original and modified channels reveals that the length of the modified channel was longer. This change in length was made so that the downstream electrode would be in a region of low electric field where transverse currents ( $J_y$ ) would be low so as to provide a means of avoiding arcing due to current concentrations at the power take-off electrodes. The upstream electrode, as it turns out, is in a lower electric field region because of the local operating conditions (notably high static pressure) so that the possibility of arcing at the upstream end is much less than at downstream end (for the original channel). In spite of this, the front end of the channel was modified with a dead zone (several rings were completely filled with alumina to reduce to a minimum transverse currents and hence the axial electric field) so as to prevent any destructive arcing at the upstream power take-off electrode.
- 4) A transition diffuser section with a converging inlet (made so as to match the original diffuser) was fabricated. It was theorized that if the thinning of the boundary layer due to cooling of the boundary layer was comparable to the convergence angle of the diffuser inlet that the diffuser performance would be improved as compared to the performance of the original diffuser.

TABLE V  
DIAMETER OF EACH RING OF ORIGINAL CHANNEL

Part No.	Diameter "C"	Part No.	Diameter "C"	Part No.	Diameter "C"	Part No.	Diameter "C"	Part No.	Diameter "C"	Part No.	Diameter "C"
1	27.367	63	28.162	125	29.092	187	30.234	249	31.704	311	33.740
2	27.383	64	28.176	126	29.108	188	30.255	250	31.731	312	33.779
3	27.398	65	28.187	127	29.125	189	30.276	251	31.759	313	33.818
4	27.413	66	28.203	128	29.141	190	30.297	252	31.787	314	33.858
5	27.426	67	28.219	129	29.158	191	30.318	253	31.815	315	33.898
6	27.439	68	28.233	130	29.175	192	30.339	254	31.843	316	33.938
7	27.451	69	28.247	131	29.192	193	30.360	255	31.870	317	33.979
8	27.463	70	28.261	132	29.209	194	30.381	256	31.899	318	34.020
9	27.475	71	28.275	133	29.226	195	30.401	257	31.927	319	34.062
10	27.486	72	28.289	134	29.243	196	30.422	258	31.956	320	34.104
11	27.498	73	28.303	135	29.260	197	30.443	259	31.984	321	34.147
12	27.509	74	28.316	136	29.277	198	30.464	260	32.012	322	34.190
13	27.522	75	28.330	137	29.294	199	30.486	261	32.040	323	34.233
14	27.534	76	28.344	138	29.312	200	30.506	262	32.070	324	34.278
15	27.546	77	28.358	139	29.329	201	30.528	263	32.100	325	34.322
16	27.557	78	28.372	140	29.347	202	30.550	264	32.130	326	34.367
17	27.569	79	28.386	141	29.364	203	30.573	265	32.160	327	34.412
18	27.574	80	28.400	142	29.382	204	30.595	266	32.190	328	34.457
19	27.593	81	28.415	143	29.399	205	30.618	267	32.220	329	34.504
20	27.605	82	28.429	144	29.416	206	30.639	268	32.251	330	34.550
21	27.615	83	28.443	145	29.433	207	30.662	269	32.282	331	34.596
22	27.630	84	28.457	146	29.451	208	30.684	270	32.312	332	34.644
23	27.642	85	28.471	147	29.468	209	30.707	271	32.344	333	34.692
24	27.654	86	28.486	148	29.487	210	30.730	272	32.374	334	34.740
25	27.666	87	28.500	149	29.505	211	30.752	273	32.406	335	34.787
26	27.678	88	28.514	150	29.523	212	30.775	274	32.437	336	34.836
27	27.690	89	28.529	151	29.541	213	30.798	275	32.469	337	34.885
28	27.703	90	28.544	152	29.559	214	30.820	276	32.500	338	34.935
29	27.715	91	28.559	153	29.578	215	30.844	277	32.532	339	34.989
30	27.728	92	28.573	154	29.596	216	30.867	278	32.563	340	35.034
31	27.740	93	28.588	155	29.614	217	30.890	279	32.596	341	35.088
32	27.753	94	28.603	156	29.633	218	30.914	280	32.628	342	35.138
33	27.766	95	28.618	157	29.651	219	30.937	281	32.661	343	35.190
34	27.778	96	28.633	158	29.670	220	30.960	282	32.694	344	35.241
35	27.791	97	28.648	159	29.688	221	30.984	283	32.726	345	35.295
36	27.803	98	28.663	160	29.706	222	31.007	284	32.759	346	35.348
37	27.816	99	28.678	161	29.725	223	31.030	285	32.792	347	35.405
38	27.829	100	28.694	162	29.744	224	31.054	286	32.826	348	35.456
39	27.842	101	28.709	163	29.761	225	31.079	287	32.861	349	35.512
40	27.854	102	28.726	164	29.781	226	31.103	288	32.896	350	35.568
41	27.868	103	28.740	165	29.801	227	31.127	289	32.930	351	35.626
42	27.888	104	28.755	166	29.820	228	31.152	290	32.966	352	35.684
43	27.894	105	28.771	167	29.839	229	31.176	291	33.001	353	35.741
44	27.907	106	28.787	168	29.858	230	31.201	292	33.036	354	35.800
45	27.920	107	28.802	169	29.877	231	31.227	293	33.072	355	35.862
46	27.934	108	28.818	170	29.896	232	31.252	294	33.108	356	35.919
47	27.947	109	28.834	171	29.915	233	31.277	295	33.144	357	35.979
48	27.960	110	28.850	172	29.935	234	31.303	296	33.180	358	36.040
49	27.973	111	28.865	173	29.954	235	31.330	297	33.217	359	36.102
50	27.987	112	28.882	174	29.973	236	31.354	298	33.253	360	36.162
51	28.000	113	28.897	175	29.993	237	31.381	299	33.290		
52	28.013	114	28.913	176	30.012	238	31.408	300	33.327		
53	28.027	115	28.929	177	30.032	239	31.434	301	33.363		
54	28.040	116	28.945	178	30.052	240	31.460	302	33.400		
55	28.054	117	28.961	179	30.072	241	31.487	303	33.437		
56	28.067	118	28.977	180	20.092	242	31.514	304	33.475		
57	28.081	119	28.993	181	20.112	243	31.540	305	33.513		
58	28.094	120	29.010	182	30.132	244	31.567	306	33.546		
59	28.111	121	29.026	183	30.153	245	31.594	307	33.585		
60	28.122	122	29.042	184	30.173	246	31.621	308	33.624		
61	28.135	123	29.059	185	30.193	247	31.648	309	33.663		
62	28.149	124	29.076	186	30.214	248	31.676	310	33.701		

TABLE VI  
CORRESPONDENCE BETWEEN RING NUMBERS IN NEW AND OLD CHANNELS

NEW CHAN. RING NO.	OLD CHAN. RING NO.	NEW CHAN. RING NO.	OLD CHAN. RING NO.	NEW CHAN. RING NO.	OLD CHAN. RING NO.	NEW CHAN. RING NO.	OLD CHAN. RING NO.	NEW CHAN. RING NO.	OLD CHAN. RING NO.
MAJ. 1	1	71	130	P. T. 141	215	211	282	281	
2	4	72	131	142	216	212	283	282	337
3	6	73	133	143	218	213	284	283	338
4	8	74	134	144	219	P. T. 214	285	284	
5	11	P. T. 75	135	145	220	215	286	285	339
6	13	76	137	146	221	216	287	286	340
P. T. 7	15	77	138	147	222	217	288	287	
8	18	78	139	148	223	218	289	288	341
9	20	79	141	149	224	219	290	289	342
10	23	80	142	P. T. 150	225	220	291	290	
11	25	81	144	S. R. 151	227	221	292	291	343
12	27	P. T. 82	145	152	228	222	293	292	344
MIN. 13	30	83	146	153	229	223	294	293	
MIN. 14	31	84	148	154	230	224	295	294	345
P. T. 15	35	85	149	155	231	225	296	295	346
16	36	MIN. 86	150	156	232	226	297	296	
17	39	MIN. 87	151	157	233	P. T. 227	298	297	347
18	41	88	153	158	234	228	299	298	348
19	43	89	154	159	235	229	300	299	
20	45	P. T. 90	155	P. T. 160	236	230	301	300	349
21	47	91	157	161	237	231	302	301	350
22	50	92	158	162	238	232	303	302	
23	52	93	159	163	239	MIN. 233	304	303	351
24	54	94	160	164	240	MIN. 234	305	304	352
P. T. 25	55	95	162	MIN. 165	241	235	306	305	
26	57	96	163	MIN. 166	242	236	307	306	353
27	59	97	164	167	243	237	308	307	
28	62	S. R. 98	167	168	244	238	309	308	354
29	63	99	168	169	245	P. T. 239	310	309	355
30	65	100	169	P. T. 170	246	240	311	310	
31	66	101	170	171	247	241	312	311	356
32	68	102	171	172	248	242	313	312	357
33	70	103	172	173	249	243	314	313	
34	72	104	173	174	250	244	315	314	358
35	73	105	174	175	251	245	316	315	
P. T. 36	75	P. T. 106	175	S. R. 176	252	246	317	316	359
37	77	107	177	177	253	247	318	317	
38	79	108	178	178	254	248	319	318	360
39	80	109	179	179	255	249	320		
S. R. 40		MAJ. 110	180	P. T. 180	256	250	321		
41	84	MAJ. 111	181	181	257	S. R. 251	322		
P. T. 42	85	112	183	182	258	P. T. 252	323		
43	87	113	184	183	259	253	324		
MAJ. 44	90	P. T. 114	185	184	260	254	325		
MAJ. 45	91	115	186	185	261	255	326		
46	92	116	187	186	262	256	327		
47	94	117	188	187	263	257	328		
48	96	118	190	188	264	258	329		
49	97	119	191	189	265	259	330		
50	99	120	192	190	266	260	331		
51	100	121	193	191	267	261	332		
52	102	122	194	P. T. 192	268	262	333		
53	103	S. R. 123	197	193	269	263	334		
P. T. 54	105	124	198	194	270	264	335		
55	106	125	199	195	271	P. T. 265	336		
56	108	126	200	196	272	266			
57	109	127	201	MAJ. 197	273	267			
58	111	128	202	MAJ. 198	274	268			
59	112	129	203	199	275	269			
60	114	130	204	200	276	270			
P. T. 61	115	131	205	201	277	271			
62	117	P. T. 132	207	202	278	MIN. 272			
63	118	133	208	P. T. 203	279	MIN. 273			
64	119	134	209	204	280	274			
S. R. 65		135	210	205	281	275			
66	123	MIN. 136	211	S. R. 206		276			
67	124	MIN. 137	212	207		277			
68	126	138	213	208		278			
69	127	139	214	209		279			
70	128	140		210		280			

TABLE VII  
NEW RINGS FOR MODIFIED CHANNEL

<u>Part No.</u>	<u>Diameter "C"</u>	<u>Part No.</u>	<u>Diameter "C"</u>	<u>Part No.</u>	<u>Diameter "C"</u>	<u>Part No.</u>	<u>Diameter "C"</u>
176 S. R.	31.743	324	36.416	362	37.927	400	39.425
191	32.143	325	36.454	363	37.968	401 P. T.	39.463
199	32.359	326	36.493	364	38.009	402	39.501
207	32.580	327	36.531	365	38.050	403	39.538
215	32.807	328	36.570	366	38.090	404	39.576
220	32.949	329	36.608	367	38.131	405	39.613
225	33.092	330	36.647	368	38.172	406	39.651
231	33.271	331 P. T.	36.685	369 MIN.	38.213	407	39.683
237	33.452	332	36.724	370 MIN.	38.254	408	39.714
242	33.604	333	36.762	371 P. T.	38.294	409	39.744
247	33.755	334	36.801	372	38.335	410	39.775
251	33.879	335	36.839	373	38.376	411 P. T.	39.806
256	34.038	336	36.877	374	38.417	412	39.837
260	34.165	337	36.916	375	38.458	413	39.868
263	34.261	338	36.954	376	38.498	414	39.899
267	34.388	339	36.994	377	38.539	415	39.929
270	34.483	340	37.034	378	38.580	416	39.960
274	34.617	341 P. T.	37.075	379	38.621	417	39.991
277	34.720	342	37.115	380	38.662	418	40.022
281	34.857	343 MIN.	37.156	381 P. T.	38.702	419	40.053
284	34.960	344 MIN.	37.197	382	38.743	420	40.083
287	35.063	345	37.237	383	38.784	421 P. T.	40.114
290	35.166	346	37.278	384	38.824		
293	35.269	347	37.318	385	38.861		
296	35.377	348	37.359	386	38.899	40 S. R.	28.429
299	35.487	349	37.399	387	38.937	65 S. R.	29.042
302	35.597	350	37.440	388	38.974	98 S. R.	29.820
305	35.706	351	37.481	389	39.012	123 S. R.	30.401
307	35.779	352	37.521	390	39.049	151 S. R.	31.103
310	35.889	353	37.562	391 P. T.	39.087		
313	35.999	354	37.602	392	39.125		
315	36.072	355	37.643	393	39.162		
318 MAJ.	36.185	356 P. T.	37.684	394	39.200		
319	36.223	357	37.724	395 MIN.	39.237		
320	36.262	358	37.765	396 MIN.	39.275		
321 P. T.	36.300	359	37.805	397	39.313		
322 S. R.	36.339	360	37.846	398	39.350		
323	36.377	361 P. T.	37.886	399	39.388		

## NOTES -

- 1 - S. R. = Split Ring as per C-66/308
- 2 - P. T. = Pressure Taps as per Det. J. D-67/401
- 3 - MAJ. = Indicates location of Major Flange
- 4 - MIN. = Indicates location of Minor Flange

5) Insulation on all parts of the exhaust were improved

- a) by removing some of the spray rings to avoid gas-to-ground contact,
- b) by supporting all components on plastic,
- c) by enlarging the path and insulation between the breech and diffuser,

and, finally,

- d) by coating the whole diffuser with an insulating material.

The modifications to the MHD generator system and to the facility itself were accomplished in the time period between April 5, 1967 and June 4, 1968.

Group II Runs were initiated on June 4, 1968. Again, the testing pattern was essentially the same--first system checkout, second, short-circuit tests, and finally, power generation tests. Table IV lists pertinent data and comments relative to the 22 tests in this series. As indicated Runs 1 through 19 were directed toward optimizing the power output at the end of which time attention was turned to obtaining a complete set of generator voltage-current characteristics for the MHD generator at various seeding rates. This was the objective of Runs 20, 21 and 22. The maximum generated power for this series of Runs was 18 mw (Run 19) at a voltage of 9213 volts and a current of 1950 amperes. The operating conditions at which the maximum power was achieved were:

- 1) Approximately 85% mass flow.
- 2) Oxidizer nitrogen to oxygen ratio of 0.7.
- 3) Methanol seed carrier.
- 4) Oxygen to fuel ratio of 2.93. (It was found that considerable improvement could be obtained by operating at an O/F ratio less than stoichiometric. Inspection of predicted flame temperatures as a function of O/F ratio shows that the temperature does rise initially as the ratio is decreased.)
- 5) Load resistance of 4.46 ohms.

The chamber pressure, power generated and exit static channel pressure are shown for this run as a function of time in Fig. 50. The generator is nearing stall at high value of generated power as evidenced by the large increase in exit static pressure.

Runs 20, 21, and 22 were to be the first of four scheduled performance mapping runs. Each of the runs was to be carried out by increasing the seed concentration until maximum output was achieved at fixed load resistance, then short-circuiting the generator and backing off the seed to obtain the short circuit characteristics. The data obtained from Runs 19,

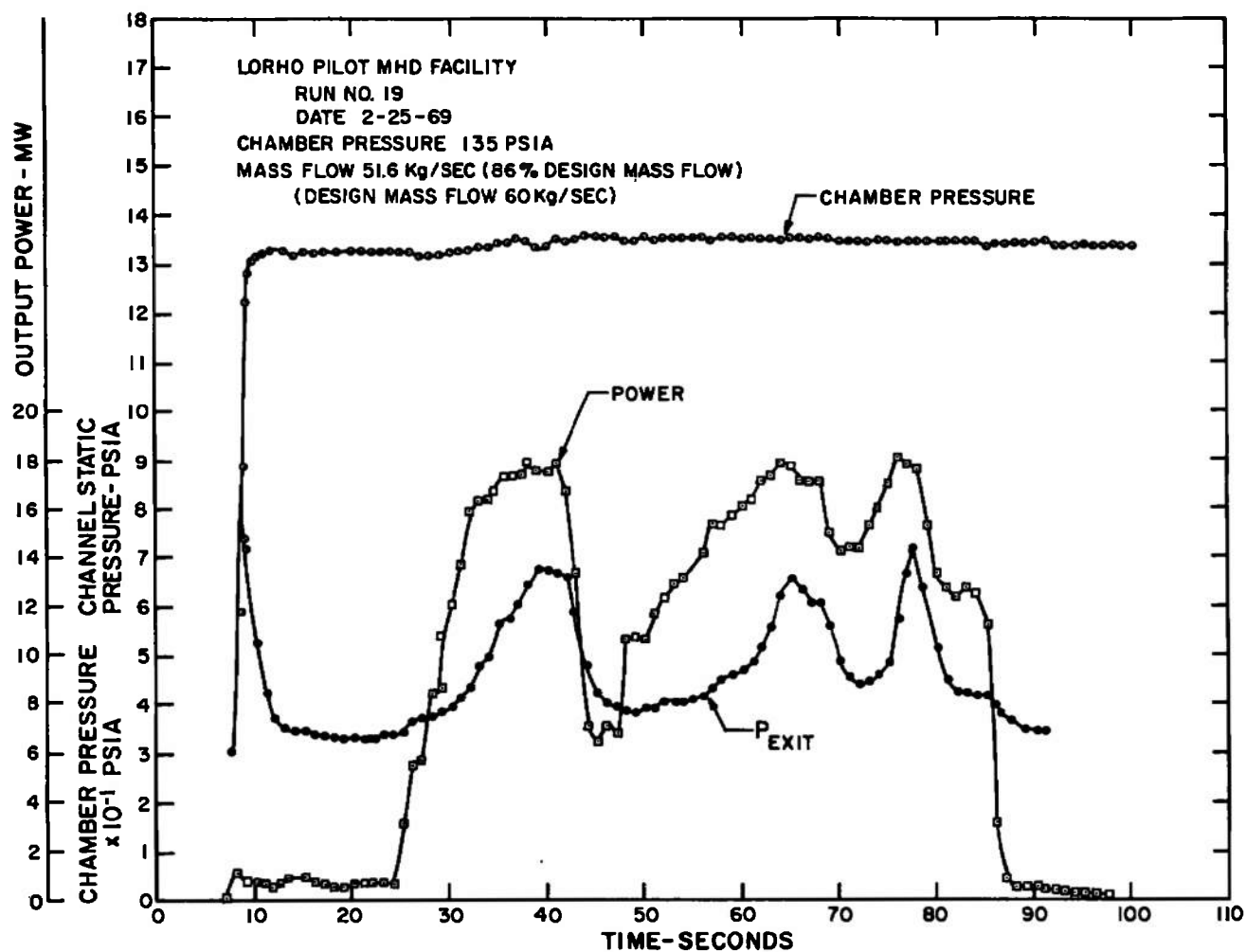


Fig. 50 Chamber Pressure, Power and Exit Static Pressure for Run 19 as a Function of Time

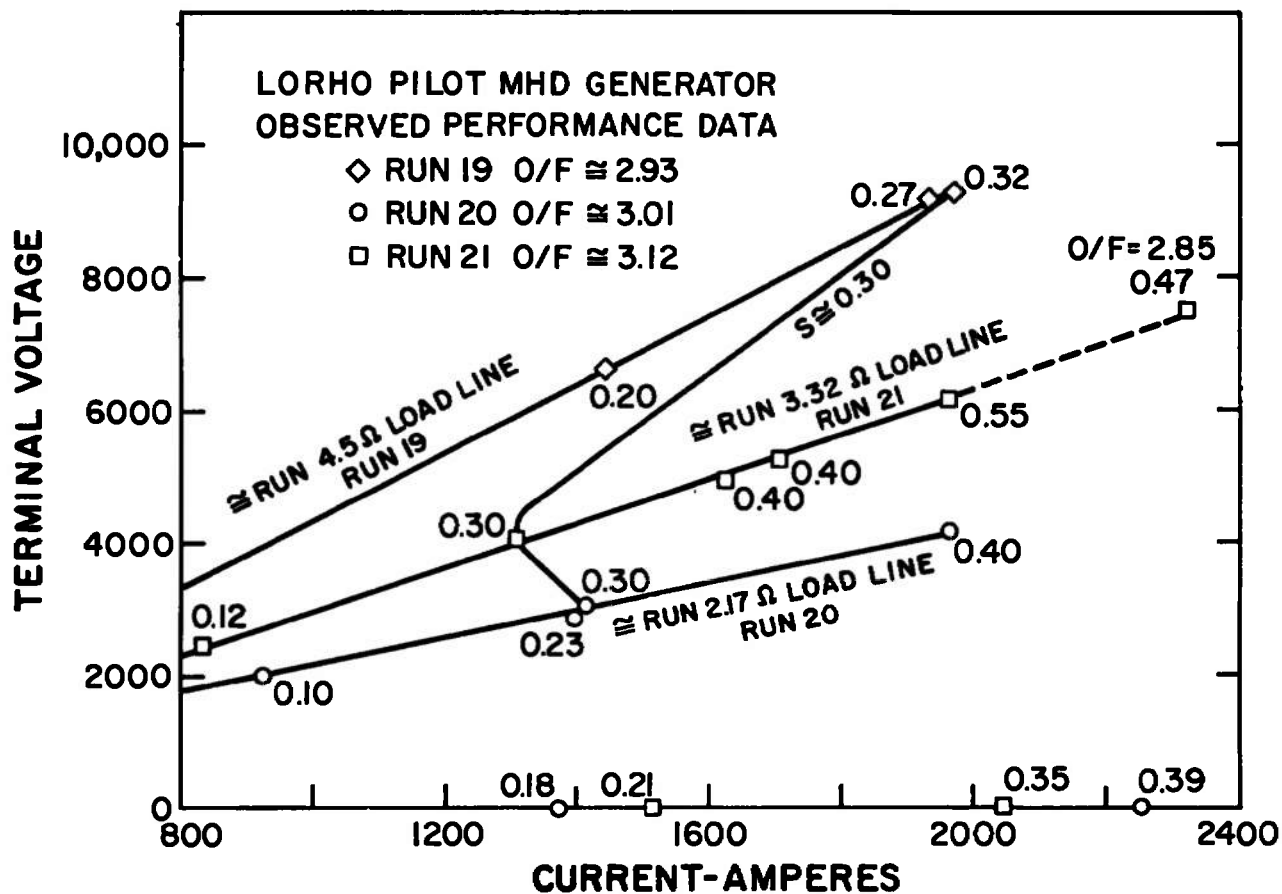


Fig. 51 Selected Data from Runs 19, 20 and 21 (Modified Channel)

20, and 21 are given in Fig. 51. The data show the load lines for the three different values of load resistance. The O/F ratios for each run are as noted. The numerical value on the load lines corresponds to the recorded seed concentrations. A curve at constant indicated seed concentration of 0.3% by weight is shown, and indicates the high degree of sensitivity of the gaseous electrical conductivity to the O/F ratio. Additionally it may be suggested that the rate of change of seed concentration is of some importance as there is some time lag between changing seed flow and influencing the generator due to the finite amount of fuel in the piping and manifold downstream of the seed injection location.

Run 22 on March 13, 1969 was scheduled for gas conditions identical to the previous three runs, including variable seed concentration, and a 4.5 ohm load. Shortly after the main burner ignition as the seed was being increased at a load current of approximately 1000 amperes, gas discharge from the burner backplate was observed on the television monitor. Although no definite conclusions can be reached in this matter, it seems as if the incident was the result of loss of cooling in the pilot burner leading to/or rupture of the pilot burner liner or to loss of a fuel spud with consequent combustion in the oxygen manifold. As a result, the existing backplate including the pilot burner was unserviceable. The Group II Runs were concluded at this time.

Based on the Group II Runs several comments and conclusions can be made relative to the performance of the modified channel. These are:

- 1) In spite of the fact that the electrodes were rebuilt as opposed to being newly fabricated (complete freedom of design was not available in the rebuild because of the existing structure), use of the most recent electrode design configurations improved the electrode durability tremendously. Whereas electrode repairs were required after each test with the original generator channel, only minor electrode repairs were required after each test in the second series of tests.
- 2) Destructive arcing at the power electrode caused severe damage to the channel in the first series of test. The addition of a dead zone upstream and extending the channel at the downstream end so as to reduce current and electric field completely relieved the arcing problems.
- 3) The change of area ratio and the area profile improve the channel as evidenced by the favorable pressure distribution, but this improvement was partly counterbalanced by the diffuser modification which did not perform as expected (it depended on reduction of boundary layer thickness against the cold diffuser wall). The pressure distribution in the modified channel was smooth without the mid-channel hump encountered in the original channel. In the original channel, stalling of the channel occurred approximately at the mid point of the channel as a result of adverse pressures being applied to the boundary layer due to the improper area profile of the original channel. Stalling of the modified generator system never occurred in the channel but rather developed as a



result of inefficient recovery in the diffuser. We believe that installation of a diffuser configuration similar to the original will result in performance approximating that shown by the theoretical channel stall curve (see Fig. 57).

- 4) Operation of a high voltage MHD generator requires that careful attention be given to the physical location and method of support of the breech, diffuser, cooling pipes and channel. Either the diffuser should exhaust into a completely open area or it should be completely coated and supported with relatively thick insulation.
- 5) Changing the seed feeding technique so that dry powder could be directly injected into the burner was not done because it would have required major modification to the facility and burner backplate. For a Hall generator, this is the most superior method of feeding seed. Solid seed material has been utilized in smaller MHD generator systems, and it should be feasible for large ones as well. Several attempts were made to reduce the water content of the combustion products by changing from a methanol carrier to a water carrier. Theoretically, the water content of the combustion products can be reduced through the use of a water carrier as opposed to methanol carrier without affecting the flame temperature. Tests, however, disproved this and revealed that the water carrier had the net effect of reducing the conductivity compared to tests with the same seeding rate using a methanol carrier.
- 6) This series of tests confirmed that high temperatures and hence high conductivities could be achieved by taking advantage of the higher flame temperatures available at O/F ratios less than stoichiometric.

Several general conclusions can be made in view of the overall performance evaluation program; these are:

- 1) Multi-megawatt MHD generator systems can be reliably designed and operated, thus making available the advantages of the MHD generator in burst power applications.
- 2) The two major causes of inference with individual tests were malfunctioning of the control and protection systems and arcing to ground. Relative to the former, reliable operation requires careful attention to the design of the control and protection system as well as the use of very reliable components. Avoidance of arcs-to-ground requires that special attention be given to insulation and supports as already discussed.
- 3) Other causes for premature shutdown derived in part from improper operating procedures, fabrication techniques and design errors. Of course, all of these faults which are the result of human error can be and should be avoided.
- 4) The information and experience obtained from this program is, of course, invaluable in terms of a Full Scale LORHO Facility and any other future MHD generator power supply.

## 5. COMPARISON OF OBSERVED AND EXPECTED PERFORMANCE

The methods of Section III-2 are here applied to analyze the experimental results with the threefold purpose of understanding the results which were obtained, choosing appropriate values for some of the undetermined parameters in the theory, and achieving a package which can be utilized for future designs with some confidence.

The latter point deserves some comments. Examination of the analytic technique reveals a number of adjustable parameters as for instance those specifying electrode drop, friction factor, nonuniformity factor and so on. As we will see, the theory as adjusted to correlate with the results with the modified channel also leads to very accurate prediction of the channel stall characteristics for the original configuration. But these two channels are very similar so that good agreement should be expected here. On the other hand, one would expect less precise agreement if the configuration differed greatly from that of LORHO, and in such cases it should be applied with caution and good judgment.

As the LORHO is a large machine designed for a practical purpose, it does not have the instrumentation density of smaller laboratory devices; so that while gross performance figures, say output voltage and current, are available continuously, measurements of pressure, voltage and current distributions, etc., are not as detailed as would be required for really precise comparison with theory. Finally while the number of runs is substantial, several more would be required to obtain a complete performance map. In addition, as we have seen, many runs, particularly in the first series, were primarily concerned with obtaining satisfactory system operation rather than with performance mapping.

In what follows, the analysis will be correlated with data from the second test series (modified channel). As performance during this series was limited by the diffuser rather than channel stall, the analysis is used to predict the stall limit with an improved diffuser. Finally, the analysis is applied to examine a high power run from the first series where channel stall was the limiting factor, and excellent agreement between the observed and calculated results is obtained.

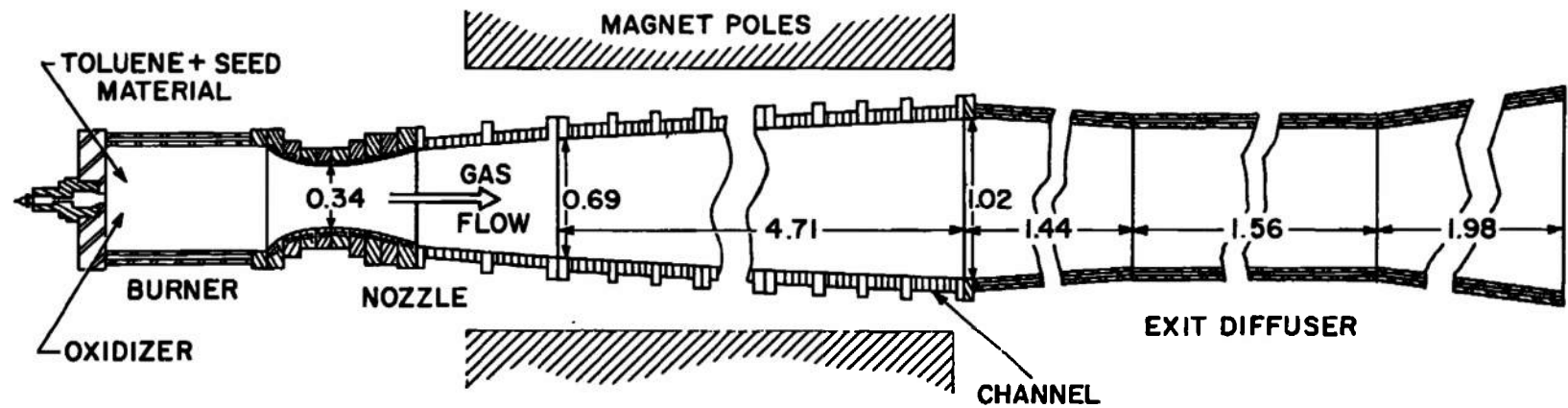
### a. Analysis of Second Series Test Data

The performance of the MHD generator system has been investigated over a wide range of operating conditions with different combinations of the mass flow, oxidizer composition, seed flow rate, and loads and loading procedures. After the channel was modified, the maximum power output of the generator was increased to 18 mw, and some information concerning voltage versus current characteristics of the generator were obtained by shorting out the load during the test and thereby obtaining results at both loaded and short-circuit conditions. Two points on each V-I curve are established in this manner. Axial distributions of static pressure, transverse currents, and Hall voltage are made. Detailed comparisons between analytical and experimental results for the above quantities are presented here.

First typical values of the important parameters will be discussed. For the maximum power output situation the values of  $p_1$ ,  $T_1$ ,  $u_1$ , and  $\Theta$  (see III-2) at the inlet of the generator are 0.415 atm, 2450°K, 2250 m/sec, and 2 mm, respectively. The value of  $\Theta$  is estimated from the expansion over the cold wall at the nozzle in a favorable pressure gradient. The total mass flow rate is 52.3 kg/sec, and the flow rate of potassium is 0.32% by weight. Average values of  $\sigma$  and  $\omega\tau$  are 4.5 mho/meter and 2.8, respectively. The magnetic field strength in the middle of the magnet is 1.9 tesla. The channel dimensions are given in Fig. 52. The electrode drop is estimated to be about 125 volts at the inlet and about 200 volts at the channel exit. These values of electrode drops are based on previously described experimental results and on other long-duration tests<sup>(20)</sup> where the same type electrodes were used. From past measurements of heat transfer and electrode temperature in this type flow<sup>(20)</sup> it is estimated that the ratio of  $h_w/h_1$  is about equal to 0.5 and that  $h_w$  is approximately independent of axial locations (the energy extraction is about 6%).

The measured static pressure distribution with no MHD interaction is compared with analytical results in Fig. 53. Two sets of data are shown, one at the beginning and another at the end of a test. It is seen that the two sets of data are very close together indicating steady state and good repeatability. The agreement between the calculations and the data are good except at three locations in the channel. This discrepancy is probably due to stagnation pressure effect in the  $M = 2.5$  flow because of misalignment of static pressure ports in this part of the channel, since no other measured quantity indicates any irregularity at this location. A large wall roughness effect is used in the analysis. The indicated friction factor at the channel inlet is about four times the corresponding smooth plate value. A small part of this factor may come from neglecting three dimensional effects due to the circular channel geometry, but the main cause is probably the roughness effects of this type of channel construction.<sup>(21)</sup> It should be noted that compressibility effects with cooled walls tend to enhance wall roughness effects. The friction factor from this unloaded situation is also used under loaded conditions.

In Fig. 54, the change in static pressure along the channel due to MHD effects is illustrated. Results for both 16 and 18 mw power output are given. The data have a fairly large scatter. The analytical prediction is in fair agreement with the experimental values for the 16 mw case; however, for the 18 mw case the data indicate a considerably larger pressure difference in the last meter of the channel than the analytical results do. This is probably due to recovery problems in the diffuser. The pressure distributions in the diffuser indicate that the diffuser barely recovers at these conditions. The analyses indicate a normal shock recovery pressure at the exit of the channel of about 1.3 atm, which should be adequate. However, compromises were made when this diffuser was made, and it does not have an optimum configuration. The boundary layer calculations do not indicate difficulties with separation. Comparisons at power levels below 16 mw also show good agreement between experiments and theory.



NOTE: ALL DIMENSIONS IN METERS

Fig. 52 Configuration of Modified Channel

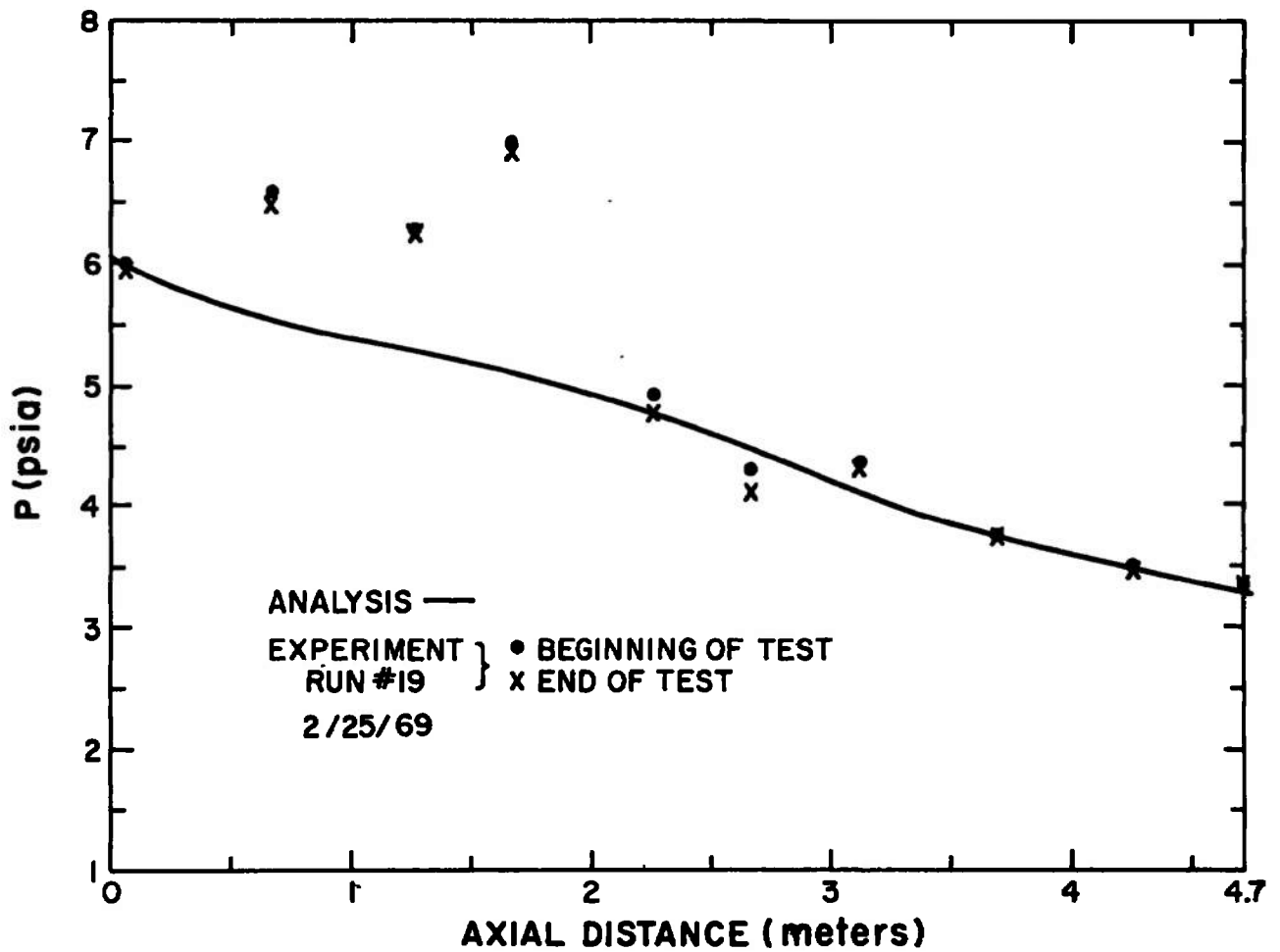


Fig. 53 Unloaded Static Pressure Distribution in MHD Channel

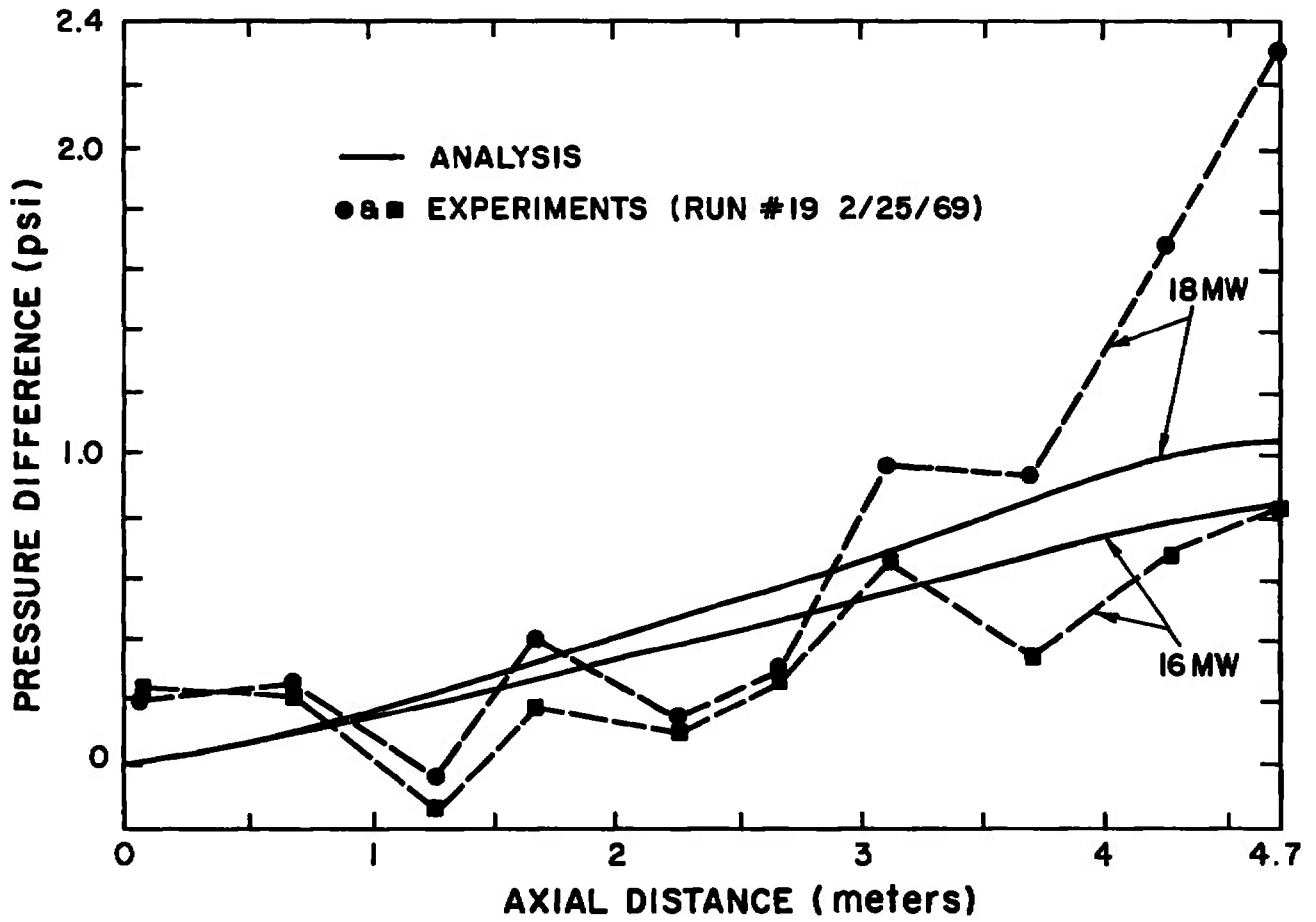


Fig. 54 Loaded Static Pressure Distribution in MHD Channel

The axial distribution of transverse current measured in selective electrode segments for the 18 MW case is shown in Fig. 55. A fair amount of scatter in the data is observed. When a comparison with the analytical results is made, one finds that the experimental values are on the average 35% larger than the calculated values. The split electrodes where the current measurements were made, were constructed more carefully than the other electrodes and it is possible that they perform better than their neighbors and therefore carry more than the average current in the channel. There are strong indications that this is the case. For instance, during the Group I runs, rings with the improved electrode configuration were substituted for the original ring at several isolated locations in the channel. Very high voltages were noted between these improved electrodes and the adjacent originals indicating unusually high currents to the new electrodes; similar results have been observed with the Mark II. In fact, with the zero impedance return path for the current, and the high ratio of channel diameter to electrode pitch, it is to be expected that there will be substantial variation in current to the individual electrodes according to their "quality". The carefully prepared split ring electrodes probably are of "high quality". This can easily be checked out in future tests. In all cases checked the same type discrepancy appears.

The Hall voltage distribution is probably the most sensitive of the presented data in terms of errors in the values  $\sigma$ ,  $\omega T$ , and nonuniformity effects when operation is near short circuit as is the case for the front part of this generator. In Fig. 56, Hall voltage data are compared with analytical predictions. Very good agreement is observed except at the end of the channel for the 18 MW case. The discrepancy in channel pressure as shown in Fig. 54 could cause an effect of this type. In addition, the behavior of the pressure distribution would tend to change the end effects. For several cases of power output below 16 MW good agreement was observed. The nonuniformity effects in terms of equivalent G-factor values (Eq. (23)) varied from about 1.15 at the inlet to 1.35 near the middle of the channel. A G-factor of 1.0 implies uniform conditions. The electrode and insulator boundary layer effects were about equal for this case and varied from about 1% at the inlet to a maximum of 10% further down into the channel. The  $j_x \times B$  transverse force contributed about 10-20% and the finite segmentation effect caused a 3-5% effect in terms of an equivalent G-effect. In these calculations 90% of the theoretical values of  $\omega T$  were used. This was justified based on earlier experiments in similar type gases. Furthermore, for argon a similar difference appears between the present type theoretical results and more accurate calculations.<sup>(15)</sup> The authors of Ref. 15 also point out that a 15% uncertainty in calculated values exists due to uncertainties in the collision cross-section values.

In Fig. 57 the Hall voltage versus Hall current characteristics of the generator are plotted. Three different experimental curves are indicated. Since only two points are available for each curve (i. e., at load and short circuit), straight lines are drawn. When these lines are drawn, one finds about a 20% spread in their slopes. The data for these characteristics were obtained in two separate runs and with slightly different conditions in the generator. Within the 20% uncertainty they all show the same characteristic behavior. Two calculated curves are shown, one of which corresponds to the 18 mw case. These characteristics are almost straight lines whose slopes correspond well with the experimental values. The analytical curves are about 10% steeper than the average experimentally observed ones. In the 18 mw case the loading parameter varied from about 0.74 at the inlet of the channel to about 0.36 at the exit with an average value of 0.5. The average electrical efficiency is about 0.37.

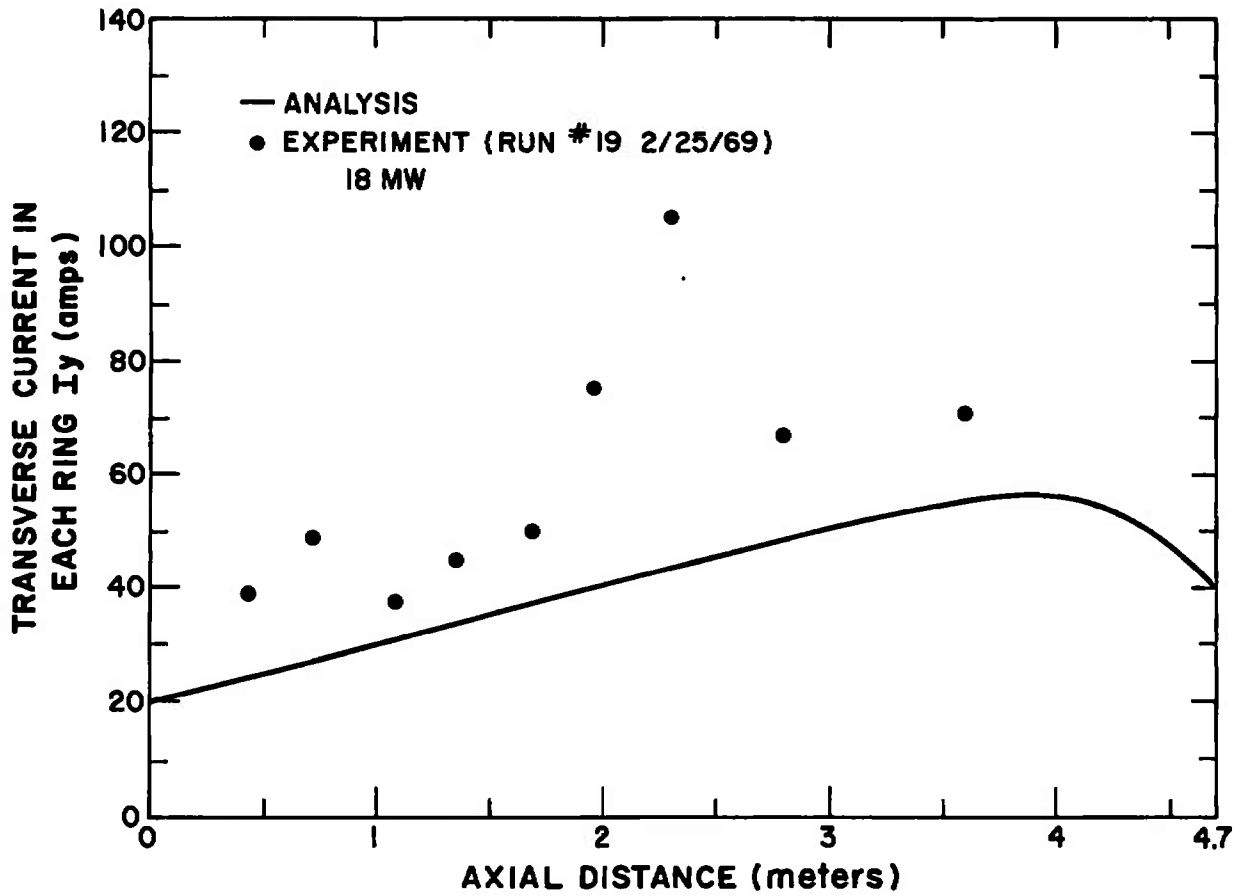


Fig. 55 Transverse Current Distribution in MHD Channel



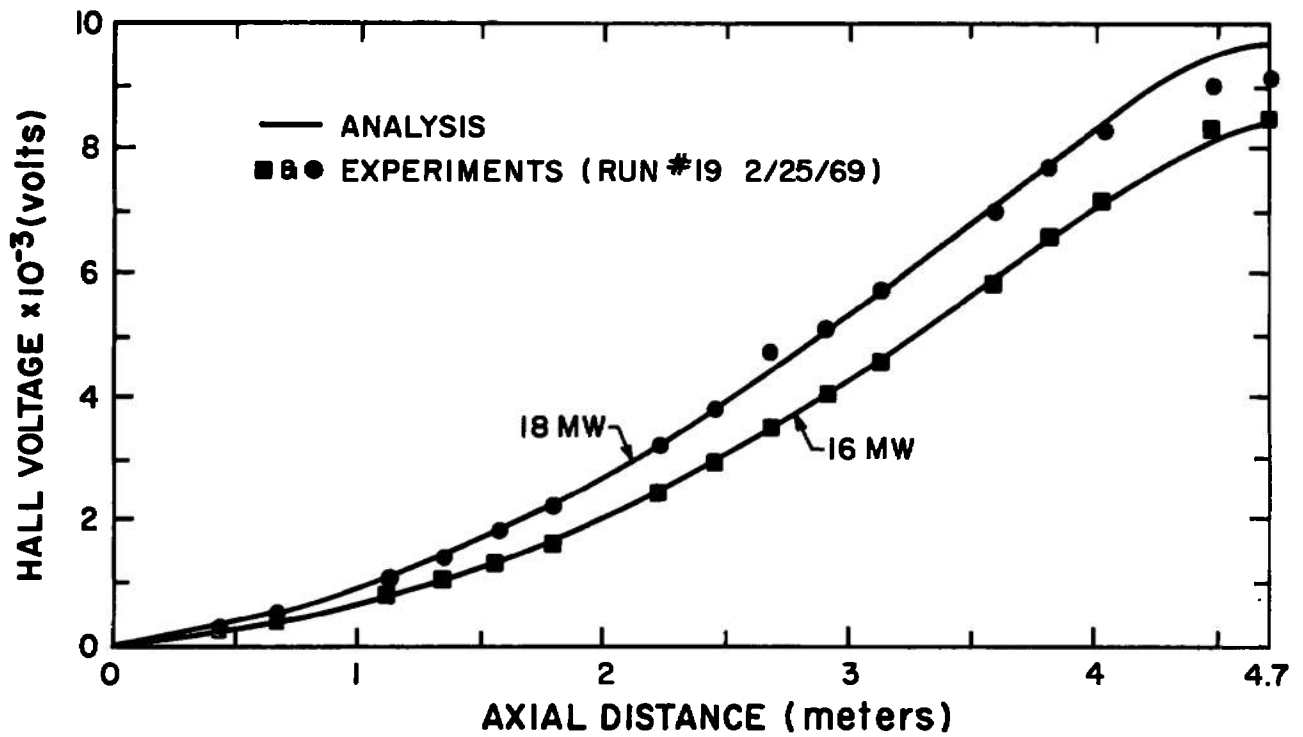


Fig. 56 Voltage Distribution on the Channel

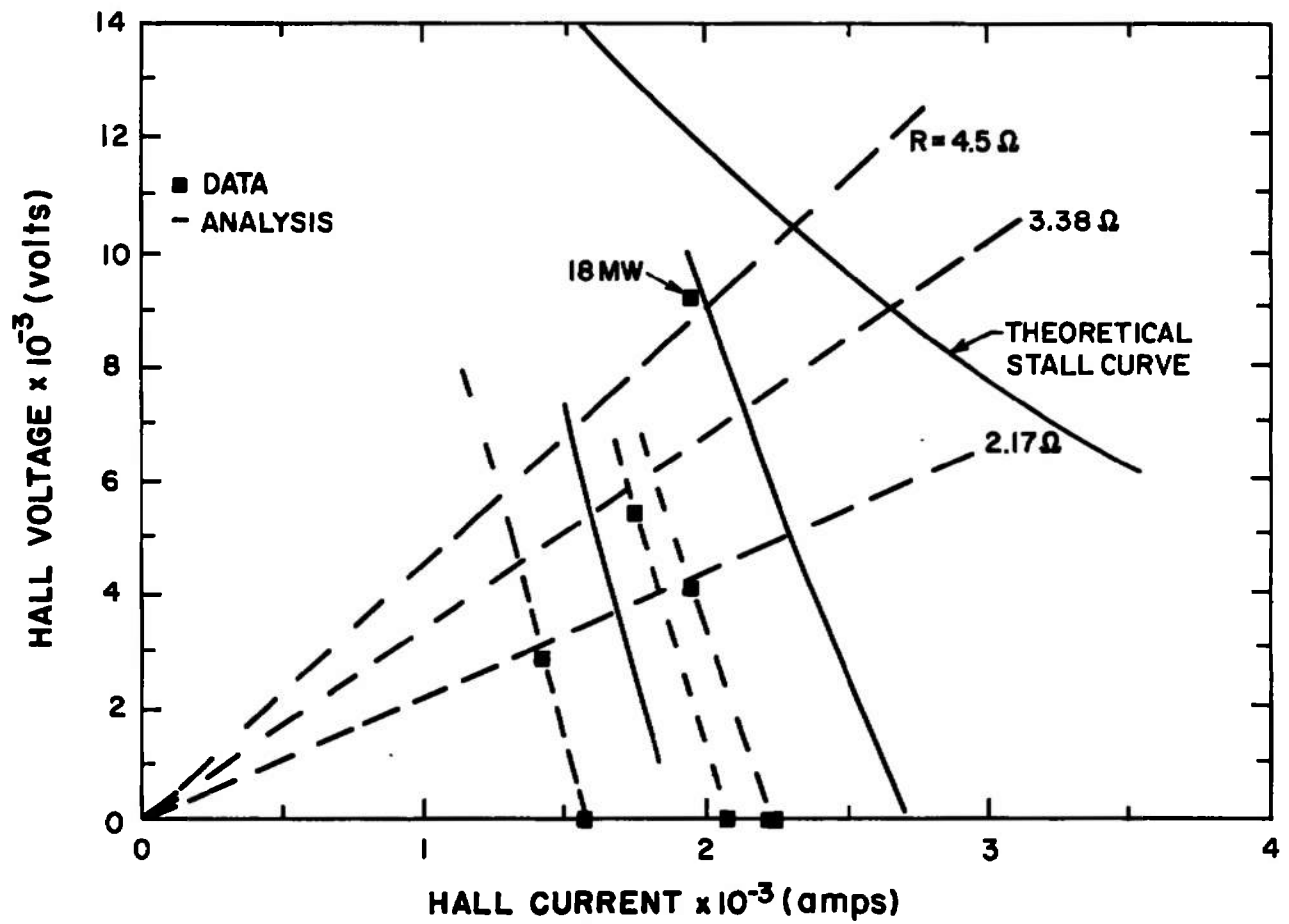


Fig. 57 Voltage-Current Characteristics at Various Seed Concentrations

Channel boundary layer stall did not occur with the modified channel as diffuser performance was inadequate due to effects previously described. It is believed that a diffuser of configuration identical to the original design but with a 40" inlet diameter would give performance which would permit the channel to operate up to its stall limit. The present method of analysis has been used to estimate this limit, and the result is also shown in Fig. 57. Stall is assumed to occur when  $\bar{H} \geq 1.8$ . The analysis predicts that, with the reconfigured diffuser, an output of about 21,500 kw should be achievable at any voltage level between 6000 and 14,000 volts. Although breach insulation would probably cause breakdown difficulty at less than 14,000 volts, the excellent indicated versatility of the design is encouraging. A reconfigured diffuser would in all likelihood, lead to regular, reliable operation at rated output.

In order to examine the adequacy of the analysis for predicting stall, the analysis has been applied to a high power run from the first series (Run 21, 2/23/67) where boundary layer stall occurred at a power output of just above 16,000 kw. The analysis was applied in a "hands off" fashion, that is, all of the adjustable parameters in the calculations, except  $\sigma$ , were put equal to the values which led to best agreement with the no stall runs of the second series. The results are shown in Figs. 58 and 59. Figure 58 shows the voltage distributions at fixed output current equal to observed current at 16,000 kw for three conductivity levels differing by a maximum of 10% from a maximum value of unity corresponding to calculated values with the recorded seed concentration (which was not known all that accurately in the first series). The observed voltage distribution is also shown, and indicates a best agreement with about  $F_1 = 0.95$ . The agreement is quite striking. Even more striking is the data displayed in Fig. 59 which shows the calculated incompressible shape factor distribution for the conditions of Fig. 58. As in the experiment the generator actually stalled with a very small increase in seed concentration above that corresponding to maximum output of 16,000 kw. The sharpness of the analysis in predicting this stall is encouraging and, it is believed, of good portent for future designs. In addition, this verification supports the conclusions above for the Group II experiments.

In conclusion, all parts of the generator performance characteristics have been predicted satisfactorily by the present analytical techniques. Small discrepancies between analysis and experiments still exist, and are probably due to effects not accounted for in the analysis or inaccuracies in the present approximations, electrical property data for the gases, and errors in measured experimental quantities.

## 6. UPRATING THE LORHO MHD POWER SUPPLY

The LORHO power supply facility itself is versatile, (see Section V) and there are numerous opportunities for variations and/or uprating should the need for these arise. The facility is capable of delivering mass flows as high as one hundred (100) kg/sec to the burner, with  $N_2/O_2$  ratios variable from 3.7 (air) to zero (pure oxygen), and with a variety of liquid fuels of various carbon/hydrogen ratios. The breach cooling and exhaust system seems ample for higher heat flux. At the higher flow,

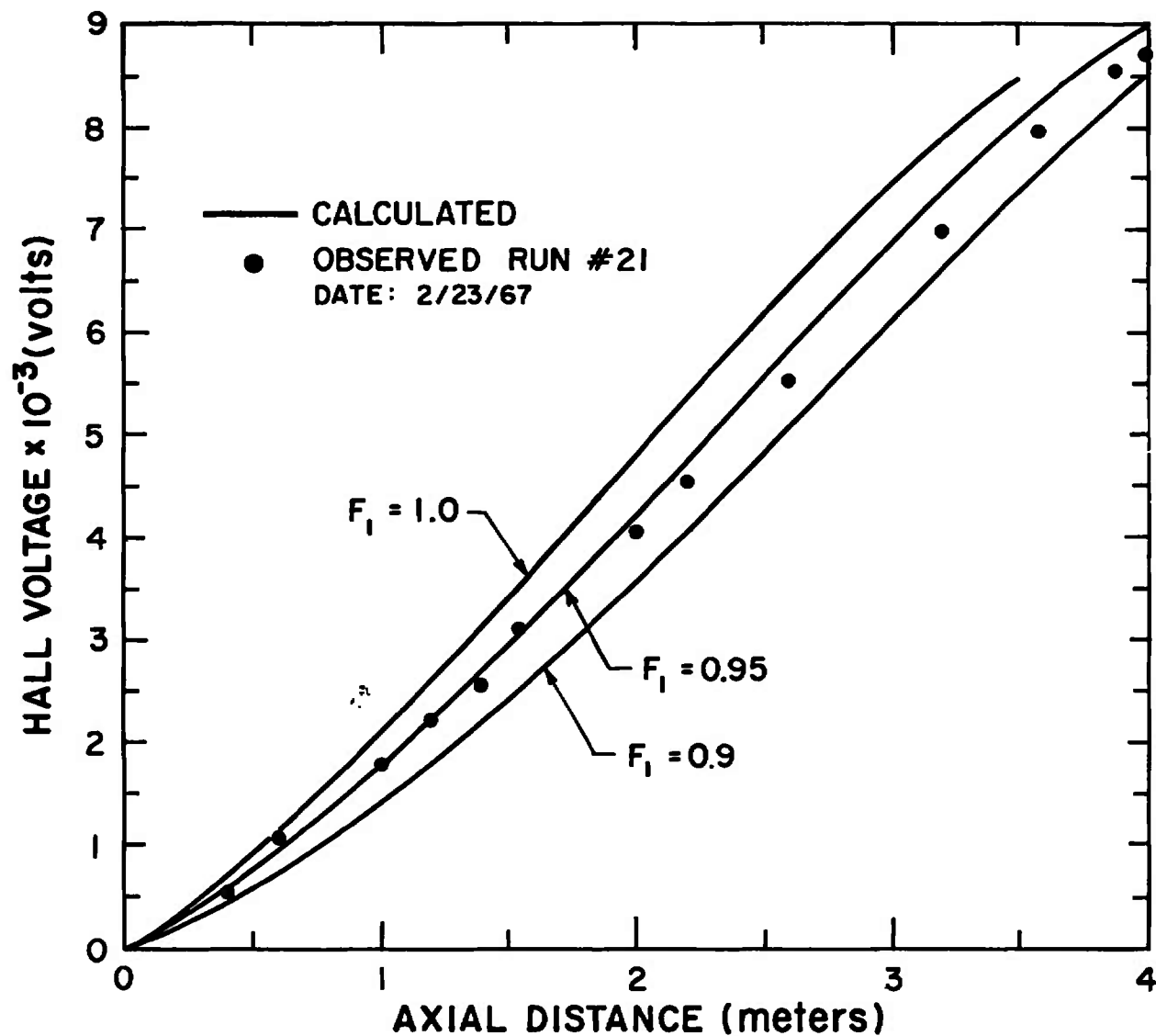


Fig. 58 Calculated Voltage Distributions for First Series Run of Three Seed Concentrations, and Measured Distribution

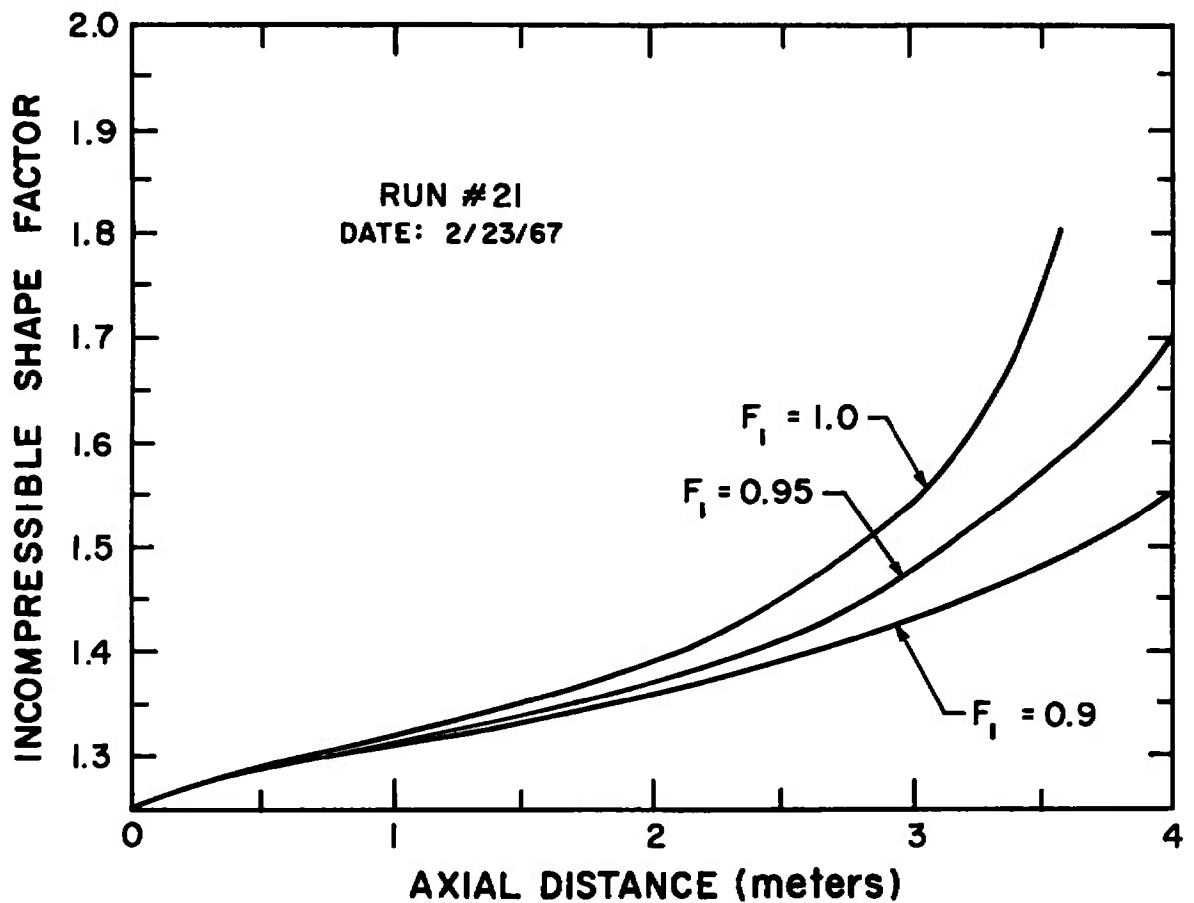


Fig. 59 Calculated Incompressible Shape Factor Distribution for First Series Run at Three Seed Concentrations

control system modifications towards automation to conserve the oxidizer supply by reducing the starting time would be in order. Thus, within this flow limitation, and the limit imposed by magnet aperture, length and field strength ( $1.1 \text{ m}^2 \times 4.5 \text{ m long} \times 2 \text{ tesla}$ ), a variety of burner-channel-diffuser combinations may be provided to handle specific power output requirements. Preliminary considerations of some of these possibilities have been carried out and are repeated here. The analytic techniques described in Section III-2 and utilized in Section III-6 are employed to calculate the channel performance. All channels up to a mass flow of  $100 \text{ kg/sec.}$  are designed to be compatible with the magnet aperture. Higher combustion pressure ( $18 \text{ atm}$ ) than presently utilized ( $10 \text{ atm}$ ) is employed. Pure oxygen is used as the oxidizer.

Two channel configurations have been studied. Both are single circuit output. These are:

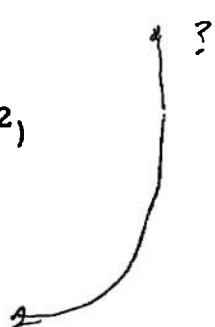
1. Single circuit output--Hall short circuited Faraday (SSF).
2. Diagonally connected Faraday (DCF) single circuit output.

The SSF above is similar to that which was employed with the modified Mark V generator which actually delivered a maximum gross output of  $24,000 \text{ kw}$  on a single circuit at  $1200 \text{ volts}$  at  $50 \text{ kg/sec. flow}$ <sup>(22, 23)</sup>. It is inherently a low voltage output device ( $1000\text{-}2000 \text{ volts}$ ). That aside, that the SSF should be at all competitive, say in terms of power output, with the DCF, may seem surprising. It really isn't in general, but when there is excess stagnation pressure available, excess seed, fixed magnet aperture and field strength quite optimum for it, as in the present case, a fairly good design results. Of course, the ideal DCF approaches the individually loaded segmented electrode generator in performance. Nonideal current distribution ( $I_x = 0$ ) as well as the power takeoff question, which, to our knowledge has not yet been resolved, lead to somewhat less than ideal performance. In addition, the Hall design was chosen in preference to the DCF for the original configuration because of constructional difficulties associated with the DCF. In spite of these problems, and also because of technical advances in channel fabrication since the original LORHO was laid out, the DCF would necessarily be the choice if maximum output were desired. In addition, fairly high output voltage can be produced with the DCF. It should also be noted that the segmented electrode generator with peg walls<sup>(24)</sup> and external connections between appropriate electrodes is equivalent to the ideal modular DCF construction and may be more flexible in practice. Some pegs will probably be required at the channel ends in any case.

The designs were not optimized; the calculations merely indicate the general possibilities for uprating the system.

1. The SSF design: The calculations indicate that a power output of about  $90 \text{ mw}$  can be generated at  $1500 \text{ volts}$  with a flow of  $100 \text{ kg/sec}$  of JP4 and oxygen, and a seed concentration of  $2\%$  by weight of potassium, about the maximum which can be considered. Details of the design are given below:

Combustion pressure: 18 atm (265 psig) (5% heat loss)  
 Mass flow: 100 kg/sec. JP4 & oxygen ( $\phi = 1.15$ )  
 Seed: 2% K by weight  
 Channel inlet conditions:  
     Mach number: 2.10  
     Gas velocity:  $2.10 \times 10^3$  meters/sec  
     Pressure: 2.0 atm absolute  
     Temperature: 2920°K  
     Conductivity: 38 mho/meter  
     Hall coefficient: 0.44  
     Dimension: 0.90 m (electrode walls) x 0.25 m (0.225 m<sup>2</sup>)  
     Loading coefficient: 0.45  
     H<sub>i</sub> (assumed) 1.25  
 Channel length: 4.72 meters  
 Field strength (central): 1.9 tesla  
 Channel exit conditions:  
     Mach number: 1.57  $P_2/P_1 \approx 2.709$   
     Velocity:  $1.57 \times 10^3$  m/sec  
     Pressure: 0.68 atm absolute  $\times 2.709 \approx 1.8$   
     Temperature: 2790°K  
     Conductivity: 32 mho/meter  
     Hall coefficient: 0.91  
     Dimension: 0.90 m x 0.90 m (0.81 m<sup>2</sup>)  
     Loading coefficient: 0.55 ( $a \times = 4.0$  meters)  
     H<sub>i</sub>: 1.66  
     Normal shock recovery pressure: 2.0 atm  
     Area ratio: 3.6  
     Output voltage: 1,500 volts  
     Current: 60,000 amperes  
     Power output: 90,000 kw



In the above,  $\phi$  is the equivalence ratio, that is, the ratio of fuel flow to stoichiometric fuel flow.

As is characteristic of the SSF design, the conditions chosen represent an attempt to minimize the effect of the shorted Hall potential by keeping  $\Omega$  low; it does not go above unity with the present design. The modest field strength, large aperture and long active length of the LORHO magnet are well suited to the SSF, and are the primary reason why an attractive design can be envisaged. The design is a mixed reaction-impulse with an outlet/inlet velocity ratio of 0.75, about the maximum which can be handled without boundary layer stall. There seems to be ample recovery pressure.

The low output voltage of the SSF is a disadvantage for some applications. High voltage DC output can be produced through the use of an DC-DC converter; an inverter would deliver AC power out. Depending on the requirements, the capital cost of the power conditioning equipment may be significant. However, advances in solid state SCR technology have led to greatly reduced costs and increased capability here and the output voltage is very compatible with SCR ratings. The possibility also exists to employ one of the many DC voltage multiplier circuits for the short running times envisioned here.

The channel construction would be similar to that employed for the Mark V SSF 24, 000 kw channel illustrated in Figs. 60, 61 and 62. (22, 23). The construction is quite simple. As the Hall potential is zero, the insulating wall is made of longitudinal metal strips and slab electrode walls can be used. At the channel ends, the strips are bent so as to approximate the desired equipotentials. Better results would be achieved by the use of some pegs in the channel ends. For the present design the distance between the electrode walls is a constant while the insulating walls diverge. This makes for simple construction and leads to fairly uniform loading.

At mass flows below the maximum facility capability of 100 kg/sec, good performance would still be obtained. For instance, at the presently utilized flow of 60 kg/sec; the estimated output would be 50, 000 kw at 1150 volts, while 75, 000 kw at 1380 volts could be delivered at 85 kg/sec.

2. The DCF design: The calculations indicate that a power output of 110, 000 kw can be generated at 8, 000-10, 000 volts with a flow of 100 kg/sec of toluene and oxygen, and a seed concentration of 0.6% by weight. Allowing for some losses in power takeoff at the channel ends, an output of 100, 000 kw corresponding to an attractive 1 mw/kg sec<sup>-1</sup> seems indicated, and could probably be sustained down to about 50, 000 kw. Thus, at the presently utilized flow of 60 kg/sec, the indicated power output is 60, 000 kw, and 75, 000 kw at 75 kg/second flow.

As the  $\sigma u/\rho$  factor indicating the power output/unit length continues to rise at Mach numbers up to three for pure oxygen combustion, and as there is excess stagnation pressure (the generator length and magnetic field are fixed) the design conditions are arrived at most simply. Just fill up the magnet volume as much as possible while still avoiding stall. Typical design conditions which do so in a slightly less than optimum manner are indicated below:



# CHANNEL LAYOUT

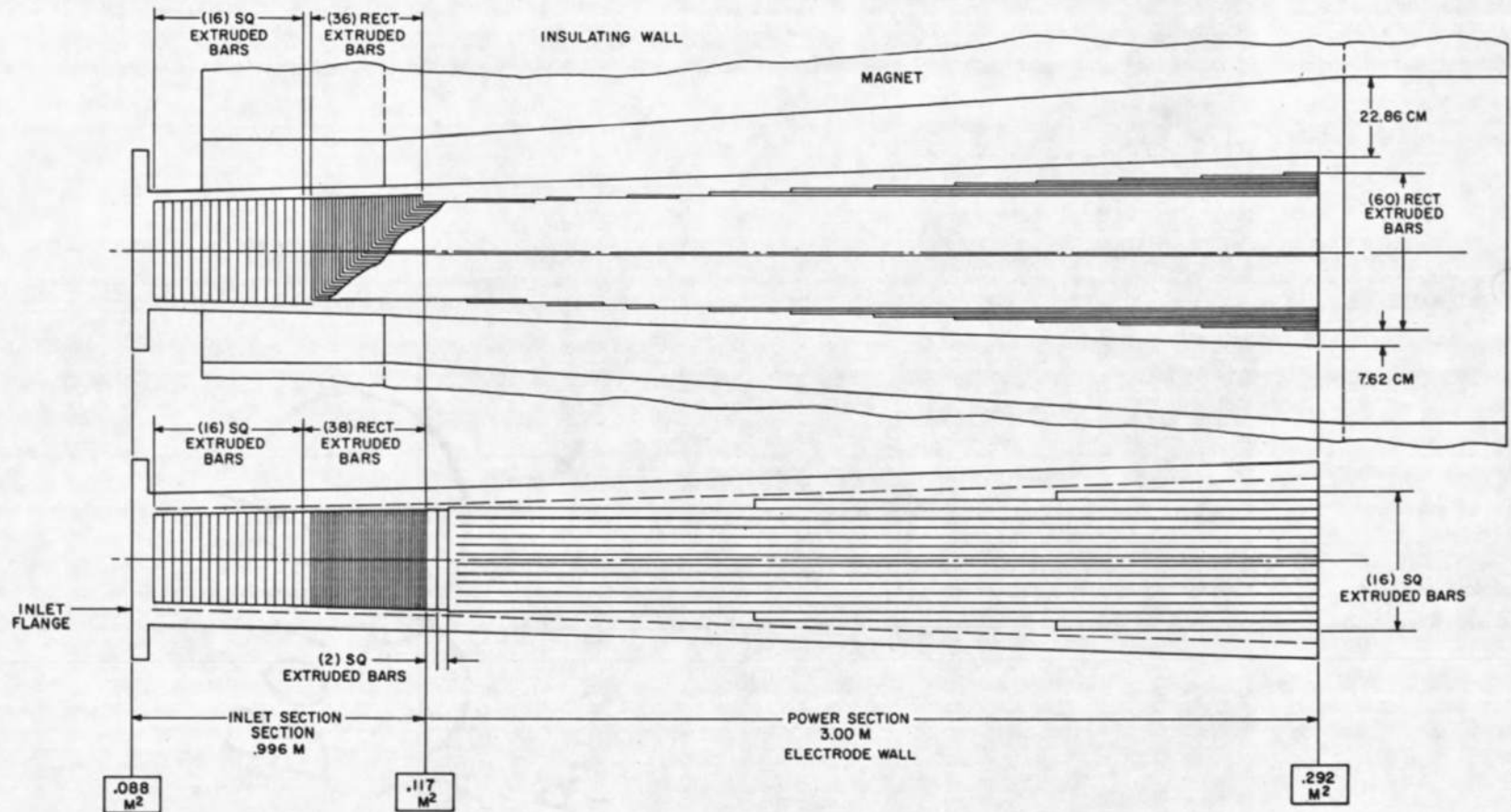


Fig. 60 Mark V SSF Channel

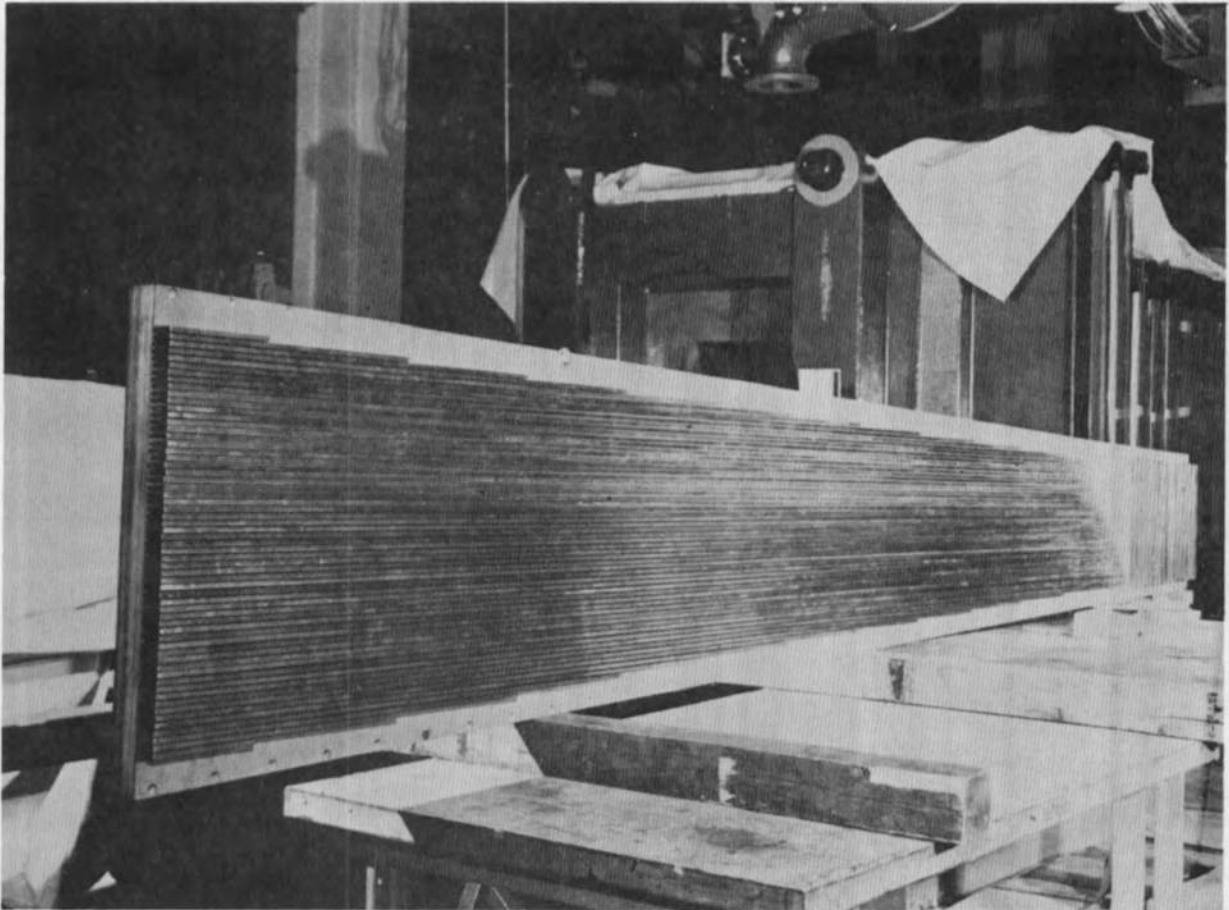


Fig. 61 Mark V SSF Channel Insulator Wall

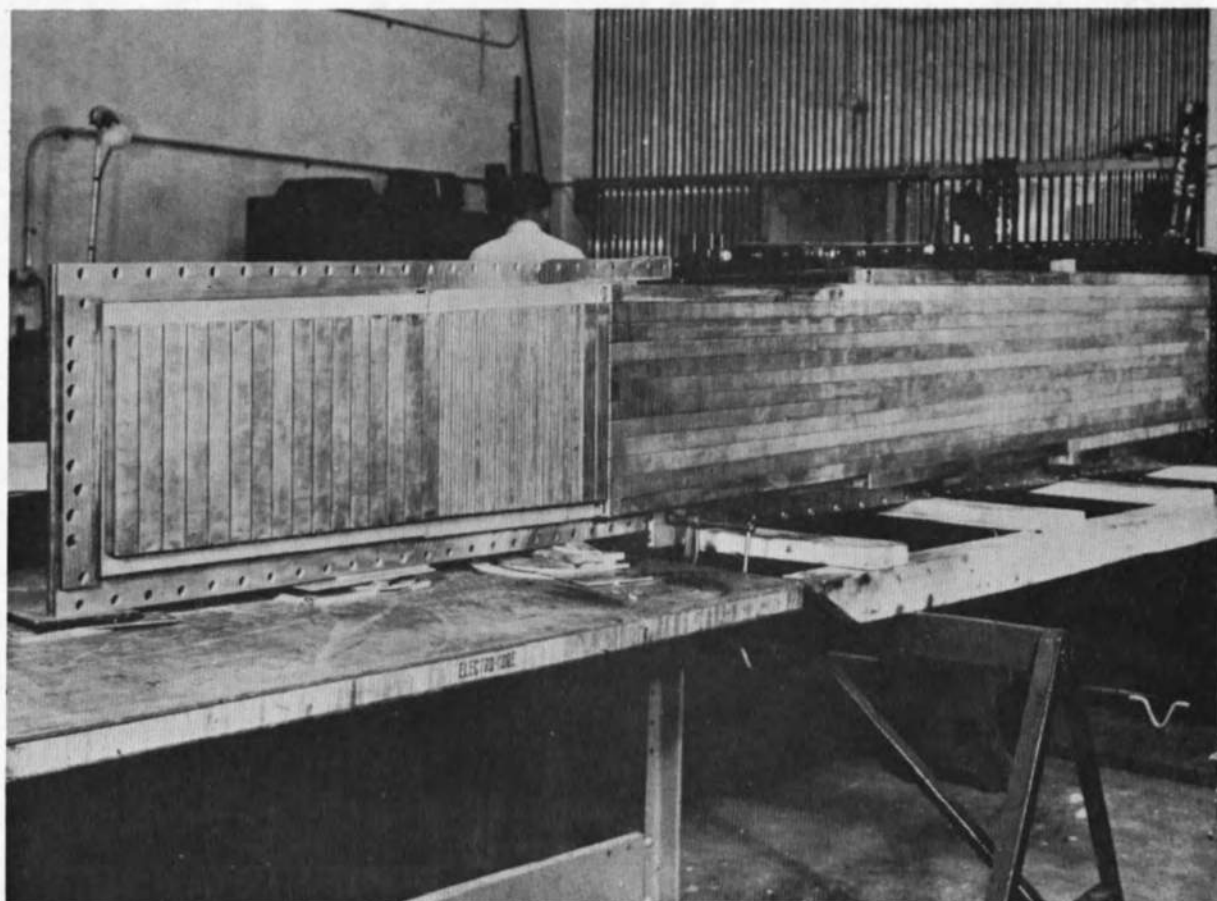


Fig. 62 Mark V SSF Channel Electrode Wall Before Filling Grooves with Zirconia Electrode Material

Combustion pressure	18 atm (5% heat loss)	
Mass flow	100 kg/sec toluene & oxygen ( $\phi = 1.15$ )	
Seed	0.6% K by weight	
$E_y/E_x$	1.4	
Channel conditions	inlet	outlet
Mach number	2.51	1.86
Gas velocity	$2.38 \times 10^3$ m/sec	$1.76 \times 10^3$
Pressure	0.86 atm abs	0.59
Temperature	2768°K	2744
Conductivity	14.2 mho/meter	16.2
Hall coefficient	1.8	2.2 ( $x = 4.0$ )
Dimension		
Electrode	0.90 meters	0.90
Insulating	0.44 meters	0.90
Area	$0.39 \text{ m}^2$	0.81
Loading coefficient	0.70	0.70 ( $x = 4.0$ )
$H_i$	1.32 (assumed)	1.71
Normal shock recovery pressure:	----	2.8 atm
Channel length	4.72 meters	
Area ratio	1.84	
Output voltage (no end losses)	9160 volts	
Current	12,000 amperes	
Power output (no end losses)	110,000 kilowatts	

$$\frac{10 \text{ mV}}{5} = 2 \text{ mV/V/A}$$

Note that as in the present LORHO channel, all parts of the DCF channel itself are below one atmosphere reducing the consequences of any leak or failure since air will go in rather than hot gas exiting. Construction of the diagonal channel would be similar to the accelerator described in Section IV.

For both configurations described above, the combustion chamber would be at about the same size as the present unit, but rated for the higher pressure. A booster pump for only the water to cool the chamber and nozzle will be required and a new fuel pump and other modest modifications would be needed.

It is seen that there are very attractive probabilities for uprating the LORHO MHD power supply to levels as high as 100,000 kw. Should an application for such a power level arise at the center, uprating of LORHO may provide an inexpensive, convenient and rapid route to satisfaction of the power supply requirement.

## SECTION IV

DESIGN AND CONSTRUCTION OF THE HIGH POWER  
MHD ACCELERATOR

## 1. INTRODUCTION

The design goals of the LORHO Pilot MHD Accelerator called for a power input of approximately 20,000 kW and an effluent velocity of 25,000 ft/sec. or greater at as high a pressure and low degree of dissociation as is practical. The working fluid should be seeded air. Of course it was most desirable to minimize the seed concentration as this undoubtedly has an effect on the test simulation which is achieved. In addition the accelerator inlet gas was to be supplied from an electric arc plasma jet provided by the Westinghouse Electric Corp., and the accelerator design had to be compatible with the operating capability of this plasma jet.

The desired limitation on axial electric field strength to 4,000 volts/meter is the most important factor in the design. Let us see what the limitation on axial field strength means to the accelerator design. The discharge velocity is approximately 8,000 meters/sec. The transverse electric field  $E_y$  is approximately equal to the axial velocity times the magnetic field strength. The axial field then is given by

$$E_x = \frac{8000 \text{ B}}{1.6} \approx 5000 \text{ B} \quad \downarrow \quad 5300 \text{ B} ?$$

$$E_x = \frac{E_y}{\phi} \approx \frac{uB}{\phi} \quad \leftarrow 4000 \text{ V/m}$$

$$\therefore B \approx 0.8 \text{ T} \approx 8000 \text{ G}$$

Now the channel, as will be seen is to be built up of rectangular modules individually water cooled, each module extending along an equipotential along the insulating wall and across the two electrode walls. This gives a rigid structure, and in addition can be cooled to a high heat transfer rate. The pitch between adjacent segments on the electrode wall can be about 1 cm or 0.4 inches. Therefore the thickness of the module along

the equipotential on the insulating wall is  $1/(1 + \phi^2)^{1/2}$  times the pitch. When the insulation thickness between modules is taken into account as well as the difficulty of fabricating long cooling passages of small cross section, we find that the value of  $\phi$  should be limited to approximately 1.6. Thus we have that  $E_x$  is approximately 5,300 B volts/meter. In order for the electric field in the axial direction to be less than 4kV/meter, the magnetic field would have to be less than approximately 7,500 gauss. At this value of magnetic field the accelerator channel length/diameter ratio and hence the viscous losses would become excessive, or alternatively the static pressure would become low. (It should be mentioned here that one of the design criteria of the accelerator

is that it discharge to atmosphere without a vacuum system.) Therefore some liberties had to be taken with electric field at the high velocity end of the accelerator, and it would be necessary to observe the test results before determining whether or not these fields can be withstood.

## 2. THEORETICAL CONSIDERATIONS

The inviscid flow in the MHD accelerator has been considered by Ring<sup>(2)</sup> and previously referred to. Here we would like to demonstrate the importance of the viscous effect in limiting the ultimate performance of an MHD accelerator

An approximate one-dimensional perfect gas analysis is to be developed. Due to the effect of dissociation and ionization, substantial differences do exist in the results as compared with the real gas case. However, the perfect gas analysis does contribute much to the understanding of the problem, and indicates the trend of accelerator performance due to the change of difference variables. The analysis also suffers from the results of averaging the friction force and heat transfer across the channel flow in the old way (as the accelerator was not operated, no updating of the analysis has been carried out as in the case of the MHD power supply).

The fluid dynamic equations for the one-dimensional Hall current free flow express continuity:

$$\rho u A = \text{const.} = m \quad (26)$$

where A is the channel area, conservation of momentum:

$$\rho u \frac{du}{dx} + \frac{dp}{dx} = \sigma u B^2 (a_1 - 1) + \frac{4C_f}{D} (1/2 \rho u^2) \quad (27)$$

and energy:

$$\rho u \left( C_p \frac{dT}{dx} + u \frac{du}{dx} \right) = \sigma u^2 B^2 a_1 (a_1 - 1) - \rho u \frac{4S_t}{D} \left[ \frac{u^2}{2} + C_p (T - T_w) \right] \quad (28)$$

$C_f$  is the friction coefficient,  $S_t$  the Stanton number, and T the absolute temperature. Here, the effects of friction and heat transfer have been included in the usual way for a channel flow.

At high Mach numbers,  $C_p(T - T_w) \ll 1/2 u^2$ , and from Reynolds analogy, for the Prandtl Number = 1, and  $S_t = C_f/2$ , the energy equation may be written as

$$\rho u \left( C_p \frac{dT}{dx} + u \frac{du}{dx} \right) = \sigma u^2 B^2 a_1 (a_1 - 1) - \frac{2C_F}{D} 1/2 \rho u^2 \quad (29)$$

For (26) (27) (29) and the equation of state for perfect gas, the following relationships may be derived:

$$\text{For } \frac{du}{dx} \geq 0$$

$$-\sigma B^2 (\gamma - 1) (\alpha_1 - 1)^2 + \sigma B^2 (\alpha_1 - 1) - C_f (\gamma + 1) \frac{\rho u}{D} \geq 0 \quad (30)$$

$$\text{For } \frac{dM^2}{dx} \geq 0:$$

$$-\sigma B^2 (\gamma - 1) (\gamma M^2 + 1) (\alpha_1 - 1)^2 + \sigma B^2 (\gamma + 1) (\alpha_1 - 1) - C_f \frac{\rho u}{D} [4\gamma + (\gamma M^2 - 1)(\gamma - 1)] \geq 0 \quad (31)$$

$$\text{For } \frac{dp}{dx} \leq 0:$$

$$-\sigma B^2 M^2 (\gamma - 1) (\alpha_1 - 1)^2 + \sigma B^2 (\alpha_1 - 1) - C_f \frac{\rho u}{D} [2 + M^2 (\gamma - 1)] \geq 0 \quad (32)$$

$$\text{For } \frac{dT}{dx} \leq 0:$$

$$-\sigma B^2 (\gamma M^2 - 1) (\alpha_1 - 1)^2 + \sigma B^2 (\alpha_1 - 1) - C_f \frac{\rho u}{D} (\gamma M^2 + 1) \geq 0 \quad (33)$$

The left hand side of (30), (31), (32) and (33) can be considered as the quadratic form of  $(\alpha_1 - 1)$ . It is apparent that when  $(\alpha_1 - 1)$  is very large or when  $\alpha_1 - 1$  is equal to zero ( $\alpha - 1$  is always positive for accelerators), these quantities are negative. If these quantities are to be positive, real roots must exist for when the equal signs apply in the above relationship. The question can thus be reduced to two aspects: the first, the condition for the real roots to exist, and the second, the ranges of permissible load factor if the above conditions are fulfilled.

For conditions for real roots to exist can be expressed as follows:

$$\text{For } \frac{du}{dx} \geq 0:$$

$$\frac{\sigma B^2 D}{\rho U} \geq 4C_f (\gamma - 1)(\gamma + 1) \quad (34)$$

$$\text{For } \frac{dM^2}{dx} \geq 0:$$

$$\frac{\sigma B^2 D}{\rho u} \geq 4C_f \frac{(\gamma - 1)(\gamma M^2 + 1)[4\gamma - (\gamma M^2 - 1)(\gamma - 1)]}{(\gamma + 1)^2} \quad (35)$$

$$\text{For } \frac{dp}{dx} \leq 0:$$



$$\frac{\sigma B^2 D}{\rho u} \geq 4 C_f [2 + M^2 (\gamma - 1)] M^2 (\gamma - 1) \quad (36)$$

For  $\frac{dT}{dx} \leq 0$ :

$$\frac{\sigma B^2 D}{\rho u} \geq 4 C_f (\gamma M^2 - 1)(\gamma M^2 + 1) \quad (37)$$

The left hand side of these relationships is in the form of an interaction parameter based on channel diameter. Thus there exist four minimum channel interaction parameters for a given set of  $C_f$ ,  $\gamma$  and  $M$ . It is also interesting to note that these interaction parameters become identical if  $M$  is equal to unity.

Because of the generally complex interactions between gas-dynamic properties and electrical properties in MHD flow, the optimum design approach of an MHD accelerator is by no means apparent. In general, a relatively isothermal device is preferred, due to the following reasons:

- a) As the electric conductivity and the Hall coefficient of a gas (generally seeded) change greatly with temperature, generally an isothermal condition is necessary if the loading is to be relatively uniform.
- b) Stability considerations.
- c) Isothermal acceleration minimizes dissociation and maximizes discharge Mach number and effective reservoir pressure.

The limit for acceleration  $\frac{du}{dx} \geq 0$  and raising the Mach number  $\frac{dM^2}{dx} \geq 0$  are thus not of great significance in MHD accelerator design, as a rapid rise in temperature is generally encountered long before these limits are reached. For instance, for a constant area channel:

$$\frac{1}{p} \frac{dp}{dx} - \frac{1}{T} \frac{dT}{dx} + \frac{1}{u} \frac{du}{dx} = 0 \quad (38)$$

It is apparent that if  $\frac{dp}{dx} = 0$ , a significant temperature rise is likely to accompany any significant rise in velocity. In addition, if  $\frac{dp}{dx} > 0$ , there is danger of separation. Thus the design should approximate the condition

$$\frac{dT}{dx} = 0$$

but should not exceed the limit

$$\frac{dp}{dx} \leq 0$$

In Fig. 63 the permissible values of  $(\alpha_1 - 1)$  are shown as a function of interaction parameter for different Mach numbers and a constant area channel. From Fig. 63 it is apparent that the limiting conditions are much more stringent for a higher Mach number than for a lower Mach number. The design should be based on the high Mach number end of the accelerator. A lower limit of channel interaction parameter can be determined from Eq. (36). If the total flow rate and the terminal temperature are specified for a given gas, the magnitude of the interaction parameter can most effectively be increased by reducing the pressure level or increasing the magnetic field.

In general, the design channel interaction parameter should be somewhat larger than the calculated minimum value for the following reasons:

- a) being away from the minimum value of channel interaction parameter, much higher loading factor can be used, as indicated in Fig. 63.
- b) being away from the  $\frac{dp}{dx} = 0$  line, much of the sharp rise in temperature and current density can be avoided.

The above analysis shows that sharp temperature rise starts before the adverse pressure gradient is encountered. The rise in temperature causes the conductivity, and consequently the current density, to increase, which would in turn cause further temperature rise. However, as long as value of  $(\alpha_1 - 1)$  remains small, the temperature change is gradual.

The possibility of balancing the temperature rise by expanding the gas may be examined as follows. As:

$$\frac{1}{A} \frac{dA}{dx} = - \frac{1}{\gamma} \left( 1 - \frac{1}{M^2} \right) \frac{1}{p} \frac{dp}{dx} \quad (39)$$

$$\frac{1}{p} \frac{dp}{dx} = \frac{\gamma}{\gamma - 1} \frac{1}{T} \frac{dT}{dx} = \frac{\gamma}{\gamma - 1} \frac{j_y^2}{\rho u h} \quad (40)$$

For air at about 3,100°K,  $\frac{\gamma}{\gamma - 1} \approx 6$ , and considerable change in cross-sectional area and pressure are required to compensate for minor temperature rise. The design thus becomes a compromise among expansion, and consequent pressure drop, axial electric field and power density

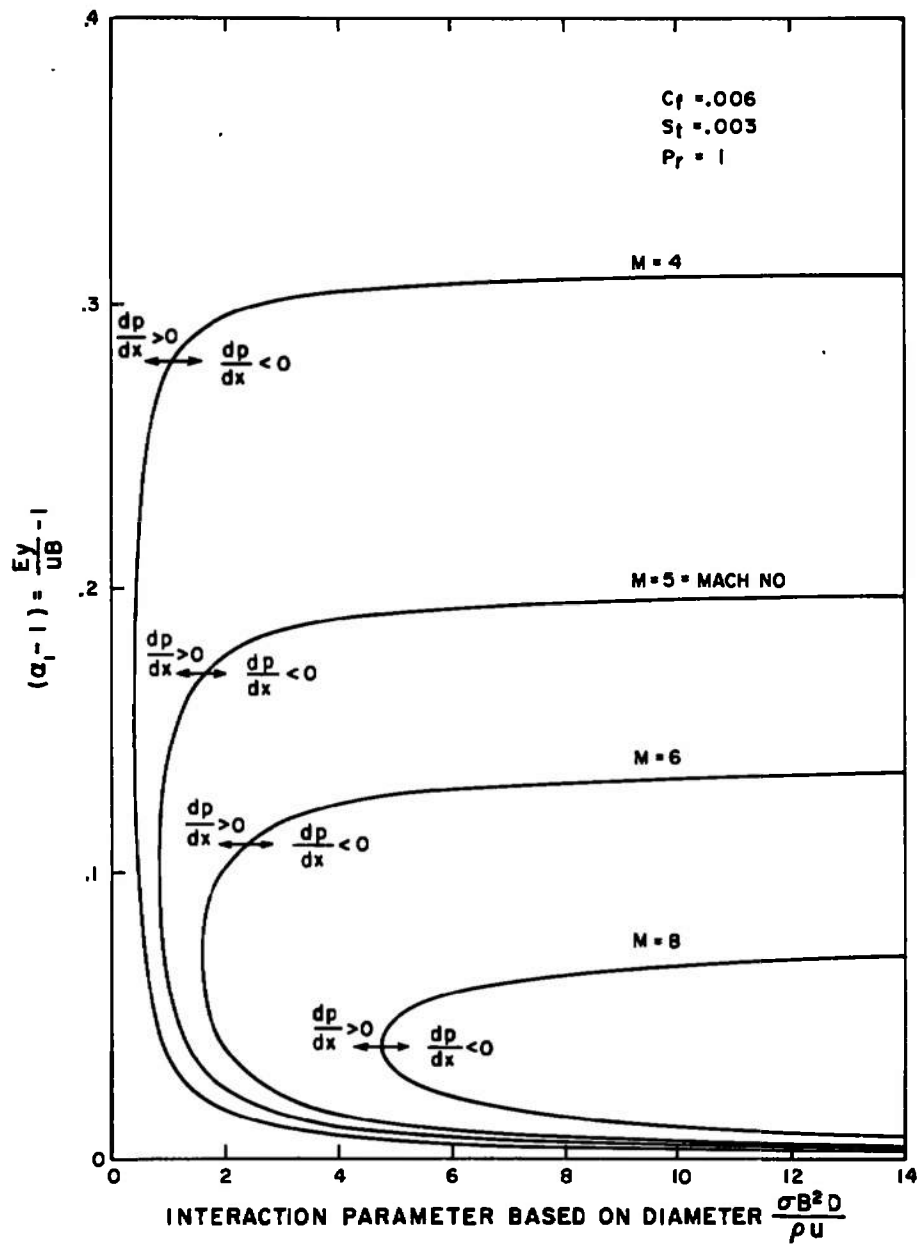


Fig. 63 Critical Loading Coefficient vs Interaction Parameter Based on Diameter and Mach Number

( $\alpha_1 - 1$ ). The design must be juggled to achieve the design goals.

Of course, the most desirable working fluid for application in a wind tunnel is air. To obtain exact simulation of flight, the air should be uncontaminated and undissociated in the free stream of the tunnel. In practice, in an MHD accelerator at the 20 mw level with air, neither the contamination nor the dissociation can be reduced to zero. This is due to the strong dependence of both the electrical properties and the dissociation properties of air on the temperature. This situation is illustrated in Fig. 64 in which the electrical conductivity and Hall coefficient of seeded air are shown as a function of temperature for various seed concentrations at a gas pressure of 0.1 atmospheres. Now appreciable dissociation of the oxygen in the air begins at a temperature of approximately 3,000°K and at 4,000°K, nearly all of the oxygen is dissociated. Therefore it will be desirable to operate the MHD accelerator at a static channel temperature below 3,000°K. The low conductivity of unseeded air at 3,000°K and indeed to well above 4,000°K makes it impossible to operate an MHD accelerator both without dissociation and without contamination. It is necessary to add some seed. The amount of seed should be minimized, both to minimize the contamination and also to minimize the degradation of the air enthalpy, since the seed is generally added downstream of the arc plasma source. We note from the figure that extremely small amounts of seed can make very large differences in gas conductivity at temperatures between 3000° and 4000°K, while at higher temperatures the conductivity is insensitive to the seed concentration. We further note that the Hall coefficient on the other hand is sensitive to the seed concentration, since the total cross section of the seed atoms is appreciable in comparison with the total cross section of the gas, even at low seed concentrations. Thus, it is possible to alter the Hall coefficient of the gas somewhat independent of the conductivity. This fact is taken advantage of in the design, and can be used to effect some flexibility in the operation of the facility. In the program the conductivity and Hall coefficient have been computed over a large range of the gas pressure and temperature and seed concentration, and these values are used in the calculations of the performance of the MHD channels.

Were gases other than air used, such as inert gases or nitrogen, it would of course be possible to operate the accelerator at higher temperatures without dissociation and possibly avoid seeding. However, it is felt that seeding with air will be less of a disturbance than the use of another gas in aerodynamic simulation.

Equations (26) (27) (28) are the governing equations for the flow in the absence of Hall current. However, we are interested in designing a machine to which the power is connected at a limited number of points. For this practical case, the constraint that the Hall current be zero cannot be applied. Rather, the total axial current flow,  $I_T$  must be specified much as in the case of a pure Hall generator. The total current is defined as the product of a total effective axial current density,  $j_T$  by the local channel area,  $A$ . These are two ways that axial current can flow in a diagonally connected device, the Hall current itself,  $j_x$ , and a

## AIR SEEDED WITH POTASSIUM

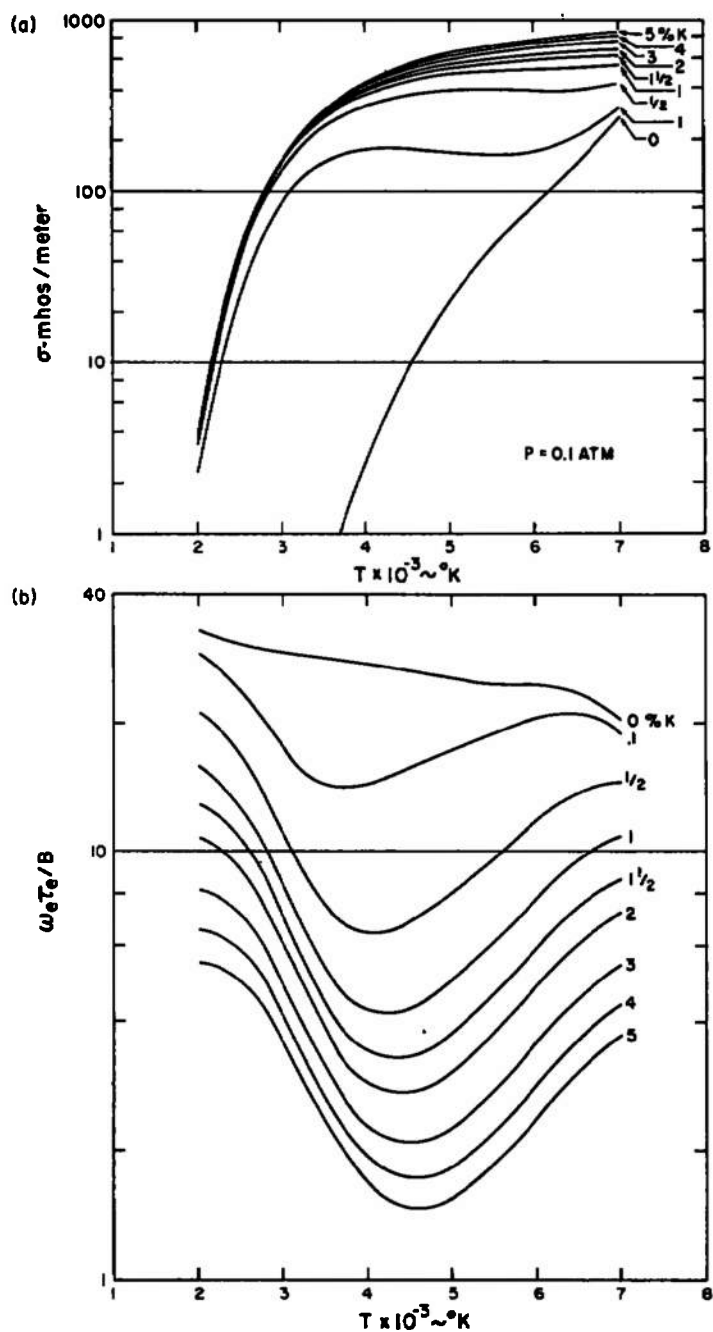


Fig. 64 Electrical Conductivity and Hall Coefficient as a Function of Temperature for Air at Various Seed Concentrations at a Pressure of 0.1 Atmospheres

proper component of the current that flows downstream through the diagonals which enclose the channel. Consider a channel of unit depth and height so that  $I_T = j_T \cdot (1)$ . The diagonal spans a distance  $\phi$  along the bottom wall of the channel when  $\phi = \frac{E_y}{E_x}$ . The current flow into the electrodes in the distance  $\phi$  is  $j_y \phi$ , and this current flows to the right and upwards along the diagonals. A fraction  $\frac{\phi}{\sqrt{1 + \phi^2}}$  of this current

flow axially across a control surface perpendicular to the flow axis. Thus:

$$j_T = j_x + \phi j_y \quad (41)$$

and

$$I_T = j_T A \quad (42)$$

This, together with the constraint,

$$\frac{E_y}{E_x} = \phi$$

allows the complete solution since now:

$$j_y = \frac{\sigma u B}{1 + \Omega^2} \left[ (\alpha - 1) + \frac{\alpha \Omega}{\phi} \right] \quad (43)$$

and

$$j_x = \frac{\sigma u B}{1 + \Omega^2} \left[ \Omega (\alpha - 1) - \frac{\alpha}{\phi} \right] \quad (44)$$

In the above two equations, only  $\alpha$  is undetermined, and is found from:

$$j_T = \frac{I_T}{A} = \frac{\sigma u B}{1 + \Omega^2} \left\{ \phi (\alpha - 1) + \frac{\alpha}{\phi} \Omega \right\} = j_x + \phi j_y \quad (45)$$

where  $I_T$  is the given total current. With  $\alpha$  known,  $E_y = \alpha u B$ , and  $E_x = \frac{\alpha u B}{\phi}$  allows the problem to be completely determined with solution of the continuity, momentum, and energy equations. In the energy equation, a term  $j_x E_x$  must be added to the right side to account for the energy transfer due to the axial current.

The boundary layer in the accelerator was analyzed approximately with a modified Pohlhausen technique which takes the inviscid MHD effects into account. It is found that the boundary layer momentum thickness grows

to about 4 mm, then remains constant and decreases somewhat in the downstream part of the channel due to rapid acceleration there. Various MHD effects of the Hartman type are believed not to be of importance because the Hall effect greatly reduces the importance of velocity defect in the boundary layer. However, the boundary layer temperature profile at high Mach number will show peaks even with a cold wall, and this may lead to some difficulty.

A large number of accelerator designs were investigated using a three step procedure. First, a calculation was made of a Hall current free ( $J_x = 0$ ) diagonal type Faraday accelerator. This established the top performance that might be obtained from a two terminal device, and provided the reference design for the calculation of the simply constructed, constant wall angle accelerator design where Hall current is considered in the analysis. As a second step, calculation of an accelerator design incorporating the effects of Hall current which theoretically met the performance objectives was carried out. Finally, a third set of calculations were performed to establish the accelerator voltage-current (V-I) curves for a wide variety of field strengths and seed concentrations. The accelerator and generator V-I characteristics were superposed to arrive at the starting procedure. Boundary layer corrections were made by simple iteration.

It does not seem profitable here to discuss in detail all of the designs that were investigated. The analysis used approximates that used for the generator design previously described, but the design is more difficult due to the sensitivity of the flow to electrical dissipation at high Mach number. Some attention was initially given to a constant area design, but although these studies were very useful in confirming the generator's required performance characteristics, it was clear that the constant area design was unsuitable. Some characteristics of a typical constant area design are illustrated in Fig. 65. To be noted, in particular, is the drastic rise in electric field and current density at the downstream end of the accelerator due to the rise in gas temperature. This is in spite of an increase in  $\phi$  from 1.25 to 1.50 at the back in order to decrease the accelerator loading. This is quite unacceptable due to inadequate electrode current carrying ability and the danger of uncontrolled current rise leading to choking. In addition, uncertainty as to the boundary layer growth and shape factor could also lead to choking with the constant area design, and did, in fact, for the low power test accelerator.

Attention was then focused on a variable area design with the objective of achieving relatively uniform loading along the entire channel length with a two or three-terminal connection to the power supply, and adequate safeguard against choking for all conditions of operation. For reasons which will be explained, the operational procedure for the MHD accelerator-generator combination is as follows:

1. With magnetic field on generator and off accelerator, establish hot flow in both units.

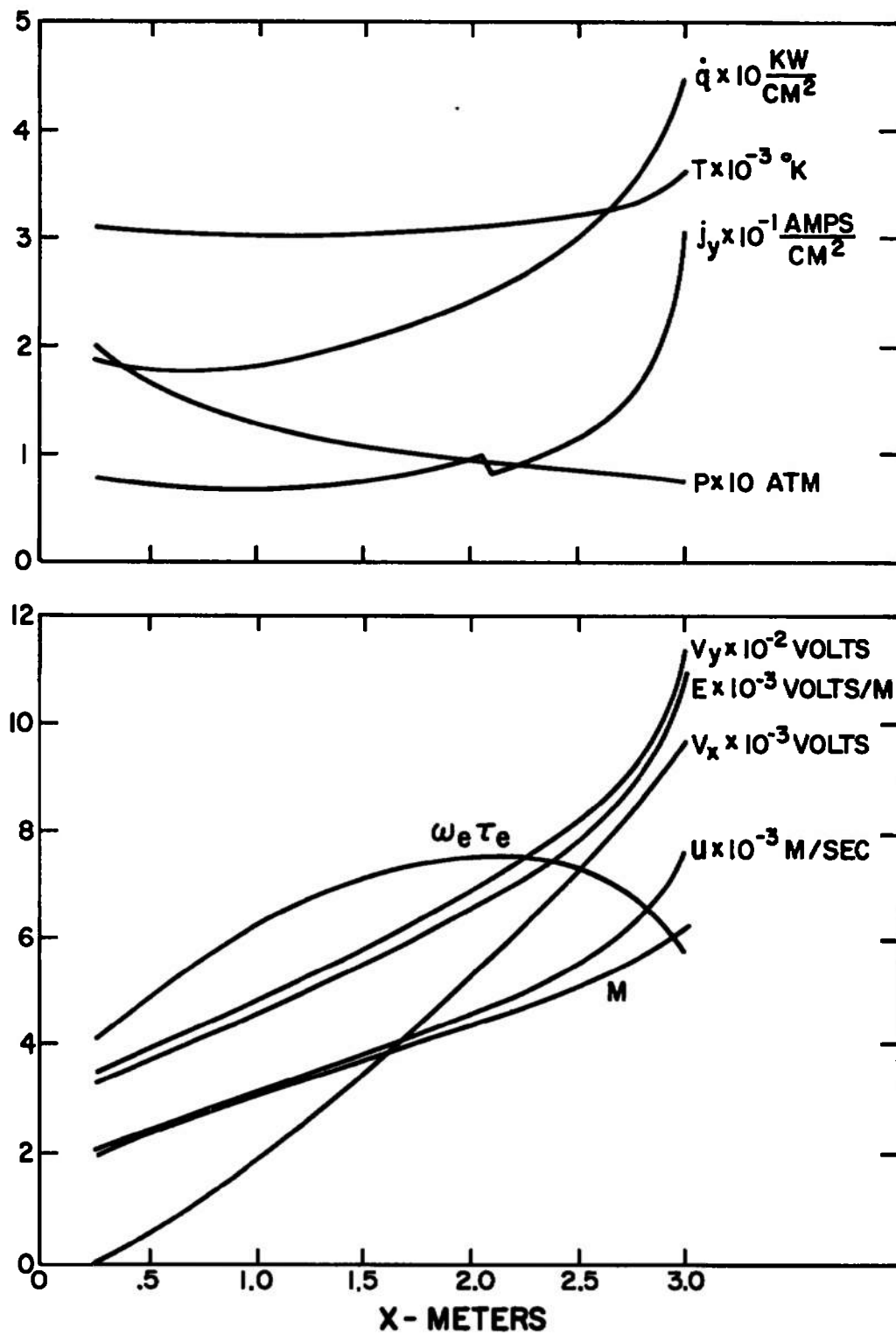


Fig. 65 Some Characteristics of an Early Constant Area Accelerator Design



2. Add seed to accelerator.
3. Add seed to generator; since no field on accelerator, it will present desirable low impedance to constant current generator.
4. Bring up field on accelerator.

Three different conditions under which the accelerator must discharge to the atmosphere may be identified from the above:

1. No power input from generator.
2. Low impedance presented to generator.
3. Design impedance presented to generator.

These will be discussed in greater detail later. However, in general, provisions to prevent choking and temperature rise in the accelerator channel lead to increase in channel exit area, reduction in exit static pressure, and increased difficulty in recovering to the atmosphere and decreased values of Reynolds number per unit length. The alternative is increased channel inlet pressure, but this must be rejected because it leads to increased electric fields in order to achieve satisfactory  $L/D$  ratios for the channel. Therefore, the design becomes something of a juggling match among all of the factors which are involved.

### 3. THE "AS BUILT" HIGH POWER LORHO MHD ACCELERATOR

The design accelerator inlet conditions which resulted from the juggling act described above are shown in Table VIII, and correspond to expansion from a settling chamber pressure of ten atm and a stagnation enthalpy ratio,  $h_s/RT_0$  of 125, conditions achievable with the arc heater design supplied. The magnetic field varies between 1.8 webers/m<sup>2</sup> at the inlet to 0.9 w/m<sup>2</sup> at the exit. A model magnet was built and tested to verify that the desired magnetic field distribution could be achieved. In this design, a third connection would distribute 371 additional amperes to a number of modules at a distance of 1.7 meters from the inlet. The total channel length is 2.5 meters. The channel is 7.5 cm x 7.5 cm at the inlet, and 13 cm x 13 cm at the exit including an allowance of 0.5 cm for boundary layer displacement thickness. Straight walls are employed. Note that the electrode boundary layer is accelerated rather than retarded so that the separation question so important for the Hall generator design is not a factor here.

Calculated variation of some of the flow and electrical parameters is shown in Fig. 66. The calculated exhaust velocity of 7600 m/sec is equal to the 25,000 ft/sec design goal. The temperature decreases very slightly so that the flow velocity and Mach number vary almost identically. The desired nearly constant temperature operation holds  $\sigma$  nearly constant but is achieved at the expense of a pressure ratio of approximately 7.5/1. The effective stagnation pressure at the accelerator exit is 990 atm at  $h_s/RT_0 = 450$ . The Hall coefficient varies from a value of 3.5 at the inlet to 9.5 at the exit; the exit value of  $\omega\tau$  is greater than that at which

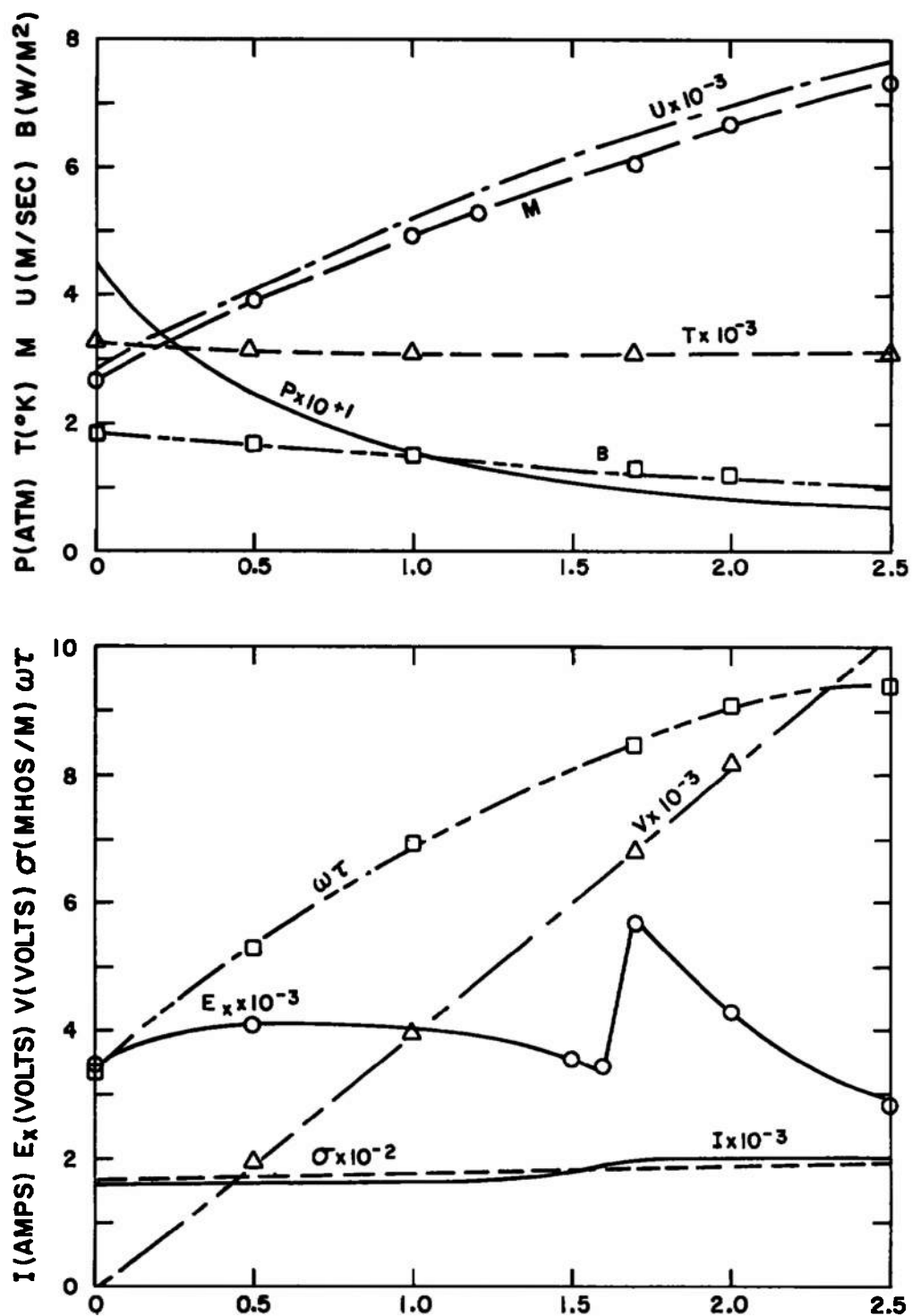


Fig. 66 Variation of Some Flow and Electrical Parameters with Length for the Center Point of the "As-Built" Accelerator Design, Three Terminal Connection

TABLE VIII  
LORHO THREE TERMINAL MHD ACCELERATOR

Inlet Conditions

$\dot{m}$  = 0.68 Kg/sec of Air

0.5% Potassium Seed

$$\frac{E_y}{E_x} = \phi = 1.8$$

Inlet = 7.5 x 7.5 cm

Exit = 12.5 x 12.5 cm

I amperes 1600

P atm .449

$\rho_o$  \_\_\_\_\_

$E_x$  Volts/M 3477

V Volts 0

T °K 3235

$\frac{hs}{RT_o}$  \_\_\_\_\_

u M/sec 2783

M 2.60

$J_x$  amps/cm<sup>2</sup> -.997

$J_y$  amps/cm<sup>2</sup> 17.2

$\alpha = E_y/uB$  1.25

$\sigma$  mhos/M 165

$\omega_e \tau_e$  3.39

B w/M<sup>2</sup> 1.80

there is experience, and operating data would be required to verify the performance predictions. The total current and axial electric field vectors are shown on an expanded ordinate in Fig. 67. The sharp stop in the electric field is due to the current increment at  $x = 1.7$  meters. The total calculated current under Hall free (segmented electrode) conditions is also shown. The figure illustrates how it is possible to achieve conditions approximating Hall current free operation.

The direction of the actual current vector in the gas at the design conditions is indicated by the arrows shown on the top of the Figure for different distances into the channel. Such diagrams are extremely useful for visualizing the situation in a non-ideal diagonally connected channel. Desirably, the current vectors are normal to the flow, that is vertical. As the electric field in the accelerator is directed downstream a tilting of the current vector to the right corresponds to power input in the form of heat, and so is undesirable. Note how the introduction of the current increment at  $x = 1.7$  meters reverses the tilt of the current vector, and increases the accelerator impedance. This is evidenced by the abrupt increase of  $E_x$  at this station. Further downstream the current vector again begins to tilt to the right, and this is usual, and indicative of the increasing difficulty of achieving efficient acceleration as the Mach number is increased. The design limit of useful acceleration has about been reached here.

After the design conditions had been established, off design calculations were carried out to verify that the accelerator-generator combination could be started up.

Figure 68 illustrates some characteristics of both machines. The accelerator characteristics (solid lines) are shown for different values of magnetic field. Generator characteristics are also shown (dashed lined). To operate, the generator would be set up for a short circuit current of about 2,200 amperes and the accelerator magnetic field gradually increased from zero to 1.8 tesla so as to stay well to the middle of the accelerator characteristics. Indeed, as might be expected, the accelerator displays characteristics similar to an axial flow compressor, which it is identical to thermodynamically. The voltage and current are analogous to pressure ratio and flow respectively, while the magnetic field is analogous to rpm. Well to the right of the peak of the accelerator V-I curve at a given value of B the accelerator may be considered in "stall," and to the left in "surge." The stable part of the V-I characteristics become much narrower as the discharge velocity is increased.

The accelerator may also be operated as a two terminal (constant  $I_T$ ) device with discharge velocities as high as about 6,800 m/sec. Matching characteristics for this case are shown in Fig. 69. The surge-stall characteristic at high discharge velocity is more clearly evident here since no current increment was utilized to bring  $j$  normal to the flow velocity. Again the figure illustrates the unique advantages of the constant current Hall generator for starting a device of this type.

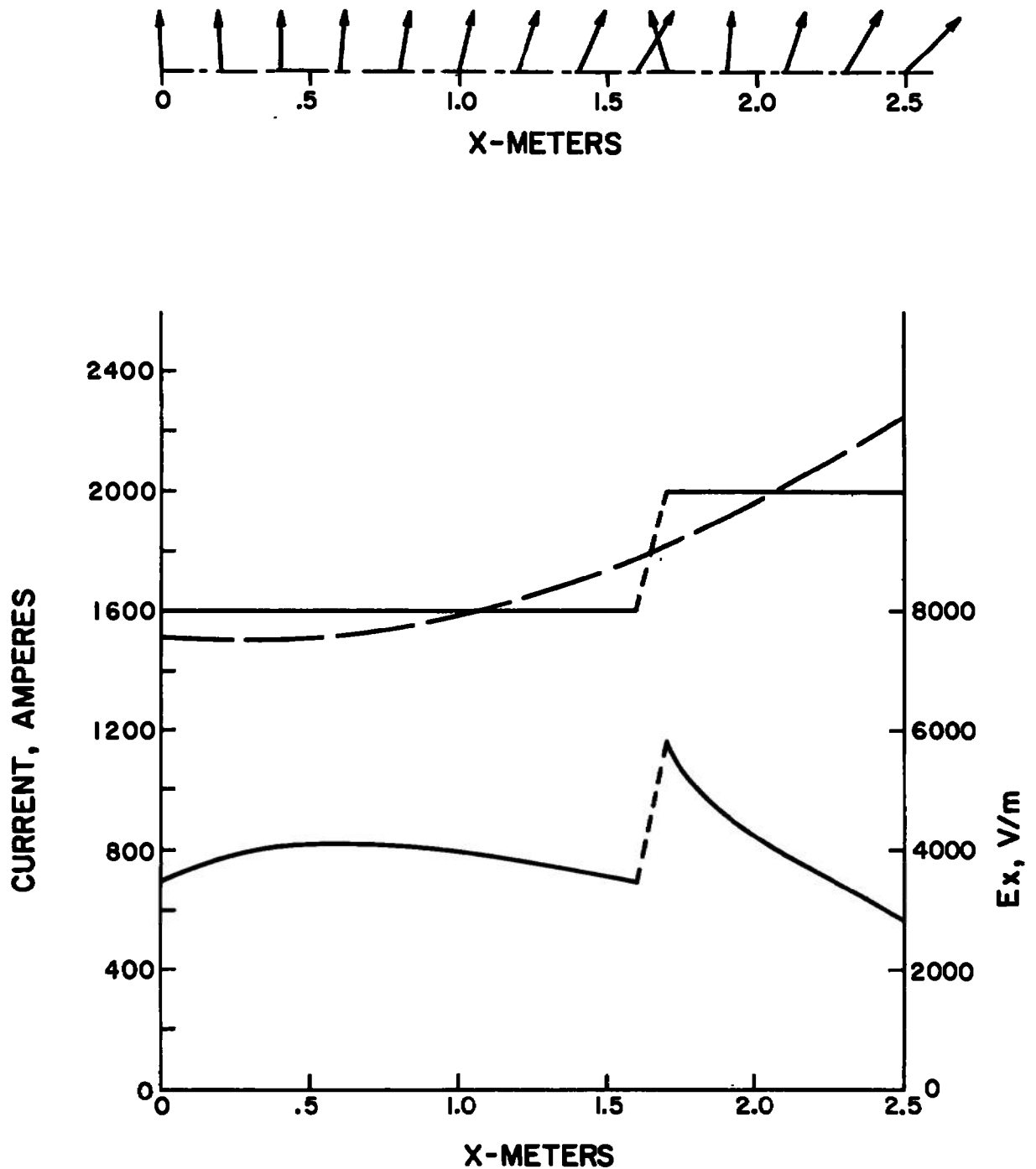


Fig. 67 Total Current and Axial Electric Field for the Three Terminal Connection at the Design Point

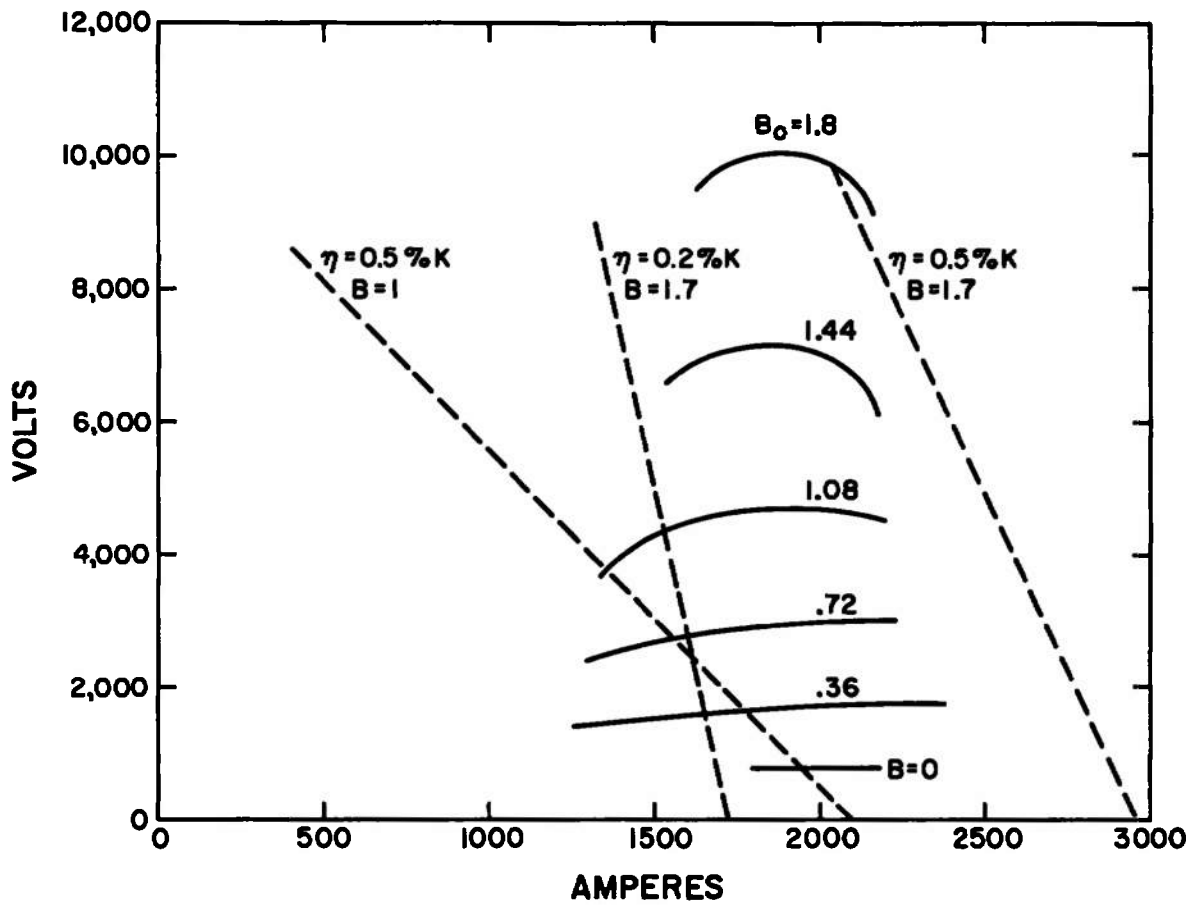


Fig. 68 Matching Characteristics for Accelerator and Generator, Three Terminal

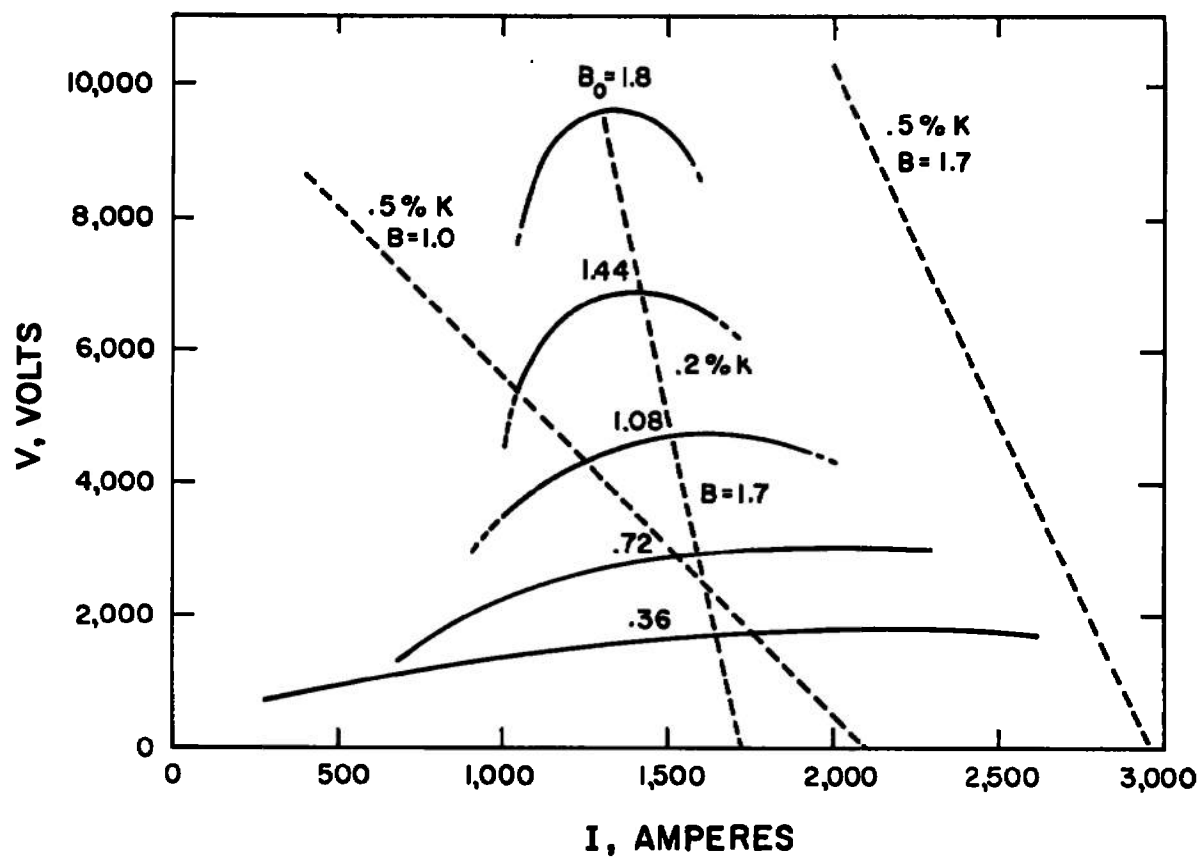


Fig. 69 Matching Characteristics for Accelerator and Generator, Two Terminal

(Perhaps it would be well to remark here that the accelerator has not been operated so that the calculated performance has never been verified. However, the actual generator operating curves closely resemble those depicted in Fig. 69.)

Figure 70 shows the electric field, total current Hall current free, and current vectors for the design operated two terminal for an outlet velocity of 6800/sec. It is seen here that Hall current free conditions are nearly approached and that the maximum electric field is less than 5000 volts/meter. Note also how the current vectors remain nearly normal to the flow along the entire length of the channel. Off design current vectors for the two terminal channel are indicated in Fig. 71 for two values of magnetic field and several values of current. It is interesting to note again how the device becomes more of a heater than an accelerator and operates at reduced voltage away from the design condition.

#### a. Supersonic Diffuser for the Accelerator

The accelerator must discharge to the atmosphere under all hot conditions to be encountered. As previously described, three critical conditions may be identified:

- a) No power input from generator.
- b) Low impedance presented to generator.
- c) Design impedance presented to generator.

Figure 72 illustrates the diffuser requirements for the operating conditions. The abscissa is the accelerator exit Mach number and the ordinate is the accelerator exit static pressure. The required static pressure for normal shock recovery to an atmosphere as a function of Mach number is indicated. Points a, b and c represent the critical design conditions enumerated above. It is seen that less than normal shock recovery is required for all cases.

Three model diffuser configurations were tested in cold air. They were: configuration #1, a straight pipe of square cross-section 14.4 diameters long; configuration #2, a 7° contraction in two walls ( $A_1/A_2 = 1.255$ ) a 14 diameter constant cross-section throat and a subsonic diffuser section (3° divergence on each wall); and configuration #3, a round diffuser with the same cross-sectional areas as configuration #2. Transition from the rectangular model channel exit to the round constant area throat takes place in the contraction.

The performance of these three diffusers is indicated in Fig. 72 and a summary of the test results appears in Fig. 73. Note that a small over pressure is necessary to "start" configurations #2 and #3.



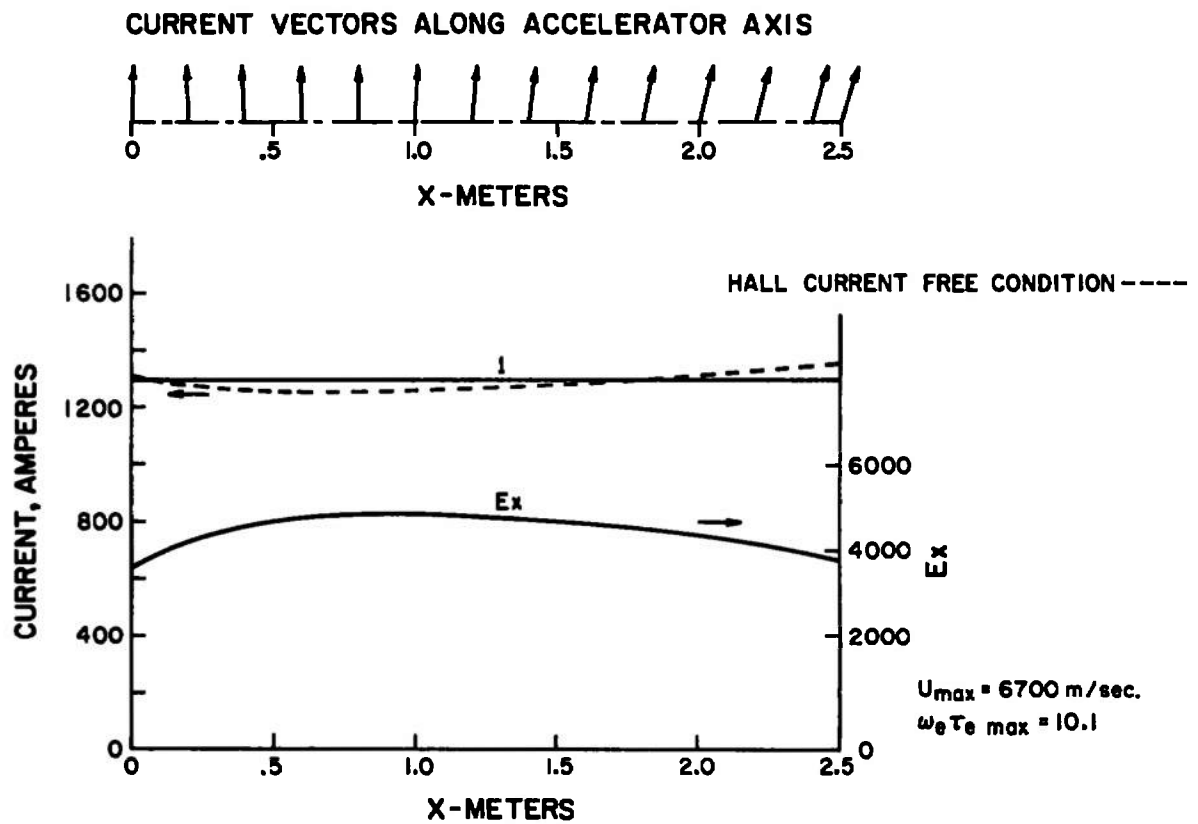


Fig. 70 Electric Field and Current Vectors for Two Terminal Design at Calculated Velocity of 6800 meters/second

TWO-TERMINAL DESIGN - ACCELERATOR, CURRENT VECTORS

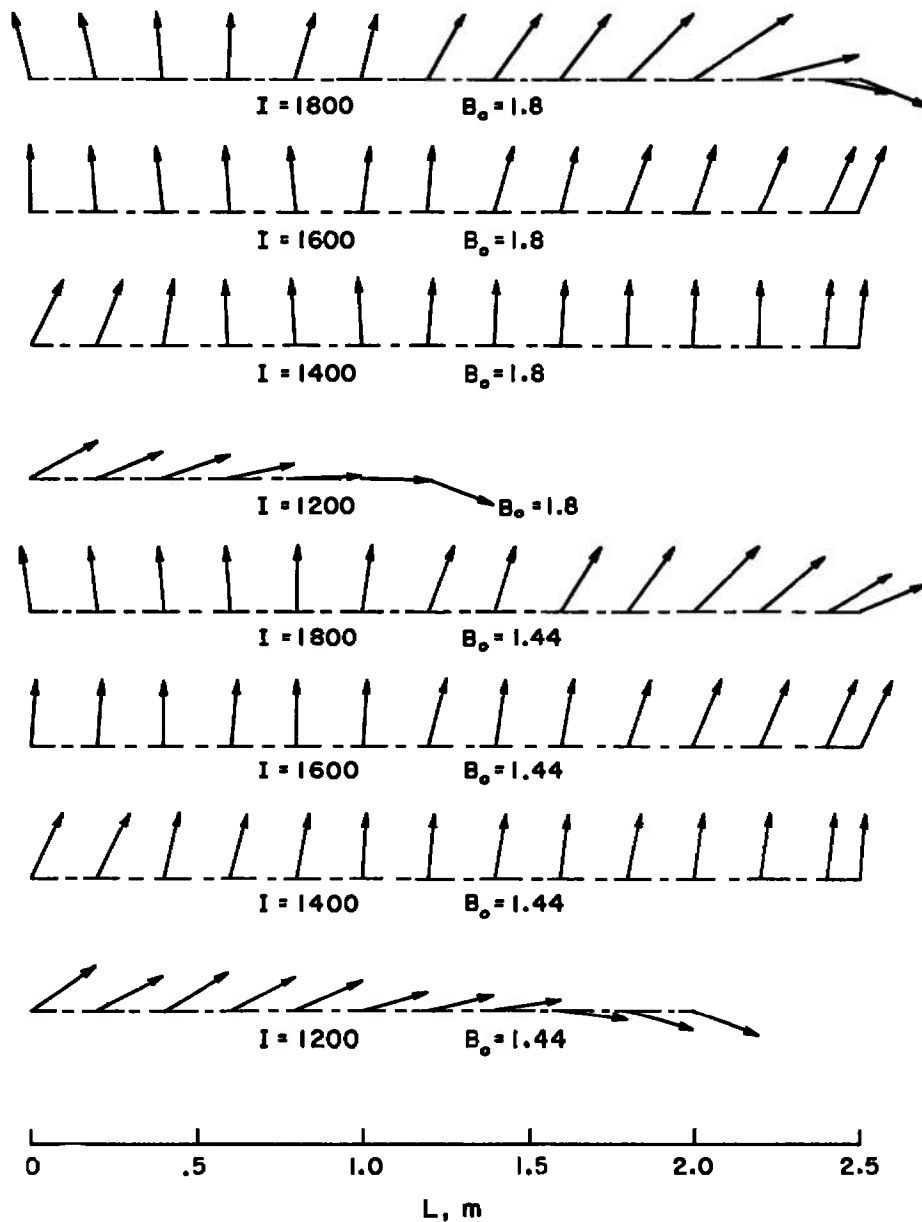


Fig. 71 Current Vectors for Various Total Currents and Magnetic Fields, Two Terminal

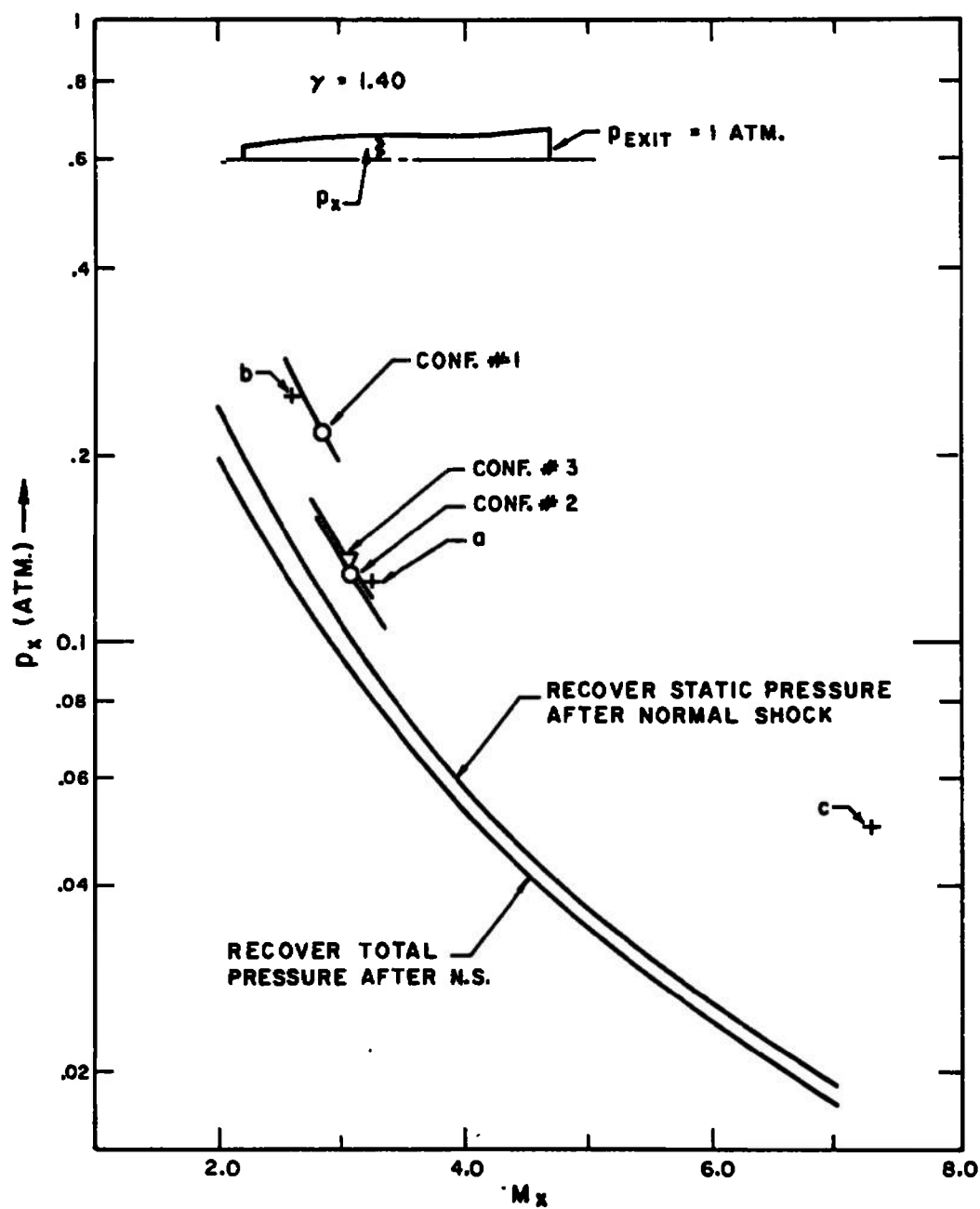


Fig. 72 Accelerator Diffuser Requirements for Three Critical Operating Points

Configuration	P <sub>min</sub> (atm)	Mach number	p <sup>o</sup> <sub>start</sub> /p <sup>o</sup> <sub>min</sub>
1	.218	2.81	-----
2	.127	3.08	1.087
3	.134	3.08	1.092

Fig. 73 Summary of Diffuser Test Results

Configuration #2 exhibited the best performance and was used as the full-scale diffuser. A sketch of this configuration appears in Fig. 74.

As previously mentioned, the Hall coefficient is a strong function of exhaust velocity. It is somewhat less sensitive to two or three terminal configurations. Figure 75 illustrates the variation of  $\omega T_{\max}$  with velocity for two and three terminal configurations achieved by varying the magnetic field. As there is little experience at the higher values of Hall coefficient, only operating experience could verify predicted performance at high Hall coefficient and discharge velocity.

The following section describes the accelerator construction in some detail.

#### 4. MECHANICAL DESIGN OF THE HIGH POWER MHD ACCELERATOR

##### A. DESCRIPTION OF SYSTEM

The 20 MW accelerator system is shown schematically in Fig. 76. The preheated air flow from the arc heater is decelerated in the diffuser and discharged into the plenum where seed is added. The flow is then accelerated in the nozzle to a Mach number of 2.7. The flow is further accelerated in the channel to a design Mach number of approximately 7. At the exit of the channel is a test section which has ports for the introduction of instrumentation into the air flow. Finally, an exit diffuser is used to provide sufficient pressure recovery to discharge to the atmosphere.

In the following sections each component will be described in detail.

##### B. INLET DIFFUSER AND PLENUM

The inlet diffuser decelerates the air discharged from the arc as described above. In the plenum mixing takes which reduces the temperature nonuniformities characteristic of arc heaters. Also in the plenum seed is introduced to increase the gas conductivity. Heat transfer rates in these sections are estimated at  $2.4 \times 10^6$  Btu/ft<sup>2</sup>/hr at the diffuser inlet, falling to  $1.0 \times 10^6$  Btu/ft<sup>2</sup>/hr at the diffuser exit and in the plenum. The diffuser and plenum have thin walled copper liners which are water cooled. The water flow is directed by filler blocks. Full advantage is taken of the high water velocities in the cooling passages to achieve convective cooling without surface boiling. Convective cooling results in lower metal temperatures, the maximum calculated metal temperature being 405°F at the diffuser inlet. The copper liners are free to expand longitudinally and radially so that the stresses in these parts are only hoop stress due to water pressure and thermal bending stress due to temperature gradient in the wall. The maximum computed stress occurs

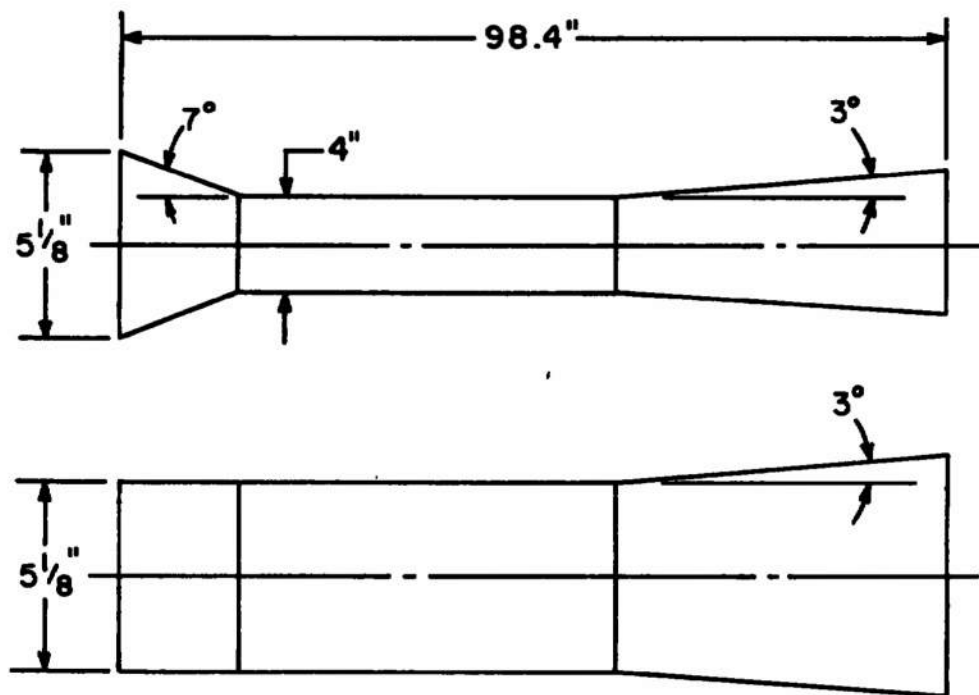


Fig. 74 Diffuser Configuration for High Power Accelerator

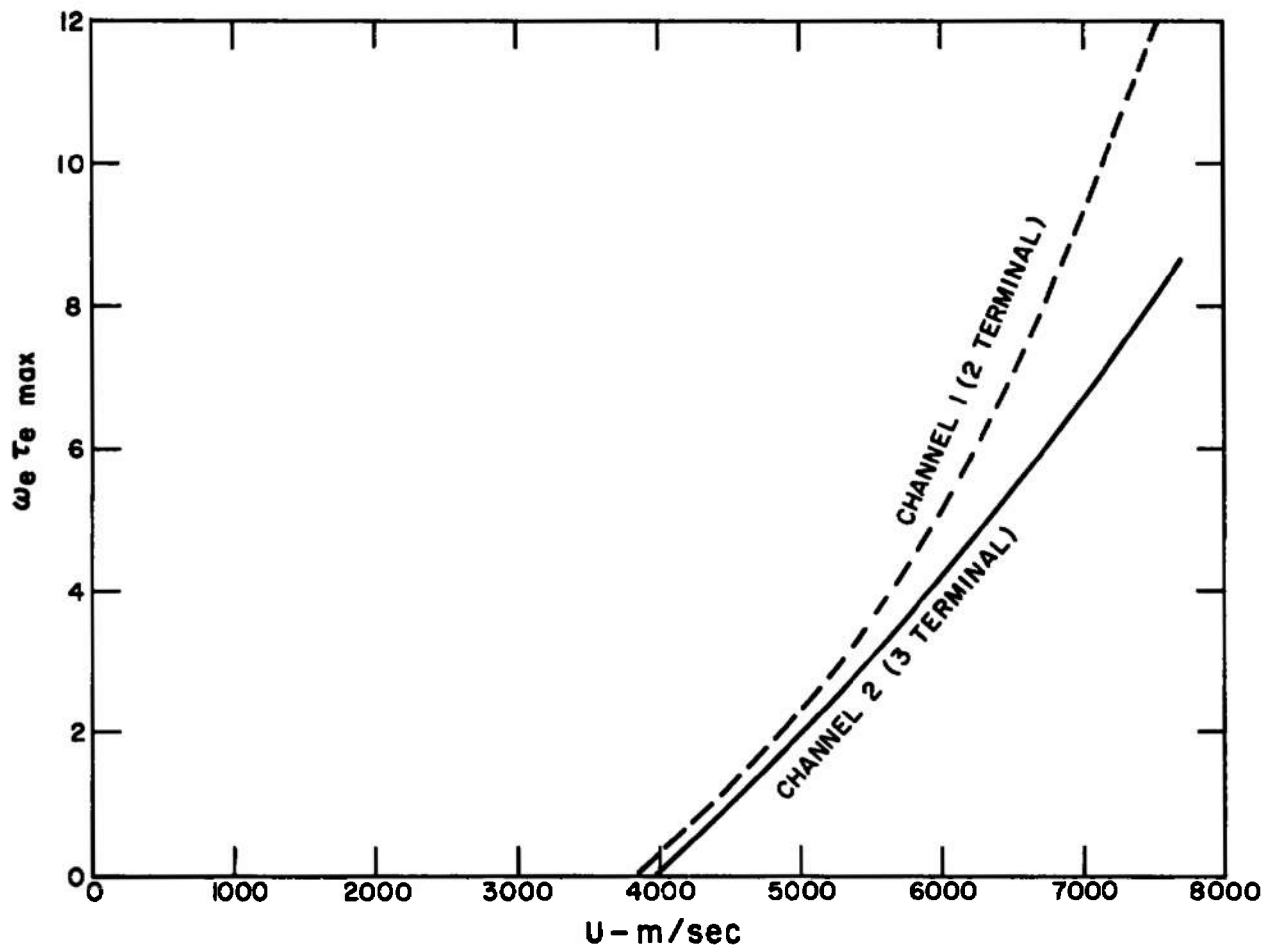


Fig. 75 Maximum Design Velocity as a Function of Hall Coefficient for "As Built" Accelerator in Two (Channel 1) and Three (Channel 2) Terminal Configurations

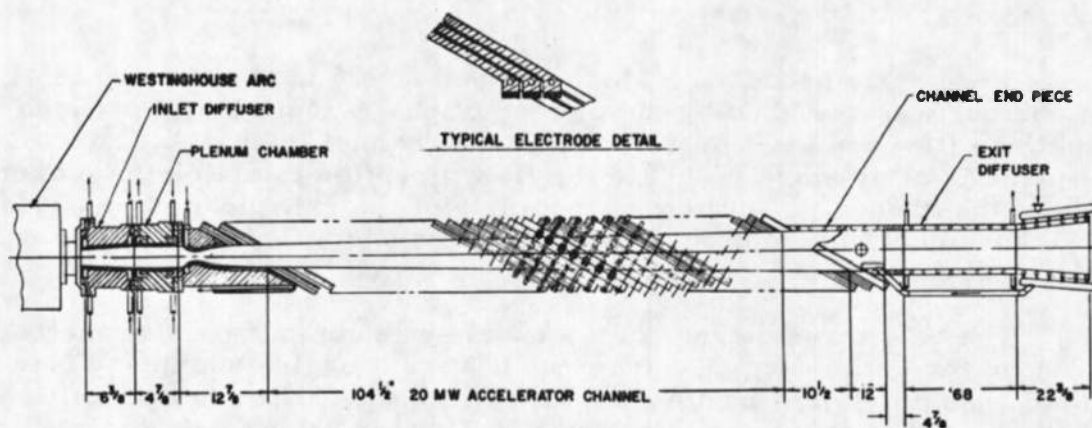


Fig. 76 Schematic of High Power Accelerator System

at the diffuser inlet and is a compressive stress of 14,000 psi. This stress is slightly above the yield point of annealed copper, and therefore some plastic deformation may occur during the first operating cycle. However, with the redistribution of stress due to the yielding, subsequent operation will not produce further yielding.

Seed is injected into the plenum through small ports located near the diffuser exit. The seed material,  $KO_2$  powder, is injected with a small amount of air carrier flow. The diffuser and plenum chamber are shown in Fig. 77.

### C. NOZZLE

The nozzle produces a Mach number of 2.7 at the channel inlet. The contour was designed by the method of characteristics to produce shock free flow and uniform velocity at the channel inlet. The nozzle exit plane is at an angle of  $29^\circ$  to the flow direction to match the diagonal angle of the channel. Because of the angle of the exit plane it was found to be convenient to complete the expansion on one wall in the first few modules of the channel.

The heat transfer rate in the nozzle was computed using methods developed for estimating heat transfer in rocket engine nozzles. This method assumes fully turbulent flow. In retrospect, it seems likely that the boundary layer would probably be in transition from laminar to turbulent flow. Therefore, the calculated heat transfer rates are probably too high. The calculated values are:  $1.0 \times 10^6$  Btu/ft<sup>2</sup>/hr at the nozzle inlet,  $4.8 \times 10^6$  at the throat, and  $1.3 \times 10^6$  at the exit.

The construction method adopted for the nozzle consisted of a liner and a housing which were shaped to produce a suitable water cooling passage between them. The liner was made with longitudinal ribs to prevent collapse due to water pressure. The liner was restrained from longitudinal expansion due to the ribs and due to being welded to the housing at assembly. However, the liner is not restrained laterally at the throat region and thereby is relieved of some thermal stress.

Due to the relatively high heat transfer rates, the nozzle cooling was investigated carefully. By employing a larger water flow (210 gpm) and by adjustment of the cooling passage area, a high water velocity of 120 ft/sec was obtained in the throat area and a minimum velocity of 40 ft/sec near the nozzle exit. These velocities result in convective cooling without surface boiling and produce an appreciably lower metal temperature and thermal stress. The estimated wall temperatures at the throat are 300°F on the water side and 550°F on the gas side.

Stresses in the nozzle are principally thermal stresses due to temperature gradient in the wall and temperature differential between the housing and the liner. In addition there are some small bending stresses due to water pressure. The highest combined stress situation is in the throat region adjacent to a rib. The total stress here is 52,000 psi



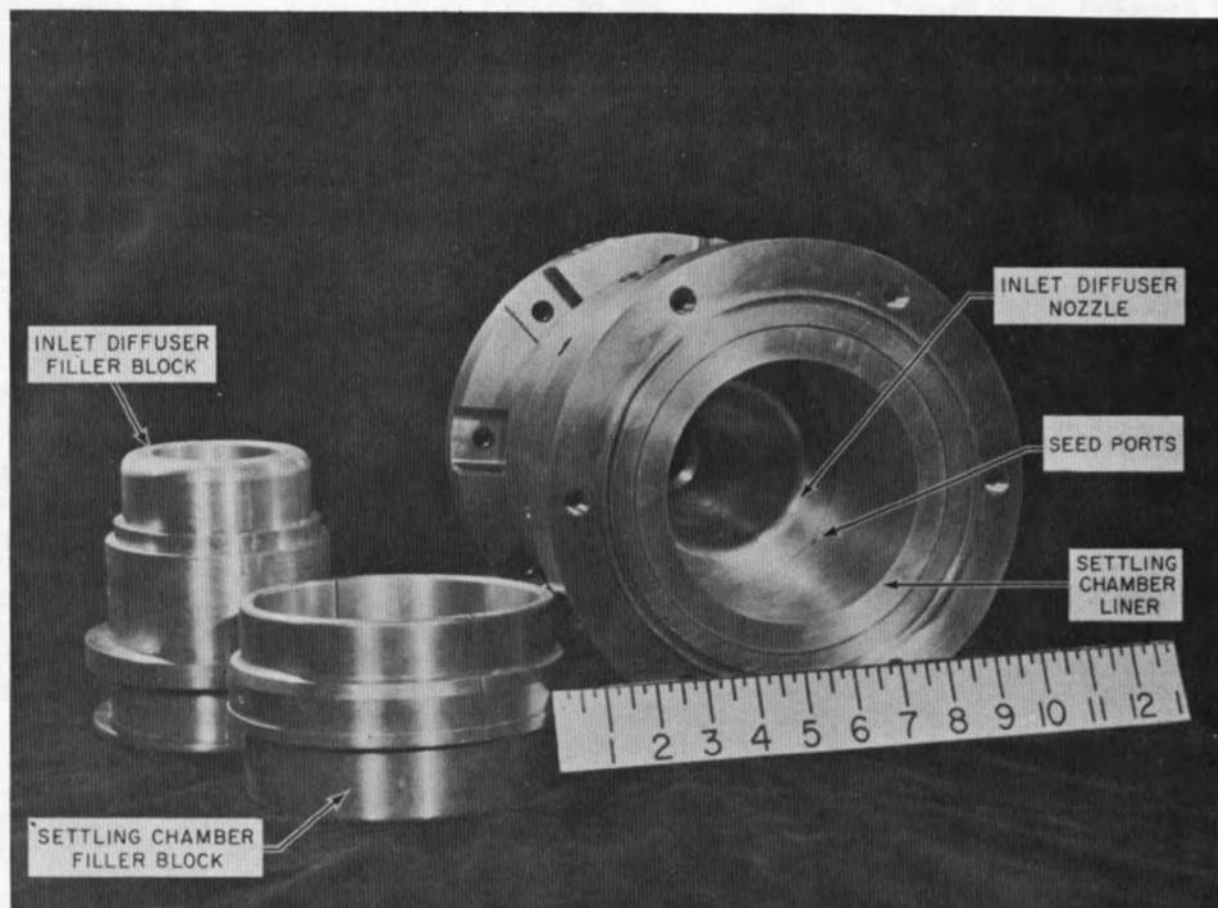


Fig. 77 Plenum Chamber Inlet Diffuser and Plenum Chamber

which is about 12% above the yield point of the material. Therefore, there will be some plastic deformation during the first operating cycle but subsequent operation should not produce further yielding.

In building the nozzle, full advantage was taken of available materials and techniques in order to produce a unit which would withstand the predicted operating conditions. The material selected for the liner was Amzirc zirconium copper. This material, by a process of cold work and heat treatment, may be made to have a unique combination of high thermal conductivity, high strength which is retained to moderately elevated temperatures, and great ductility. The material for the liner was specified to have 40% minimum cold reduction which when followed by precipitation hardening results in a yield point of 42-45,000 psi.

Assembly of the nozzle was by electron beam welding. The liner was made in two halves to facilitate machining of the gas passage. The two halves were welded together and inserted in the halves of the housing. The housing halves were then welded together and to the liner at the ends. The nozzle is shown before and after welding in Figs. 78 and 79.

#### D. CHANNEL

The channel consists of 282 diagonal plate modules arranged at  $29^\circ$  to the flow direction and having gas passage dimensions of 2.95 in. square at the inlet and 5.14 in. square at the outlet. The pitch of the modules is nominally .375 in. in the axial direction and .182 in. normal to the plane of the plates. The plates are assembled in groups of three and the groups are assembled to form seven subassemblies which in turn are butted together to form the complete channel.

The channel modules are of the flat plate type which are easier to make and assemble than the bent plate type used in the 2 MW accelerator. A finished module is shown in Fig. 80. The modules are made from ETP copper throughout. There is a separate piece to form the electrode groove and cooling water hole. These electrode pieces are brazed to the plate module. The cooling passage for the insulating walls is made by milling grooves in one side of the plate and brazing a cover plate over the groove. At assembly, during the brazing operation, water inlet and outlet tubes are also brazed to the edge of the module. Because of the thinness of the modules (.165 in.) there were some quality-control problems particularly with the brazing operation. The milled water passage frequently filled with the brazing alloy, thereby blocking the passage. Modules with blocked passages were repaired by machining off the cover plate, cleaning out the water passage, and brazing on a new cover plate. The final step in the module construction was the preparation of the electrode. The surfaces exposed to the plasma were silver plated to retard oxidation. The bottom of the electrode groove was flame sprayed with a thin layer molybdenum to make better contact between the electrode material and the copper. Finally the electrode grooves were packed with a mixture composed of 15% zirconium diboride with 85% zirconium oxide stabilized with 5% calcium oxide. This mixture is made up into a paste and trowelled into the grooves.

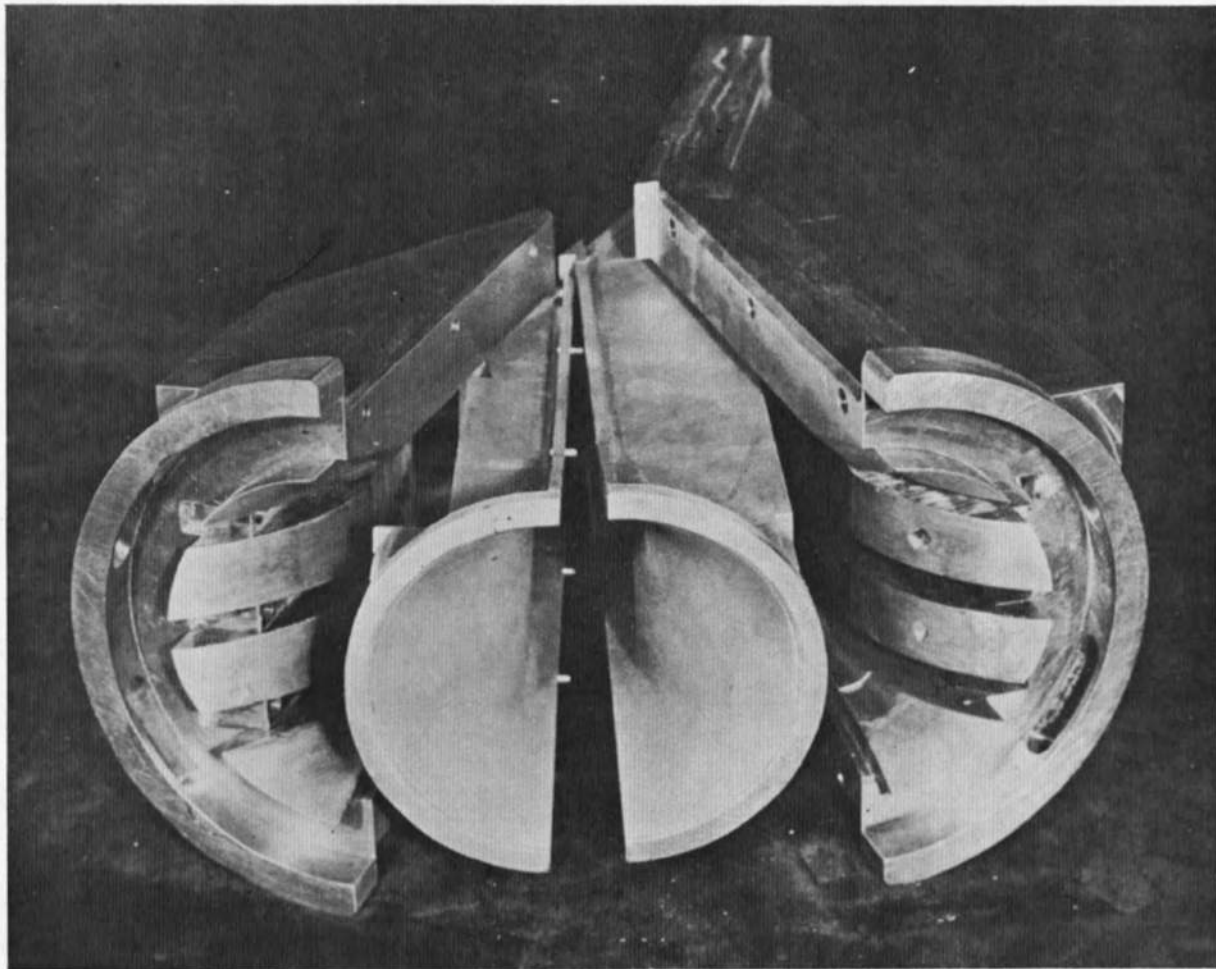


Fig. 78 Supersonic Expansion Nozzle Before Welding

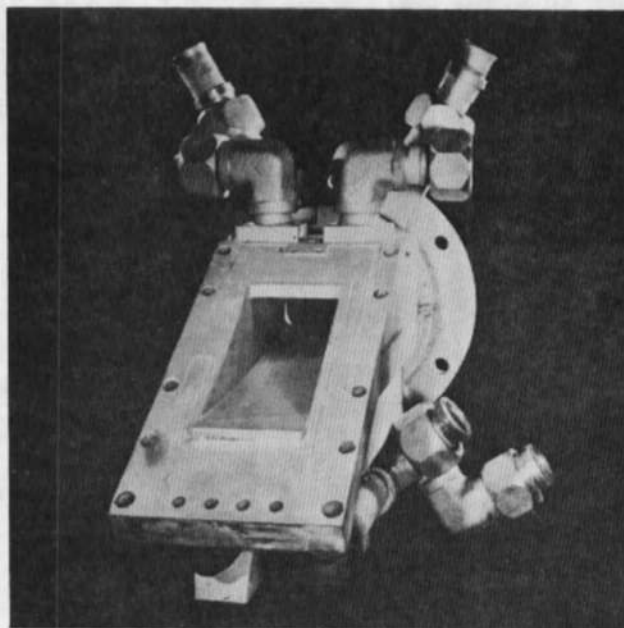


Fig. 79 Completed Nozzle After Welding

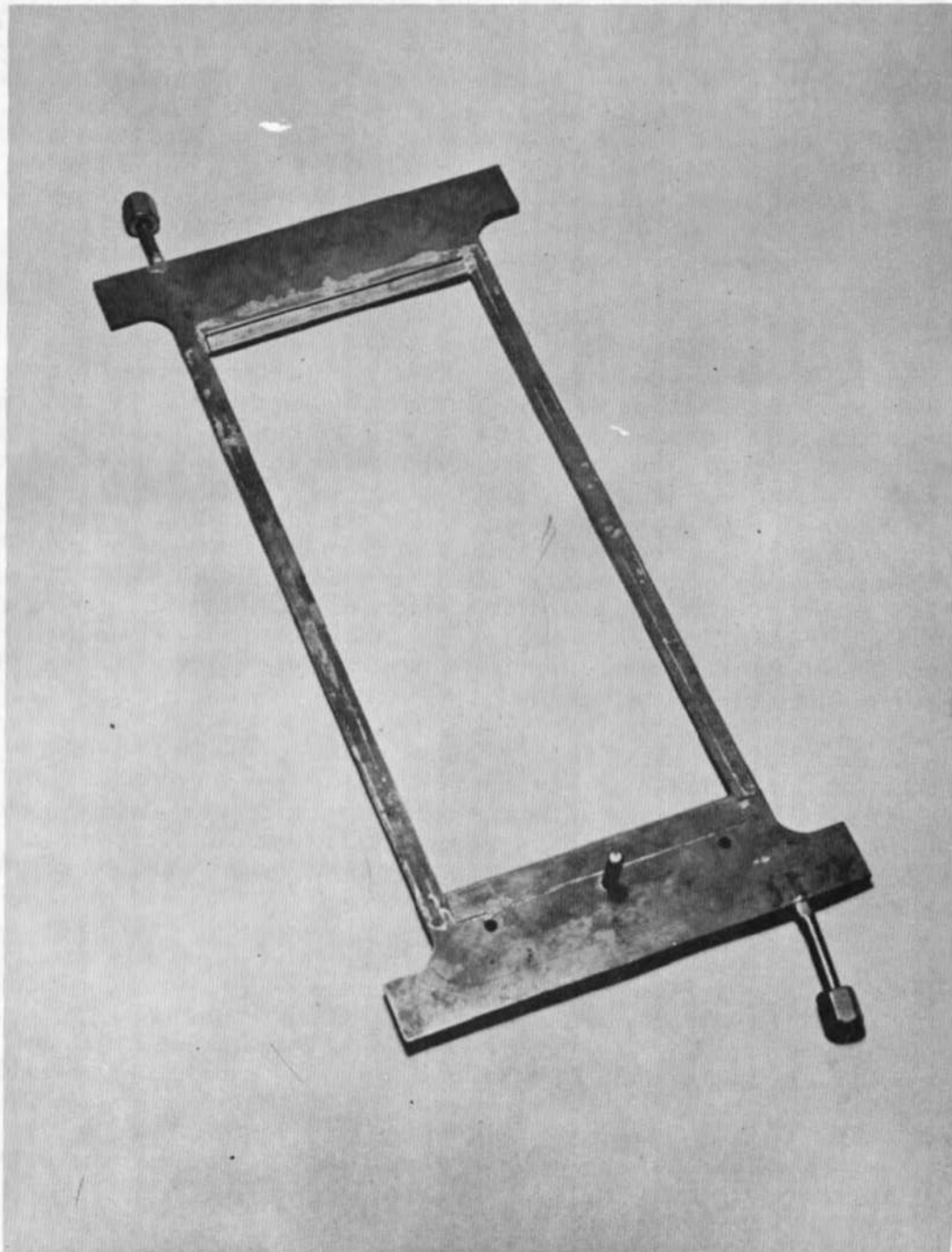


Fig. 80 Accelerator Channel Module

At assembly the modules are assembled in groups of three. That is, starting at the nozzle, the first three modules form a group, the next three form another group, etc. The modules are separated and insulated from each other by a .016 thick silicone-fiberglass laminate spacer. The modules in a group are held together by studs which were brazed to the module. Then 13 or 14 groups are assembled to form a subassembly. The first and last module in a subassembly are provided with flanges. Plastic tie rods are used to clamp all the modules between the flanges. Finally, the subassemblies are bolted together with plastic bolts to form the complete channel. Figure 81 shows three subassemblies partially completed. Figure 82 shows the completed channel.

In the design and construction of the channel considerable care was devoted to the electrical insulation so as to withstand the 10 kv input voltage. In addition to the plastic tie rods used for channel assembly, the mechanical support for the channel and the water inlet and outlet manifolds were constructed of nonconducting materials. The channel was mounted on an epoxy-fiberglass beam which ran longitudinally underneath the channel. The water manifolds were constructed of nylon and connections to each module were made with nonconducting hose. The electrical hook-up of the accelerator results in the inlet end being at 10 kv while the exit diffuser is grounded. Therefore, it was necessary to insulate the inlet diffuser, plenum, and nozzle by using nonconducting hoses and plastic structural supports.

At the exit end of the channel an extension piece is provided which has two 1 1/2 inch dia. ports for inserting instrumentation into the gas stream. The extension is made from four copper slabs which have drilled holes for cooling passages. The extension also contains electrode grooves on one side for the power input to the exit end of the channel.

The average heat transfer rate to the insulating wall is estimated to be  $1.5 \times 10^6$  Btu/ft<sup>2</sup>/hr while the rate to the electrode wall is increased to  $2.2 \times 10^6$  Btu/ft<sup>2</sup>/hr due to power dissipation in the boundary layer. There is a local peak in the electrode wall heat transfer at a distance of approximately 67 in. from the channel inlet where additional current is fed into the downstream end of the accelerator. This peak amounts to  $2.8 \times 10^6$  Btu/ft<sup>2</sup>/hr. The channel is cooled with approximately 1100 gpm water flow. The cooling passages have been designed so that the cooling is entirely by convection with no surface boiling.

## E. DIFFUSER

A diffuser is provided to produce sufficient pressure recovery to discharge to atmospheric pressure. A study of supersonic wind tunnel diffuser designs and some experiments with three model diffusers resulted in the selection of the diffuser configuration to be described. The first section of the diffuser is a converging section with 7° half angle that produces a 22% area reduction. The next section is of constant area and is 68" long (approximately 14 diameters). The last section is a diverging



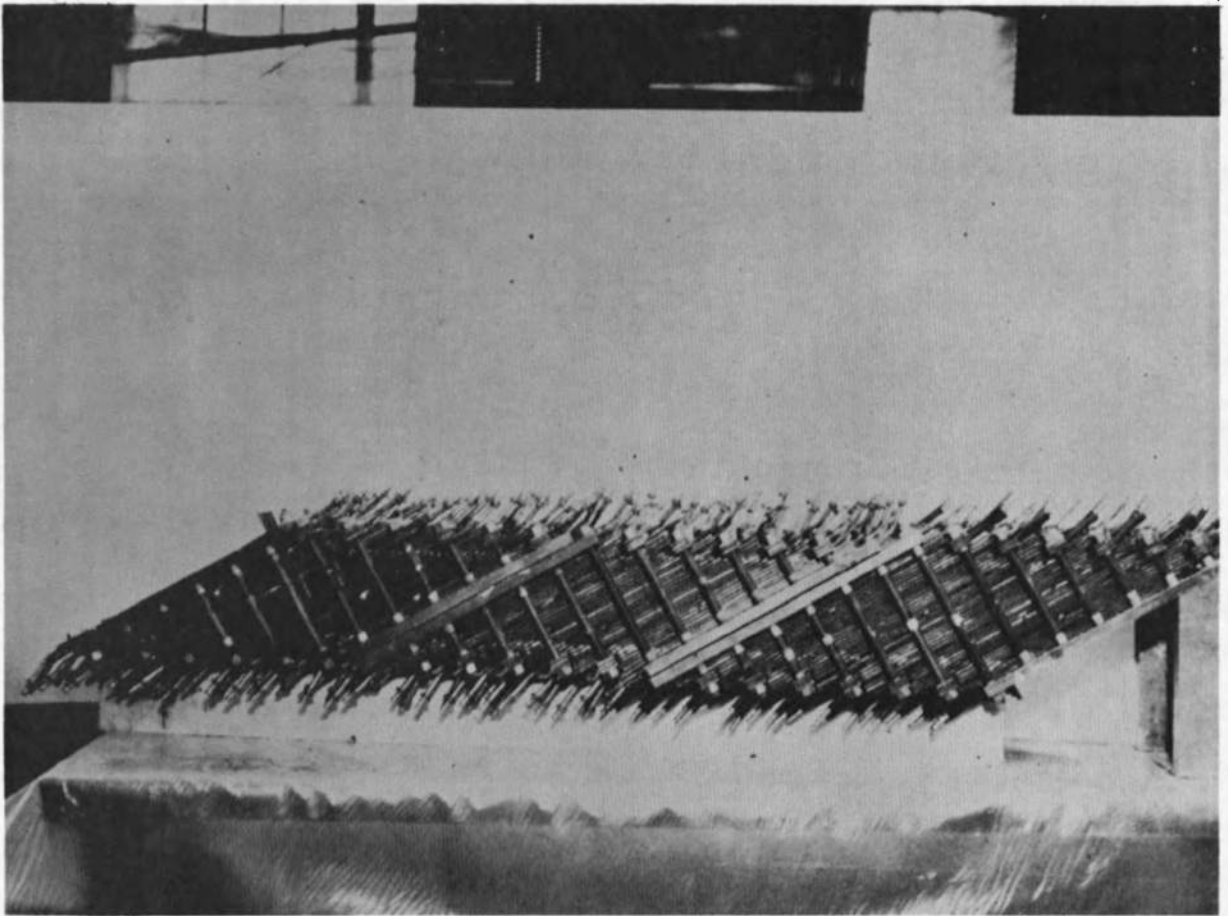


**Fig. 81    Channel Subassembly Partially Completed**

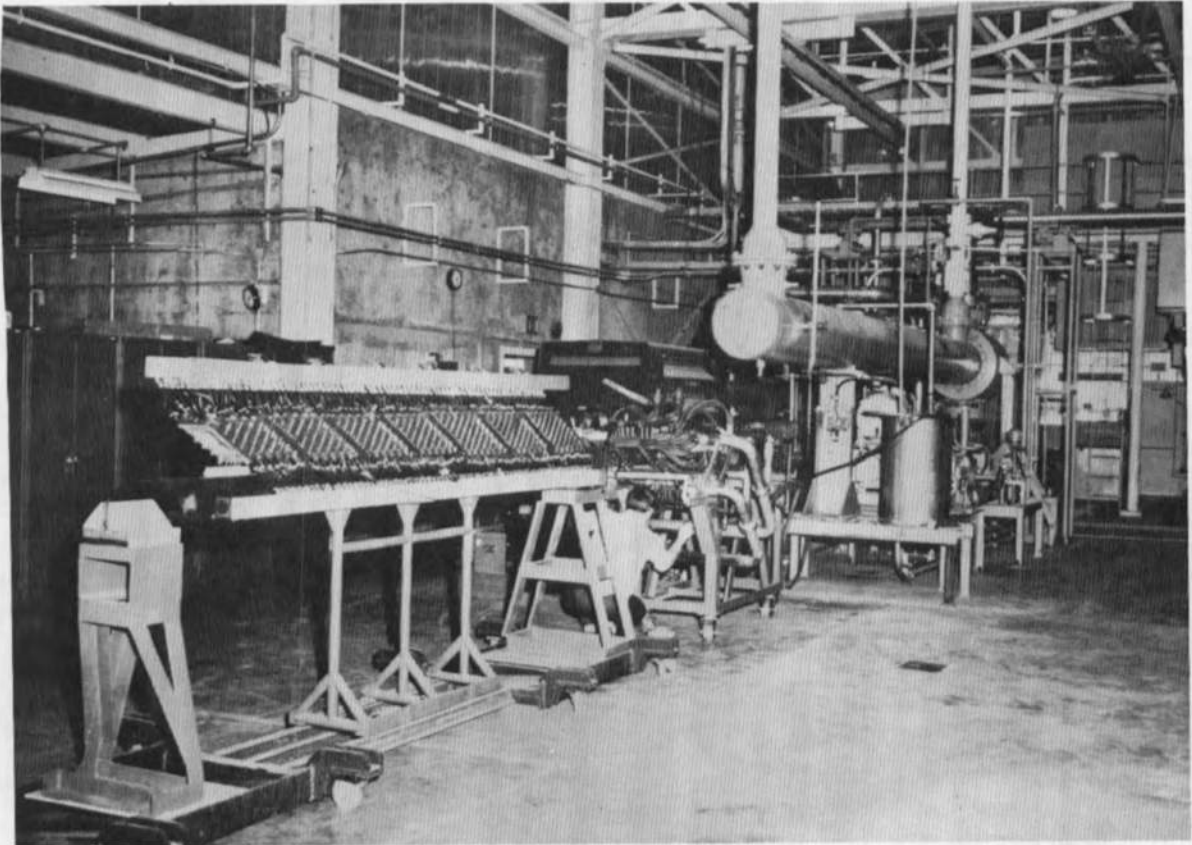


Fig. 82 Completed High Power Accelerator Channel



3° half angle subsonic diffuser. The inlet and exit sections are made from copper slabs which have a drilled hole cooling system. The constant area section is composed of four walls made by brazing hollow copper extrusions to copper plates. The holes in the extrusions form the water cooling passages. The diffuser is designed for a heat transfer rate of  $1.5 \times 10^6$  Btu/ft<sup>2</sup>/hr. A water flow of approximately 700 gpm is adequate to cool this unit. The complete diffuser is shown in Fig. 83.

#### F. SEEDER

A dry powder seeding system is utilized to feed KO<sub>2</sub> powder into the plenum chamber upstream of the accelerator channel. The design seed rate is .5 mole percent potassium but the system is capable of approximately three times this rate. A piping schematic is shown in Fig. 84. The seed is contained in a pressurized hopper which will hold enough for 10 minutes of operation. At the bottom of the hopper the seed falls into a toothed rotor which resembles a gear wheel. This rotor turns, picks up seed from the hopper and deposits it into a pipe at the bottom of the rotor housing. An air flow of approximately .04 lbs/sec. is maintained through this pipe, and the air picks up the seed and carries it to the plenum chamber. The whole system operates at the air pressure which is approximately 400 psi. The rotor is turned by a variable speed gear motor at a normal speed of 50 rpm and a maximum speed of 180 rpm. A photograph of the completed seeder is shown in Fig. 85.

The seeder incorporates an air control system consisting of regulators, valves, and metering orifices which provide the necessary flow through the seeder. In addition, the air system is used to provide up to 17% boost in air flow through the accelerator to "start" the diffuser, that is, to ensure that supersonic flow is established throughout the accelerator channel.

#### G. MAGNET

The magnet is an iron core design having nominal gap dimensions of 10 x 24 x 100 in. Water-cooled coils permit continuous operation. The iron yoke has been designed so that the magnet may be separated into two halves to provide access to the accelerator channel. The two halves are mounted on wheels that ride on inverted angle irons rails. A photograph of the magnet is shown in Fig. 86.

Operation of the accelerator is quite sensitive to field strength and field distribution. At the channel ends, the tapering off of the magnetic field produces electrical end effects in the channel. In order to determine the exact field distribution to be expected in the accelerator magnet, a one quarter scale model was built and tested. The magnetization characteristic was measured and field distributions taken at many different field strengths. In addition the effect of shimming on the distribution at the ends was investigated carefully to determine what corrective action might be taken in the event that problems were encountered in the accelerator channel.

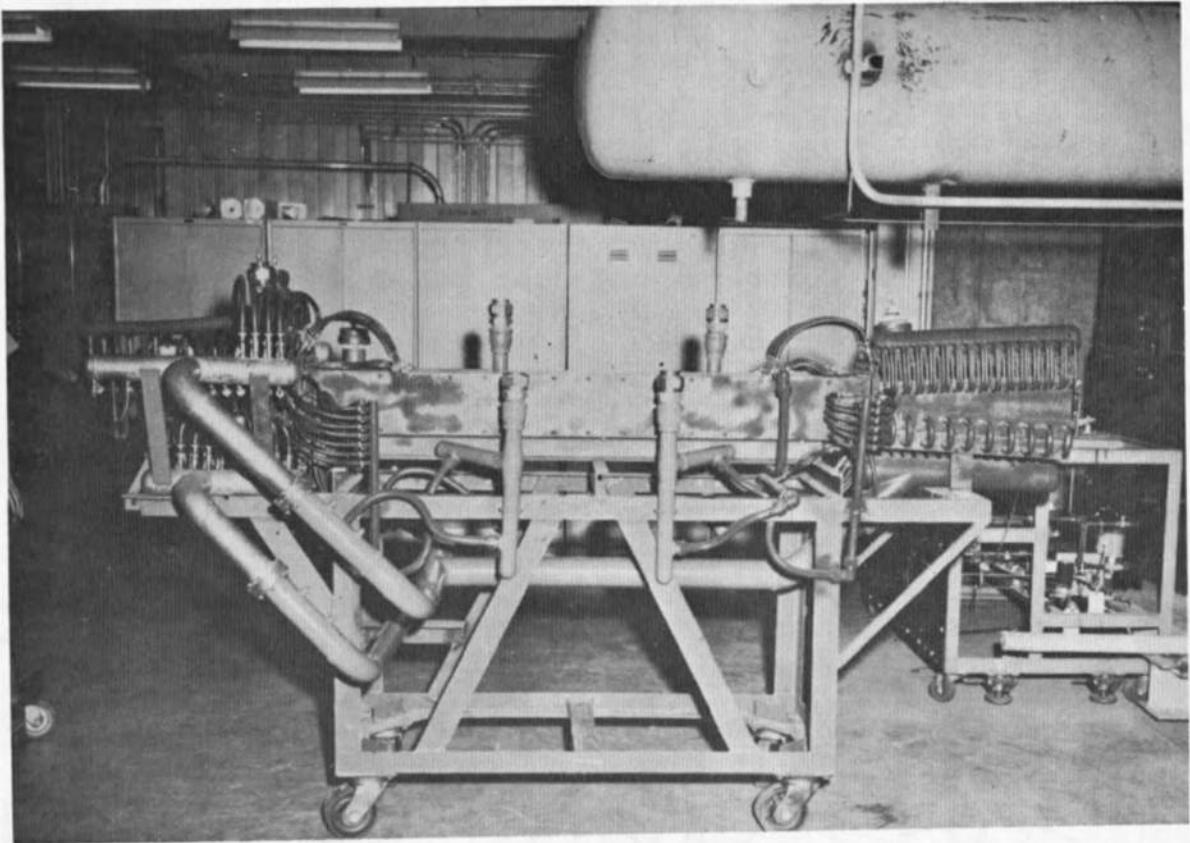


Fig. 83 Supersonic Exit Diffuser for Accelerator

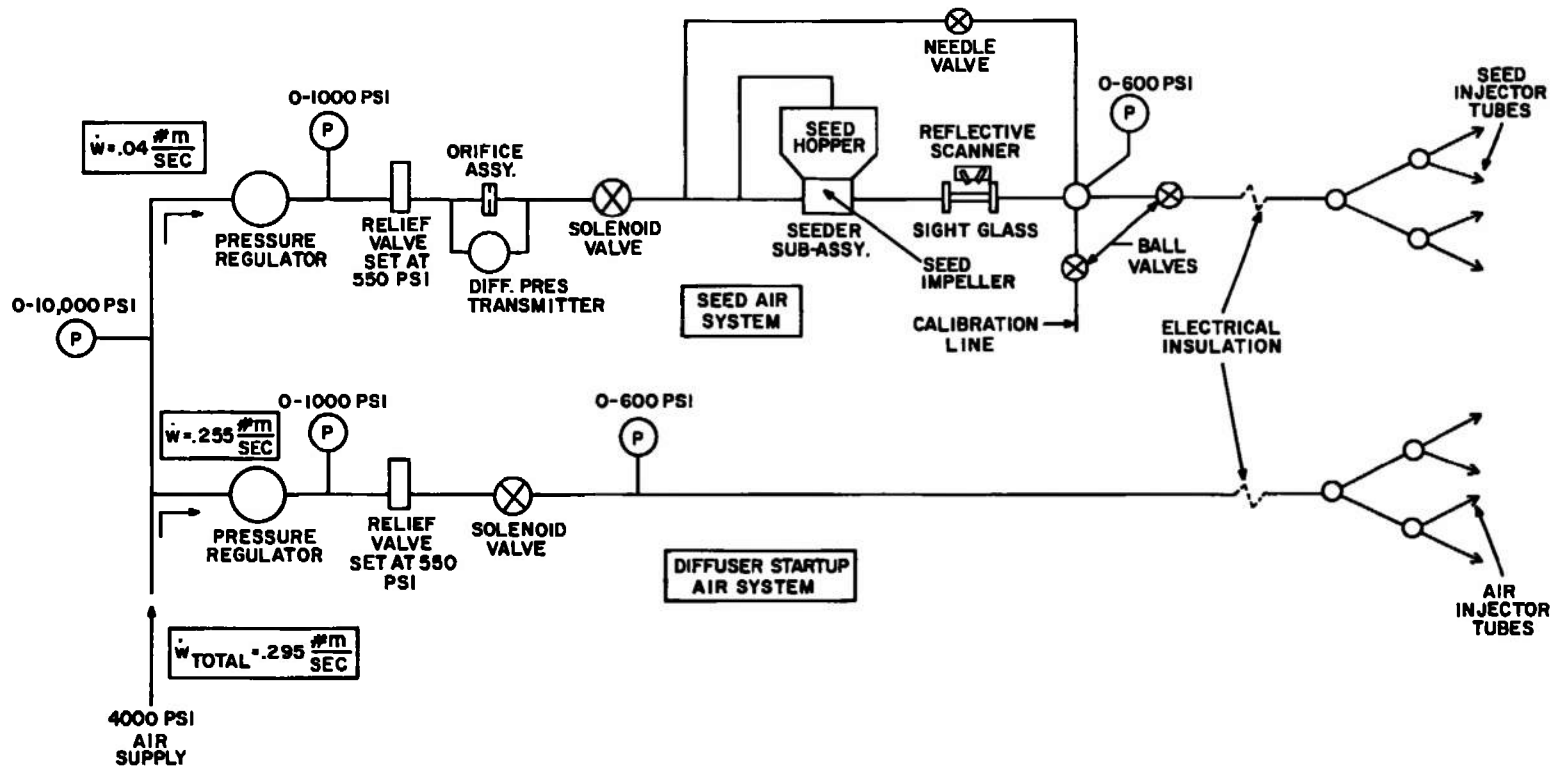


Fig. 84 Piping Schematic for Accelerator System

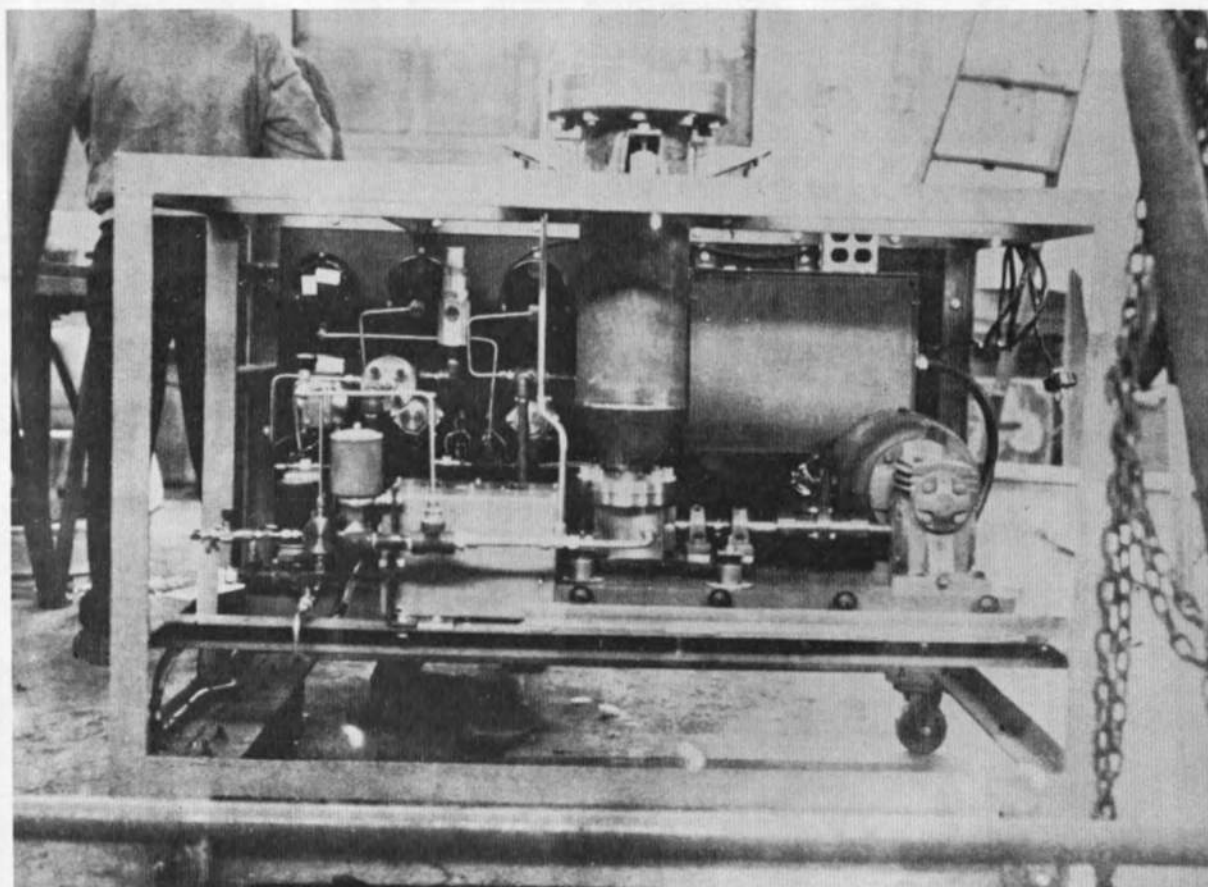


Fig. 85 Accelerator Seeder System

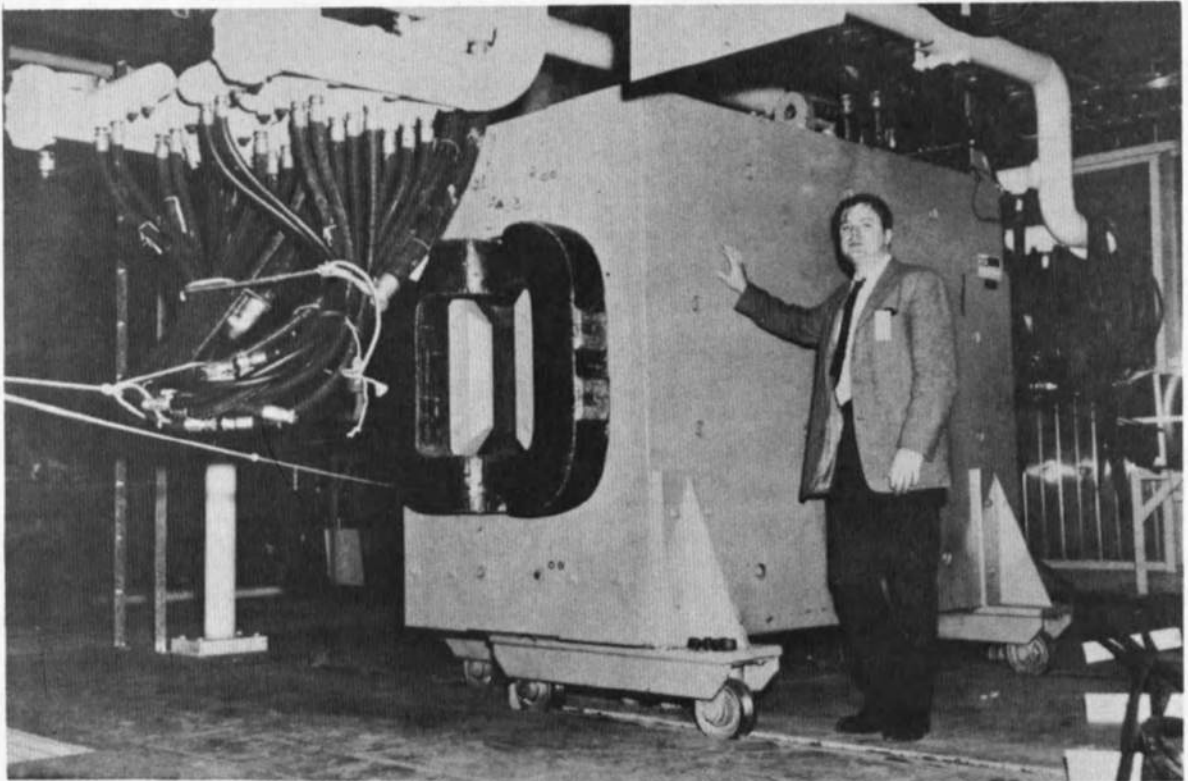


Fig. 86 Magnet for High Power Accelerator

The final magnet design has a low carbon steel yoke weighing approximately 45 tons. The coil is constructed of hollow copper extrusions which are 7/8 inch square with a 1/2 inch diameter cooling passage. The coil is made in two halves of 54 turns each and designed to carry 4000 amps at 250 v (1000 kW). The required cooling water flow is 150 gpm. The magnet pole faces have been made tapered to produce a graded field distribution. The desired field strengths were 18 kilogauss at the inlet and dropping linearly to 9 kilogauss at the exit end. The gap was made 6 1/2 in. at the inlet and 13 in. at the exit. In addition, two 3 in. shims were added at the inlet and three 3 in. shims at the exit to produce the desired shape to the ends of the field distribution curves.

Figure 87 shows schematically the pole configuration and the measured field distributions at two current values. Also shown is the desired distribution. At a current of 2250 amps, the desired distribution should be closely matched except for a few inches at the channel inlet.

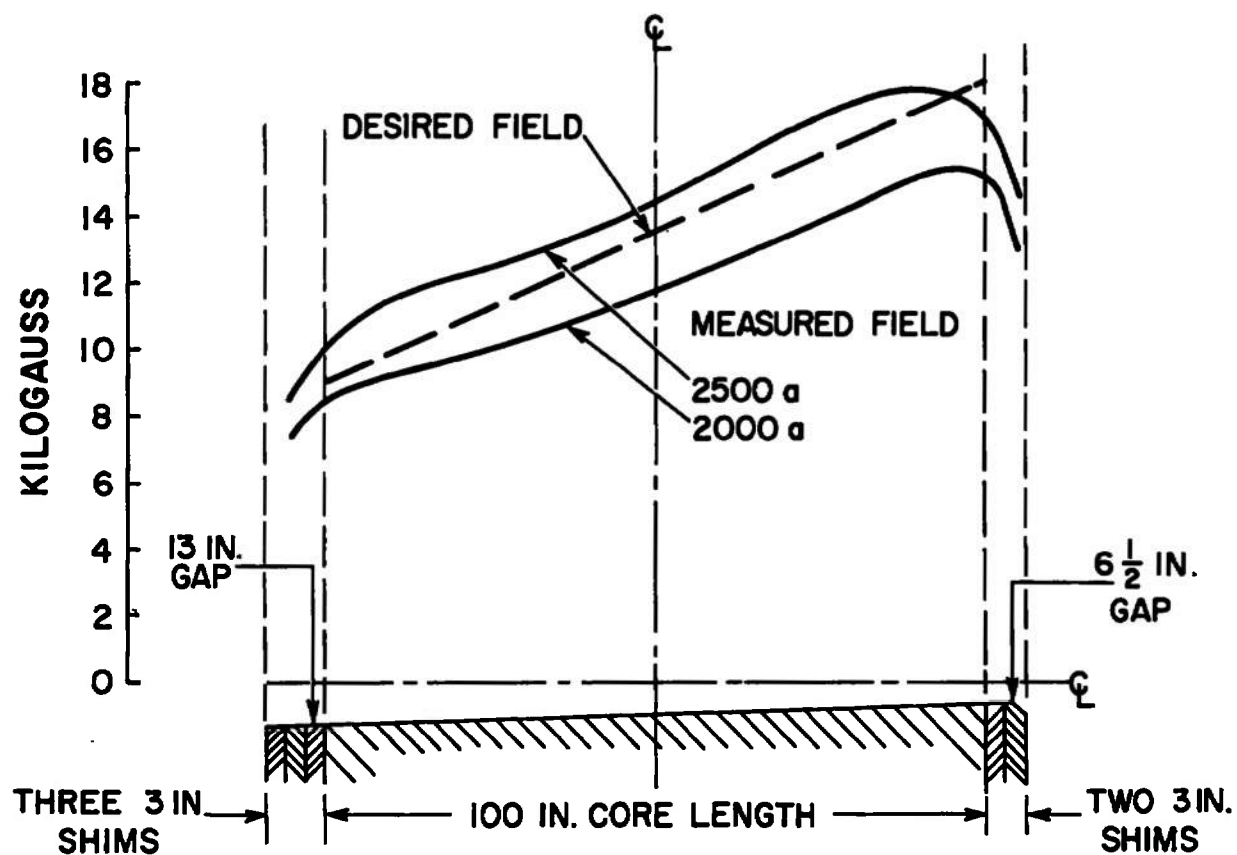


Fig. 87 Field Distribution High Power Accelerator Magnet

## SECTION V

## BRIEF DESCRIPTION OF THE LORHO PILOT FACILITY

While not a part of the present contract, a short description of the LORHO facility is included here for the sake of completeness. The LORHO facility was designed by AERL under separate contract AF 40(600)1077. The facility includes a structure, electrical and mechanical auxiliaries, instrumentation, and operators controls.

The MHD generator and its associated auxiliary equipment are housed in a 10,000 square foot laboratory (see Fig. 88) composed of a single large test and preparation area and an operator's control room. A separate but adjacent building houses the fuel storage and pumping equipment. The gaseous oxidizer storage farm is located outdoors on the opposite side of the laboratory. A sectioned drawing of the building identifying major items of equipment is shown in Fig. 89.

Due to the extreme weight of its iron core magnet (~1,000,000 lbs) the MHD generator is located on a specially reinforced foundation isolated from the building structure. Care was taken in keeping magnetic materials of construction outside the fringe field of the magnet.

The high temperature exhaust gases exiting from the generator are expelled into a 10 foot diameter horizontal breech equipped with water spray nozzles and isolated electrically from the rest of the building and the adjoining vertical exhaust stack. Initial arcing problems from the breech to ground were cured by improving the insulating structural sections and relocating and modifying water spray nozzles. During normal operation the breech was found to float at several hundred volts dc above ground and it was determined that approximately 400 kw of power could be lost through the cooling water which runs off the bottom of the breech and is somewhat conducting due to dissolved seed.

The centrifugal fuel pump is capable of pressures to 600 psig to permit good injection and atomization characteristics in the burner. A three way valve located on the burner fuel manifold permits purging of the MHD generator with nitrogen gas at the termination of a run. An upstream regulator keeps the nitrogen at the same pressure as the fuel to permit a smooth shutdown when the three way valve is switched. Fuel flows are measured with a turbine type flowmeter and indicated on a circular chart recorder.





Fig. 88 External View of LORHO Pilot Facility

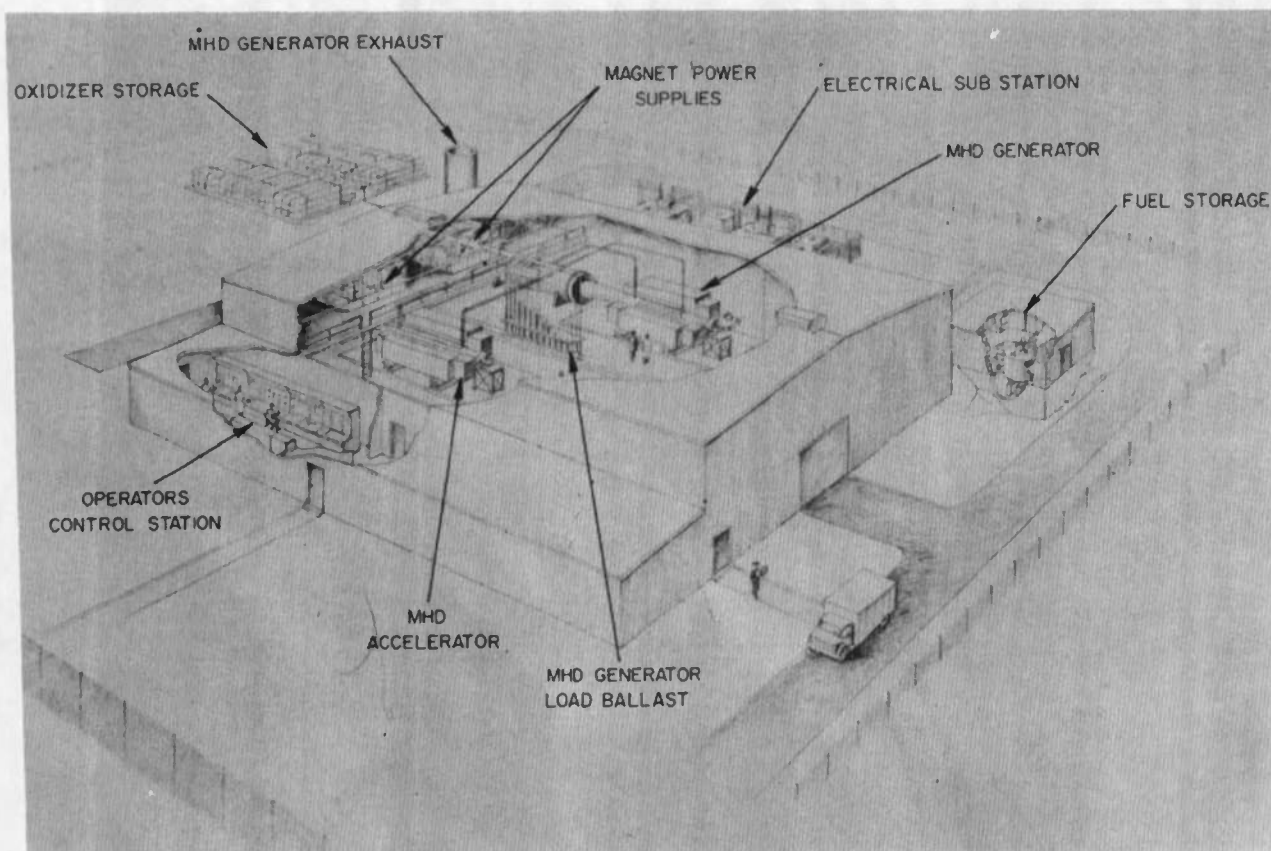


**Fig. 89    Sectional View of LORHO Pilot Facility Identifying Major Equipment Items**

Oxidizer (normally molar ratios of  $N_2/O_2 = 1$  to  $0.75$ ) storage consists of sixteen 300 cubic foot storage vessels which hold approximately 60,000 pounds of gas when fully charged to 2400 psig. This permits generator operating times of up to five minutes before depleting the storage to 1200 psig required for pressure drop and control allowances as well as keeping the burner back plate injectors sonic. The storage can be recharged overnight by means of valved tie lines to existing LOX and  $N_2$  facilities at the Center. Oxidizer flow to the generator is measured with a venturi type flow nozzle and is controlled automatically by an analog computer which receives signals of pressure, temperature and differential pressure and transmits a pneumatic signal to a regulating valve. This control will hold mass flow constant to within 1% as the storage pressure and temperature decrease during a test run.

Seeding of the generator was accomplished in a system independent of the main fuel so that rate variations and levels of generator loading may be controlled during operation. Seed is potassium hydroxide dissolved in water or alcohol. The solution is pressure fed into the fuel manifold of the burner by a Moyno screw type pump with a metal rotor running in a rubber stator. Control is accomplished with speed variation of the drive motor as well as fluid regulating valves. Flow schematics of the MHD generator fluid systems described above are shown in Figs. 90 and 91.

The generator output power is dissipated in water cooled resistance tubes manifolded to supply and return headers by electrically insulating hose connectors. The tubes are stainless steel, .010" wall, 20 feet in length and arranged vertically. Two sizes of tubes are used - 5/8" O. D. each capable of dissipating 900 kw and 3/8" O. D. capable of 250 kw each. There are a total of 32 - 5/8" dia. tubes (resistance per tube =  $.35\Omega$ ) and 17 - 3/8" dia. tubes ( $.6\Omega$  per tube) arranged in several groupings for series or parallel connection and equipped with sliding connectors so that virtually infinitely variable load resistances for up to 30 mw dissipation can be handled. Similar water cooled tubes, measuring 1/4" O. D. x .01 wall and having a resistance of .9 ohms each, are used as dropping resistors to effect an even distribution of current flow to and from the accelerator electrodes. A schematic diagram of the various arrangements of load and ballast resistors for the LORHO Pilot is shown in Fig. 92 .

Control during the operation of the MHD generator essentially consists of manipulating the seed and burner controls (igniter, pilot and main burner propellant valves). These remote operators controls are manual with the exception of the main oxidizer computer-regulator system. This allows for a maximum of flexibility in an experimental facility of this kind limited however by a series of interlocks which prevent an unsafe condition (during start-up, operation or shut down) due to equipment malfunction or operator error. A view of the operators control station is seen in Fig. 93. Visual monitoring of the operating equipment is done via closed circuit television. A key interlock system is provided whereby the master key to initiate a test cannot be removed from a key transfer block until 12 function keys are in place. These function keys must be removed from various remote auxiliary systems insuring that these are in a ready situation.

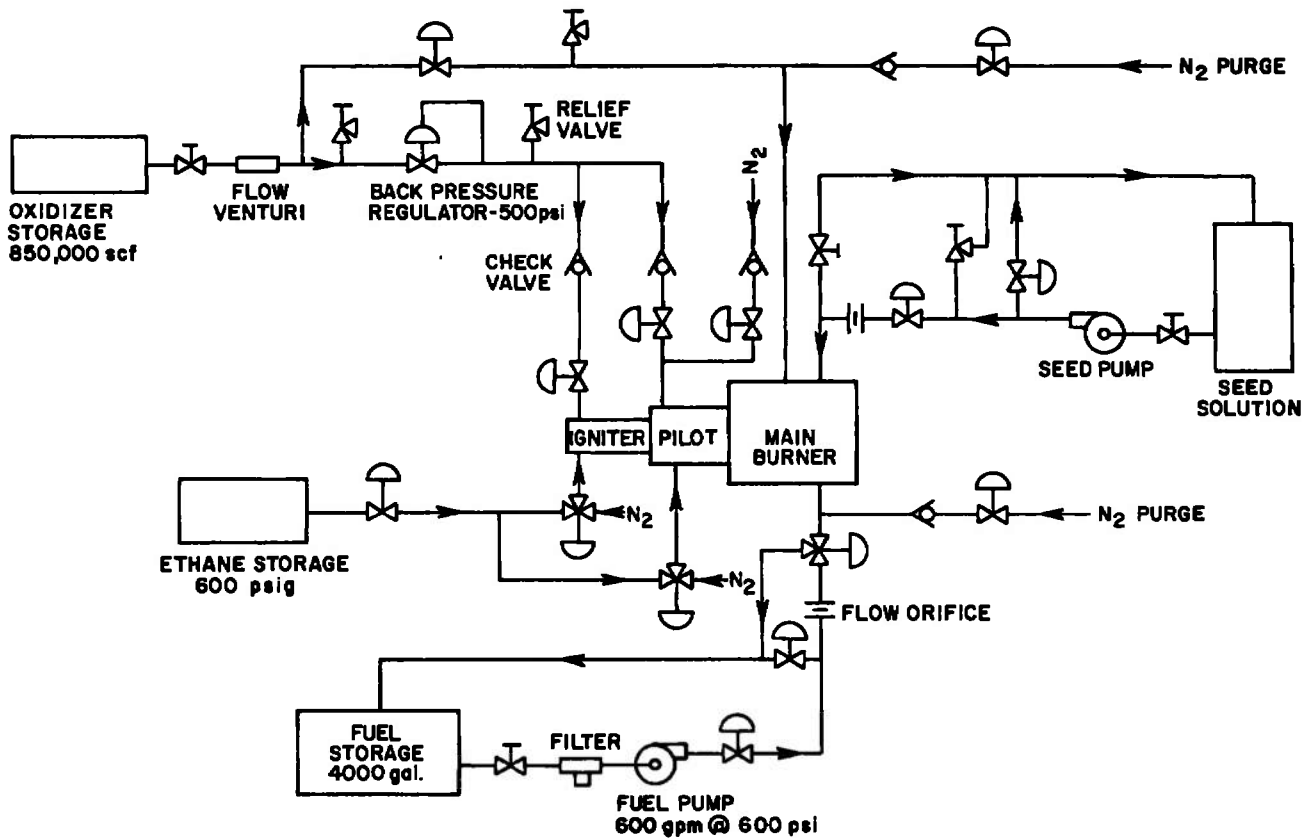


Fig. 90 Fluid System Schematic

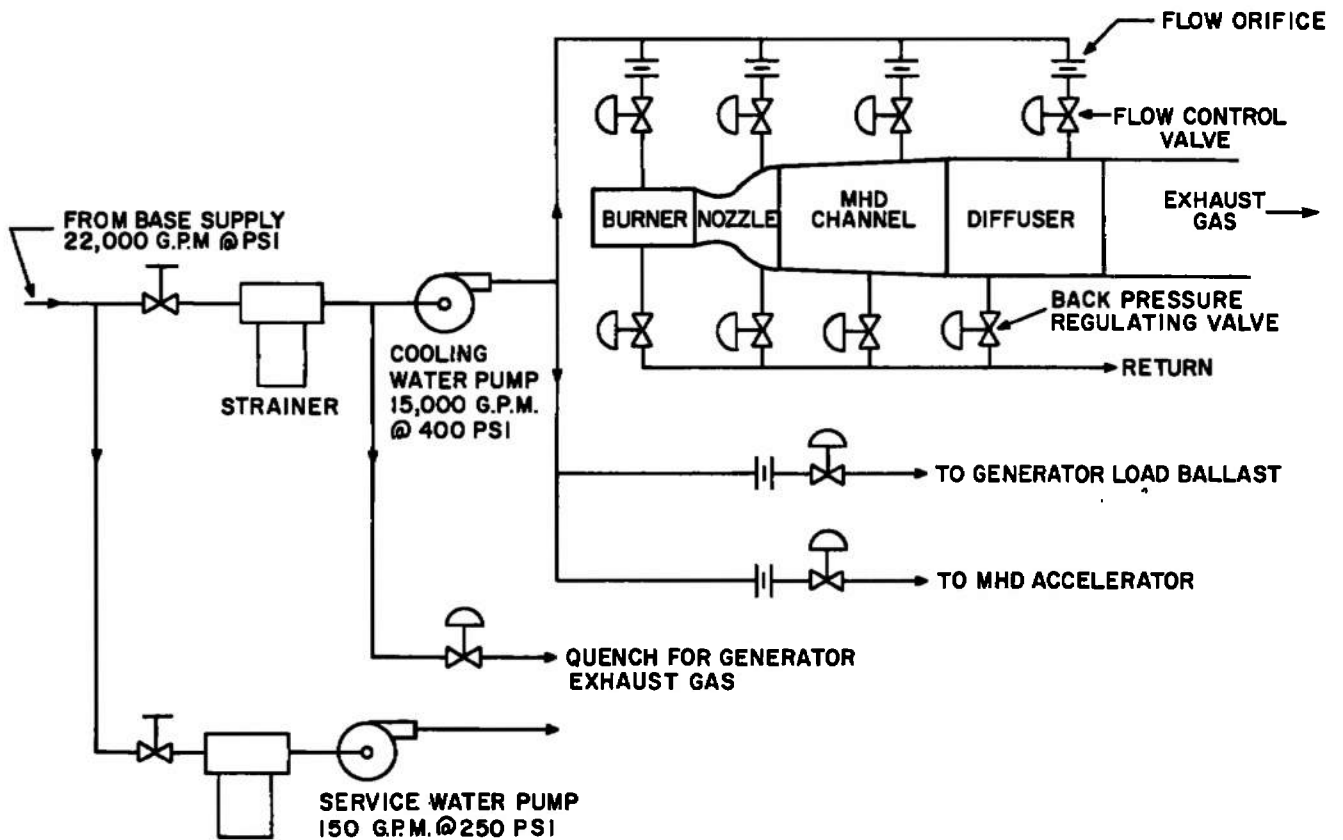
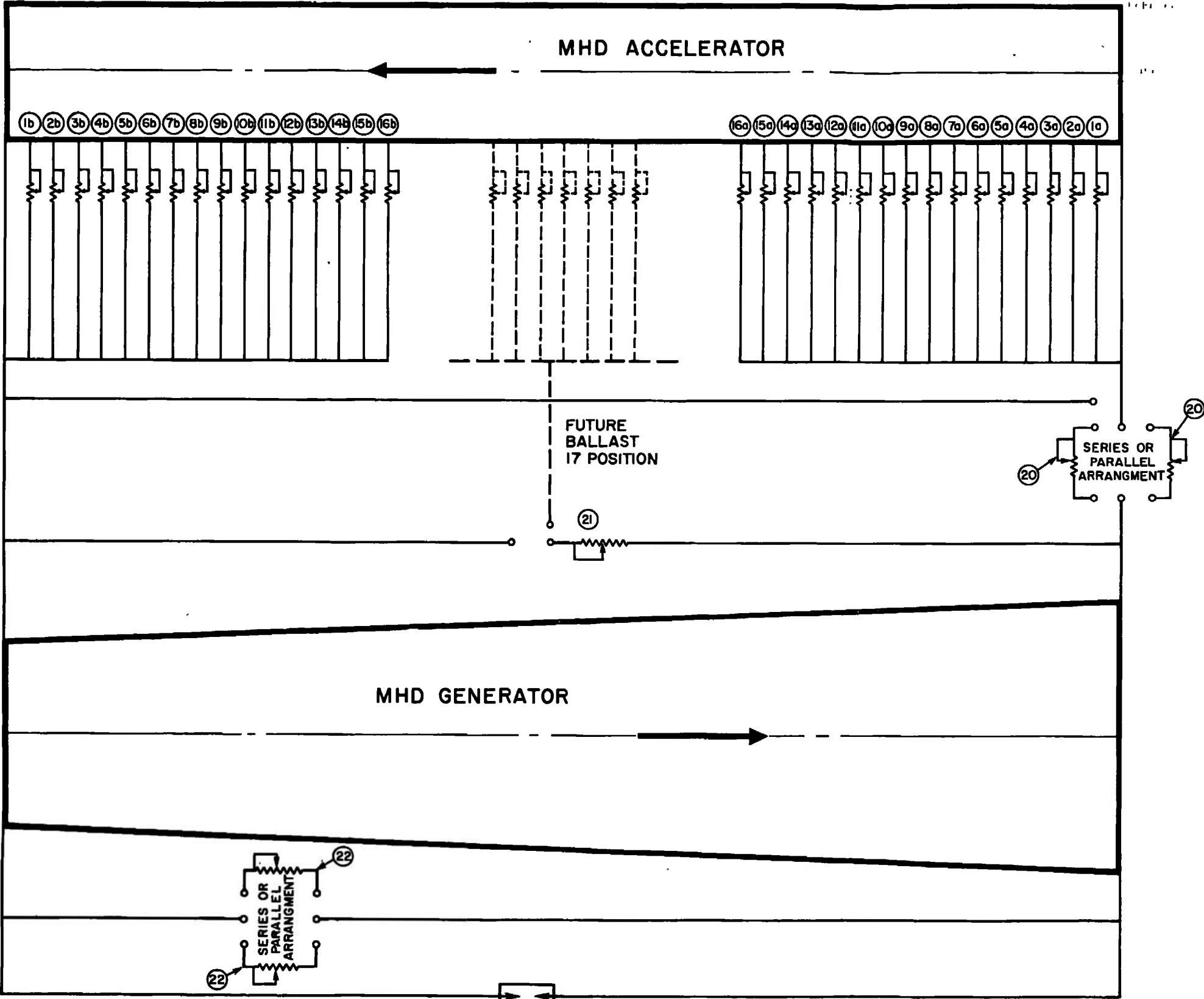


Fig. 91 Fluid System Schematic Continued



CIRCUIT NUMBER	DESIGN CURRENT Amps	DESIGN VOLTAGE DROP	TUBE SIZE OD x WALL	No of TUBES per SERIES CIRCUIT	RESISTANCE per TUBE
1 a	120	60	1/4" x .01	1	.9 Ω
2 a	120	120	1/4" x .01	1	.9 Ω
3 a	120	180	1/4" x .01	2	.9 Ω
4 a	120	240	1/4" x .01	2	.9 Ω
5 a	120	300	1/4" x .01	3	.9 Ω
6 a	120	360	1/4" x .01	4	.9 Ω
7 a	120	420	1/4" x .01	4	.9 Ω
8 a	120	480	1/4" x .01	5	.9 Ω
9 a	120	540	1/4" x .01	5	.9 Ω
10a	120	600	1/4" x .01	6	.9 Ω
11a	120	660	1/4" x .01	6	.9 Ω
12a	120	720	1/4" x .01	7	.9 Ω
13a	120	780	1/4" x .01	7	.9 Ω
14a	120	840	1/4" x .01	8	.9 Ω
15a	120	900	1/4" x .01	9	.9 Ω
16a	120	960	1/4" x .01	9	.9 Ω
1 b	250	100	1/4" x .01	1	.9 Ω
2 b	250	200	1/4" x .01	1	.9 Ω
3 b	250	300	1/4" x .01	2	.9 Ω
4 b	250	400	1/4" x .01	2	.9 Ω
5 b	250	500	1/4" x .01	2	.9 Ω
6 b	250	600	1/4" x .01	3	.9 Ω
7 b	250	700	1/4" x .01	3	.9 Ω
8 b	250	800	1/4" x .01	4	.9 Ω
9 b	250	900	1/4" x .01	4	.9 Ω
10b	250	1000	1/4" x .01	5	.9 Ω
11b	250	1100	1/4" x .01	5	.9 Ω
12b	250	1200	1/4" x .01	6	.9 Ω
13b	250	1300	1/4" x .01	6	.9 Ω
14b	250	1400	1/4" x .01	6	.9 Ω
15b	250	1500	1/4" x .01	7	.9 Ω
16b	250	1600	1/4" x .01	7	.9 Ω
20	1250	5000	5/8" x .01	12	.35 Ω
21	1250	8000	5/8" x .01	20	.35 Ω
22	500	5000	3/8" x .01	17	6 Ω

Fig. 92 MHD Generator Load and Ballast Arrangement

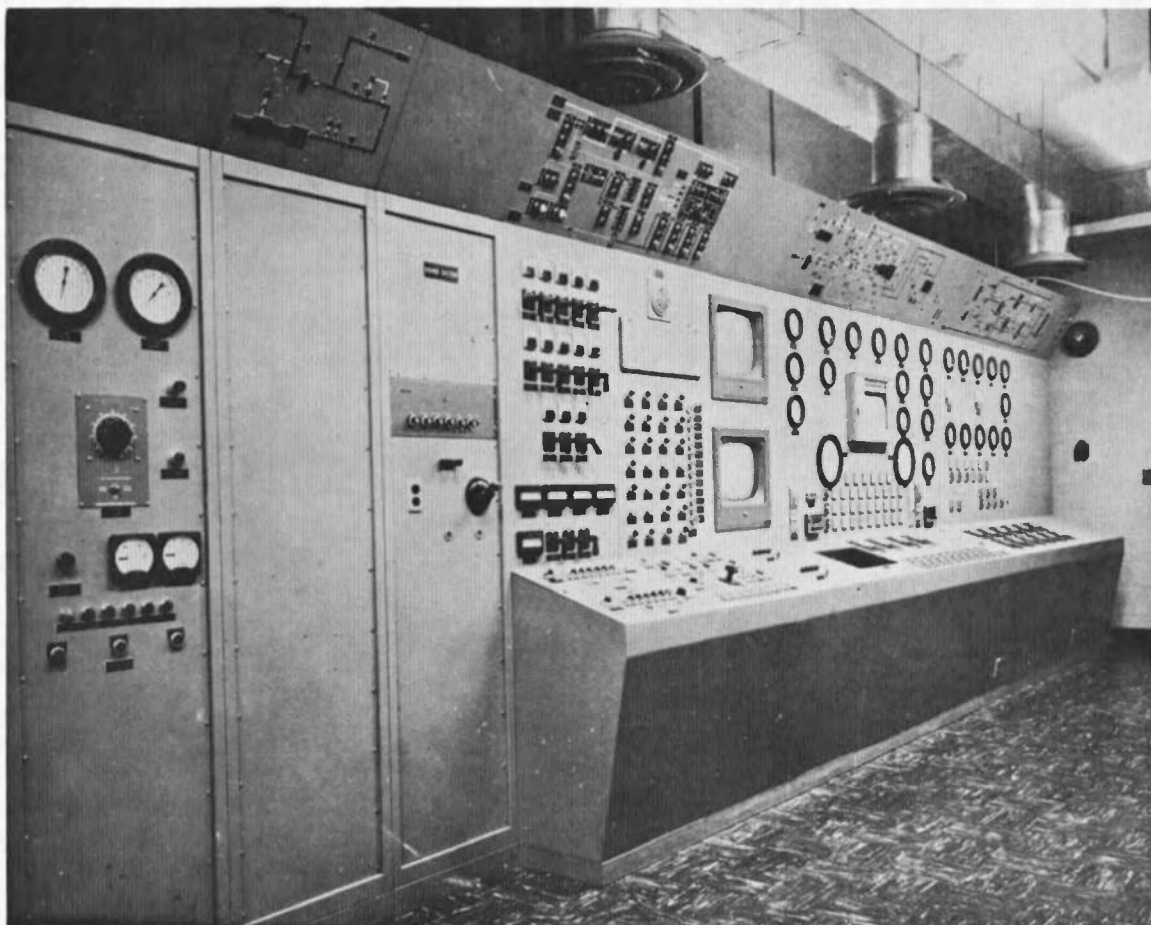


Fig. 93 LORHO Pilot Operators' Control Station

An additional control feature is provided with a multi-point flashing light type annunciator panel indicating what subsystem has faulted and where the fault is located.

Operators controls for the MHD accelerator consist mainly of presetting the channel cooling water control valves and the flow and pressure regulators for the air to the arc heater. Regulation of the powered seed injection to increase gas conductivity and effect load control is discussed in Section IV. A piping schematic of the air supply for the arc heater - MHD accelerator working fluid is shown in Fig. 94.



# AIR SUPPLY SCHEMATIC ARC HEATER - MHD ACCELERATOR

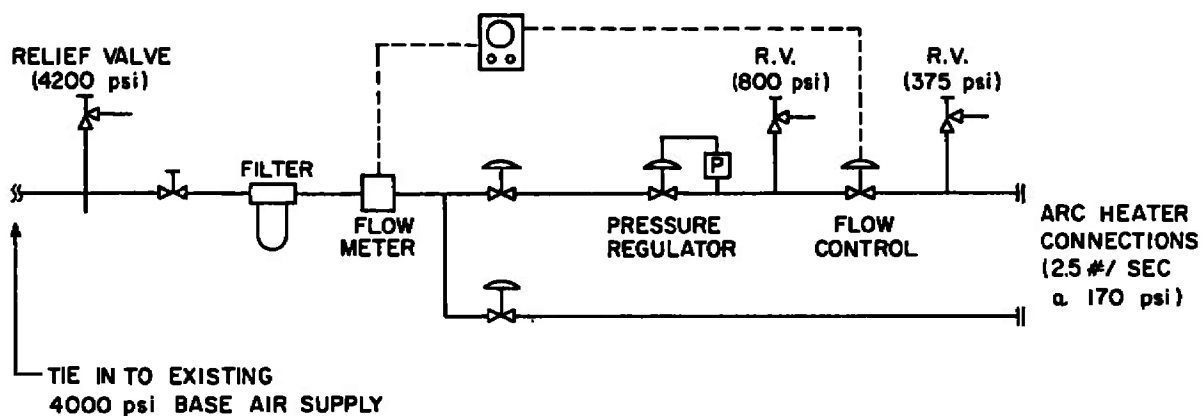


Fig. 94 MHD Accelerator Air Supply System

## APPENDIX I

## BOUNDARY LAYERS IN MHD GENERATORS

J. Teno, C. Liu and T.R. Brogan

## ABSTRACT

So that viscous losses will not be excessive, the length/diameter ratio in an MHD generator is typically limited to values less than ten. Thus, since the Reynolds number is high (of the order of  $10^6$ /meter) the turbulent flow in the MHD generator is not fully developed as in a long pipe, but closely resembles the classical boundary layer situation where the body of the flow is inviscid with the viscous effects confined to the immediate neighborhood of the walls. Thus, as in classical aerodynamics, analysis of the flow may, as an approximation, be divided into two parts, the inviscid core flow with MHD body force and energy transfer, and the boundary layers which may be treated as a flat plate with velocity gradients imposed both by the static pressure gradient and the MHD forces.

The paper presents a discussion of the boundary layers in MHD generators, and results of very approximate methods of boundary layer analysis. Primary emphasis is given to the aerodynamic aspects of the boundary layer flow, that is, boundary layer growth and separation in heavily loaded MHD generators, rather than to electrical effects such as dissipation and electrode drop, etc. It is seen that there is a fundamental difference between the boundary layer on the insulating wall, and that on the electrode wall. The latter is subjected to the retarding magnetic body force, the effect of which is similar to an adverse pressure gradient in the classical situation. It is seen that electrode wall boundary layer stability is a vital consideration in the design of heavily loaded generators. The manner in which the boundary layer influences the channel design and the diffuser performance is pointed out, and it is seen that boundary layer considerations are most critical for the linear impulse-type generator. In addition, boundary layer cross-flow in the Hall configuration may be important.

An adaptation of the Karman momentum integral method has been used to analyze the electrode wall boundary layer. The analysis neglects heat transfer and electrical dissipation in the boundary layer. The analysis is presented and the results correlated with performance of several MHD generators. Limitations of the method of analysis are discussed.

## 1. INTRODUCTION

In a heavily loaded MHD generator in which a significant fraction of the gas energy appears as electrical output, the non-dimensional interaction parameter  $s$  :

$$s = \frac{\sigma B^2 L}{\rho u^2} \quad \text{impulse mode}$$

or

$$s = \frac{\sigma B^2 L}{p} \quad \text{reaction mode}$$

will be at the order of unity, Here  $\sigma$  is the gas conductivity,  $B$  the magnetic field strength,  $L$  the channel length,  $\rho$  the density,  $p$  the pressure and  $u$  the fluid velocity. Such a generator will operate thru an appreciable pressure ratio, and successful operation is dependent on careful analysis of the aerodynamics in the generator.

In general, when one attempts to exceed the limiting performance (typified by maximum output) of an MHD generator, the generator will "stall" due to excessive magnetohydrodynamic body force. Stall is generally characterized by reduction of gas velocity and electrical output and increase in static pressure in the MHD channel. In an open cycle generator where the gas exhausts to the atmosphere, three different phenomena can be responsible for stall:

1. Channel exit mean total pressure inadequate for recovery to the atmosphere in the diffuser which follows the channel.
2. Choking of the inviscid core flow, particularly with supersonic operation.
3. Boundary layer separation in the MHD channel.

With a perfect diffuser, the channel exit mean total pressure (stagnation pressure) may be equal to atmosphere pressure. With a real subsonic diffuser, about eighty percent dynamic pressure recovery may be expected in the diffuser, while, for supersonic channel exit conditions, diffuser shock losses must be considered. In general, however, it is preferable that pressure recovery in the diffuser shall limit the maximum output achievable with an MHD generator rather than choking or boundary layer separation in the MHD channel, since, if this is the case, maximum output consistent with recovery to the atmosphere will have been achieved.

The form taken by inviscid flow choking stall depends on whether the flow is subsonic or supersonic and on the particular generator configuration. With subsonic generator flow, choking begins as the loading is increased when the generator exit becomes sonic. In this case, stall is rather gradual and not too well defined. With supersonic flow, choking

is usually accompanied by shock waves in the channel, and abrupt deterioration of generator output. The stall is particularly abrupt with a Hall or diagonally connected configuration since the transverse current can rise to very high values behind the shock wave with further increase in magnetic body force. This will often cause the shock to move all the way to the channel inlet with consequent subsonic or separated supersonic flow throughout the channel, both totally uninteresting for practical operation. Under these conditions, generator output may drop to a fraction of the maximum value just before stall.

Techniques for predicting the inviscid core flow for conditions more or less uniform in the generator channel cross section are well developed, and, with proper design, in a generator operating in the near reaction mode, where boundary layer separation is not important, the inviscid core flow can be predicted and the channel discharge conditions matched to diffuser capability.

The situation is somewhat more complex when stability of the aerodynamic boundary layer and prevention of boundary layer separation are important considerations for the design of the MHD channel. The outward effect of channel boundary layer separation is identical to that of a choking stall and causes shock waves in the channel which may propagate all the way to the channel inlet with drastic reduction of output.

Boundary layer separation can occur in situations where the flow is decelerated in the absence of adequate favorable static pressure gradient, or, in other words, for a generator operating in the impulse mode. The phenomenon is very important because if it is not accounted for, separation can occur before stall due to choking or low total pressure at the diffuser inlet.

This paper presents a discussion of the boundary layer in heavily loaded MHD generators with emphasis on prevention of boundary layer separation. The paper is primarily concerned with the aerodynamic aspects of the boundary layer flow rather than with electrical effects such as electrical dissipation shorting and electrode drop.

## 2. THE ELECTRODE-WALL BOUNDARY LAYER

Due to the relatively low value of  $L/D$  which can be tolerated without excessive viscous losses, and the high Reynolds number (typically of the order of  $10^6$ /meter), the flow in the generator is not fully developed as in a long pipe, but closely resembles a boundary-layer type situation where the body of the flow is inviscid with the viscous effects confined to the immediate neighborhood of the walls. Thus, as in classical aerodynamics, analysis of the flow may be divided into two parts; the inviscid core flow with MHD body force and energy transfer, and the boundary layers which may be treated as a flat plate with velocity gradients imposed both by the static pressure gradient and the MHD forces.

In an ordinary boundary layer analysis, velocity gradients arise due to the presence of curved surfaces or to shock waves which lead to pressure discontinuities. In the case of a high-speed compressible flow, the flow is generally at least streamwise isentropic except in the immediate neighborhood of shock waves or other discontinuities, so that there are unique relationships between the pressure distribution and the velocity gradient at the edge of the boundary layer. In an MHD flow with body forces, however, a careful distinction between electrode and insulating walls is necessary. For the electrode boundary layer, the current flows across the boundary layer normal to the flow so that the velocity gradient, computed from the equations of motion, must be used in the boundary layer calculation. However, in the case of the insulating wall, the magnitude of the apparent velocity gradient depends on wall temperature. If the wall temperature is below that of the stream so that the gas near the wall in the region of high shear is a poor conductor of electricity, the body force on the insulating wall boundary layer will be small and the effective velocity gradient is favorable in the presence of any favorable static pressure gradient. Thus, the insulating wall boundary layer can be very stable while, at the same time, the electrode boundary layer is experiencing an adverse gradient and may be near separation. Since separation at any location must be prevented, investigation of the electrode boundary layer only is required.

In the case of operation in the pure reaction mode, the velocity gradient is zero as the  $\mathbf{j} \times \mathbf{B}$  forces are precisely balanced by the static pressure gradient. The electrode wall boundary layer is effectively that of a flat plate with a change of scale normal to the wall as the pressure falls. The insulating wall boundary layer is in a highly favorable pressure gradient. Because of this, the boundary layer is generally not a problem in generators operating in, or near, the reaction mode, and must be considered only in order to correct the channel area for boundary-layer thickness.

It should be mentioned here that absence of the electrode wall in the disc configuration is an important advantage for that geometry in that it can be operated much more in the impulse mode than can a linear generator of any configuration. This is particularly useful because the disc generator desirably operates with very small static pressure gradient.

Another consideration which may be of importance is boundary layer cross flow. In channels with an appreciable axial current flow such as the Hall, single electrode Faraday or mixed or off design diagonal, there is a transverse body force on the fluid so that one electrode wall is at a higher pressure than the other. As the boundary layer gas is deficient in momentum, it will tend to flow along the insulating wall on to the low pressure electrode wall, thickening the boundary layer on that wall. The situation is not unlike the flow in a curved pipe. This cross flow has not been analyzed in this paper. It seems likely that the favorable axial pressure gradient on the insulating wall will reduce the importance of the cross flow by accelerating the boundary layer on the insulating wall.

### 3. APPROXIMATE ANALYSIS OF THE BOUNDARY LAYER FLOW

#### A. General Remarks

In the usual boundary layer analysis, it is assumed that the flow quantities,  $u_1$ ,  $\rho_1$ ,  $p_1$  in the free stream or inviscid core are given and these are used to determine the boundary layer flow. This can be called the "design" case for the MHD channel when an electrical parameter such as the total axial current flow in a Hall or diagonal generator, or transverse voltage of a Faraday channel, the magnetic field distribution, and the variation of one thermodynamic parameter is specified and the loft of the channel is to be calculated. The thermodynamic parameter could, for instance, be the values of temperature or static pressure or their gradients or the ratio of static pressure gradient to body force (degree of reaction), or any number of others. In addition, the inlet conditions and mass flow are given. Analysis of one dimensional core flow is then a simple initial value problem for the inviscid channel cross section as a function of length along the channel. Let us assume that this cross section is rectangular with distance  $D_{ie}$  between the electrode walls, and  $D_{ii}$  between insulating walls, where  $D_{ie}$  and  $D_{ii}$  are functions of distance  $x$  along the channel. The law of conservation of mass states that:

$$\rho_1 u_1 D_{ie} D_{ii} = \dot{m} \quad (46)$$

where  $\dot{m}$  is the mass flow.

The boundary layer flow may now be analyzed. Assuming that separation does not occur in the channel at "design" (for such a design would be uninteresting) the four quantities  $\delta_i^*$ ,  $\delta_e^*$ ,  $\theta_i$  and  $\theta_e$  are calculated from the boundary layer analysis. Here  $\delta^*$  and  $\theta$  are the boundary layer displacement and momentum thickness respectively, and the subscripts  $i$  and  $e$  refer to insulating and electrode walls. The displacement thickness is given by:

$$\delta^* = \int_{y=0}^{\infty} \left(1 - \frac{\rho u}{\rho_1 u_1}\right) dy \quad (47)$$

where  $y$  is the coordinate normal to the wall, and  $\rho$  and  $u$  are the density and velocity at any distance from the wall. The displacement thickness is the distance for which the stream mass flow corresponds to the mass flow defect in the boundary layer. The momentum thickness is the distance for which the stream momentum corresponds to the momentum defect in the boundary layer:

$$\theta = \int_{y=0}^{\infty} \frac{\rho u}{\rho_1 u_1} \left(1 - \frac{\rho u}{\rho_1 u_1}\right) dy \quad (48)$$

The ratio  $\delta^*/\theta$  is an important parameter in the boundary layer analysis. It is called the shape factor and is denoted by  $H$ . The channel loft can now be specified. The cross section should be  $(D_{ie} + \delta_e^*)$  by  $(D_{ii} + \delta_i^*)$ . Let:

$$D_{ie} + \delta_e^* = D_e$$

and

$$D_{ii} + \delta_i^* = D_i \quad (49)$$

The effective dynamic pressure,  $p_D$ , at any station is given by:

$$p_D = \rho_1 u_1^2 \frac{D_{ie} D_{ii}}{(D_{ie} + \theta_e)(D_{ii} + \theta_i)} \quad (50)$$

The effective dynamic pressure should be utilized for evaluation of the diffuser performance, i.e., the effective inlet Mach number is less than the core Mach number so that the diffuser pressure recovery will be less than if calculated using the core Mach number. For the design case, the calculations at the core flow and boundary layer can be carried out in series, although simultaneous calculation is convenient if a computer is being employed.

In the "off design" case, the channel configuration and inlet conditions are given and an electrical parameter is specified. The problem then is to calculate the flow and boundary layer simultaneously subject to Eq. (49) and conservation of mass. These solutions require a little more computing than do the "design" solutions, but offer nothing new fundamentally. Therefore, in what follows, it will be assumed that the flow quantities in the inviscid core are given for the boundary layer analysis. It should be noted, however, that the necessity to satisfy Eq. (49) for the closed MHD channel means that, in the off design case, there can be important feedback from the boundary layer analysis to the core flow analysis.

#### B. Analysis of the Electrode Wall Boundary Layer

It is necessary to note here that the analysis to be presented is approximate, semi-empirical and contains many assumptions which have not been verified for general cases. It should be received in that context, and improvements by those specializing in analysis of boundary layer flow are invited. The analysis is used to develop an indication rather than an absolute determination of boundary layer stability.

The flow in an MHD generator of interesting size is turbulent, with Reynolds numbers of the order of  $1 - 5 \times 10^6$ /meter. The flow is compressible, generally supersonic, with the wall enthalpy substantially below that of the gas, even on the electrode wall. Aerodynamically, the channel walls are very rough, that is to say, the typical roughness dimension can be

large compared to the thickness of the laminar sublayer on an aerodynamically smooth wall at the same Reynolds number. On a segmented electrode wall, the wall surface temperature varies in cyclic fashion along the channel with a frequency equal to the electrode pitch. On the electrode wall, also, the transverse current flows through the boundary layer normal to the wall and produces drag on the boundary layer and influences the turbulence. Moreover, at appreciable Hall parameter the current concentrates as it approaches the electrode so that the body force is highly nonuniform throughout the boundary layer. The fact that the flow is turbulent is itself sufficient to render impossible a complete analytical solution of the problem. Lest the additional complications tempt one to despair, it should be noted that the situation is not all that much worse than on an airplane wing or turbine blade and these devices can be analyzed so as to give satisfactory performance. One reason for this is that, in spite of extreme approximations which follow, the boundary layer equation for the u-component of velocity

$$\rho u \frac{\partial u}{\partial x} + \rho v \frac{\partial u}{\partial y} + \frac{\partial p}{\partial x} = -jB + \frac{\partial}{\partial y} \left( \mu \frac{\partial u}{\partial y} \right) \quad (51)$$

where  $j$  is the normal component of the current (the value of  $j$  is taken positive, hence the negative sign in Eq. (51) can be integrated exactly for a boundary layer type flow.<sup>(25)</sup> The integration utilizes the continuity equation to eliminate  $v$ , and the solution for the core flow, together with the fact that  $\partial p / \partial y \approx 0$  to get (for a compressible flow with MHD forces):

$$\frac{d\theta}{dx} + (H + 2) \frac{\theta}{u_1} \frac{du_1}{dx} + \frac{\theta}{\rho_1} \frac{d\rho_1}{dx} = \frac{C_f}{2} + \int_0^\infty \frac{J_1 - J}{\rho_1 u_1^2} B dy \quad (52)$$

where  $C_f = \frac{\tau_w}{(1/2)\rho_1 u_1^2}$ , and  $\tau_w$  is the shear at the wall. The last term on

the right is the only addition to the standard "boundary layer momentum integral equation." In this term,  $J_1$  is the core mean transverse current density and  $J$  the local current density, which is different than the core density due to concentration at the electrode edges. However, integration of the last term in the  $x$ -direction over a distance equal to the electrode pitch will give zero since the average current to the electrode is equal to  $J_1$ . Thus:

$$\frac{d\theta}{dx} + (H + 2) \frac{\theta}{u_1} \frac{du_1}{dx} + \frac{\theta}{\rho_1} \frac{d\rho_1}{dx} = \frac{C_f}{2} \quad (53)$$

It should be noted here that while the last term in Eq. (52) is zero on the average, the experimental data indicates a value of  $C_f$  larger than would be expected even for a rough wall, and this may, in part, be due to the fact that the current concentration at electrode edges has the effect of producing



rib like obstructions normal to the flow at regular intervals, a form of roughness leading to large values of  $C_f$ . Equation (53) is a first order, nonlinear, total differential equation for  $\theta = \theta(x)$ . It contains  $H = \delta^*/\theta$  so that  $H$  must be found, as well as  $C_f$  which, in general, will be a function of  $\theta$ ,  $H$  and the Reynolds number.

To complete the analysis of the boundary layer, a solution for  $H$  (or  $\delta^*$ ) as a function of  $x$  must be found. As there is no analytical method for accomplishing this, even for incompressible turbulent flow, semi-empirical auxiliary relations, usually derived from data correlations, must be utilized. A variety of assumptions are possible, and there are over fifty separate formulations in the literature for completing the method for incompressible flow. Critical surveys of various schemes have been given (26, 27, 28). There are no really useful methods for determination of  $H$  for the turbulent compressible boundary layer with heat transfer and roughness, and nothing at all for the case with MHD body forces. Thus, as described from this point, the analysis contains many assumptions which have not been verified and for which the only justification is a certain utility in situations which have been encountered in practice.

In view of the fact that not even semi-empirical correlation equations are available for the situation of interest, the following procedure has been adopted:

1. Utilize an existing correlation equation for incompressible flow to calculate  $\bar{H}$ , where  $\bar{H} = \bar{\delta}^*/\theta$ , and  $\bar{\delta}^*$  is a fictitious "equivalent incompressible displacement thickness" which is not equal to the value of  $\delta^*$  defined by Eq. (47) for the compressible flow with heat transfer.

2. Use the generally accepted separation value of  $\bar{H}$  for the correlation equation employed as the separation criteria for the present case.

3. In the boundary layer momentum integral equation (Eq. (53)) use a value of  $H$  given by  $H = \delta^*/\theta$  where  $\delta^*$  is the value given by Eq. (47) for the compressible flow.  $H = H(\bar{H}, M_1, h_w/h_1, r, n)$ , where  $h_w$  and  $h_1$  are the core and wall enthalpy respectively,  $M_1$  the core Mach number,  $r$  an equivalent specific heat ratio, and  $n$  a boundary layer similarity parameter to be discussed. This is justified since  $\delta^*$  defined by Eq. (47) is the appropriate one to use with Eq. (53). In fact, since  $H$  appears only as  $(H + 2)$  the precise choice of  $H$  in Eq. (53) is probably not extremely critical.

4. Use  $\delta^*$  from Eq. (47)  $\delta^* = H \theta$  to determine the channel loft.

The definition of  $\bar{\delta}^*$  is:

$$\bar{\delta}^* = \int_0^{\infty} \left(1 - \frac{u}{u_1}\right) dy \quad (54)$$

and that of  $\bar{H}$  is:

$$\bar{H} = \frac{\int_0^{\infty} (1 - \frac{u}{u_1}) dy}{\int_0^{\infty} \frac{u}{u_1} (1 - \frac{u}{u_1}) dy} \quad (55)$$

In order to obtain an equivalence between  $H$  and  $\bar{H}$ , a relation between velocity and density, and a boundary layer profile is required. For the latter it is usual to assume that

$$\frac{u}{u_1} = (\frac{y}{\delta})^{1/n} \quad (56)$$

where  $\delta$  is a characteristic length and  $n$  is a similarity parameter and it is assumed that one such parameter defines the profile. The value  $n = 7$  corresponds to a turbulent flat plate without pressure gradient in incompressible flow. Lower values of  $n$  correspond to increasing dead water in the boundary layer, and hence higher values of  $H$  (or  $\bar{H}$ ). With this assumption,  $\bar{H}$  can be found from Eq. (55) as a function of  $n$ . In order to evaluate the equivalent  $H$ , the usual relation between velocity and enthalpy for a Prandtl number of unity and also strictly for no pressure gradient is assumed:

$$\frac{h + \frac{u^2}{2} - h_w}{h_1 + \frac{u_1^2}{2} - h_w} = \frac{u}{u_1} \quad (57)$$

The above equation does not apply where there is heat generation in the boundary layer as for instance due to  $j^2/\sigma$  electrical dissipation. If the total electrical dissipation gets to be of the order of the electrode wall heat transfer rate, serious deviations from Eq. (57) may be expected. This will occur at high current densities and/or relatively low electrode temperature, and can occur in practical situations. This is a serious shortcoming of the analysis, which can only be removed by detailed inclusion of the energy equation in the analysis. In view of the already highly approximate nature of the analysis, it has not seemed worthwhile to go to this extent until greater experience with the present method has been accumulated.

Equations (56) and (57) can be used together with  $\rho = \rho(h)$  with constant pressure normal to the wall in Eqs. (47) and (48) to evaluate  $\delta^*$ ,  $\theta$ , and

H for the compressible flow. The result of  $H = H(m, n, h_w/h_1, \gamma)$  are shown in Fig. 95 for  $\gamma = 1.12$ , roughly appropriate for combustion gases, and  $h_w/h_1 = 0.5$ , a mean value for highly segmented zirconia electrodes held in a metal U-shaped retainer.

The shape factor correlation equation of Garner (29) has been chosen for the calculation of  $\bar{H}$ . The choice is somewhat arbitrary, and was arrived at mainly because of ease of computation and relatively good agreement with experiment (in the sense of predicting the onset of separation) in a variety of circumstances. The method due to Head (30), might have been a better choice, but is less adaptable for high speed computation. Garner's equation is:

$$\left(\frac{\rho_1 u_1 \theta}{\mu_1}\right)^{1/6} \theta \frac{d\bar{H}}{dx} = \epsilon^{5(\bar{H} - 1.4)} \left[ -\left(\frac{\rho_1 u_1 \theta}{\mu_1}\right)^{1/6} \frac{\theta}{u_1} \frac{du_1}{dx} - 0.0135 (\bar{H} - 1.4) \right] \quad (58)$$

The value of  $\theta$  is that computed from Eq. (53). The choice of  $\mu = \mu_1$ , where  $\mu$  is the viscosity, as the appropriate value of viscosity for the Reynolds number based on momentum thickness is also somewhat arbitrary.

To begin the calculation, at the channel inlet, a value of  $\bar{H} = 1.25$  is assumed. This value is slightly below the flat plate value, but is justified by the favorable gradient through which the flow has passed during the expansion to channel inlet velocity. This yields an equivalent inlet  $H$  dependent on the inlet Mach number. Inlet values of  $\theta$  and Reynolds number appropriate to the expansion nozzle are chosen.

The choice of the friction coefficient,  $C_f$ , to use in Eq. (53) has presented some difficulty. Aerodynamically, the electrode walls on generators built to date are in the so called "completely rough" regime, where the Reynolds number based on mean protrusion height and "turbulence velocity" (31) is greater than 70. For the incompressible turbulent flow without pressure gradient, the expression for the local coefficient of skin friction in the completely rough regime is given by:

$$C_f = (2.87 + 1.58 \log_{10} \frac{x}{k_s})^{-2.5} \quad (59)$$

where  $x$  is the distance from the leading edge of the plate and  $k_s$  is the "equivalent sand roughness" of the protrusion. In a segmented electrode channel, the form of the roughness consists of ordered ribs normal to the flow at a pitch equal to the electrode spacing. As reported by Schlichting (31) such a form of protrusion leads to unusually high values of equivalent sand

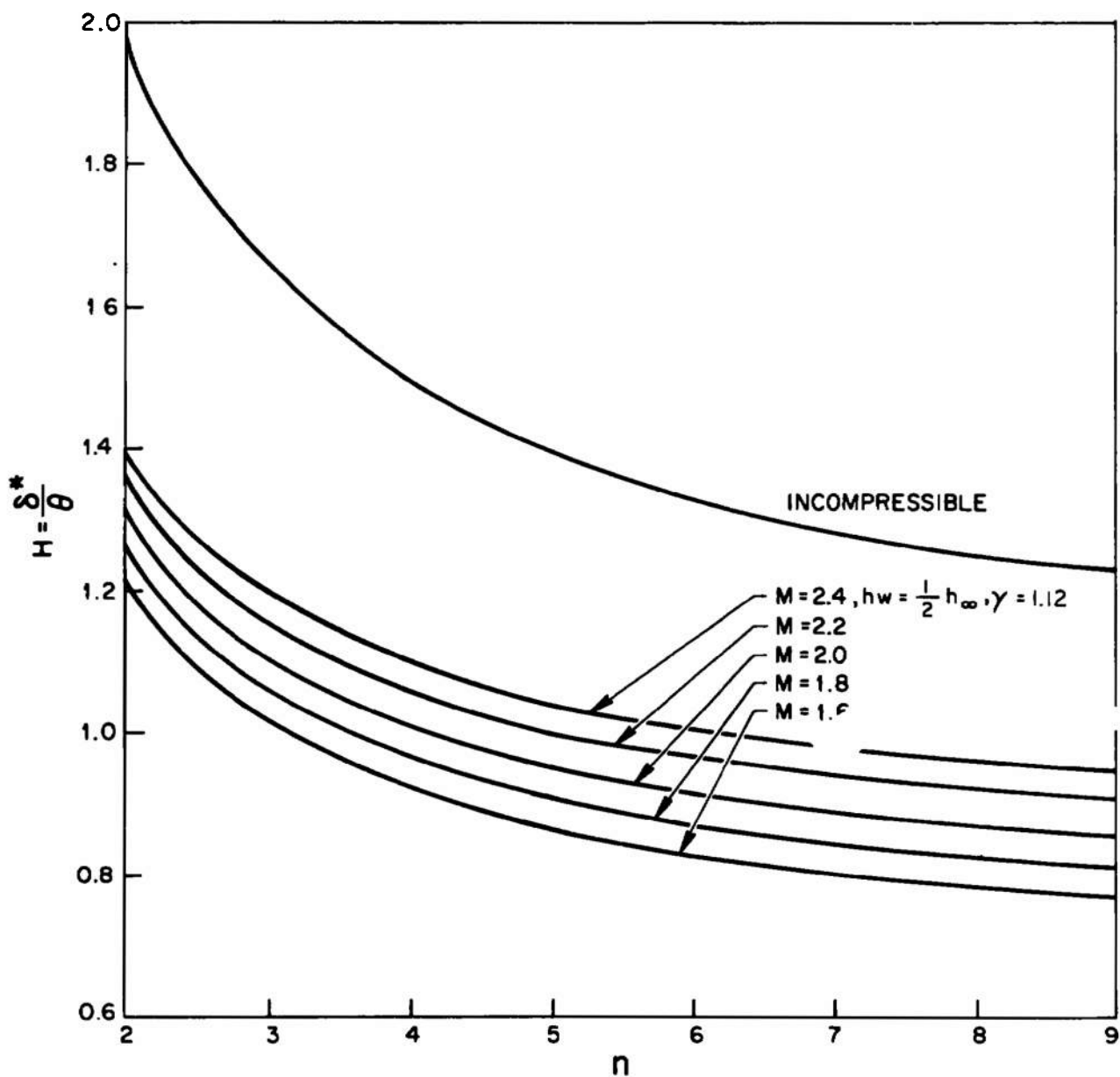


Fig. 95

Boundary Layer Shape Factor as a Function of Mach Number  $M$  and Velocity Profile Parameter  $n$  for  $hw/hi = 0.5$ , and  $r = 1.12$

roughness and greatly increased friction coefficients. Moreover, the effect of the rib like geometrical protrusion must somehow be augmented by the current concentration at the electrode which occurs in the same location as the rib. In the case of pressure gradient, the skin friction relationship must be modified since the wall shear is a function of  $n$  and hence of  $H$ , as, for instance, following Ref. 32. There seems to be no real basis for a proper choice of  $C_f$  for the present situation. Experience with Mark II<sup>(33)</sup> and the LORHO Pilot generator described here seems to best correlate with a choice of  $C_f$  three times the value given by Eq. (59). These generators have similar current densities, electrode configurations and operating conditions. Whether this is a real friction coefficient, or a product of neglect of such things as boundary layer heating has not been determined. Nevertheless, the high apparent value of  $C_f$  indicates that it would be profitable to devise methods to reduce wall roughness; these methods would need to be compatible with acceptable electrode performance and endurance.

With the above choice of  $C_f$ , all the quantities for solution of Eqs. (53) and (58) are available, and the solution may proceed. We now proceed to discuss the solutions for various generators, which are distinguished by their values of  $du/dx$ . In the reaction or constant velocity generators, the velocity gradient is zero so that  $\bar{H}$  remains relatively constant and there is little possibility of boundary layer separation in a constant velocity generator. When some impulse is employed  $du/dx < 0$  so that  $\bar{H}$  increases with distance from the channel inlet, and increases rapidly once  $\bar{H}$  exceeds 1.4 to any degree. For incompressible flow, a value of  $\bar{H} = 1.8$  is generally taken as the point of separation. It is recommended that the design, by the method described, should indicate maximum values of  $\bar{H}$  less than about 1.5 due to the assumptions in the analysis.

#### 4. COMPARISON WITH EXPERIMENT

Some conclusions regarding the extent to which the previous analysis correlates with performance can be made based on experience with a number of actual installations. The general experience is that:

a. Electrode wall boundary layer separation will not be a consideration for generators operating in the reaction mode. Both channels of the Mark V self-excited generator<sup>(34, 35)</sup> were designed to operate at nearly constant velocity, and, although actual optimum performance with the first channel was achieved with slight flow deceleration in the power output section of the channel, no boundary layer separation was achieved with either channel.

b. The boundary layer will not be the dominant factor in the design if the design channel exit velocity is greater than 85% of the inlet velocity, and a modest favorable pressure gradient can be provided.

c. If the exit velocity is less than 85% of the inlet velocity, care must be exercised to prevent separation. It appears that the maximum

deceleration which can be achieved is to about 78% of the channel inlet velocity regardless of how much favorable gradient is provided. This correlates closely with experience for non-MHD type flow in unfavorable pressure gradients.

An example of a boundary layer type stall is shown in Figs. 96 and 97. The data are taken from Ref. 33, but have not been previously displayed. For the run, the load resistance on the Hall configuration channel was maintained at a constant value ( $20\Omega$ ) as the seed was increased from zero until the generator stalled. Figure 96 shows the measured pressure distribution for the no load (no seed, isentropic expansion), full load just before stall and after stall. Figure 97 shows the voltage, current and power output as a function of time. Immediately prior to stall, there is actually a slight adverse static pressure gradient in the channel, while after stall has occurred, the channel pressure rises to high values and the output is markedly reduced. The stall is definitely of the boundary layer separation type since the diffuser pressure recovery capability at the channel exit immediately prior to stall is well above one atmosphere. It should be noted here that higher output prior to stall could be (and was) achieved by simply decreasing the load resistance so as to operate at a higher value of the loading coefficient.

In Fig. 98, the calculated value of the shape factor  $\bar{H}$  and the calculated velocity are plotted as a function of distance along the channel for the run described in Figs. 96 and 97 for the situation just before stall. The indicated value of  $\bar{H}$  at the channel exit is 1.66, but more importantly, the value of  $d\bar{H}/dx$  is very high, as one would expect from Eq. (58) for those values of  $\bar{H}$  typical of a near fully loaded situation. This is the reason why it is recommended that a calculated value of  $\bar{H} = 1.5$  should be considered the maximum safe value.

In the design calculations for the LORHO Pilot generator the value of  $C_f$  was underestimated due to the limited experience at the time the generator was designed. As a result, boundary layer growth was more rapid than had been calculated, and this tended to "pinch off" the inviscid core and decelerate the flow still further. As a result, boundary layer type stall was experienced with the original channel configuration of a power output of about 80% of the design value (20,000 kilowatts). The channel has since been modified to allow for greater boundary layer growth, and no further difficulties of this type have been encountered.

#### ACKNOWLEDGMENT

The authors would like to express their gratitude to Mr. R. T. Jones who provided many helpful suggestions during the progress of the work described here.

## AXIAL PRESSURE DISTRIBUTION

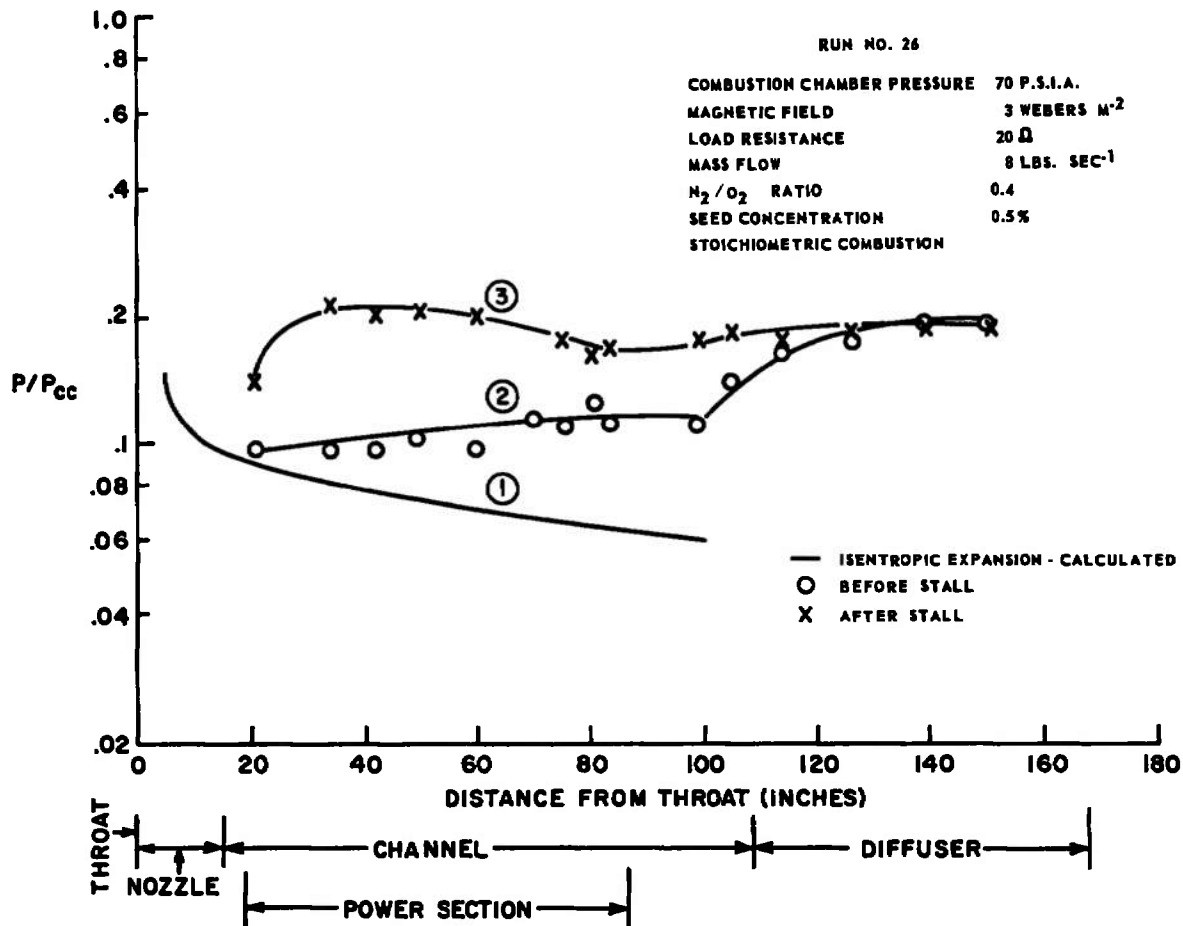


Fig. 96 Channel Static Pressure Distribution

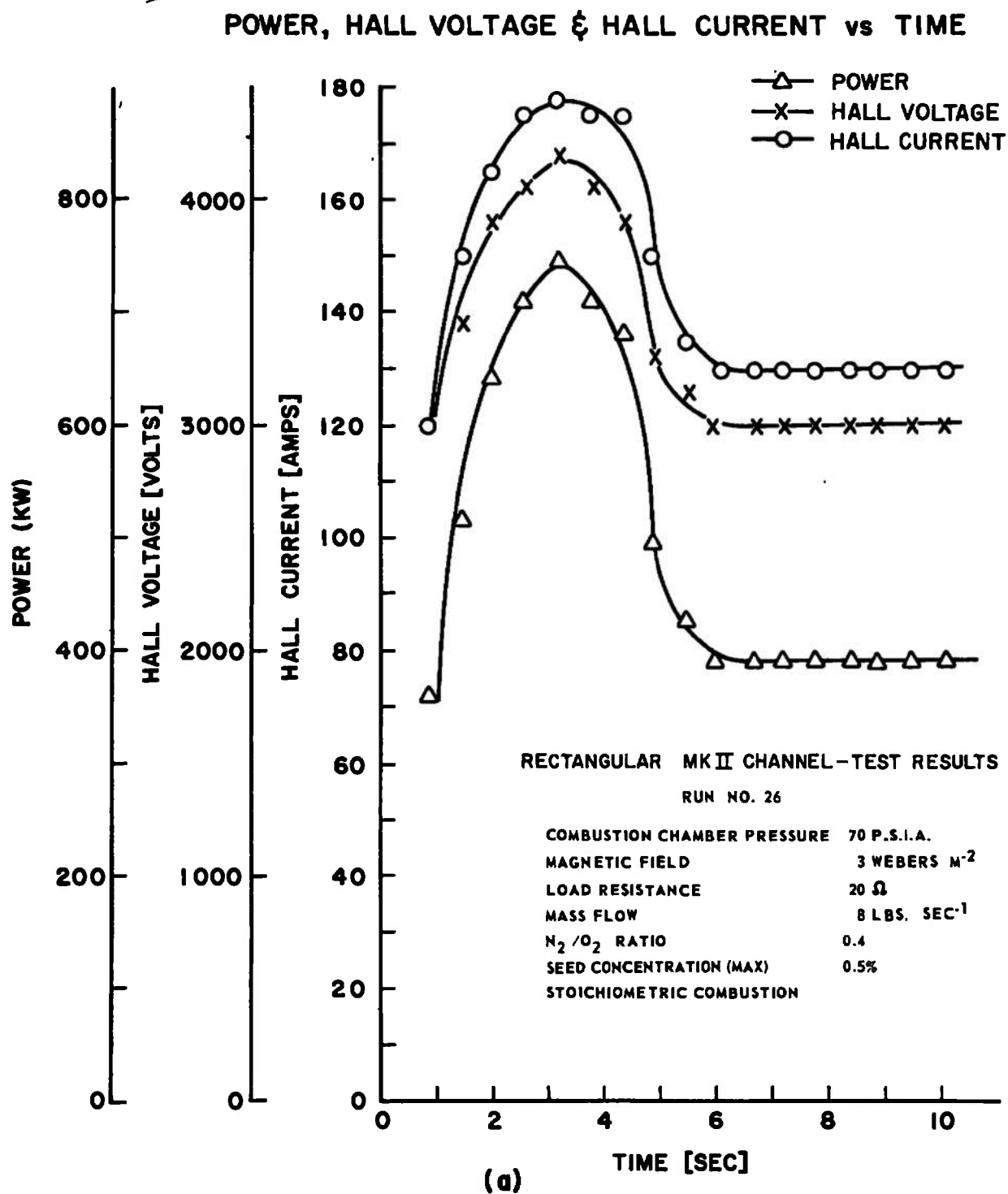


Fig. 97

Voltage, Current and Power Output as a Function of Time



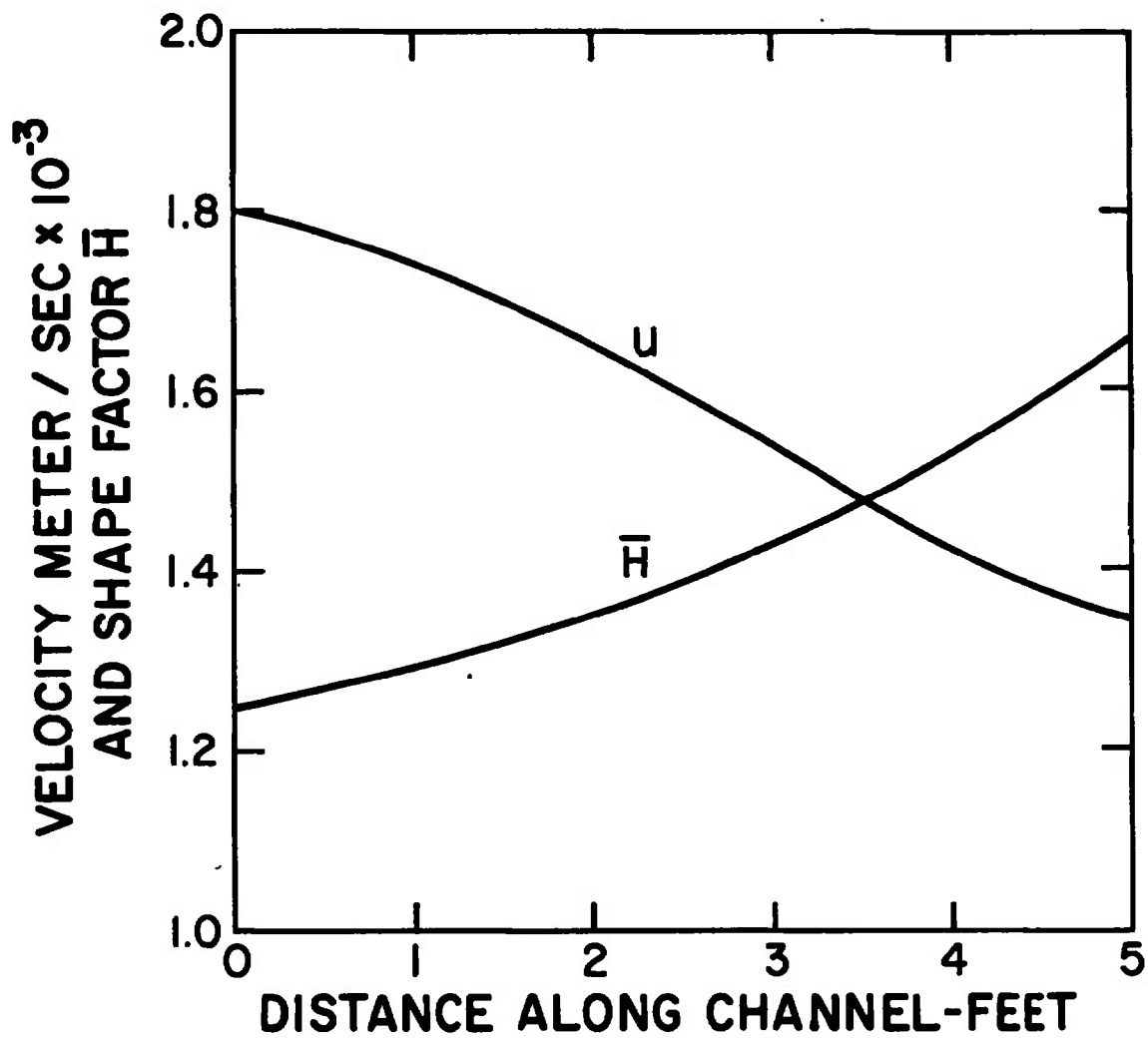


Fig. 98

Calculated Incompressible Shape Factor and Velocity Distribution in MHD Channel

## APPENDIX II

## ANALYSIS OF HALL GENERATOR END EFFECTS

F. J. Fishman

## 1. INTRODUCTION

In this section electrical end effects in Hall configuration generators are investigated. The "output" current of a Hall generator is an axial current within the channel. In principle, it could be directly extracted by a fine mesh electrode across the channel. This mesh electrode presents certain practical difficulties, and it seems much simpler to force the current to turn, so that it may be extracted through electrodes on the channel walls outside of the power generating section. In particular, it seems simplest to use the channel nozzle and diffuser as the pick-off electrodes. Nonuniform electric fields and current densities are implied by this current turning. That these effects may reach serious proportions was suggested by early test runs of the LORHO pilot generator in which arcing was observed between the last several electrode rings before the diffuser.

To isolate and understand these effects a highly idealized theoretical model was studied. Since the scale of these end effects is a small part of a channel diameter, the two ends may be considered separately; without loss of generality we adopt terminology appropriate to the downstream termination. Further, since the various flow parameters vary relatively little on this scale, the gas is assumed to have uniform flow velocity in the  $x$  direction of magnitude  $U$ , and uniform properties including electrical conductivity ( $\sigma$ ) and Hall parameter ( $\omega_e \tau_e$ ). The generator channel proper is very finely segmented, while the diffuser is assumed to be a good conductor, and in electrical contact with the gas. The diffuser potential is taken to be zero. The magnetic field ( $B$ ) is assumed to be uniform in the neighborhood of the channel end and for a distance of a channel height or more into the diffuser, where it ends abruptly. In most of this report attention is restricted to two-dimensional problems appropriate to channels whose cross sections have extreme aspect ratios. Since the effects of current turning along the magnetic field and across it are different, both the cases of a channel much wider in the direction of  $B$  than in the direction of  $U \times B$  and the opposite case are considered. The two-dimensional restriction is dropped in the final section.

In Appendix II, 2 of this report the electric field and current distributions at the channel diffuser interface are calculated. Axial electric fields of serious magnitude are noted. It is also noted that the net current to the diffuser walls in this region is not the output current of the generator, but rather an inflow of current to increase the axial current to the level appropriate to a shorted Hall generator. The section of diffuser between the channel termination and the magnetic field termination

clearly is a shorted Hall generator. The conduction current, and hence, pressure loss is minimized in a shorted Hall generator, so this configuration is not a priori unsatisfactory. In Appendix II, 3 of this report the fields and currents at the magnetic field termination are calculated to confirm that the output current can indeed be extracted in this way and to verify that no serious deleterious effects occur here. In the latter regard the pressure drop is estimated. Appendix II, 4 of this report notes that the high fields at the channel diffuser interface may be avoided at the expense of a certain power loss by bleeding current from the channel rings with graded resistors. The value of these resistors, as well as power loss, is estimated. Appendix II ends in a brief section of conclusions and recommendations.

A few words about the generality and realism of some of the above idealization are in order. a) Perhaps the weakest assumption is that of constant conductivity. The current concentrations inherent in the turning process lead to significant joule heating of the gas and enhanced conductivity if the overall current level is high enough. Calculations of this non-linear effect are very difficult, and are not undertaken here for that reason alone.\* b) A diffuser made of cold metal is certainly a very good conductor, but may not be in electrical contact with the gas because of a cold boundary layer. c) Because the scale of magnetic field fringing is typically greater than the current turning scale, the assumption of uniform magnetic field at the channel terminations is generally reasonable. On the other hand the same reason implies the assumed sudden field termination in the diffuser is unrealistic. However it is expected that the results of Appendix II, 2 apply qualitatively to a tapered field termination and hence still confirms that the current is extracted in this region without adverse effects.\*\* A certain arbitrariness remains in this choice, since the field could terminate upstream of the diffuser, for example. d) The results calculated in this report for a very finely segmented generator are expected to be good approximations to those of a channel with finite segmentation in the core of such a channel, in the diffuser, and within one segment width of the segmented wall. Further, it is believed that the potentials assumed by the individual segments would be between the extreme values predicted by the present results for the two ends of that segment.

## 2. ENHANCED AXIAL FIELD

The effect on electric field and current distribution of turning the current to the walls across the magnetic field may be evaluated by considering

---

\* There have been some attempts to consider this effect under rather different circumstances. (36, 37)

\*\* Reasoning by analogy with the Faraday generator end effects, one would expect the tapered termination to result in lower pressure drop than the sudden termination. (38, 39)

a rectangular channel that is much wider in the direction of the magnetic field (taken along the  $z$  axis) than " $h$ ", the height in the  $U \times B$  (or  $-y$ ) direction. Centering the channel along the  $x$  axis thus locates walls at  $y = \pm h/2$ , with the orthogonal walls receding to  $z = \pm \infty$ . The plane  $x = 0$  marks the boundary between the channel proper and the diffuser. Derivatives with respect to  $z$  may be neglected. Ohm's law for this case is:

$$J_y = \frac{\sigma}{1 + (\omega_e \tau_e)^2} \left[ -\frac{\partial \phi}{\partial y} - UB - \omega_e \tau_e \frac{\partial \phi}{\partial x} \right] \quad (60)$$

$$J_x = \frac{\sigma}{1 + (\omega_e \tau_e)^2} \left[ -\frac{\partial \phi}{\partial x} + \omega_e \tau_e (UB + \frac{\partial \phi}{\partial y}) \right] \quad (61)$$

Conservation of charge requires  $\nabla \cdot J = 0$ , which becomes with Ohm's law

$$\nabla^2 \phi = 0 \quad (62)$$

The boundary condition on the diffuser walls is

$$x > 0, y = \pm h/2: \phi = 0$$

Fundamentally, the boundary condition on the channel walls is that  $x < 0$

$$\phi(x, \frac{h}{2}) = \phi(x, -\frac{h}{2}) \quad (63)$$

$$J_y(x, \frac{h}{2}) = J_y(x, -\frac{h}{2}); \quad (64)$$

in the present two dimensional case an equivalent condition is  $x < 0, y = \pm h/2: \partial \phi / \partial y = 0$ .

$$\text{Finally, as } x \rightarrow \infty; \phi \rightarrow 0 \quad (65)$$

$$\text{and as } x \rightarrow -\infty \frac{\partial \phi}{\partial x} \rightarrow E_\infty \quad (66)$$

where  $E_{\infty} = UB [\omega_e \tau_e - (1 + \overline{\omega \tau})^2] \frac{J}{\sigma U A B}$  with  $J$  the total output current and  $A$  the channel area in the end region.

This problem is solved using conformal mapping techniques. The desired mapping is illustrated in Fig. 99; Fig. 99(a) represents the actual channel. An analytic function maps the channel interior into the region illustrated in Fig. 99(b) where the segments representing the channel walls are at right angles to the diffuser walls. Whereas the field equations for the actual configuration, Fig. 99(a) are not readily available, the field equations for the configuration shown in Fig. 99(b) are known. All that remains to obtain the field equations and hence precise knowledge of voltage distribution for the actual configuration, is to transform the results from the  $w$ -plane to the case under consideration - the  $z$ -plane. The determination of this function is facilitated by consideration of the intermediate transformation illustrated in Fig. 99(c) that carries the channel interior into the upper half plane. The requisite transformations are of the Schwartz-Christoffel form.

To unfold the channel into the upper half  $t$  plane the transformation has the form

$$\frac{dz}{dt} = \frac{A}{t} \quad (67)$$

Performing the integration and evaluating the constants to correspond to Fig. 99 yields

$$z = \frac{h}{\pi} \ln i/t \quad (68)$$

The map from the  $t$  plane to the  $w$  plane has the form

$$\frac{dw}{dt} = B (t-1)^{-1/2} (t+1)^{-1/2} \quad (69)$$

Performing the integration and evaluating the constants to correspond to the orientation of Fig. 99 and scaling so that the correct asymptotic fields are obtained yields

$$w = \psi + i\phi = i \frac{E_{\infty} h}{\pi} \left[ \ln(t + \sqrt{t^2 - 1}) - i \frac{\pi}{2} \right] \quad (70)$$

Figure 100 is a plot of this result along the electrode wall. The solid curve in the region  $x < 0$  is the electrode potential normalized by  $h E_{\infty}$ .

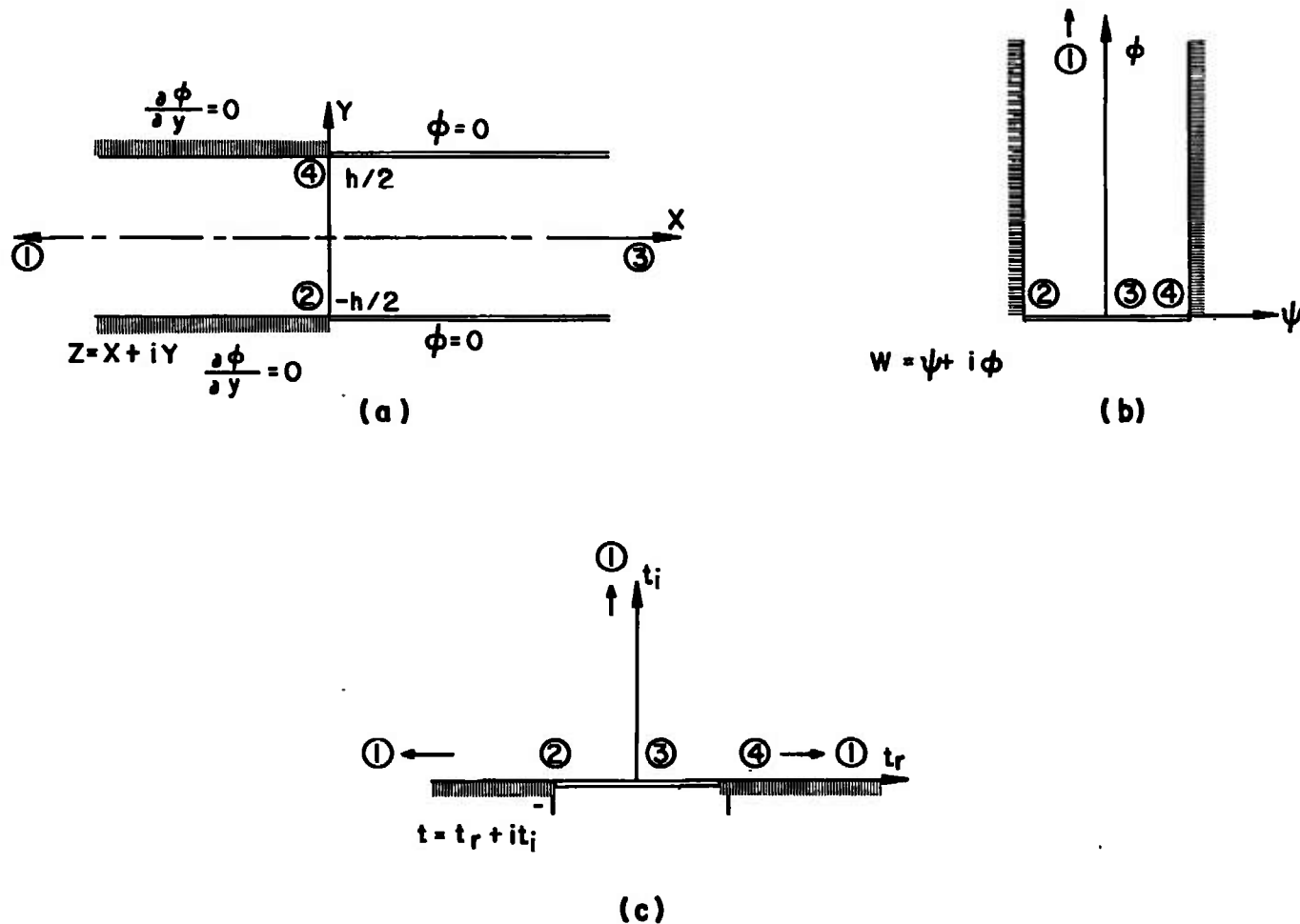


Fig. 99 Mappings Representing Solution of Idealized Problem:  
a) Channel in Physical Space, b) Channel Mapped to  
Potential Space, c) Intermediate Mapping.

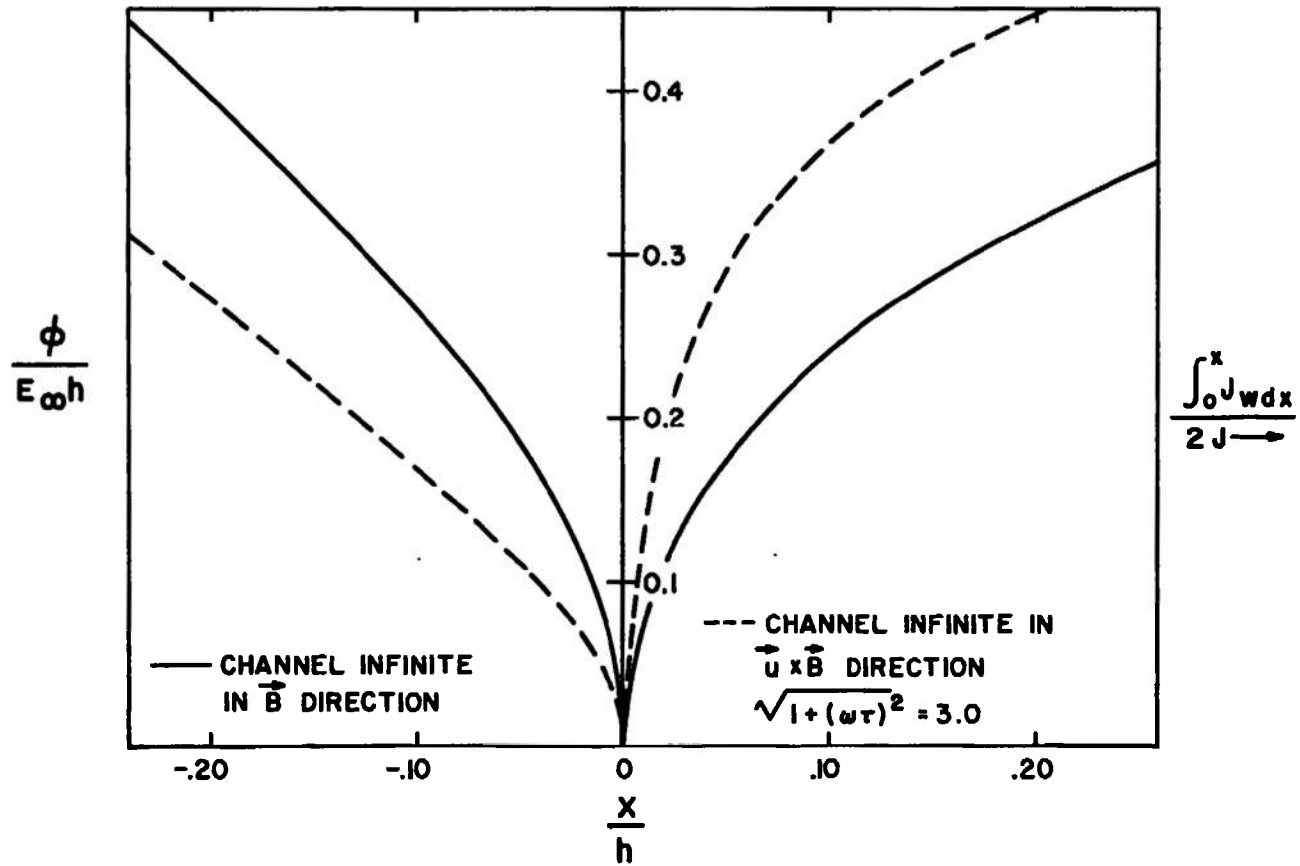


Fig. 100 Electric Potential Distribution in Power Section and Integrated Net Wall Current in Diffuser due to End Effect.

The end effect increases the overall machine potential by  $\pi^{-1} (\ell n 2) h E_{\infty} = 0.220 h E_{\infty}$ ; this enhancement occurs principally within a distance equal to a fifth of a channel height from the end of the machine.

The solid curve for  $x > 0$  is one half of the integral of the net normal current into the walls between the beginning of the diffuser and the plotted axial position, normalized by the total net current. This current is the current associated with the channel termination, and is symmetrically distributed to the two walls. It is not the total local current, which is not the same for the two walls because of the additional circulating current driven by the UB induced emf. Neither is it the output current, since in the diffuser there is still a substantial axial current corresponding to the current of a shorted Hall generator. In fact, this current is current into the gas to increase the axial current from the loaded Hall channel to that of the short circuited Hall channel represented by the diffuser.

The electric fields are obtained from the previous result by differentiation:

$$E_x - i E_y = E_{\infty} t [t^2 - 1]^{-1/2} \quad (71)$$

The normalized axial field at the wall is plotted by the solid line for  $x < 0$  in Fig. 101. This field exhibits a weak singularity at the channel end, and is still twice its normal value at a twentieth of a channel diameter from the end. This solid curve for  $x > 0$  is the end effect current density at either

wall normalized by  $\frac{\sigma E_{\infty}}{1 + (\omega_e \tau_e)^2}$ .

The complementary affect of turning the current to the walls along the magnetic field may be studied with a model similar to the one described above, but the walls normal to the field a distance  $h$  apart and the walls normal to  $\vec{U} \times \vec{B}$  much further apart. For this case, the  $z$  component of the Ohm's law

$$J_z = -\sigma \frac{\partial \phi}{\partial z} \quad (72)$$

must be included, but now  $y$  derivatives may be dropped. Charge conservation then implies

$$0 = \frac{\partial^2 \phi}{\partial x^2} + [1 + (\omega_e \tau_e)^2] \frac{\partial^2 \phi}{\partial z^2} \quad (73)$$



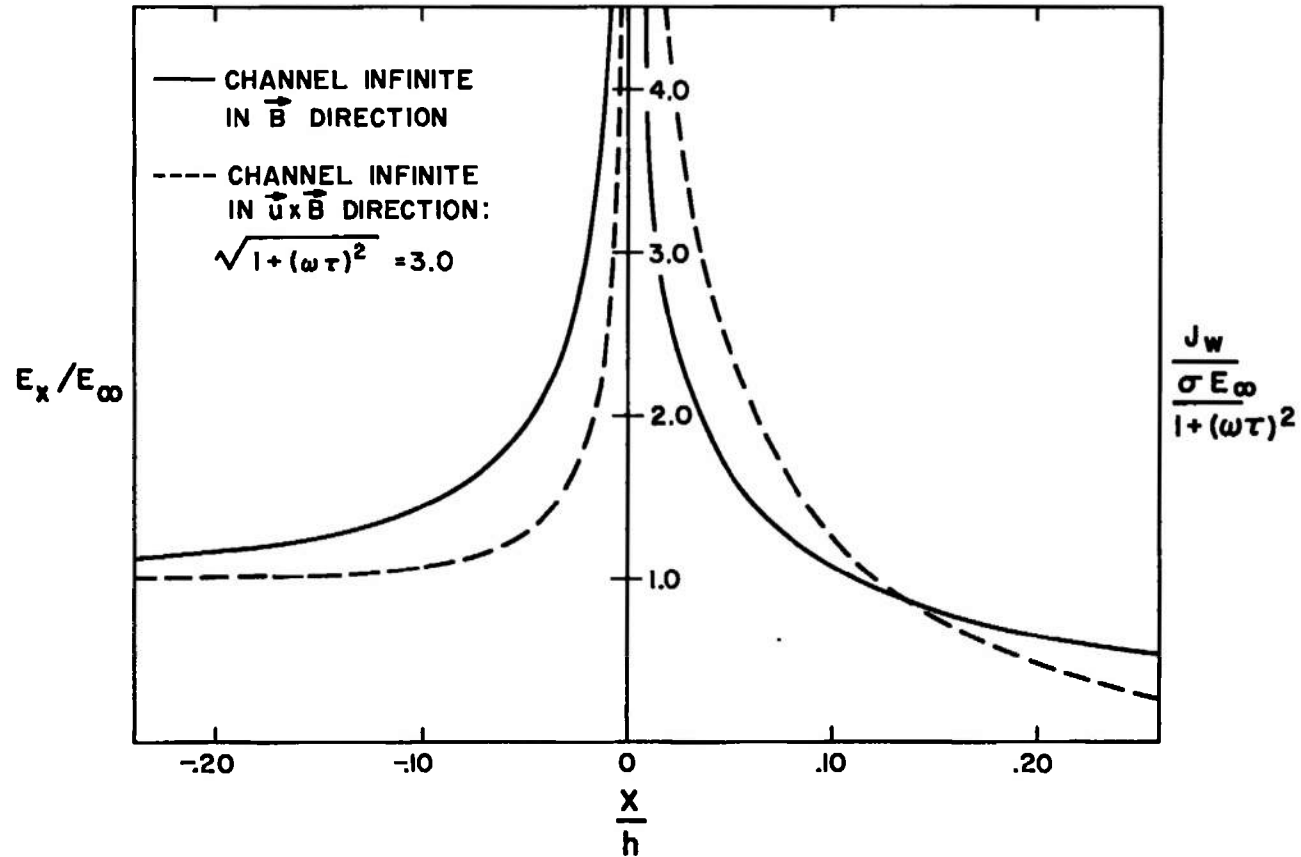


Fig. 101 Axial Electric Field Enhancement in Power Section and End Effect Wall Current Density in Diffusers.

This equation may be reduced to Laplace's equation by the introduction of a contraction along the magnetic field, defined by a new variable

$$z' = \sqrt{1 + (\omega_e \tau_e)^2} \cdot z \quad (74)$$

The boundary conditions remain that  $\phi$  vanishes on the diffuser walls and its normal derivative vanishes on the channel walls, so that the mathematical problem in the contracted space is identical (with  $y$  replaced by  $z'$ ) to the previous model. Then the results can be written down immediately. They are presented by the dashed curves of Figs. 100 and 101, for the case  $\sqrt{1 + (\omega_e \tau_e)^2} = 3$ . In comparing these results with the previous ones it may be noted that the axial electric field in the second model attains the value at a station  $x$  that was attained at station  $x \sqrt{1 + (\omega_e \tau_e)^2}$  in the earlier model, while the integrated end effect wall currents bear that same relationship. The end effect current crossing magnetic field lines enhances the axial field much more than that which flows along field lines, but this effect is partly compensated by the fact that the lower impedance along field lines leads to a greater current bunching in the second model.

In both cases the axial field does exhibit a singularity of sufficient strength that the field is more than twice its asymptotic value over a sensible portion of the channel. Unless the segmentation is considerably finer than this scale, or unless the asymptotic field is much less than that which will produce breakdown between adjacent electrodes (as is usually the case at the upstream end of the channel) breakdown will occur.

### 3. MAGNETIC FIELD TERMINATION

Since the output current does not leave the machine at the channel termination, and cannot continue down the diffuser far past the magnetic field, it must turn to the walls in the vicinity of the magnetic field termination. The situation is readily investigated in the two, two-dimensional cases treated in the previous section. It is convenient to shift the plane  $x = 0$  to be the plane of discontinuity of the magnetic field, and to label the region in the diffuser for  $x < 0$  as region 1 and specify variables in that region by a subscript one, and similarly region 2 for  $x > 0$ .

Thus for the case of a channel infinite in the  $B$  direction, the Ohm's law in region 1 is the same as before, and again there exists a potential that satisfies Laplace's equation. In region 2 the Ohm's law is simply

$$J_{x_2} = \sigma E_{x_2} \quad (75)$$

$$J_{y_2} = \sigma E_{y_2} \quad (76)$$

so here too there exists a potential that satisfies Laplace's equation. Thus, in each region the complex function  $\mathcal{E} = E_x - i E_y$  (which is simply  $i dw/dz$ ) is analytic. The boundary conditions are that

$$y = \pm h/2: E_x = 0$$

$$x \rightarrow -\infty: \mathcal{E}_1 \rightarrow 0$$

$$x \rightarrow \infty: \mathcal{E}_2 \rightarrow 0$$

The following matching conditions obtain along  $x = 0$ . Energy conservation requires  $E_{y1} = E_{y2}$ , while charge conservation requires  $J_{x1} = J_{x2}$  or

$$E_{x1} + \omega_e \tau_e (UB - E_{y1}) = [1 + (\omega_e \tau_e)^2] E_{x2} \quad (77)$$

The presence of a charge sheet along the plane  $x = 0$  leads to a discontinuity in the normal electric field there. The strength of such a sheet would be expected to be proportional to the local normal field in either region; thus we write

$$x = 0: E_{x2} - E_{x1} = \alpha E_{x1}$$

where  $\alpha$  is a constant whose value will be determined to permit a consistent matching of the solutions in regions 1 and 2. The above three matching conditions can be combined to give a relation involving only quantities defined in region 1 and another for region 2; viz.

$$E_{y1} = \frac{\alpha + (\omega_e \tau_e)^2 + \alpha (\omega_e \tau_e)^2}{\omega_e \tau_e} E_{x1} = UB \quad (78)$$

$$E_{y2} + \frac{\alpha + (\omega_e \tau_e)^2 + \alpha (\omega_e \tau_e)^2}{\omega_e \tau_e (1 + \alpha)} E_{x2} = UB \quad (79)$$

These relations complete the boundary conditions for each region separately.

The solution for  $\mathcal{E}$  in each region subject to the above boundary condition is conveniently obtained by two consecutive mappings of the Schwartz-Christoffel form as before. The mapping from intermediate upper half planes to the half strips in physical space are

$$z = -\frac{h}{\pi} \left[ \ln(t_1 + \sqrt{t_1^2 - 1}) - i \frac{\pi}{2} \right] \quad (80)$$

$$z = \frac{h}{\pi} \left[ \ln(t_2 + \sqrt{t_2^2 - 1}) - i \frac{\pi}{2} \right] \quad (81)$$

(the upper half  $t_1$  plane maps to region 1 and the upper half  $t_2$ -plane to region 2). The linear relation between  $E_{y1}$  and  $E_{x1}$  holding along  $x = 0$  derived above requires that the segment of the real  $t_1$  axis such that  $|t_1| < 1$  maps along a straight line in the  $\mathcal{E}_1$ -plane making an angle  $\phi$  with the imaginary axis, where

$$\tan \phi_1 = \frac{\omega_e \tau_e}{a + (1 + a)(\omega_e \tau_e)^2} \quad (82)$$

Similarly, the segment  $|t_2| < 1$  of the real  $t_2$  axis maps along a line in the  $\mathcal{E}_2$ -plane making an angle  $\phi_2$  with the imaginary axis, where

$$\tan \phi_2 = \frac{(1 + a)\omega_e \tau_e}{a + (1 + a)(\omega_e \tau_e)^2} \quad (83)$$

The remaining segments of the real  $t_1$  and  $t_2$  axes map along the real  $\mathcal{E}_1$  and  $\mathcal{E}_2$  axes, respectively. The Schwartz-Christoffel prescription for such mappings is

$$\frac{d\mathcal{E}}{dt} = \frac{A}{(t-1)^{1+\phi/\pi} (t+1)^{1-\phi/\pi}} \quad (84)$$

which integrates to

$$\mathcal{E} = \frac{A\pi}{2\phi} \left( \frac{t+1}{t-1} \right)^{\phi/\pi} + B \quad (85)$$

The boundary conditions and the condition that  $\mathcal{E} \rightarrow 0$  as  $|t| \rightarrow \infty$  determine the constants A and B so that

$$\mathcal{E} = i U B \left[ \left( \frac{t+1}{t-1} \right)^{\phi/\pi} - 1 \right] \quad (86)$$

Finally, the matching condition that  $E_{y1} = E_{y2}$  along  $x = 0$  (where  $t_1 = -t_2$ ) yields the result that  $\phi_1 = -\phi_2$  hence  $\alpha = -2$ .

Figure 102 represents some typical electric fields calculated from these results. The fields are normalized by the induced field  $E_0 = UB$ . The fields exhibit no symmetry about the channel centerplane, so the normal fields at the lower wall ( $y = -h/2$ ) and upper wall ( $y = h/2$ ) are plotted separately. However,  $E_y$  is symmetric about the plane  $x = 0$ , while  $E_x$  is antisymmetric in that plane. In this idealization an infinite normal field -- implying an infinite current density into the wall -- is exhibited along the lower wall, but the order of singularity is much weaker than that displayed at the channel-diffuser interface. It is remarkable that the singularity is strongest for  $\omega_e \tau_e = \sqrt{2}$ , and vanishes as  $(\pi \omega_e \tau_e)^{-1}$  for  $\omega_e \tau_e \gg 1$ .

The treatment of the complementary problem, with the current extracted along magnetic field lines is somewhat different. Again, we distinguish regions 1 and 2. The Ohm's law and charge conservation conditions in region 1 are the same as the channel-diffuser interface, so that a contracted co-ordinate must be introduced to recover Laplace's equation. Thus, in this region the function

$$\mathcal{E}_1 = E_{x1} - i \sqrt{1 + (\omega_e \tau_e)^2} E_{z1} \quad (87)$$

is an analytic function of

$$V_1 = x + i \frac{z}{\sqrt{1 + (\omega_e \tau_e)^2}} \quad (88)$$

In region 2 the classical Ohm's law applies, so that

$$\mathcal{E}_2 = E_{x2} - i E_{z2} \quad (89)$$

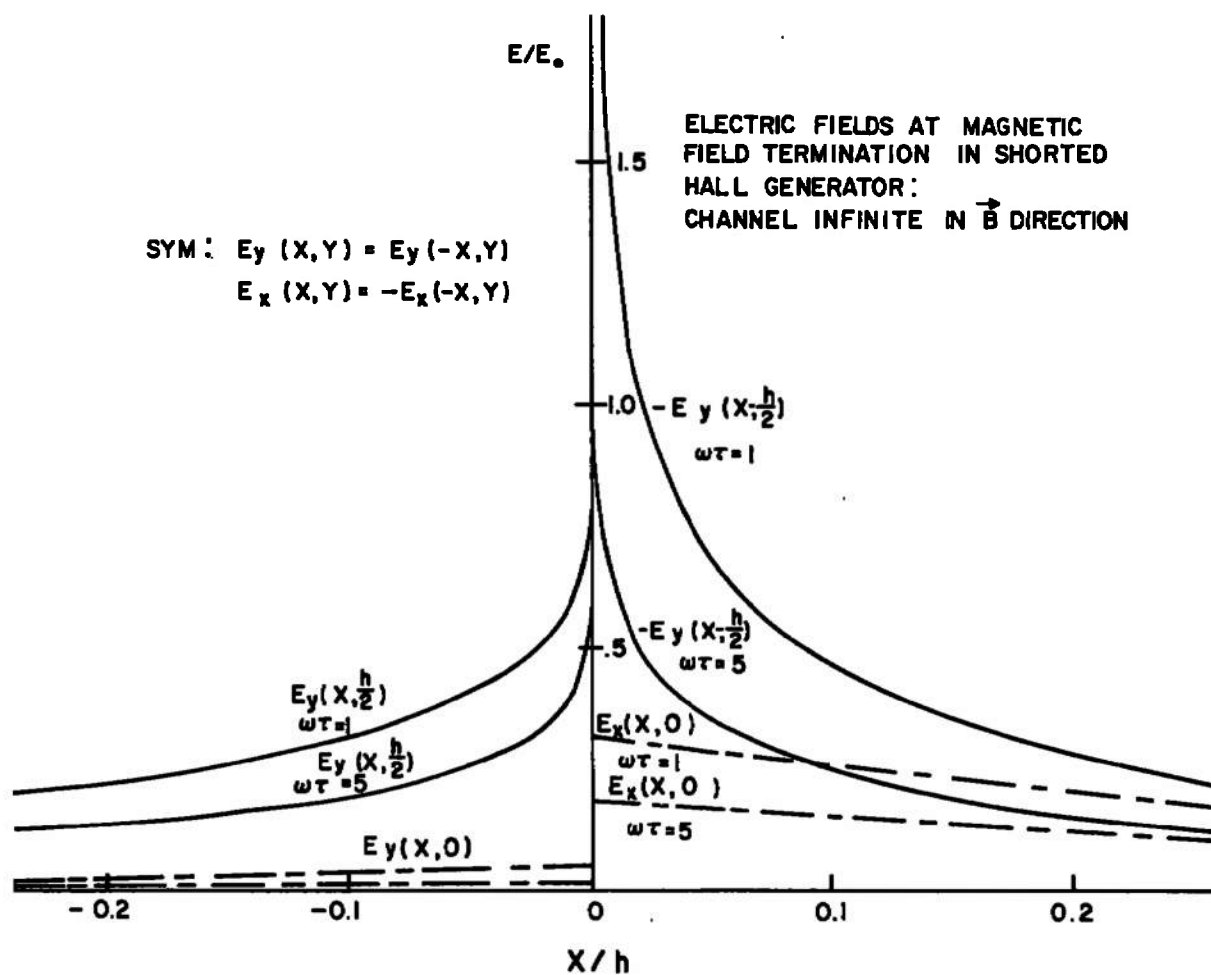


Fig. 102

Typical electric fields associated with the sudden termination of the magnetic field in a shorted Hall generator. The channel has a width  $h$  in the  $u \times \vec{B}$  direction and is much higher in the  $\vec{B}$  direction.

is an analytic function of

$$V_2 = x + iz \quad (90)$$

The boundary conditions in region 1 are that  $E_{x_1} = 0$  for  $I_p \{V_1\} = \pm \frac{h}{2\sqrt{1+(\omega_e \tau_e)^2}}$ ,

$\mathcal{E}_1 \rightarrow 0$  as  $R_p \{V_1\} \rightarrow -\infty$ ; and in region 2  $E_{x_2} = 0$  for  $I_p \{V_2\} = \pm h/2$ , and

$\mathcal{E}_2 \rightarrow 0$  as  $R_p \{V_2\} \rightarrow \infty$ . The matching conditions at  $x = 0$  are

$$E_{z_1} = E_{z_2} \quad (91)$$

$$E_{x_1} + \omega_e \tau_e U B = [1 + (\omega_e \tau_e)^2] E_{x_2} \quad (92)$$

$$E_{x_1} - E_{x_2} = \beta E_{x_1} \quad (93)$$

and in this case the last two conditions may be replaced by the relations

$$E_{x_1} = \frac{\omega_e \tau_e U B}{[1 + (\omega_e \tau_e)^2] (1 - \beta) - 1} \quad (94)$$

$$E_{x_2} = \frac{(1 - \beta) \omega_e \tau_e U B}{[1 + (\omega_e \tau_e)^2] (1 - \beta) - 1} \quad (95)$$

Again, it is convenient to map the channel half-strips into upper half planes by the transformation

$$V_1 = \frac{-h}{\pi [1 + (\omega_e \tau_e)^2]} \left[ \ln(t_1 + \sqrt{t_1^2 - 1}) - i \pi/2 \right] \quad (96)$$

$$V_2 = \frac{h}{\pi} \left[ \ln(t_2 + \sqrt{t_2^2 - 1}) - i\pi/2 \right] \quad (97)$$

As an alternate to defining a mapping from the upper half  $t$  planes to strips in the  $\mathcal{E}$  planes, the boundary conditions can be interpreted as specifying the sources of the function  $i\mathcal{E}$ , so that

$$i\mathcal{E}_1 = \frac{1}{\pi} \int_{-\infty}^{\infty} \frac{E_{x_1}}{s-t_1} ds = \frac{1}{\pi} \frac{\omega_e \tau_e U B}{[1 + (\omega_e \tau_e)^2]^{1-\beta}} \ln \frac{t_1 - 1}{t_1 + 1} \quad (98)$$

$$i\mathcal{E}_2 = \frac{1}{\pi} \int_{-\infty}^{\infty} \frac{E_{x_2}}{s-t_2} ds = \frac{1}{\pi} \frac{(1-\beta) \omega_e \tau_e U B}{[1 + (\omega_e \tau_e)^2]^{1-\beta} - 1} \ln \frac{t_2 - 1}{t_2 + 1} \quad (99)$$

Finally the condition that  $E_{z_1} = E_{z_2}$  at  $x = 0$  requires

$$\beta = 1 + \frac{1}{\sqrt{1 + (\omega_e \tau_e)^2}} \quad (100)$$

Figure 103 represents some typical electric fields calculated from these results. With the normalization indicated on the ordinate, the curves in the magnetic field free region ( $x > 0$ ) hold for all values of the Hall parameter. These results are extended into the region of uniform field by the relations:

$$E_z \left( \frac{-x}{\sqrt{1 + (\omega_e \tau_e)^2}}, y \right) = E_z(x, y) \quad (101)$$

$$E_x \left( \frac{-x}{\sqrt{1 + (\omega_e \tau_e)^2}}, y \right) = -\sqrt{1 + (\omega_e \tau_e)^2} E_x(x, y) \quad (102)$$

$E_z$  is anti-symmetric in the plane  $y = 0$ , while  $E_x$  is symmetric in this plane.



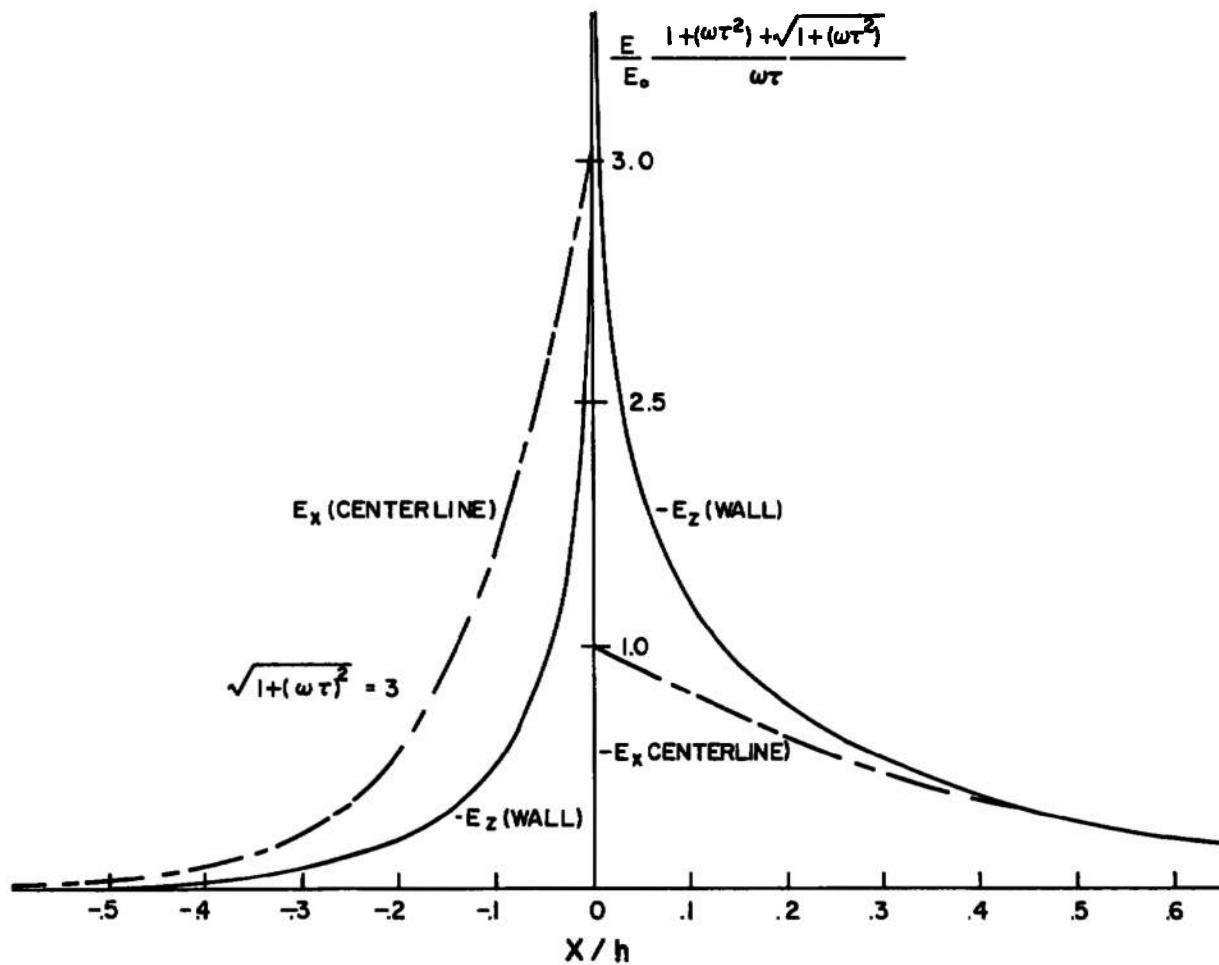


Fig. 103 Typical electric fields associated with the sudden termination of the magnetic field in a shorted Hall generator. The channel has a height  $h$  in the  $\vec{B}$  direction and is much wider in the  $u \times B$  direction.

The field scaling factor is plotted in Fig. 104. These fields are substantially weaker (and extend to a significantly greater distance from the point  $x = 0$ ) than any previously discussed. The singularity at the field discontinuity is exceedingly weak, being only logarithmic. Hence, designs that permit the output current to flow parallel to the magnetic field towards the electrodes are preferred.

Because of the assumption that the diffuser is an equipotential, the magnetic field termination does not change the output power of the generator for a given flow. However, the transverse currents in the field region do create additional drag on the working fluid. In a shorted Hall generator

of length  $L$  there is an MHD drag per unit channel width  $F_D = \frac{\sigma U B^2 h L}{1 + (\omega_e \tau_e)^2}$ .

The second curve of Fig. 104 represents the equivalent length (normalized by  $h$ ) that should be added to the actual length  $L$  of diffuser in the magnetic field, in order to account for the drag in the diffuser due to the end effects. This figure assumes current extraction along the field. Results of the same order (but somewhat larger) obtain for the case of current extraction across the field. In any case, the relative increase is small. Moreover, since the drag in a shorted Hall channel is substantially reduced from that of a loaded generator, these modest additions would seem to pose no serious problems.

#### 4. GRADED CURRENT PICKOFF

The most serious effect arising from the interface between generator channel and diffuser noted in previous sections is the enhanced axial electric field at the channel wall, which may produce breakdown and destructive arcing between generator segments. The extreme field enhancement noted is the result of the "suddenness" of the postulated transition from channel to diffuser. It may be alleviated by making this transition gradual by permitting some net current to flow to electrode segments in the neighborhood of the diffuser.

Consider a rectangular Hall generator of height " $a$ " parallel to the everywhere uniform magnetic field, and width " $b$ " perpendicular to the field and flow. Introduce the channel perimeter " $p$ " and the hydraulic diameter " $D$ ".

$$p = 2(a + b) \quad (103)$$

$$D = \frac{2ab}{a + b} \quad (104)$$

The channel-diffuser interface is marked by the plane  $x = 0$ . The channel walls ( $x < 0$ ) are finely segmented conductors, so that the intersection of a plane  $x = -x_1$  with the walls is a closed equipotential line; while the diffuser wall is an equipotential (taken to be zero) surface. Away from the interface in the channel (i. e.,  $-x \gg D$ ) there is a uniform axial electric field -  $E_\infty$ .

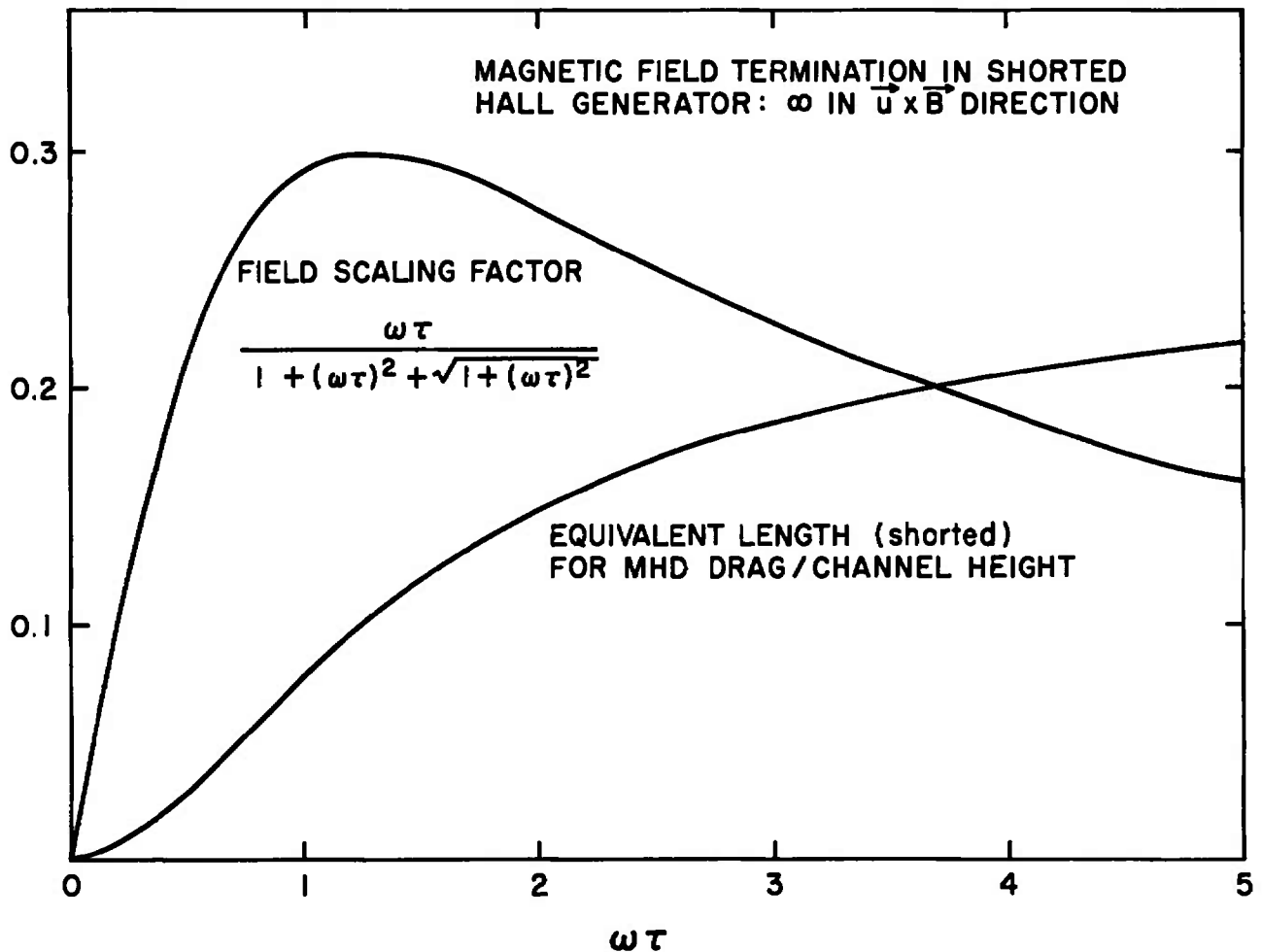


Fig. 104

Equivalent length and field scaling factor as a function of the wall parameter. The length of a shorted Hall generator that has the same MHD drag as is produced by the end effect associated with a sudden termination of the magnetic field in a shorted generator which has a height  $h$  in the  $\vec{B}$  direction and is very wide. The field scaling factor is for the same geometry as that of Fig. 100

Further it is required that this uniform axial electric field be maintained at the channel walls all the way to the diffuser. Thus if  $\phi_w(x)$  represents the potential at any point on the wall,  $\phi_w(x) = 0$  for  $x > 0$  and  $\phi_w(x) = E_\infty x$  for  $x < 0$ . This requirement will imply strong normal fields at the walls and a net current flow into the electrode segments in the neighborhood of  $x = 0$ , as well as into the diffuser wall.

It is again convenient to divide the region into two regions, with region 1 corresponding to  $x < 0$ . In both regions the three components of Ohm's law are

$$J_x [1 + (\omega_e \tau_e)^2] = \sigma \left[ -\frac{\partial \phi}{\partial x} - \omega_e \tau_e \frac{\partial \phi}{\partial x} + \omega_e \tau_e U B \right] \quad (105)$$

$$J_y = -\sigma \frac{\partial \phi}{\partial y}$$

$$J_z [1 + (\omega_e \tau_e)^2] = \sigma \left[ -\frac{\partial \phi}{\partial z} + UB + \omega_e \tau_e \frac{\partial \phi}{\partial x} \right] \quad (106)$$

(Again, Laplace's equation may be recovered by introducing a contracted coordinate  $y' = \frac{y}{\sqrt{1 + (\omega_e \tau_e)^2}}$ ). Formal expressions for  $\phi$  satisfying the

boundary conditions on the channel and diffuser walls with the proper behavior for large  $x$  in the two regions may be written immediately:

$$\phi_1 = E_\infty x + \sum_{n,m} A_{nm} \sin \frac{n\pi y}{a} \sin \frac{m\pi z}{b} \exp \left( \pi \sqrt{(nB)^2 + m^2} \frac{x}{b} \right) \quad (107)$$

$$\phi_2 = \sum_{n,m} C_{nm} \sin \frac{n\pi y}{a} \sin \frac{m\pi z}{b} \exp \left( -\pi \sqrt{(nB)^2 + m^2} \frac{x}{b} \right) \quad (108)$$

where  $B = \frac{b}{a} \sqrt{1 + (\omega_e \tau_e)^2}$

The matching conditions at  $x = 0$  are continuity of  $\phi$  and the normal current. Applying these determines all of the expansion coefficients and hence the potential:

$$A_{nm} = C_{nm} = + \frac{2}{\pi^3} \frac{(1 - \cos n\pi)(1 - \cos m\pi)}{n m \sqrt{(nB)^2 + m^2}} E_\infty b. \quad (109)$$

These result, in conjunction with Ohm's law permit the calculation of the net current that must be permitted to flow from the channel walls to yield the required constant axial field at the wall. These results are plotted in

Fig. 105 for the case  $\sqrt{1+(\omega_e \tau_e)^2} = 3$  with the channel aspect ratio as the parameter. There is a similar distribution of current from the diffuser walls. The total current per unit channel area is the same for each curve and is the additional current required by the shorted Hall generator represented by the diffuser. It is noteworthy that higher current concentrations are necessary when this make-up current flows primarily along the magnetic field, and the geometrically square channel is closer to this case than to the limit  $b/a \rightarrow 0$ , where the make-up current flows across the field.

Since this current flows into the channel at regions of lower electric potential than the diffuser, it can be supplied simply by connecting each channel segment to the diffuser through an appropriate resistor. This plan also restores the two terminal nature of the machine. The appropriate distribution of resistance for a square channel is indicated in Fig. 106. Here  $\delta$  is the width of an electrode segment ( $\delta/D$  is the pitch).

A system of bleeder resistors distributed according to Fig. 106 thus leads to a constant potential gradient along the Hall channel, completely avoiding the breakdown problem implied by a sudden termination, yet maintains the desirable "two terminal" feature. However, it does this at the cost of the power dissipated in the bleeder resistors, which will not in general be useful. Fortunately, this power is only a small fraction of the total generator power. Figure 107 is a plot of the power dissipated in all the bleeder resistors as a function of  $\omega_e \tau_e$ . The power is normalized by  $\sigma E_\infty^2 p D^2$ : since  $E_\infty \sim uB$  and  $p D^2 \sim$  channel volume (for an  $L/D = 4$ ) this quantity is of the order of the total power of the generator, while according to Fig. 107 the power loss is less than 0.1% of this when  $\omega_e \tau_e > 2.8$ . For a typical LORHO design this bleeder resistor loss is about 1% of the design output power. Thus, a bleeder resistor system seems to be a satisfactory solution to the Hall generator end problem.

## 5. CONCLUSIONS

The sudden termination of a Hall generator and the associated turning of the output current to the diffuser walls leads to an enhanced axial electric field along the channel wall. Since the electric potential difference per segment is usually one of the critical design limitations on Hall generators, this enhancement can often lead to serious arcing between segments near the channel-diffuser interface. The normally lower axial fields in the upstream portion of the generator reduces this danger at the nozzle-channel interface.

This field enhancement can be eliminated with a properly graded set of resistors between the final group of electrode segments and the diffuser. The power dissipated in these resistors is a very modest fraction of the generator output power for typical generator designs.

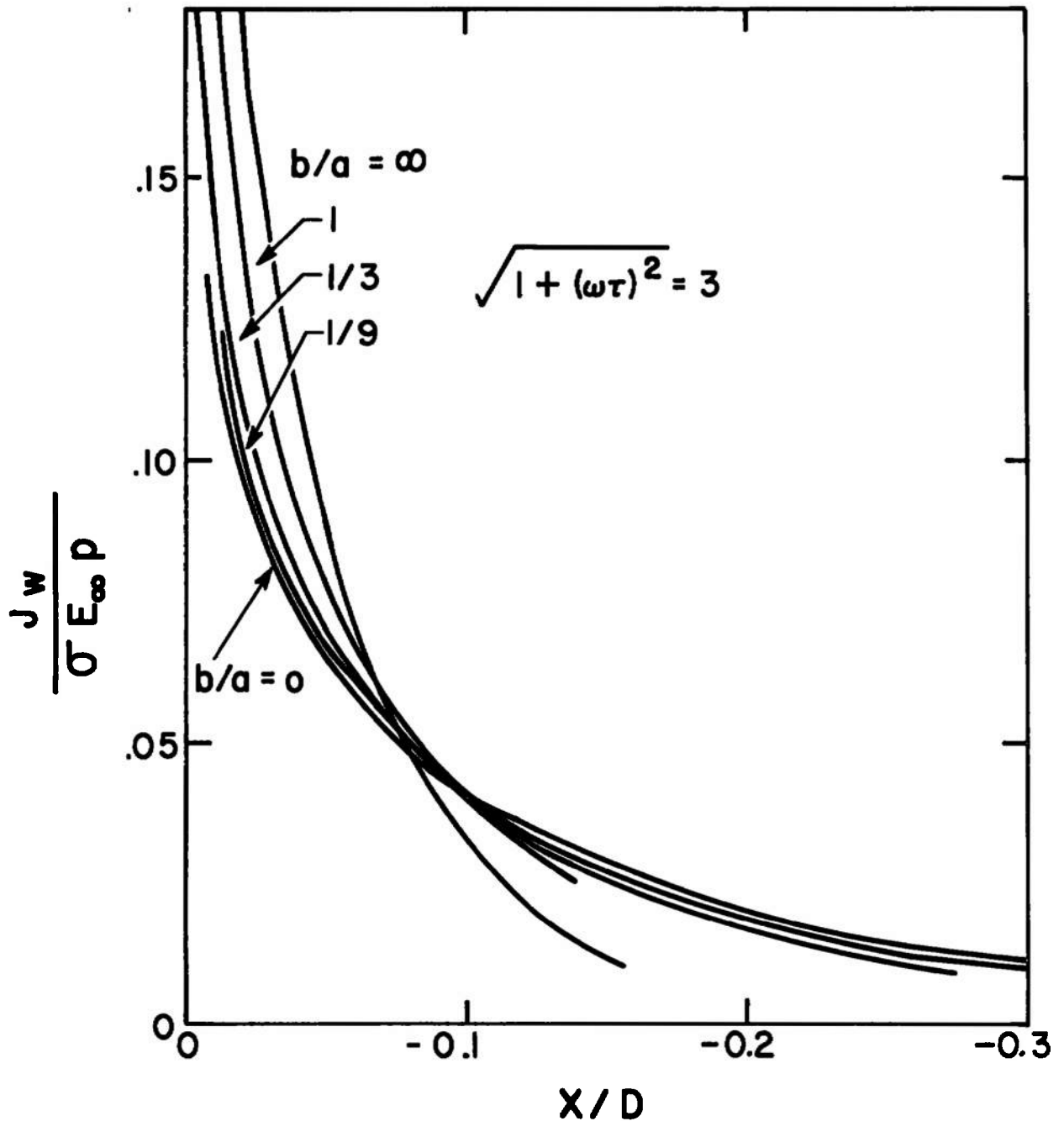


Fig. 105

Distribution of net current into electrode segments near the end of a Hall generator that results in constant axial electric field at the wall. The magnetic field is assumed uniform substantially beyond the channel end and the diffuser is a conductor. The channel section is rectangular of sides "a" and "b": side "a" is parallel to the magnetic field, p and D are the channel perimeter and hydraulic diameter, respectively.  $E_\infty$  is the axial electric field far from the end.

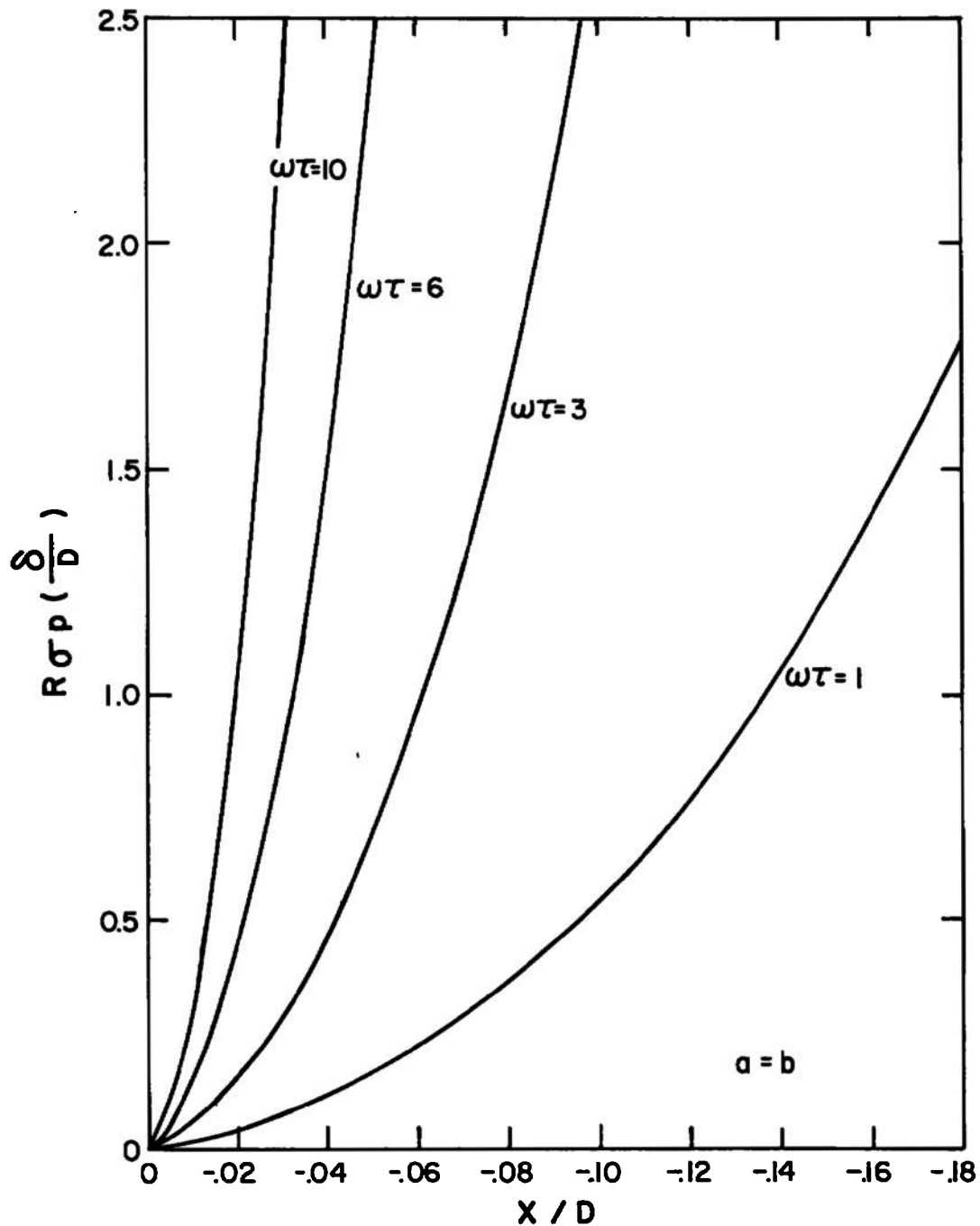


Fig. 106

Distribution of bleeder resistors from segment (at  $-x$  from channel end) to diffuser to produce the current distribution of Fig. 105 and hence a constant axial field at the wall. The electrode pitch is  $\delta/D \ll 1$ . Computed for a channel of square section.

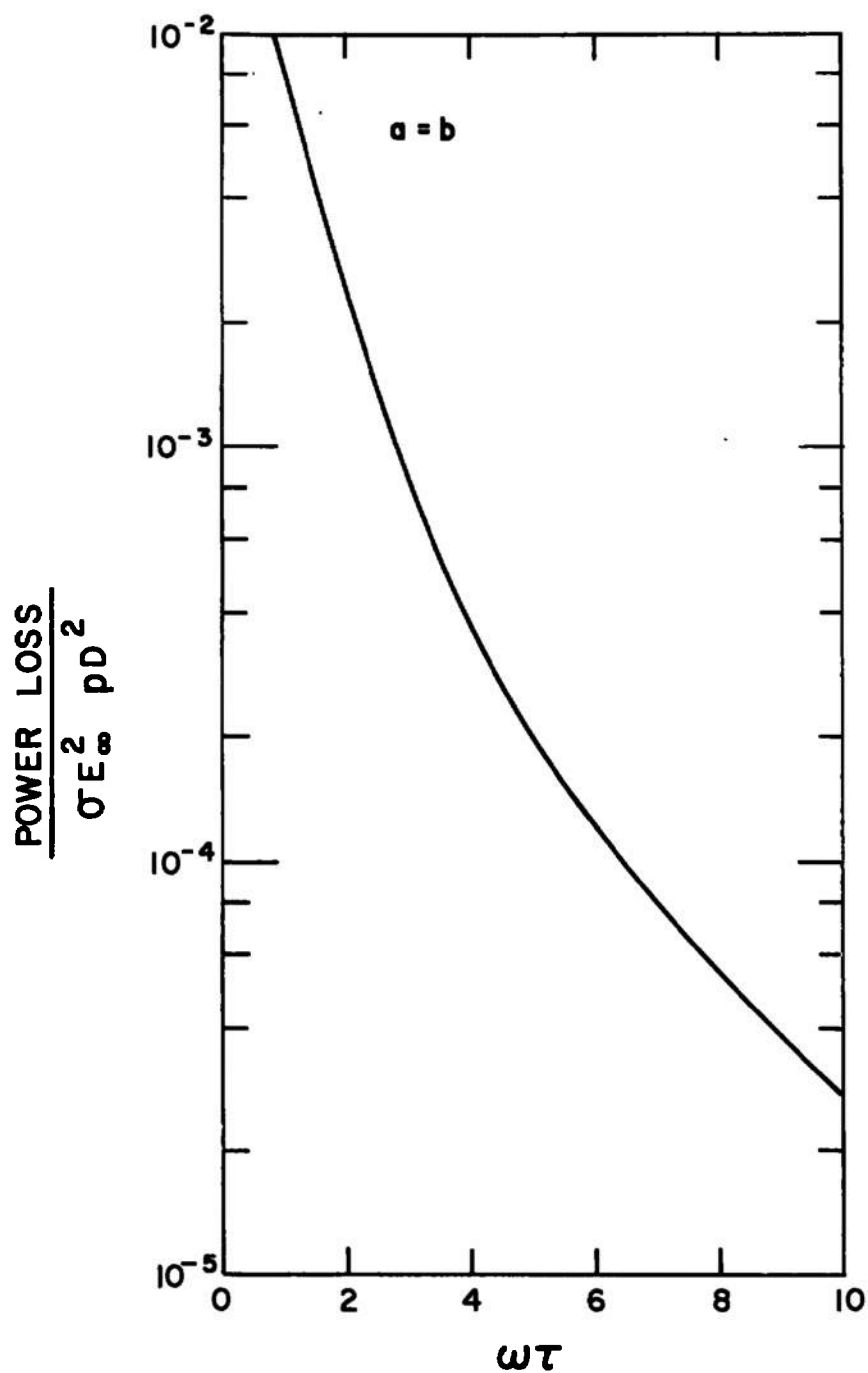


Fig. 107

Total power dissipated in the bleeder resistor system of Fig.106. The power lost is normalized by a power that is typically of the order of the channel output power.



Another way to eliminate the danger of arcing is to lower the "asymptotic" axial field  $E_\infty$  in the neighborhood of the channel termination, since all the fields scale with this value. This can be done by decreasing the magnetic field in the neighborhood of the channel end; the expression for  $E_\infty$  in fact indicates there always exists a magnetic field less than the design field for which  $E_\infty = 0$ . A section of channel in which  $E_\infty = 0$  contributes to the pressure drop without producing output power and hence, lowers the efficiency of the generator, but because of the small scale of the end effect it need not be a very long segment. In fact, a practical solution might be simply to terminate the channel in the natural fringing field of the magnet near the point of the critical field for  $E_\infty$  reversal.

The ratio of the axial field,  $E_x$ , to its value far from the ends,  $E_\infty$  is given by:

$$\frac{E_x}{E_\infty} = \left( \frac{B}{B_o} \right)^2 \frac{(1 - a_o) - \frac{a_o}{(\omega\tau)_o^2} \left( \frac{B}{B_o} \right)^2}{(1 - a_o) - \frac{a_o}{(\omega\tau)_o^2}}$$

where  $B$  and  $B_o$  are the local field and the field far from the junction, respectively, and  $a_o$  the loading coefficient far up the channel. This goes to zero when

$$\frac{1 - a_o}{a_o} = \frac{1}{(\omega\tau)_o^2} \left( \frac{B_o}{B} \right)^2$$

which is where the power takeoff should occur. Extension of the channel into the region of lower field causes little additional pressure loss, since if the diffuser were to be moved upstream, it would essentially be a short-circuited Hall generator in any case.

For the channel modifications carried out after the first series of tests (See Section III ), the power takeoff was shifted as described immediately above, and no difficulty with arcing was experienced during the second series of tests.

## APPENDIX III

FLOW STABILITY IN HALL CONFIGURATION  
MHD GENERATOR

F. J. Fishman

## FOREWORD

Much has been written regarding the possibility of magneto-acoustic instabilities in MHD generators, particularly with respect to the Hall configuration where these instabilities seem most likely to occur. The work which follows describes an investigation into these waves and it is believed that this is the only work which has examined the problem for the realistic boundary conditions of an actual MHD channel as opposed to a fictitious medium of infinite extent.

Following the initial generalized analysis, stability conditions with regard to two specific generators are examined in some detail. These are the AERL Mark II Hall configuration<sup>(45)</sup> and the high interaction arc-driven generator described by Klepeis and Olin.<sup>(46)</sup>

The LORHO Pilot MHD Power Supply is not discussed specifically in the text since at the time the work was undertaken, release of this information was not permitted. However, the remarks regarding the stability of the Mark II apply almost without change to the LORHO Pilot Power Supply since the governing nondimensional parameters (interaction length, energy extraction, flow Mach number) are nearly identical for the two machines. As indicated by Fig. 111, the Mark II, and by inference, the LORHO Power Supply, seem to have a wide margin of stability. In fact, instability has not been observed in any of the LORHO tests, in agreement with these predictions. (Output fluctuations due to aerodynamic buffeting at the onset of stall should not be taken as a magneto-acoustic instability.)

## 1. INTRODUCTION

Magneto-acoustic waves, propagating pressure fluctuations which in the limit of small MHD interaction become normal acoustic waves, may exhibit growth in dense, weakly ionized plasmas with strong electric currents and magnetic fields. Perturbation currents interacting with the magnetic field, when properly phased with the pressure fluctuations, lead to growth. Velikhov first called attention to the possible importance of such waves for MHD electric power generators and discussed a growth mechanism involving perturbation currents due to fluctuations of the Hall parameter with density fluctuations.<sup>(40)</sup> McCune generalized the concept to include fluctuations of all plasmas properties which depend on the thermodynamic properties of the gas, and noted that in many circumstances conductivity fluctuations may provide the dominant mechanism of wave growth.<sup>(41)</sup> Recognizing that conditions in Hall MHD generators were especially favorable to growth of axial waves of this type, Locke and McCune examined wave growth under plasma conditions appropriate to such machines and attempted to estimate the effects of the axial plasma inhomogeneities that exist in useful generators.<sup>(42)</sup> More recently, Powers and Dicks have published somewhat more refined calculations of axial wave growth in the segmented diagonal connected generator (which includes the Hall generator as a special case) and have emphasized the possible growth of the "entropy wave." <sup>(43)</sup>

The works cited above are inadequate to assess Hall generator stability on two grounds. The more basic of the two is that these authors only treated wave growth in an essentially infinite medium. While it seems clear that a mechanism of wave growth is a necessary condition of overall machine instability, there is no easy way to estimate what growth rate will lead to instability. This quantitative question certainly depends on the nature of the generator load circuit, which may serve as a feedback path for wave energy, allowing continued growth even for slowly growing waves. An assessment of the stability of a finite machine calls for the solution of a proper boundary value problem, including a correct treatment of the load circuit, rather than the simple determination of the unbounded plasma eigen functions. McCune has treated the effects of boundaries and load connection for transverse waves in a Faraday generator.<sup>(44)</sup> The linearized boundary-value problem for axial, magneto-acoustic disturbances in Hall generators with supersonic flow is the subject of this paper.

The other shortcoming of previous studies has been their limitation to short wave length (high frequency) disturbances. The present work, which is valid for arbitrarily low frequencies, indicates that disturbances with period comparable to the flow time (channel length/fluid velocity) generally are the most liable to lead to instability. In a Hall generator with significant MHD interaction, the spatial variation of these waves does not permit WKB type treatments.<sup>(43)</sup> The axial variations of plasma velocity and thermodynamic properties inherent in the steady generator flow must be treated correctly, for they may dominate the growth of the important low frequency waves.

The procedure adopted in the present work is as follows. The general equations describing time dependent channel flow are written down. The steady solution of these equations, corresponding to the usual Hall generator channel flow, is determined. The equations describing small time dependent departures from this solution are derived. Because of the prescribed linear nature of these equations, a complex exponential time dependence of the solution may be assumed; a similar spatial dependence is not permitted because the coefficients appearing in the equations have a spatial dependence prescribed by the steady solution. The resulting ordinary linear differential equations are solved subject to the appropriate boundary conditions to determine the spatial dependence of the perturbation. The axial electric field thus determined is integrated over the channel length to find the perturbation Hall voltage. The ratio of this voltage to the perturbation axial current is the external load impedance at the assumed frequency that will lead to the assumed time dependence. Thus the time dependence of a disturbance in a channel with fixed external connections is indirectly calculated. This "indirect" calculation is relatively convenient since the primary object is to determine stability: stability is assured if the load circuit that corresponds to a purely periodic disturbance requires active elements (energy sources).

## 2. METHOD OF ANALYSIS

The equations of unsteady magnetohydrodynamic channel flow are

$$A \frac{\partial \rho}{\partial t} + \frac{\partial}{\partial x} (\rho u A) = 0 \quad (110)$$

$$\rho \left( \frac{\partial}{\partial t} + u \frac{\partial}{\partial x} \right) u + \frac{\partial p}{\partial x} + j_z B = 0 \quad (111)$$

$$\rho \left( \frac{\partial}{\partial t} + u \frac{\partial}{\partial x} \right) (h + u^2/2) - \frac{\partial p}{\partial t} = j_x E_x + j_z E_z \quad (112)$$

where viscosity and heat conductivity have been neglected. It is assumed that the channel cross sectional area,  $A$ , may be a slowly varying function of the axial coordinate,  $x$ , but is time independent. The magnetic field,  $B$ , is constant and normal to  $x$  and  $z$ . The flow variables, axial velocity,  $u$ , density,  $\rho$ , pressure,  $p$ , and enthalpy,  $h$ , along with the current density,  $j$ , and electric field,  $E$ , may be arbitrary functions of both  $x$  and  $t$ . These quasi-one dimensional equations are valid for all axial disturbances in channels of length,  $L$ , much greater than a typical diameter ( $\sim A^{1/2}$ ). Further, all disturbances of frequencies sufficiently low that their characteristic dimension is large compared to this diameter must be essentially axial and hence correctly described by these equations. The relevant Ohm's law is:

$$j_x = \sigma(\rho, h) E_x + \omega\tau(\rho, h) j_z \quad (113)$$

$$j_z = \sigma(\rho, h)(E_z + uB) - \omega\tau(\rho, h) j_x \quad (114)$$

where the conductivity  $\sigma$  and Hall parameter  $\omega\tau$  are taken as general functions of the state parameters  $\rho$  and  $h$ . Maxwell's equations require that the current density field be solenoidal and the electric field irrotational. For a Hall generator, the solenoidal nature of the current is simply expressed by the uniformity of the total axial current  $J(t)$

$$J(t) = A(x) j_x(x, t) \quad (115)$$

where  $j_x(x, t)$  is the axial current density averaged over the channel section. It is here assumed that the electric field  $E$  is a function of  $x$  and  $t$  alone; this is compatible with the fields necessary irrotational nature if either a) the transverse field  $E_z$  is small (we assume  $E_y \equiv 0$ ) or b) this field varies only slowly with  $x$ . In an ideal Hall generator the transverse field vanishes identically, but in order to apply analyses of the present type to certain small experimental generators it is necessary to allow for the effect of electrode voltage drop, which leads to transverse fields in the core of the gas.

The model of electrode drop adapted here is that there is a fixed voltage drop  $V_e$  that always opposes current flow from the electrodes, and that when the net electromotive force across the channel is less than  $V_e$ , no current flows. This model, along with Ohm's law yields the following prescription for the transverse field:

$$\begin{aligned} V_i > V_e &\rightarrow E_z = -V_e/d \\ |V_i| < V_e &\rightarrow E_z = -uB + \omega\tau J/\sigma A \\ V_i < -V_e &\rightarrow E_z = V_e/d \end{aligned} \quad (116)$$

where  $d(x)$  is the height of the channel in the  $\underline{u} \times \underline{B}$  direction and

$$V_i = (uB - \omega\tau J/\sigma A)d \quad (117)$$

Thus condition a) above is satisfied if  $V_e \ll uBd$ , while condition b) is satisfied at low frequencies in any event.

Equations (113)-(116) can be used to eliminate the fields and current densities from Eqs. (110)-(112). If the pressure is eliminated from these by an equation of state of the form  $p = p(\rho, h)$  there remains a system of three first order equations involving the dependent variables  $u$ ,  $\rho$ ,  $h$ ,  $A$ ,  $J$ . These equations describe both the steady flow and the perturbation or stability analysis. These descriptions may be formally separated by assuming all variables have the form of a sum of a time independent part and a small part that is periodic in time, viz

$$\begin{aligned}
J(t) &= J_0 (1 + \epsilon e^{i\omega t}) \\
u(x,t) &= u_1(x) + \epsilon u_2(x) e^{i\omega t} \\
\rho(x,t) &= \rho_1(x) + \epsilon \rho_2(x) e^{i\omega t} \\
h(x,t) &= h_1(x) + \epsilon h_2(x) e^{i\omega t}
\end{aligned} \tag{118}$$

where the linearization parameter  $\epsilon$  is an arbitrary but small number. It is convenient to define the quantities  $A_0 = A(0)$ ,  $u_0 = u_1(0)$ ,  $\rho_0 = \rho_1(0)$ ,  $h_0 = h_1(0)$ ,  $\sigma_0 = \sigma(\rho_0, h_0)$ ,  $\omega \tau_0 = \omega \tau(\rho_0, h_0)$  and use these to normalize the quantities appearing in the equations, namely  $a = A/A_0$ ,  $v_1 = u_1/u_0$ ,  $v_2 = u_2/u_0$ ,  $r_1 = \rho_1/\rho_0$ ,  $r_2 = \rho_2/\rho_0$ ,  $\theta_1 = h_1/h_0$ ,  $\theta_2 = h_2/h_0$ ,  $\xi = x/L$ ,  $w = \omega L/u_0$ . The interaction parameter  $S = \sigma_0 L B^2 / \rho_0 u_0$  and the inlet loading parameter  $\alpha_0 = \omega \tau_0 J_0 / \sigma_0 A_0 u_0 B$  emerge as fundamental parameters from this normalization. Requiring that the dynamic equations hold separately for terms of order  $\epsilon^0$  and  $\epsilon^1$  leads to the separation into steady and stability analyses, respectively. The steady flow equations are:

$$\frac{d}{d\xi} (r_1 v_1 a) = 0 \tag{119}$$

$$r_1 v_1 \frac{dv_1}{d\xi} + \frac{1}{u_0^2} \frac{\partial p}{\partial \rho} \frac{dr_1}{d\xi} + \frac{h_0}{\rho_0 u_0^2} \frac{\partial p}{\partial h} \frac{d\theta_1}{d\xi} = S \psi_1 \tag{120}$$

$$\frac{h_0}{u_0^2} \frac{d\theta_1}{d\xi} + v_1 \frac{dv_1}{d\xi} = S \Gamma_1 \tag{121}$$



where

$$V_i > V_e \rightarrow \psi_1 = -\frac{\sigma_1}{\sigma_o} v_1 + \frac{\sigma_1}{\sigma_o} \frac{V_e}{u_o B d} + a_o \frac{\omega \tau_1}{\omega \tau_o} r_1 v_1$$

$$\begin{aligned} \Gamma_1 = a_o \left[ a_o \frac{\sigma_o}{\sigma_1} \frac{1 + \omega \tau_1^2}{\omega \tau_o^2} r_1 v_1 - \frac{\omega \tau_1}{\omega \tau_o} \left( v_1 - \frac{2 V_e}{u_o B d} \right) \right. \\ \left. - \frac{1}{r_1 v_1} \frac{\sigma_1}{\sigma_o} \frac{V_e}{u_o B d} \left( v_1 - \frac{V_e}{u_o B d} \right) \right] \end{aligned}$$

$$|V_i| < V_e \rightarrow \psi_1 = 0$$

$$\Gamma_1 = \frac{a_o^2}{\omega \tau_o^2} r_1 v_1$$

The perturbation equations are:

$$r_1 \frac{dv_2}{d\xi} + v_1 \frac{dr_2}{d\xi} = \frac{r_1}{v_1} \frac{dv_1}{d\xi} v_2 - \left( i\omega - \frac{v_1}{r_1} \frac{dr_1}{d\xi} \right) r_2 \quad (122)$$

$$\begin{aligned} r_1 v_1 \frac{dv_2}{d\xi} + \frac{1}{u_o^2} \frac{\partial p}{\partial \rho} \frac{dr_2}{d\xi} + \frac{h_o}{\rho_o u_o^2} \frac{\partial p}{\partial h} \frac{d\theta_2}{d\xi} = - \left( i\omega r_1 + r_1 \frac{dv_1}{d\xi} \right) v_2 \\ - \left( v_1 \frac{dv_1}{d\xi} + \frac{\rho_o}{u_o^2} \frac{\partial^2 p}{\partial \rho^2} \frac{dr_1}{d\xi} + \frac{h_o}{u_o^2} \frac{\partial^2 p}{\partial \rho \partial h} \frac{d\theta_1}{d\xi} \right) r_2 \\ - \left( \frac{h_o}{u_o^2} \frac{\partial^2 p}{\partial \rho \partial h} \frac{dr_1}{d\xi} + \frac{h_o^2}{\rho_o u_o^2} \frac{\partial^2 p}{\partial h^2} \frac{d\theta_1}{d\xi} \right) \theta_2 + S \psi_2 \end{aligned} \quad (123)$$

$$\begin{aligned}
v_1 \frac{dv_2}{d\xi} + \frac{h_o}{u_o} \frac{d\theta_2}{d\xi} = & - \left( iw + \frac{1}{v_1} \frac{h_o}{u_o} \frac{d\theta_1}{d\xi} + 2 \frac{dv_1}{d\xi} \right) v_2 \\
& - \left( \frac{1}{r_1} \frac{h_o}{u_o} \frac{d\theta_1}{d\xi} + \frac{v_1}{r_1} \frac{dv_1}{d\xi} - \frac{iw}{r_1 v_1 u_o} \frac{\partial p}{\partial \rho} \right) r_2 \\
& - \frac{iw}{v_1} \frac{h_o}{u_o} \left( 1 - \frac{1}{r_1 \rho_o} \frac{\partial p}{\partial h} \right) \theta_2 + S \Gamma_2
\end{aligned} \tag{124}$$

where

$$\begin{aligned}
V_i > V_e \rightarrow \psi_2 = & - \frac{\sigma_1}{\sigma_o} v_2 - \left( \frac{\rho_o}{\sigma_o} \frac{\partial \sigma}{\partial \rho} v_1 - \frac{\rho_o}{\sigma_o} \frac{\partial \sigma}{\partial \rho} \frac{V_e}{u_o B d} \right. \\
& \left. - a_o \frac{\rho_o}{\omega \tau_o} \frac{\partial \omega \tau}{\partial \rho} r_1 v_1 \right) r_2 \\
& - \left( \frac{h_o}{\sigma_o} \frac{\partial \sigma}{\partial h} v_1 - \frac{h_o}{\sigma_o} \frac{\partial \sigma}{\partial h} \frac{V_e}{u_o B d} - a_o \frac{h_o}{\omega \tau_o} \frac{\partial \omega \tau}{\partial h} r_1 v_1 \right) \theta_2 \\
& + a_o \frac{\omega \tau_1}{\omega \tau_o} r_1 v_1
\end{aligned}$$

$$\begin{aligned}
\Gamma_2 = & - \left( a_o \frac{\omega \tau_1}{\omega \tau_o} + \frac{V_e}{u_o B d} \frac{\sigma_1}{\sigma_o} \frac{1}{r_1 v_1} \right) v_2 \\
& - a_o \left[ -2 a_o \frac{\omega \tau_1}{\omega \tau_o} \frac{\sigma_o}{\sigma_1} \rho_o \frac{\partial \omega \tau}{\partial \rho} r_1 v_1 + a_o \left( \frac{\sigma_o}{\sigma_1} \right)^2 \frac{1 + \omega \tau_1^2}{\omega \tau_o^2} \frac{\rho_o}{\sigma_o} \frac{\partial \sigma}{\partial \rho} r_1 v_1 \right. \\
& \quad \left. + \frac{\rho_o}{\omega \tau_o} \frac{\partial \omega \tau}{\partial \rho} \left( v_1 - \frac{2 V_e}{u_o B d} \right) + \frac{1}{a_o r_1 v_1} \frac{V_e}{u_o B d} \frac{\rho_o}{\sigma_o} \frac{\partial \sigma}{\partial \rho} \left( v_1 - \frac{V_e}{u_o B d} \right) \right] r_2 \\
& - a_o \left[ -2 a_o \frac{\omega \tau_1}{\omega \tau_o} \frac{\sigma_o}{\sigma_1} h_o \frac{\partial \omega \tau}{\partial h} r_1 v_1 \right. \\
& \quad \left. + a_o \left( \frac{\sigma_o}{\sigma_1} \right)^2 \frac{1 + \omega \tau_1^2}{\omega \tau_o^2} \frac{h_o}{\sigma_o} \frac{\partial \sigma}{\partial h} r_1 v_1 + \frac{h_o}{\omega \tau_o} \frac{\partial \omega \tau}{\partial h} \left( v_1 - \frac{2 V_e}{u_o B d} \right) \right. \\
& \quad \left. + \frac{1}{a_o r_1 v_1} \frac{V_e}{u_o B d} \frac{h_o}{\sigma_o} \frac{\partial \sigma}{\partial h} \left( v_1 - \frac{V_e}{u_o B d} \right) \right] \theta_2 \\
& + a_o \left[ 2 a_o \frac{\sigma_o}{\sigma_1} \frac{1 + \omega \tau_1^2}{\omega \tau_o^2} r_1 v_1 - \frac{\omega \tau_1}{\omega \tau_o} \left( v_1 - \frac{2 V_e}{u_o B d} \right) \right]
\end{aligned}$$

$$|v_i| < v_e \rightarrow \psi_2 = 0$$

$$\Gamma_2 = - \frac{a_o^2}{\omega \tau_o^2} \left( \frac{\sigma_o}{\sigma_1} \right)^2 \left[ \frac{\rho_o}{\sigma_o} \frac{\partial \sigma}{\partial \rho} r_2 + \frac{h_o}{\sigma_o} \frac{\partial \sigma}{\partial h} \theta_2 - 2 \frac{\sigma_1}{\sigma_o} \right] r_1 v_1$$

Because of the normalization, the boundary conditions for the steady flow are simply

$$v_1 = r_1 = \theta_1 = 1 \text{ at } \xi = 0. \quad (125)$$

For steady flows that are everywhere supersonic, no hydrodynamic disturbance can propagate to the channel entrance from downstream regions. Then for such flows the boundary conditions for the stability analysis are

$$v_2 = r_2 = \theta_2 = 0 \text{ at } \xi = 0 \text{ at } \xi = 0 \quad (126)$$

where such essentially spurious effects as unsteadiness in the gas supply have been neglected. These conditions do not mean that there is no disturbance at the inlet, but only that that part of the disturbance that propagates through the load circuit (i. e., electric current and field) can be there. The boundary conditions for subsonic flow are more subtle and not discussed here.

The generator terminal (Hall) voltage, and hence the external impedance,  $Z$ , is determined by integrating the axial electrical field over the length of the machine; i. e., for  $0 \leq \xi \leq 1$ . This field may be expressed in terms of the solution of Eqs. (119)-(124) by means of Ohm's law. Separating as before the steady and perturbation contributions, one obtains:

$$\begin{aligned} V_i > V_e \rightarrow \frac{dZ_1}{d\xi} &= \frac{\omega \tau_o^2 L}{a_o \sigma_o A_o} \left[ -a_o \frac{\sigma_o}{\sigma_1} \frac{1 + \omega \tau_1^2}{\omega \tau_o^2} r_1 v_1 + \frac{\omega \tau_1}{\omega \tau_o} \left( v_1 - \frac{V_e}{u_o B d} \right) \right] \\ |V_i| < V_e \rightarrow \frac{dZ_1}{d\xi} &= \frac{\omega \tau_o^2 L}{a_o \sigma_o A_o} \left[ -\frac{a_o}{\omega \tau_o^2} \frac{\sigma_o}{\sigma_1} r_1 v_1 \right] \end{aligned} \quad (127)$$

$$\begin{aligned} V_i > V_e \rightarrow \frac{dZ_2}{d\xi} &= \frac{\omega \tau_o^2 L}{a_o \sigma_o A_o} \left\{ \frac{\omega \tau_1}{\omega \tau_o} v_2 + \left[ \frac{\rho_o}{\omega \tau_o} \frac{\partial \omega \tau}{\partial \rho} \right. \right. \\ &\quad \left. \left( v_1 - \frac{V_e}{u_o B d} - 2a_o \frac{\sigma_o}{\sigma_1} \frac{\omega \tau_1}{\omega \tau_o} r_1 v_1 \right) + a_o \left( \frac{\sigma_o}{\sigma_1} \right)^2 \right. \\ &\quad \left. \frac{1 + \omega \tau_1^2}{\omega \tau_o^2} r_1 v_1 \frac{\rho_o}{\sigma_o} \frac{\partial \sigma}{\partial \rho} \right] r_2 + \left[ \frac{h_o}{\omega \tau_o} \frac{\partial \omega \tau}{\partial h} \right. \\ &\quad \left. \left( v_1 - \frac{V_e}{u_o B d} - 2a_o \frac{\sigma_o}{\sigma_1} \frac{\omega \tau_1}{\omega \tau_o} r_1 v_1 \right) + a_o \left( \frac{\sigma_o}{\sigma_1} \right)^2 \right. \\ &\quad \left. \frac{1 + \omega \tau_1^2}{\omega \tau_o^2} r_1 v_1 \frac{h_o}{\sigma_o} \frac{\partial \sigma}{\partial h} \right] \theta_2 - a_o \frac{\sigma_o}{\sigma_1} \frac{1 + \omega \tau_1^2}{\omega \tau_o^2} r_1 v_1 \left. \right\} \\ |V_i| < V_e \rightarrow \frac{dZ_2}{d\xi} &= \frac{\omega \tau_o^2 L}{a_o \sigma_o A_o} \left\{ a_o \frac{\sigma_o}{\sigma_1} \frac{r_1 v_1}{\omega \tau_o^2} \left[ \frac{\sigma_o}{\sigma_1} \frac{\rho_o}{\sigma_o} \frac{\partial \sigma}{\partial \rho} r_2 + \frac{\sigma_o}{\sigma_1} \frac{h_o}{\sigma_o} \frac{\partial \sigma}{\partial h} \theta_2^{-1} \right] \right\} \end{aligned} \quad (128)$$

where  $Z_1$  is the ratio of the steady voltage to the steady current  $J_o$ , and  $Z_2$  is the ratio of the perturbation voltage to the perturbation current. Should  $V_i < -V_e$  at some station in the machine, the transverse current changes sign and that section of the machine becomes an accelerator rather than a generator. The formal expressions for the  $\psi$ 's,  $\Gamma$ 's, and  $Z$ 's are the same as for the case  $V_i > V_e$  except that  $V_e$  is replaced with its negative.

The eight ordinary differential Eqs. (119)-(126) are a complete description of both the steady behavior of the channel and its stability against axial magneto-acoustic waves. It may be noted that these equations separate in groups so that it is possible to determine the steady behavior from the solution of Eqs. (119)-(121) first and then use these results for the coefficients in the dynamical perturbation Eqs. (122)-(124) and finally evaluate the integrals implied in Eq. (126) to answer the stability question. However, Eqs. (122)-(124) require numerical treatment so that it is more convenient to solve all eight equations simultaneously.

Besides the parameters  $S$  and  $\alpha_0$ , and the specification of the inlet gas state, the equations involve a number of coefficients which describe the plasma. These include the five independent first and second order derivatives of the pressure with respect to the state variables, and the conductivity and Hall parameter and their first derivatives. It is also necessary to specify the channel core area  $a(\xi)$  and the electrode drop parameter  $V_e/u_0 B d(\xi)$ . A computer program has been developed that has among its inputs eleven two dimensional tables for the plasma properties and a one dimensional table for  $a(\xi)$ ; it was assumed  $d \propto a^{1/2}$ . This program may be used to predict the stability of specific Hall generators with respect to axial magneto-acoustic waves.

### 3. IDEALIZED STABILITY MAP

The very specificity of the treatment described above, while necessary to provide realistic stability estimates, causes the treatment to be a poor vehicle for revealing any general insights into the nature of the possible instability and the isolation of the most relevant factors leading to instability. Certain simplifying assumptions facilitate the generation of surveyable results.

For an ideal gas with constant heat capacities, the equation of state is

$$p = \frac{\gamma - 1}{\gamma} \rho h \quad (129a)$$

where  $\gamma$  is the ratio of heat capacities. For this gas the five two dimensional tables of pressure derivatives may be replaced with simple analytical expressions involving the single parameter  $\gamma$ . The electrical transport properties of a number of gases may be approximated by the expressions

$$\sigma = \sigma_0 (h/h_0)^N \quad (129b)$$

$$\omega\tau = \omega\tau_0 (\rho_0/\rho) \quad (129c)$$

Making these assumptions leads to the replacement of six two dimensional tables with analytic expressions involving only the parameter  $N$ . The only inlet conditions that need be specified are  $u_0 h_0^{-1/2}$ ,  $\omega\tau_0$ ,  $a_0$ , and  $S$ . In place of  $u_0 h_0^{-1/2}$ , it is convenient to introduce the entrance Mach number  $M_0 = u_0 \left[ (\gamma - 1) h_0 \right]^{-1/2}$ .

The stability calculation yet requires the specifications of the core area  $a(\xi)$ . Rather than choosing an arbitrary but fixed area contour that would result in different gradients of the steady flow variables for different values of  $S$  (and the other input parameters), and no doubt lead to quite poor generator design for some  $S$  values, the values of  $a(\xi)$  were chosen such that the enthalpy of the steady flow was uniform, i. e.,

$$\theta_1 = 1 \quad (130)$$

for all cases considered. This is accomplished by setting  $d\theta_1/d\xi = 0$  in Eqs. (120) and (121), solving them for  $r_1$  and  $v_1$ , and computing  $a(\xi)$  from Eq. (119). This particular choice was made, because (with Eq. (129)) it leads to a constant loading parameter and approximately constant electrical efficiency throughout the channel. Since the enthalpy of the gas does not change, any electrical energy delivered to the load must be extracted from the kinetic energy of the gas. For reasons described in Section III, the LORHO generator is operated in this way. Defining  $\eta$  as the ratio of the power delivered to the load to total energy flux in the flow at the channel entrance yields for this case

$$\eta = (u_o^2 - u_f^2) / (2h_o + u_o^2) \quad (131)$$

where  $u_f$  is the gas speed at the channel exit.

The equations have been solved and the perturbation impedance  $Z_2$  computed for a spectrum of input parameters. Typical results for the impedance are plotted in Fig. 108. The solid curve is the locus of the complex impedance consistent with a perturbation of (real) frequency  $\omega$  as  $\omega$  varies from 0 to  $10 u_o/L$ . All impedances in the right half plane can be synthesized with passive elements, but active elements (energy sources) are required in the left half plane. Thus this particular generator is absolutely stable against both extremely low and high frequency perturbations of this type, since to simply maintain such a perturbation without growth requires an active element in the external circuit. However, for angular frequencies  $\omega$  such that  $1.4(u_o/L) < \omega < 2.1(u_o/L)$  this generator may be either stable or unstable, depending on the nature of the external circuit. If the load impedance at the frequency in question lies inside the spiral locus the system will be unstable, while it will be stable for load impedances outside. This interpretation may be confirmed and an estimate of the growth rate of the instability obtained by redoing the calculation for perturbations that grow or decay; i. e., for complex values of  $\omega$ . The dashed curves of Fig. 108 are the result of such a calculation. The curve inside the solid spiral has a negative imaginary part and hence corresponds to a growing disturbance, while that outside represents a decaying one. Thus if the external impedance coincides with a point on the inner curve at a particular frequency, a disturbance of this frequency will grow with a characteristic growth time of twenty flow times. While this growth is slow compared to the flow time or disturbance frequency, it is of course extremely rapid on the time scale of most practical applications of magnetohydrodynamic generators.

The general scale of impedance curves such as Fig. 108 increases with the machine length as measured by  $S$  or equivalently  $\eta$ . Sufficiently "short" machines are absolutely stable. If the machine discussed in Fig. 108 were shortened so that  $\eta = .070$  the solid curve would be tangent to the imaginary axis; this would then be the highest value of  $\eta$  (i. e., largest machine) for which a generator of this description is absolutely stable. Similar calculations for various values of  $\alpha_o$ ,  $\gamma$ , and  $N$  lead to the stability map presented in Fig. 109 where the maximum value of  $\eta$  for which a constant enthalpy generator is absolutely stable is plotted as a function of the load parameter  $\alpha$ . The increased tendency toward instability as  $\alpha$  increases is primarily a reflection of the lowering of the power density as  $\alpha$  increases towards  $\alpha = 0.9$  (at which value the power density vanishes for  $\omega\tau = 3$ ), so that the generator must become physically longer to generate the same power. The maximum stable  $\eta$  generally slightly more than doubles as  $N$  is decreased from 8 to 4, suggesting that the fluctuations of conductivity with enthalpy are the dominant mechanism of instability in this region. The specific heat ratio  $\gamma$  (or better  $\gamma - 1$ ) also seems to have an important influence on stability, though not as strong as  $N$ . A few calculations at other values of the inlet Mach number and Hall parameter not plotted here suggest that stability is less sensitive to these inlet conditions than it is to the plasma properties  $\gamma$  and  $N$ . It may be noted that, typically, instabilities may develop in generators that extract about 10% of the thermal flux.

$$Z = \frac{L(\omega\tau_0)^2}{\sigma_0 A_0} [R + iX]$$

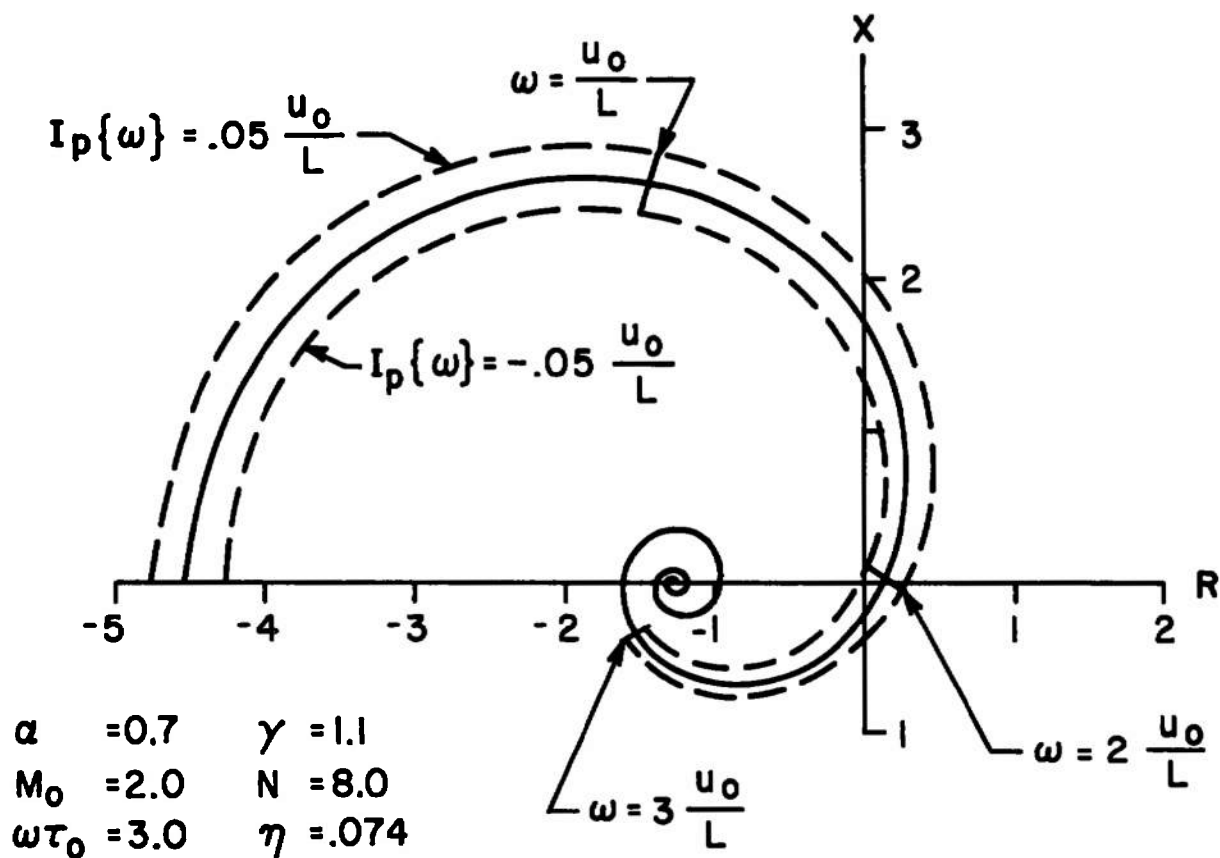


Fig. 108 Complex perturbation impedance for idealized Hall generator. The solid curve is the impedance locus for a periodic disturbance with disturbance angular frequency as the parameter. The dashed curves are for disturbances that have growth and decay times about twenty times the gas flow time. Impedance in the right half plane can be synthesized with passive elements.



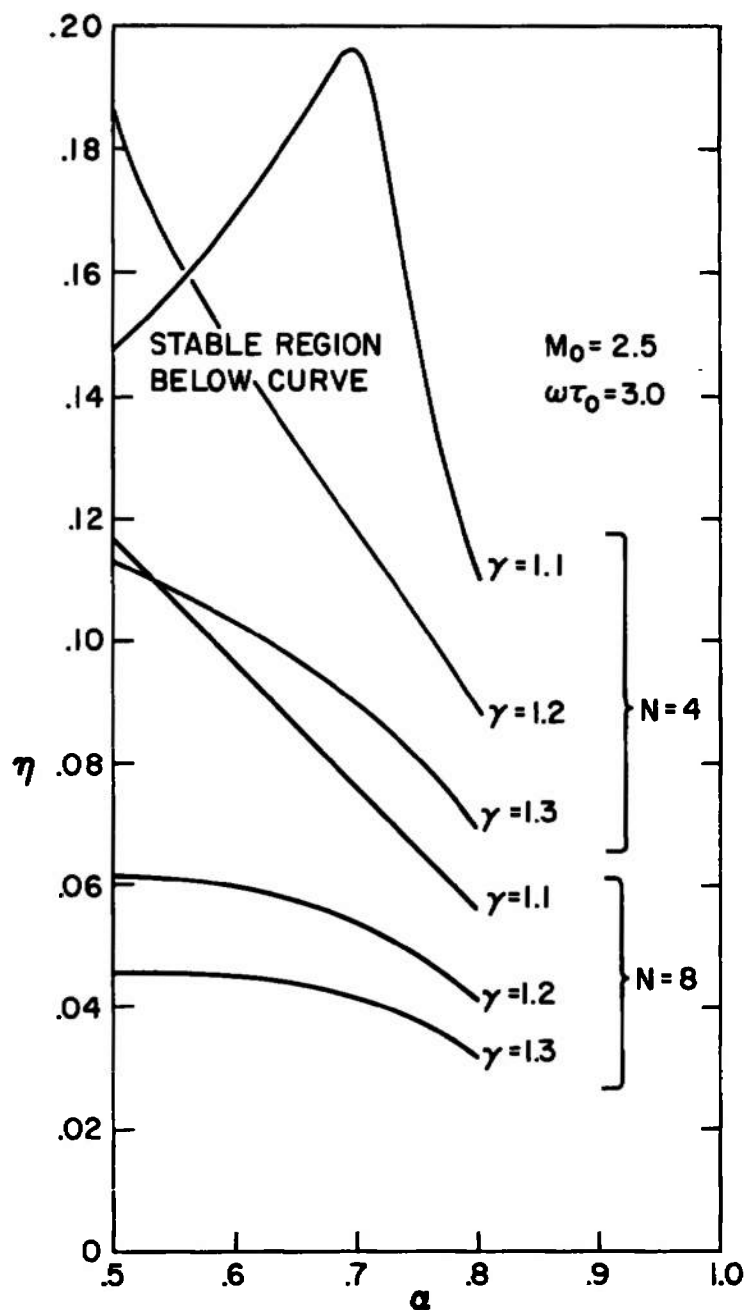


Fig. 109 Absolute stability map for idealized generator: fraction of energy flux converted versus load parameter.

The instability possible above the curve for  $\gamma = 1.1$ ,  $N = 4$ ,  $\alpha < 0.7$  is somewhat different than that possible above the other curves in that it is an instability at very low frequencies (especially 0) rather than over a limited "resonant" band bounded away from zero. This result may be interpreted as a positive slope to the generator voltage-current curve, or a negative internal resistance of the zero frequency Thevenin equivalent circuit. Actual instability still depends on the relation between this resistance and the internal load, but at zero frequency the external load is specified by the operating condition, and is proportional to  $Z_1$  (Eq. (127)). Thus actual instability results if  $Z_1 - Z_2(\omega = 0) < 0$ .

If instead of the maximum value of  $\eta$  for which these machines are absolutely stable, the largest value of the interaction parameter for absolute stability,  $S_{cr}$  is plotted, the somewhat more orderly Fig. 110 is obtained. An examination of this figure reveals that  $S_{cr}$  is closely proportional to  $(\gamma - 1)^{-1}$ , and indeed, except for the degenerate case of  $\gamma = 1.1$  and  $N = 4$  discussed above, all of the data represented on this figure can be represented by the correlation formula

$$S_{cr} \approx 0.8 \alpha / N (\gamma - 1) \quad (132)$$

within about 10%. It must be emphasized that this is purely an empirical relation based on Fig. 110, and no claim is made for its validity outside of the range of parameters considered in that data. In particular, the dependence on  $\alpha$  is rather suspect, since even over the very limited variation of  $\alpha$  considered in Fig. 110, the curvature of  $S_{cr}$  versus  $\alpha$  is evident. It is expected that the coefficient 0.8 varies significantly with  $M_0$ . Much variation with  $\omega\tau_0$  is not expected however, since an examination of Eqs. (119)-(126) reveals that  $\omega\tau_0$  enters only in the combination  $(1 + \omega\tau_1^2) / \omega\tau_0^2$ , and since  $\omega\tau_1 > \omega\tau_0$ , this combination cannot vary much even for  $\omega\tau_0$  only modestly greater than unity.

The very features that permit the present analysis to be used to evaluate overall machine stability make it quite difficult to seek out a justification for the success of Correlation (132), these features being the treatment of a proper boundary value problem and the integration over the entire machine, taking into account the varying gradients and parameters. A detailed comparison of the cases  $\gamma = 1.1$ ,  $N = 8$  with  $\gamma = 1.2$ ,  $N = 4$  at  $\alpha = .6$  is suggestive, however. Under condition (130), Eqs. (119)-(121) are independent of  $N$  and only weakly dependent on  $\gamma$  (i.e.,  $\gamma$  rather than  $\gamma - 1$  is involved, so that the two cases compared here differ by 10%), so that the equilibrium conditions and gradients on a distance scale normalized by  $S$  are essentially the same for these two cases. Under these conditions, the perturbation growth as measured by any of the quantities  $|v_2|$ ,  $|r_2|$ , or  $|\theta_2|$   $(\gamma - 1)^{-1}$  on this same scale are essentially the same for the two cases. It must be noted here that this remark does not justify the "adiabatic" approximation of primitive wave-growth theories which assume

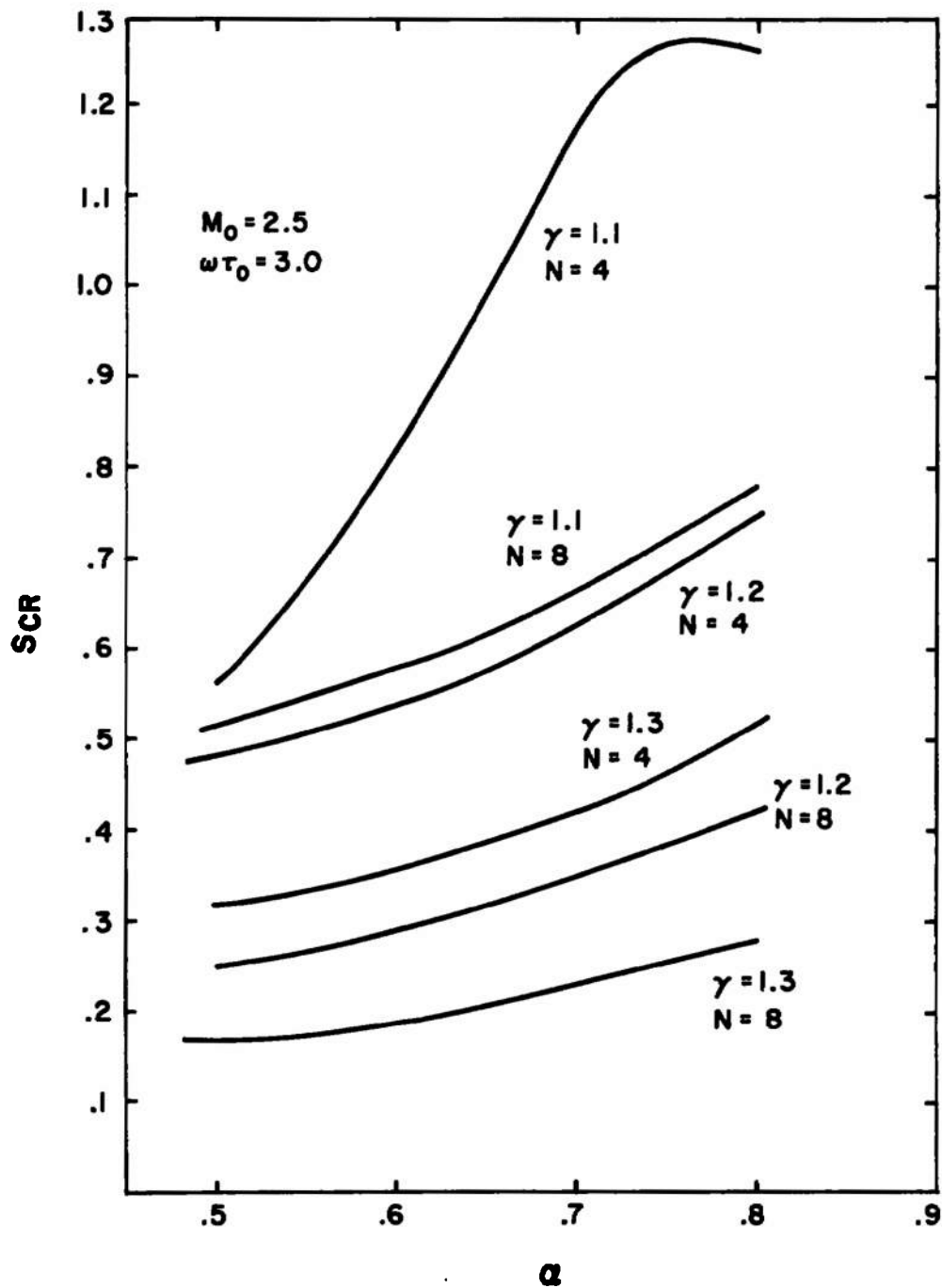


Fig. 110 Absolute stability map for idealized generator: critical interaction parameter versus load parameter.

$v_2 \approx r_2 M^{-1}$ ,  $\theta_2 \approx (\gamma - 1) r_2$  appropriate for an up-stream acoustic wave in the absence of magnetohydrodynamic interaction and gradient effects. Indeed, for these particular cases  $|\theta_2| \sim 7 (\gamma - 1) |r_2|$  and  $|v_2| \sim 4 M_0^{-1} |r_2|$ . Further, even the relative importance of the various terms contributing to perturbation growth varies substantially with position ( $\xi$ ), with the gradient terms dominating at the exit. Thus all that can be said presently toward understanding Correlation (132) is that conductivity fluctuations are the principal mechanism of perturbation growth in the range of parameters considered, and that the enthalpy fluctuations appear to be proportional to  $\gamma - 1$ , so that  $S_{cr} \propto N^{-1} (\gamma - 1)^{-1}$ . It is not to be expected that this simple correlation could embrace situations with very different equilibrium flows, or cases where the principal mechanism of perturbation growth was not conductivity fluctuations (if any such can lead to instability). The specific calculations reported in the next section also shed some oblique light on this point.

A comparison of the order of magnitude of the critical interaction parameter computed by the present theory with earlier wave growth calculations is instructive. The most direct comparison is with the work of Locke and McCune,<sup>(42)</sup> who plot the wave growth rate normalized by the interaction parameter for the fastest growing wave mode (the "slow down-stream" wave) as a function of  $\gamma$  for  $N = 10$ ,  $\alpha = .75$ , and  $M_0 = 3$ , values that are close to those for which Correlation (132) was observed to hold. Assuming that this correlation is approximately correct for these slightly different values yields values of the exponential growth rate,  $K_i L$ , varying from 0.6 to 1.8 at the critical interaction parameter as  $\gamma - 1$  varies from 0.1 to 0.6. While the limitations of the wave growth theory, especially the fact that it is limited to short wave lengths while the "wavelength" of the disturbance that contributes most critically to the instability characterized by Correlation (132) is of the order of the machine length, invalidate any more detailed conclusions, it seems reasonable to conclude that wave growth rates of the order of unity are enough to lead to machine instability. The physical interpretation is that the load feed-back path permits continual growth that is not terminated when an individual wave packet is convected from the channel.

#### 4. SPECIFIC MACHINES UNDER VARIOUS LOADS

While stability maps of the type discussed previously do give at least an approximate indication of the possibility of instability for generators that approach the model implied by Eqs. (129) and (130), other types of machines may present rather different characteristics, and resort must be made to the general apparatus of Eqs. (119)-(126). To illustrate, calculations specific to the mathematic models of two particular machines are presented. The first is the Avco Everett "Mark II" combustion driven experimental facility whose operation and model is reported in Ref. 45. Electrical power output of about 1 megawatt at a thermal heat flux of about 30 megawatts have been achieved. A one dimensional flow model with suitable allowance for electrode voltage drop and a self-consistent boundary layer calculation has been shown to be in good agreement with the experiments at typical operating conditions. The core area calculated by this model, along with the results of thermodynamic equilibrium calculations for the appropriate combustion products, have been used as inputs to the present stability calculations; perturbation impedance plots are presented in Fig. 111. The results for three different values of steady current,  $J_o$ , are presented and distinguished in the figure by the load resistance that corresponds to each current; they range from the lightly loaded  $3.6\Omega$  case to a  $13\Omega$  case, which corresponds about to maximum power operation. A wide margin of absolute stability is indicated for each case, i. e., all points lie far into the active load zone.

It is instructive to attempt to locate these results on Figs. 109 and 110. Such an attempt is reasonable since this machine was indeed designed to have only small gradients in enthalpy and loading parameter; for the  $9\Omega$  load the model predicts a 5% rise in enthalpy and an 18% decrease in load parameter over the length of the channel. The equilibrium calculation for the appropriate combustion products indicates that Eqs. (129b, c) are indeed a good approximation for this case with  $N = 4$ . The derivatives of pressure with the state variables are not completely consistent with those implied by Eq. (129a) for any value of  $\gamma$ , as they imply a weaker but higher order dependence of  $p$  on  $h$ . However, if the gas is modeled by an ideal gas with temperature dependent heat capacities, the calculated derivatives imply a (local) heat capacity ratio  $\gamma \approx 1.12$ . The initial loading parameter for the  $9\Omega$  case is  $\alpha_o = 0.743$ , falling to  $\alpha = 0.62$  at the exit. If  $\eta$  is evaluated as the ratio of the total change in energy flux in the core to the input flux a value  $\eta = 0.05$  is obtained. (Not all of the energy extracted from the core is available as electrical output, but some is lost through the electrode drop mechanism.) Locating this operating point on Fig. 109 suggests that this machine has a wide margin of stability, in agreement with the specific calculation represented by Fig. 111.

The interaction parameter of this model generator is  $S = 0.88$ . Simply locating this point on Fig. 110 would leave considerable doubt as to the stability of the generator, considering the uncertainties in  $\gamma$  and the effective value of  $\alpha$ . It is strongly suggested that were the gas somewhat different, having a higher value of  $N$  or  $\gamma$ , the possibility of instability would be easily reached, as opposed to the suggestion of Fig. 109. However,

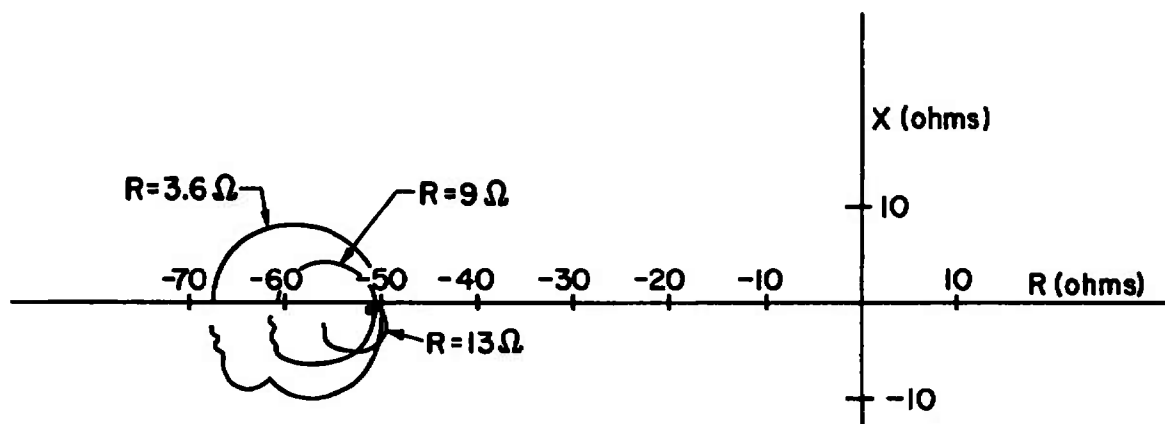


Fig. 111 Complex perturbation impedance for the 'Mark II' combustion driven Hall generator at three loads.

there is no direct contradiction, either for the specific case under consideration, which is uncontroversially stable by Fig. 111, or for somewhat modified machines, since the relation between  $\eta$  and  $S$  depends on  $\gamma$ ,  $\alpha_0$ ,  $N$ , as well as channel contour and electrode drop, among other parameters. Perhaps the wisest conclusion that can be drawn from this "near contradiction" is that Figs. 109 and 110 must be used with caution, even for machine designs that diverge from the idealizations (e. g., Eqs. (129) and (130),  $V_e/u_0 B d \gg 1$ ) on which they were based by relatively small amounts.

The second example presented here is related to the Avco Everett high interaction inert gas generator and analytical model reported in Ref. 46. A de facto degradation of Hall parameter had to be introduced into the model to obtain approximate agreement with experiment; that degradation factor was not adopted in the present analysis of the model's stability. This model has a relatively high interaction parameter  $S = 1.25$  and the design tended toward constant velocity rather than constant enthalpy. In the particular configuration analyzed electrode-drop phenomena are quite significant, with  $V_e/u_0 B d \cong 0.7$ . Under these conditions the enthalpy can vary by 25% through the machine and the loading parameter varies widely. A number of different loading conditions were studied, ranging from overall short-circuit to a case loaded so heavily that the machine would certainly stall. In the latter case the loading parameter varied from  $\alpha_0 = 0.12$  to  $\alpha = 0.6$ , and the transverse current decayed monotonically to zero. In the short-circuit case the loading parameter varies from  $\alpha_0 = 0.14$  to  $\alpha = 1.7$ , and three regions can be distinguished within the machine; an initial "generator" portion which powers an exit "accelerator" region, which is separated from the "generator" by an "idling" region in which the electrode drop prevents sensible transverse currents of either sign. The perturbation impedance plot for five different loadings are presented in Fig. 112. The various curves are labeled not only with the load resistance, but also with the calculated ratio of the electrical output to the input thermal flux; because of the high electrode drop, values of  $\eta$  calculated from the change of core energy flux would be substantially larger, ranging upward to 15% for the most heavily loaded case. Also indicated along the curves is the perturbation frequency in kilohertz.

The most striking aspect of Fig. 112 is that this model is subject to potential instability at both low and very high loading levels, but absolutely stable at a certain intermediate level. It would be very difficult to predict this behavior solely on the basis of Fig. 109 or 110: even a qualitative understanding requires cognizance of the three regions noted above in the short-circuited case. For all of the cases presented here, the perturbation growth over the initial generator region is essentially the same. This region fills the heavily loaded machine. In this case the perturbation grows essentially exponentially throughout the channel, attaining a substantial magnitude at the exit, resulting in possible instability under unfavorable frequency - phase circumstances. However, as the loading is decreased an "idling" region moves up the machine from the exit; in this region the perturbation does not grow but decays slowly instead. In the 9  $\Omega$  case this region occupies the final 20% of the channel and perturbations

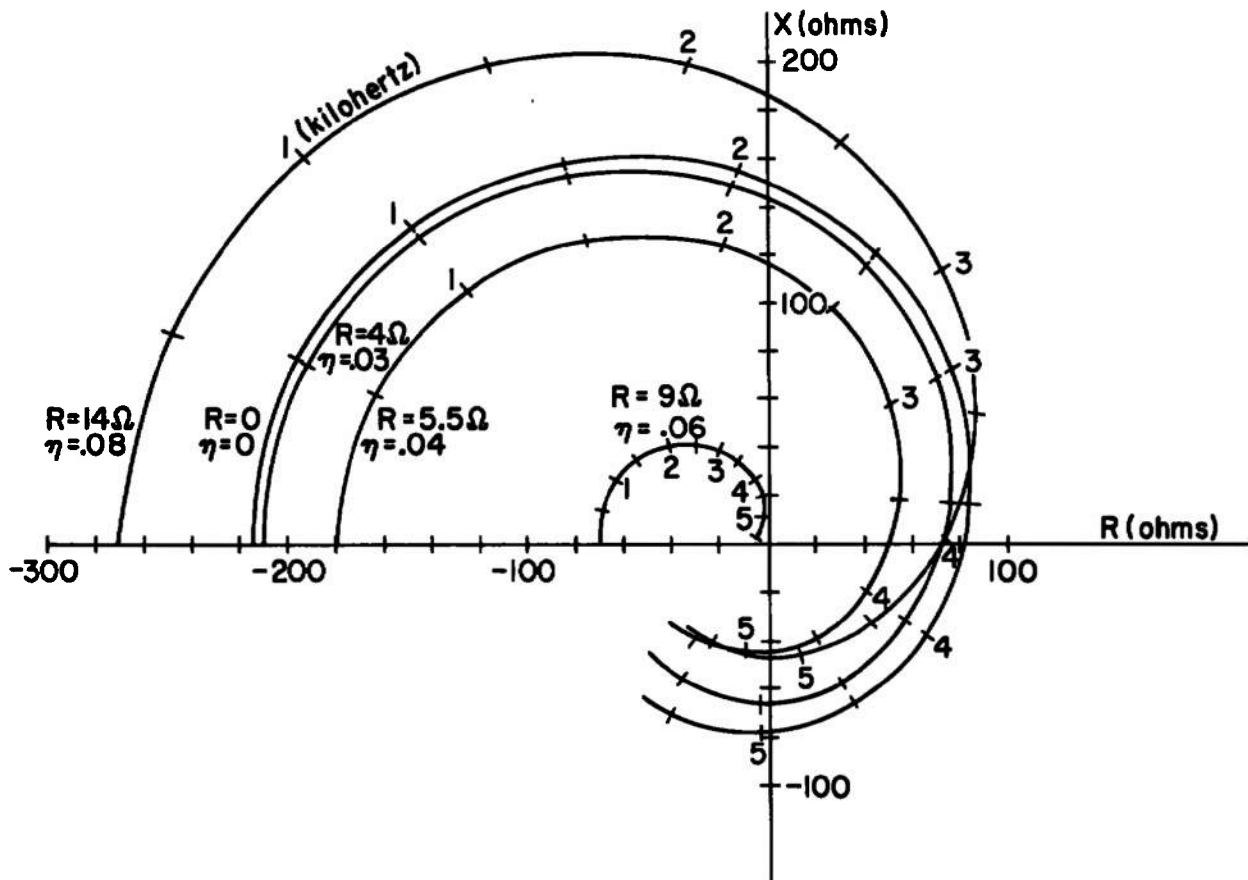


Fig. 112 Complex perturbation impedance for the 'high interaction' Hall generator at five loads.



sufficiently large to lead to instability do not occur. At loads of  $6\Omega$  or less an "accelerator" region appears at the channel exit; in such regions the nature of the perturbation changes rapidly, with a strong tendency toward instability evident. In circumstances such as these, an overall stability assessment clearly requires an integration over the full channel, such as provided by the present formalism.

Notice also that the load resistances are generally much smaller than the magnitude of the perturbation impedances plotted in Fig. 112. In particular, for the four cases indicating potential instability, the load resistances lie inside the perturbation impedance spiral. Thus if the machine is terminated with a simple resistance, the generator should actually be unstable for the loads that are indicated as being potentially unstable in this illustration.

## 5. STABILIZATION

A careful distinction has been made between "absolute stability" and stability that depends on the load circuit. The present results suggest that any generator can be made stable against magneto-acoustic waves by the insertion of an appropriate filter in the load circuit. A sufficient (it is more restrictive than necessary) design criteria for a stabilizing filter, in terms of perturbation impedance charts like Figs. 108, 111 and 112 is that the load impedance lie outside of the perturbation impedance locus for all frequencies for which the real part of the perturbation is positive, and that the load impedance corresponds to the loading condition at zero frequency. One such filter is a sufficiently large pure inductor in series connection with the loading resistor. For example, the machine discussed by Fig. 112 can be stabilized at all loads less than  $14\Omega$  (the entire useful range) by connecting a 15 mh inductance in series with the load. Then for frequencies above 2000 Hz, the load reactance will be greater than  $190\Omega$ , and hence outside the region of perturbation growth. More sophisticated filter design permits stabilization with elements of lower Q.

One apparent exception to the theorem that all machines can be stabilized is any generator that exhibits instability at zero frequency with  $Z_1 - Z_2 (w = 0) < 0$ . However, since any generator must be characterized by a positive short circuit current and open circuit voltage, for any given load resistance, there must be at least one operating point where the generator voltage-current characteristic is negative, so that  $Z_1 - Z_2 (w = 0) > 0$ , and the machine is stable. In a sense then, the zero frequency instability is an artifact of the calculation scheme that has  $\alpha_0$  as an input parameter, rather than the physical parameter load resistance.

One circumstance might exist in which stabilization attempts by load impedance control would be ineffective. It is possible that a disturbance injected at the channel entrance could grow so rapidly that it could become large enough to seriously effect generator performance before it was swept from the machine or controlled by a suitably filtered feedback signal through the load. The present analysis which assumes linear, basically continuous wave phenomena, is not appropriate for the discussion of such "single pass" disturbances.

As a filter in the load circuit may be used to stabilize an otherwise unstable generator, so too may a filter be used to promote the growth of a disturbance of a particular frequency in any generator that is not absolutely stable at that frequency. The present linear theory describes the initial growth rate of all disturbances, but unfortunately cannot describe the ultimate flow in an unstable generator, nor even suggest the nature of the non-linearity that limits disturbance growth. Thus, it provides no predictions as to whether these instabilities can become a useful source of AC power. For the same reason, the diagnosis of an experiment possibly subject to these instabilities is less than certain.

## 6. COMPARISON WITH EXPERIMENT

No experiments have been designed explicitly to confirm this theory. However several observations made of the operation of the "Mark II"<sup>(45)</sup> and "high interaction"<sup>(46)</sup> generators may be cited, though the caution of the preceding paragraph must be observed. Large scale ( $\epsilon \sim 0.3$ ) voltage fluctuations with a characteristic frequency of a few kilohertz have been observed in the output of the "high interaction" generator when it was terminated with a pure resistance. Such fluctuations are in accord with the present theory. During a single, minimally instrumented, experiment, an inductor, theoretically adequate to stabilize the generator, was connected in series with the load. The observed output voltage fluctuations increased by about a factor of two, but the order of magnitude increase in impedance at these frequencies implies that the fluctuation power decreased by a greater factor. Fluctuations are also observed in the output of the theoretically stable "Mark II" generator with resistive load. These fluctuations also have a period comparable to the gas flow time in this longer channel, and they are of a somewhat smaller relative amplitude than those observed in the resistively loaded "high interaction" generator.

One possible explanation of these observations is that there is a source of fluctuations in these machines besides the instability considered here. One might imagine unsteadiness in the energy source or in the seeding process (though limited attempts to isolate such effects in the "Mark II", were unsuccessful). Such a source might be responsible for the observed "Mark II" fluctuations and for the fluctuations observed in the "high interaction" machine with inductive load. The reduction in fluctuation level in the latter machine by the addition of the inductor could then be attributed to the complete elimination of the type of disturbance discussed in this paper.

Another speculation may be offered concerning the size of the observed fluctuations. In the resistively terminated "high interaction" generator these corresponded to a 30% current fluctuation. If this current fluctuation is attributed to a disturbance of the type considered in this paper, relative conductivity fluctuations of 30% and Hall parameter fluctuations of 10% should occur near the middle of the channel, the fluctuation being much smaller near the channel entrance but larger at the exit. Rosa has considered the effect of non-uniformities in MHD generators and has concluded that non-uniformities of the geometry considered here (a non-uniformity in the stream direction in a Hall generator) causes a reduction in the effective Hall parameter without influencing the effective conductivity.<sup>(47)</sup> While the details of Rosa's calculations are not applicable to a channel with large steady gradients, an order of magnitude estimate based on his results suggests that the 30% conductivity fluctuations deduced above could cause a reduction of Hall parameter of the order that was found necessary to describe the "high interaction" generators steady performance. Because of the lower fluctuation level in the "Mark II" and especially because of the lower theoretical Hall parameter, no degradation in this parameter would be expected in this machine, and none has been observed.

## 7. CONCLUSIONS

It has been demonstrated that Hall MHD generators may be unstable to magneto-acoustic waves. The dominant disturbances contributing to the instability have a period comparable to the gas flow time in the channel. It is suggested that instabilities may occur when the fastest growing pure waves exhibit a growth rate of order unity. This instability is more likely to occur in generators of high interaction or high fractional energy extraction than low, and also increases in probability with the sensitivity of the conductivity of the plasma to enthalpy changes and with the plasma's  $\gamma$ . While no parameter, or set of parameters, that describe the dependence have been isolated, the equilibrium channel gradient distribution has an important effect on stability. An extreme example of this last effect was noted in the "high interaction" generator, where the existence of even a very short section of channel with accelerator like action was decisive.

Finally, it may be pointed out that within the limitations of the linearization and geometrical assumptions, the formalism developed here is a general description of the time dependent Hall generator flow, and hence, has potential applications beyond the assessment of stability. In particular, the impedance function  $Z_2(w)$  is the ratio of the change in terminal voltage to the corresponding change in output current, whatever the cause of these changes. Thus, this function completely describes the electrical behavior of the generator viewed as a linear, two terminal "black box"; i. e., it is sufficient to characterize the generator as a circuit element within a larger network. One important application of this description is the analysis of a generator-inverter circuit to deliver AC power.

## ACKNOWLEDGMENTS

The author wishes to acknowledge numerous clarifying conversations with E. V. Locke and J. E. McCune over the past four years. He is especially indebted to R. D. Gillespie, who efficiently and sympathetically bridged the communications gap with the IMB System 360 installed at Avco Everett.

## APPENDIX IV

## EXPLORATORY STUDIES WITH A LOW POWER MHD ACCELERATOR

## 1. OBJECTIVES

The design, construction, and operation of the low power accelerator was intended to be a checkout of mechanical design concepts as well as to provide some indications of aerodynamic and electrical performance. Design details to be investigated included ease of fabrication and assembly, sealing methods, electrical insulation, electrode construction, heat transfer, cooling, and thermal stress. Information gathered from the 2 mw accelerator program would be useful in the mechanical design of the 20 mw accelerator.

## 2. DESIGN CONCEPTS

The channel is composed of a group of diagonal water-cooled modules simulating the intended construction of the 20 mw unit. The modules are arranged at an angle to the channel axis such that they form the equipotential lines on the insulating wall. Figure 113 shows some test modules which illustrate the construction. Electrode material is retained in grooves machined in the electrode wall faces of the modules.

The modular construction results in a considerable simplification of the construction of the insulating wall. The alternative construction would be a peg wall which would require several hundred water-cooled pegs. The peg wall would clearly be more expensive and probably less reliable due to the multiplicity of seals required. In addition, the modular construction makes finer segmentation practical, and therefore permits the use of higher electric fields in the channel.

The final low power accelerator design is shown in Fig. 114. A water-cooled nozzle accelerates the flow from the arc to a Mach number of 1.4. The nozzle is followed by an inlet adapter section, then 53 modules, and finally an outlet adapter section. The channel gas passage measured 1.023" x 1.980" at the inlet and 1.023" x 2.126" at the outlet. The segmentation is .380" in the axial direction and .250" normal to the equipotentials. The diagonal angle is  $41^\circ$  to the flow direction.

## 3. DESIGN DETAILS

## a. Nozzle

The nozzle was designed to provide the following channel inlet conditions: Mach No. = 1.4; pressure = .5 atm; temperature =  $3150^\circ\text{K}$ ;

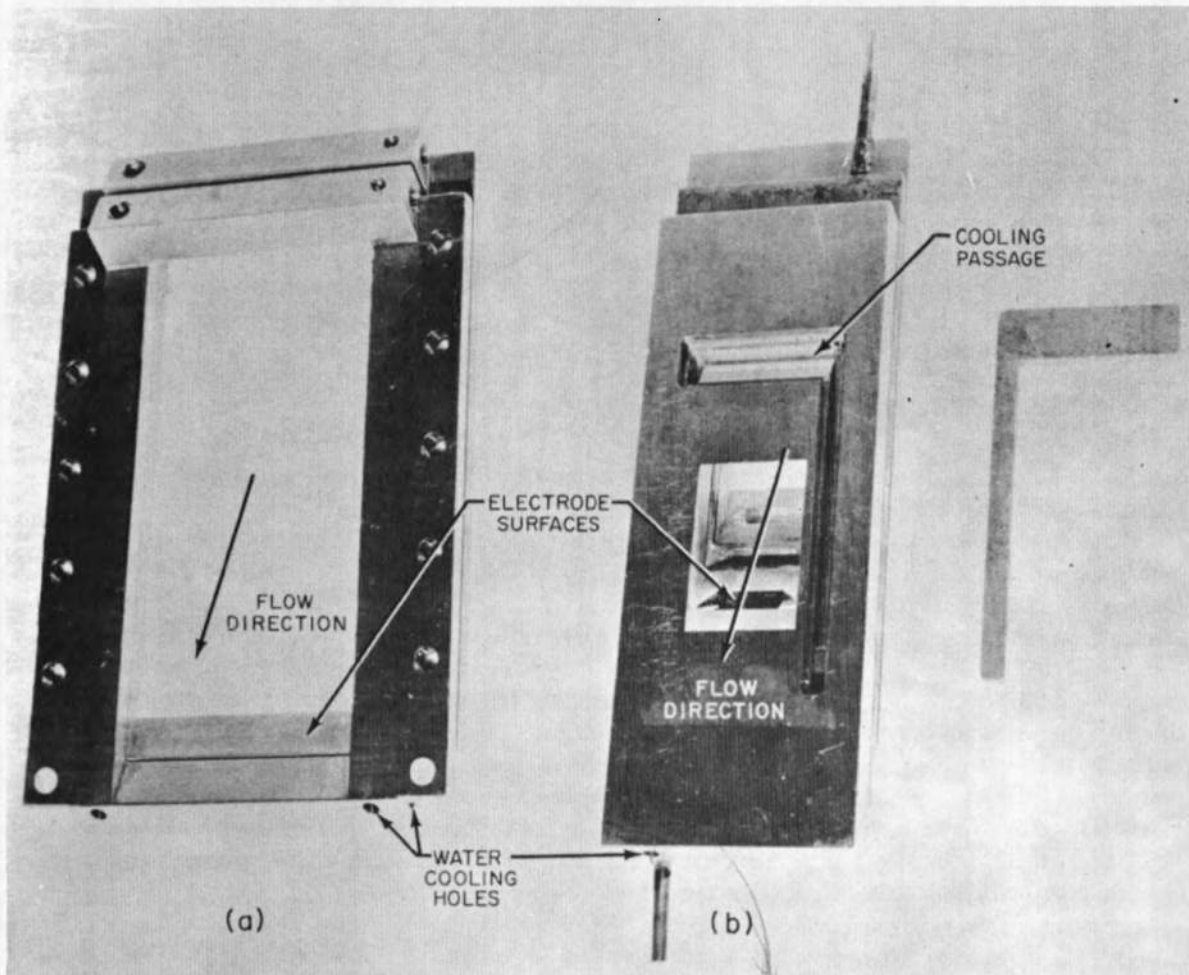
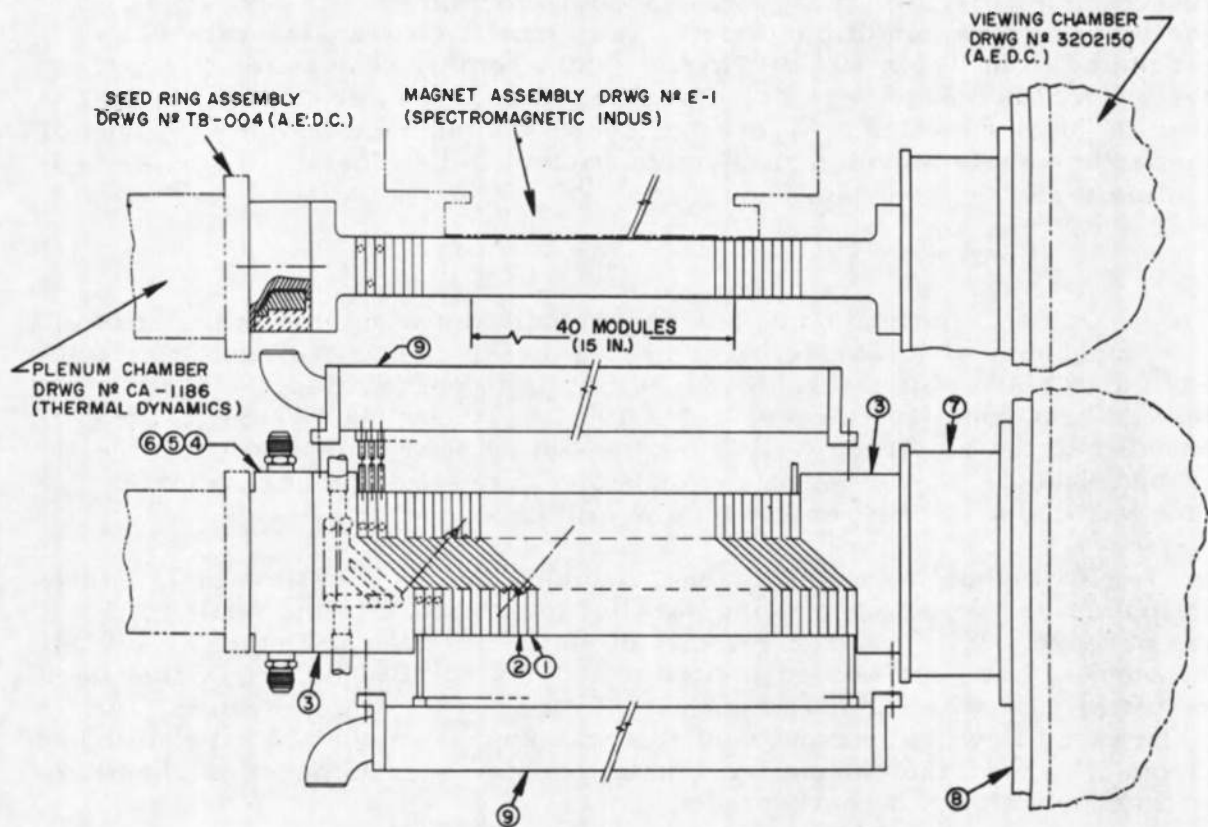


Fig. 113 Test Modules for Low Power Accelerator Channel



ITEM NO.	NOMENCLATURE	NO. REQ'D	MAT'L AND SPEC NO.
1	MODULE "O"	27	E.T.P. COPPER
2	MODULE "E"	26	"
3	INLET SECTION	2	"
4	NOZZLE INSERTS	1	"
5	NOZZLE	1	"
6	NOZZLE HOUSING	1	BRASS
7	EXIT EXTENSION	1	STEEL
8	ADAPTOR PLATE	1	ALUMINUM
9	MANIFOLD	2	NYLON (ZYTEL)

Fig. 114      Design of Low Power Accelerator

and velocity = 4700 ft/sec. Because of the small dimensions of the nozzle and the relatively low pressure, the Reynolds numbers is less than  $10^5$ , and laminar flow conditions exist. The throat heat transfer rate was estimated to be  $1.5 \times 10^6$  Btu/hr/ft<sup>2</sup> (500 w/cm<sup>2</sup>). The water cooling system for the nozzle was calculated to produce a safety factor of eight over the burnout value. Figure 115 shows the nozzle assembly. Figure 116 shows the nozzle mounted on a combustion chamber for heat transfer and cooling tests.

#### b. Channel

Gas flow in the channel is undoubtedly turbulent due to the unavoidable roughness of the walls. The heat transfer rate to the insulating wall was calculated using a turbulent flow flat plate correlation. The calculated heat transfer rate was  $1.1 \times 10^6$  Btu/ft<sup>2</sup>/hr (340 w/cm<sup>2</sup>). Heat transfer to the electrode wall is augmented by power dissipation in the boundary layer as previously described. The estimated heat transfer rate was  $2.0 \times 10^6$  Btu/hr/ft<sup>2</sup> (620 w/cm<sup>2</sup>).

Water cooling of the channel modules was by a system of 1/8-inch drilled holes, the holes running parallel to and close to the walls of the gas passage. With a water velocity of 40 ft/sec and a pressure of 400 psi the burnout heat flux was estimated to be  $17 \times 10^6$  Btu/hr/ft<sup>2</sup>. Subsequently the water flow was reduced due to limitations of the water system. At the reduced flow the burnout heat flux was approximately  $12 \times 10^6$  Btu/hr/ft<sup>2</sup>. Figure 117 shows the channel assembly mounted on a combustion chamber for heat transfer and cooling tests.

#### c. Inlet and Outlet Adapters

These pieces were essentially short water-cooled ducts with one end machined at a 41° angle to match the channel modules. They were cooled by a combination of drilled holes and milled slots which had cover plates welded over them. Heat transfer and water cooling figures are the same as for the channel.

#### d. Oxygen and Seed Injection Rings

The arc which supplied the accelerator with preheated air operated on pure nitrogen. Therefore, the oxygen and seed injection rings were necessary to produce simulated air and to produce the conductivity necessary for accelerator operation. These two rings were inserted between the arc plenum chamber and the nozzle.

### 4. DESIGN COMMENTARY

The "bent plate" module construction which was used for the 2 mw accelerator was found to be difficult to seal in the hot gas flow. The gasket between modules had to be compressed in two directions simultaneously. As a result it was difficult to obtain a good seal and proper



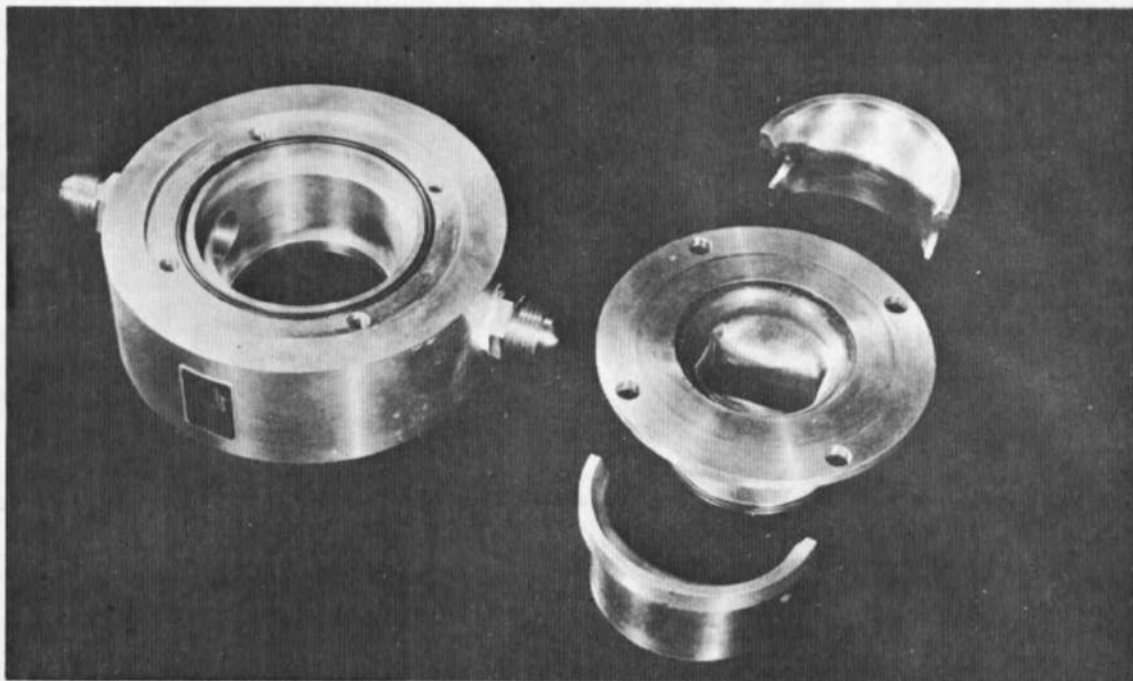


Fig. 115      Nozzle Assembly for Low Power Accelerator

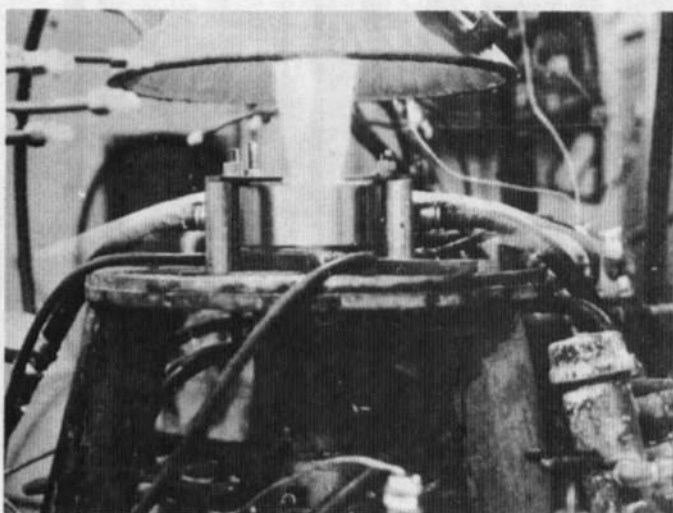
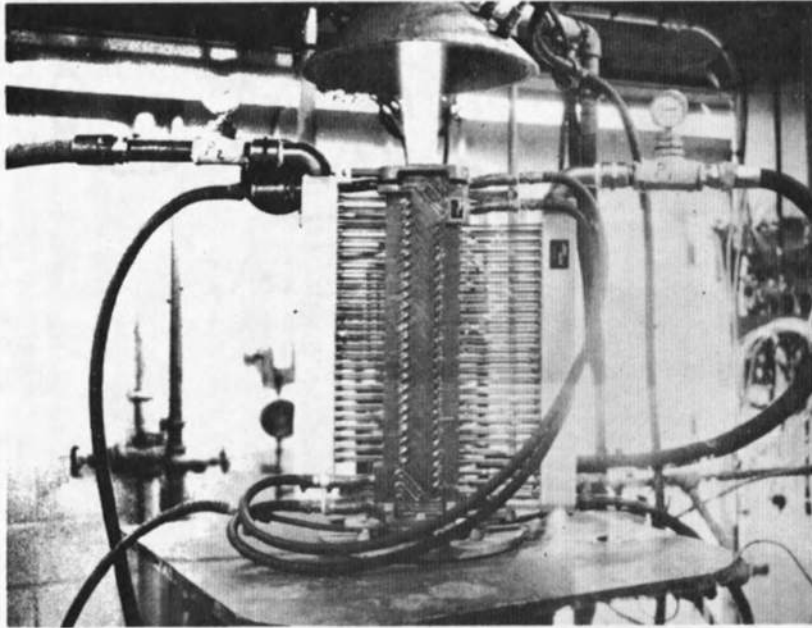


Fig. 116 Low Power Accelerator Nozzle Assembly on Combustion Chamber Test



**Fig. 117**      **Low Power Accelerator on Combustion Chamber Heat  
Transitor Test**

alignment of the modules. The problems encountered with these modules led to the adoption of a flat plate module construction for the 20 mw accelerator as previously described.

## APPENDIX V

## ACCELERATOR ELECTRODE DEVELOPMENT

The 20 mw accelerator was to operate in a regime where there was no previous experience in electrode design for linear MHD devices. The working fluid (air), the gas enthalpy, the heat transfer rate and the current density all contributed to this situation. Therefore, a series of tests were run to develop suitable electrodes for the accelerators. Testing was done on three different rigs. A 300 kW arc which was available was used for initial testing. The 300 kW arc was subsequently replaced by a 2 mw arc which permitted the use of larger test channels. A combustion gas system was used for longer duration testing. This latter system did not simulate the gas enthalpy or composition and therefore had only limited usefulness. The 300 kW arc and simple "brick rig" for it and the test channel are shown in Figs. 118 and 119. Figure 120 shows the excitation circuit used for the 300 kW brick rig channel, Fig. 121 shows the 300 kW unit in operation. The 2 mw arc heater by Thermal Dynamics is shown schematically in Fig. 122 and installed in Fig. 123. Figure 124 shows the high power arc in operation. Powdered seed was used for all experiments.

Test channels were of the simple design shown in Fig. 119. The channels were operated at atmospheric pressure, and therefore, needed no insulating walls. Power applied to the electrodes from a battery bank allowed the electrode V-I curve to be constructed. Figure 125 shows the characteristics of the electrode design used with the 2 mw accelerator.

Early electrode tests using the arc heaters showed that although a satisfactorily low electrode drop could be attained the lifetime was short when operating in air in the important current density range (20-40 amps/cm<sup>2</sup>), and this led to high power accelerator designs with reduced current density below 10 amps/cm<sup>2</sup>. Furthermore, the copper channel segments tended to oxidize quite rapidly. The latter problem was solved by silver plating the copper surfaces exposed to the hot gas. Silveroxide is an electrical conductor. The short electrode life problem was gradually improved by experiments with different groove configurations and with various ceramic mixtures.

During the course of electrode testing it was observed that at high current densities the power dissipation in the boundary layer was considerable and could increase the rate of heat transfer to the electrode walls by as much as a factor of two. In fact, it appeared that almost all of the electrical dissipation in the vicinity of the electrode actually

wound up as heat loss to the electrode rather than remaining in the gas. It was also observed that the heat loss at the anode walls was measurably greater than at the cathode walls due to the absorption of electrons at the former and emission of electrons at the latter.

Anode walls gave reasonably satisfactory performance when made of an alumina refractory cement. Cathode walls require a good emitter and for the great majority of the tests refractory mixtures containing zirconia were used. The most satisfactory mixture contained 15% zirconium diboride with 85% stabilized zirconia (stabilized with 5% calcia). Finally, since the zirconia mixture gave performance equal to the alumina, the zirconia was used for both electrodes.

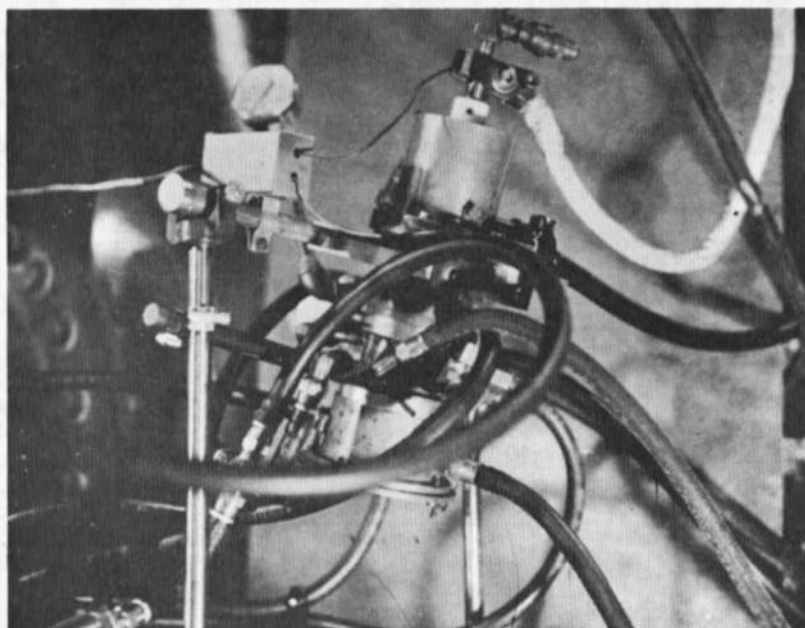


**Fig. 118**      **300 Kilowatt Arc Heater Used for Early Electrode Development Tests**

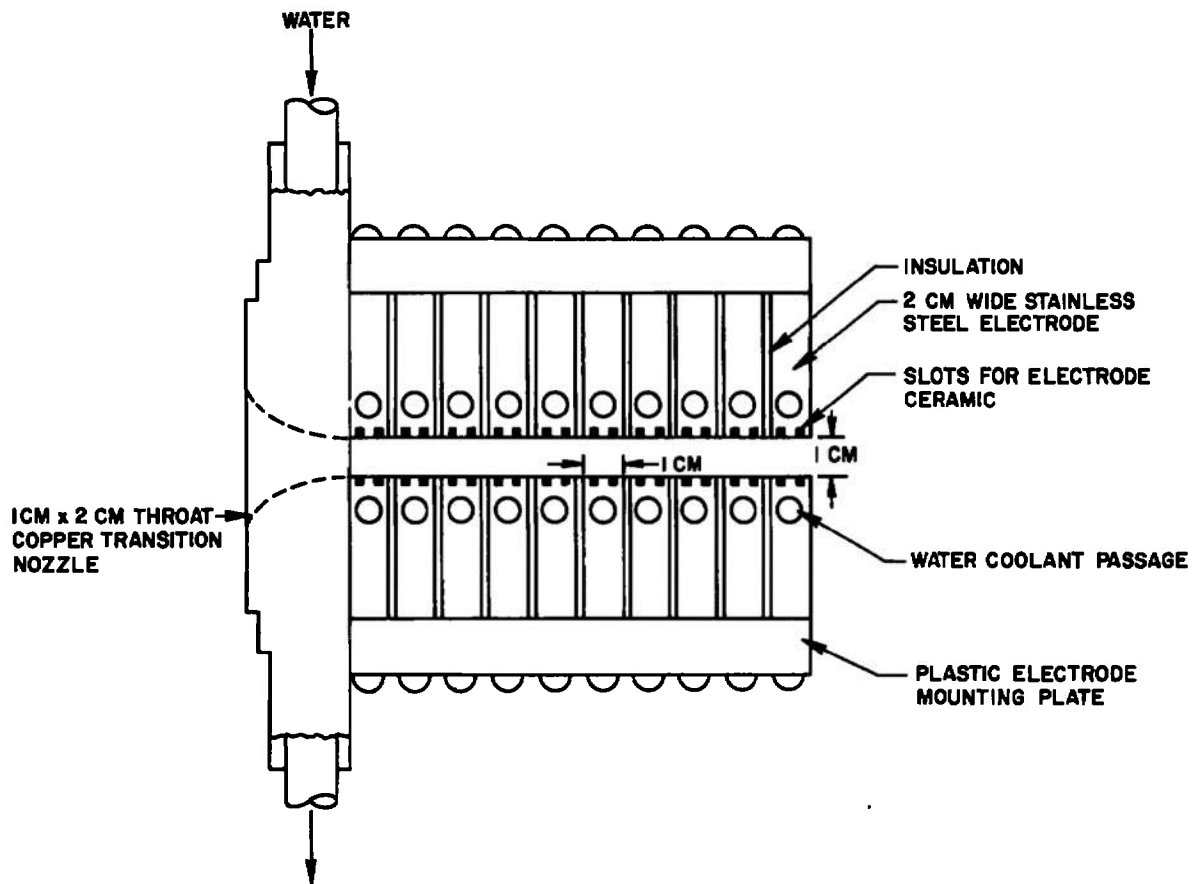


Fig. 119 "Brick Rig" Test Channel for 300 Kilowatt Arc Heater



**CIRCUIT FOR INDIVIDUAL ELECTRODE PAIRS**

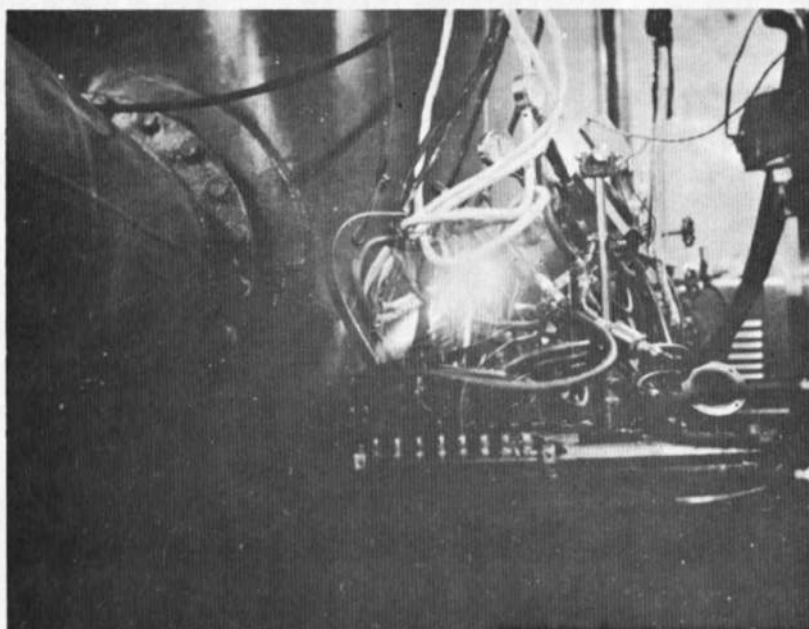


Fig. 121 300 Kilowatt Arc Heater in Operation

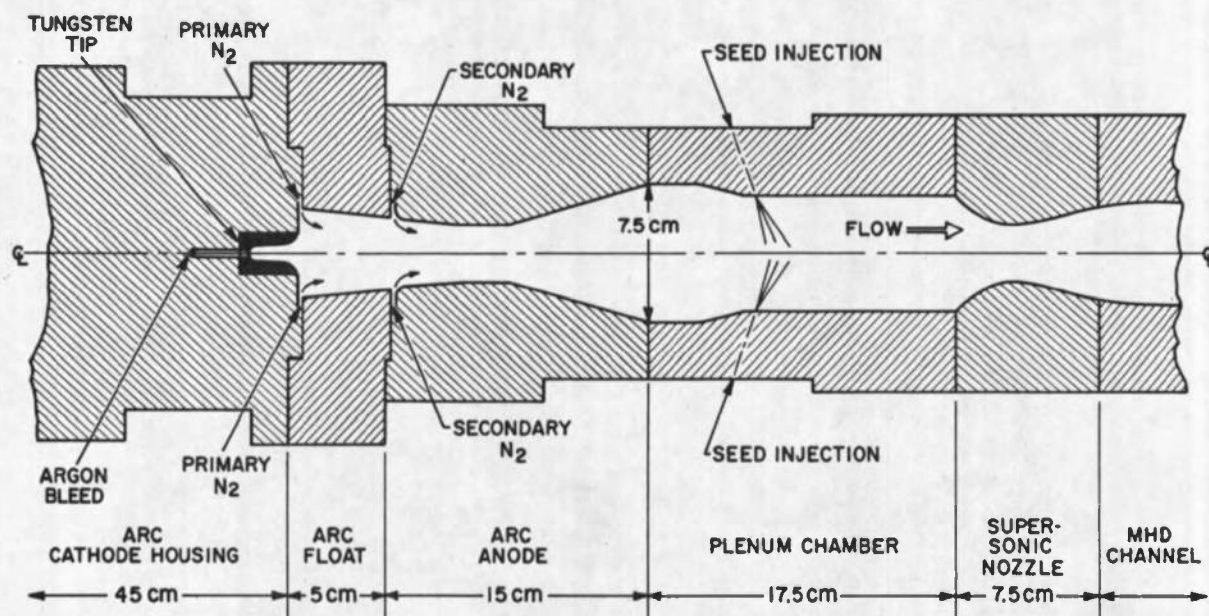


Fig. 122

Schematic of Thermal Dynamics 2000 Kilowatt Arc Heater Utilized for Electrode Development

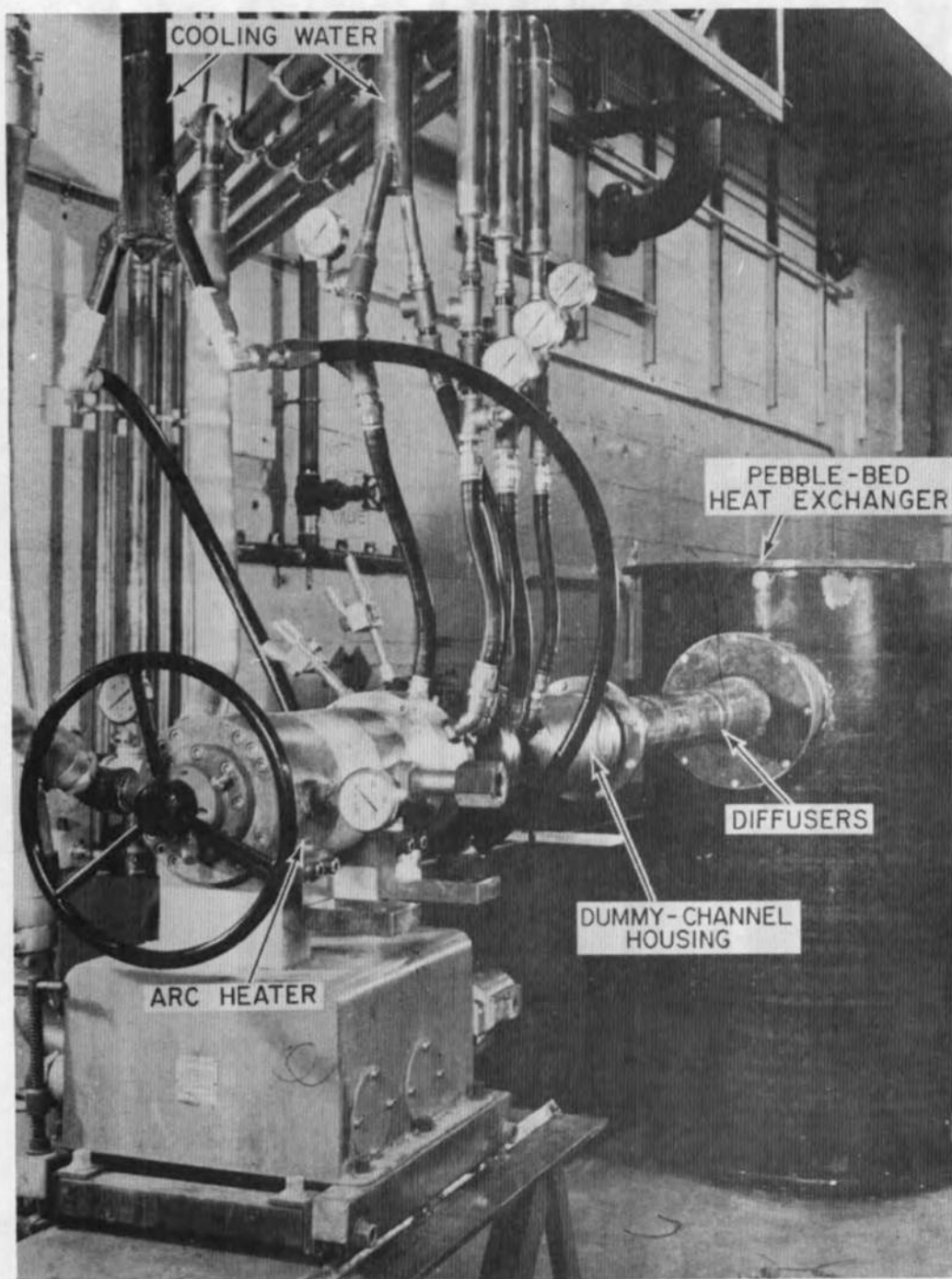
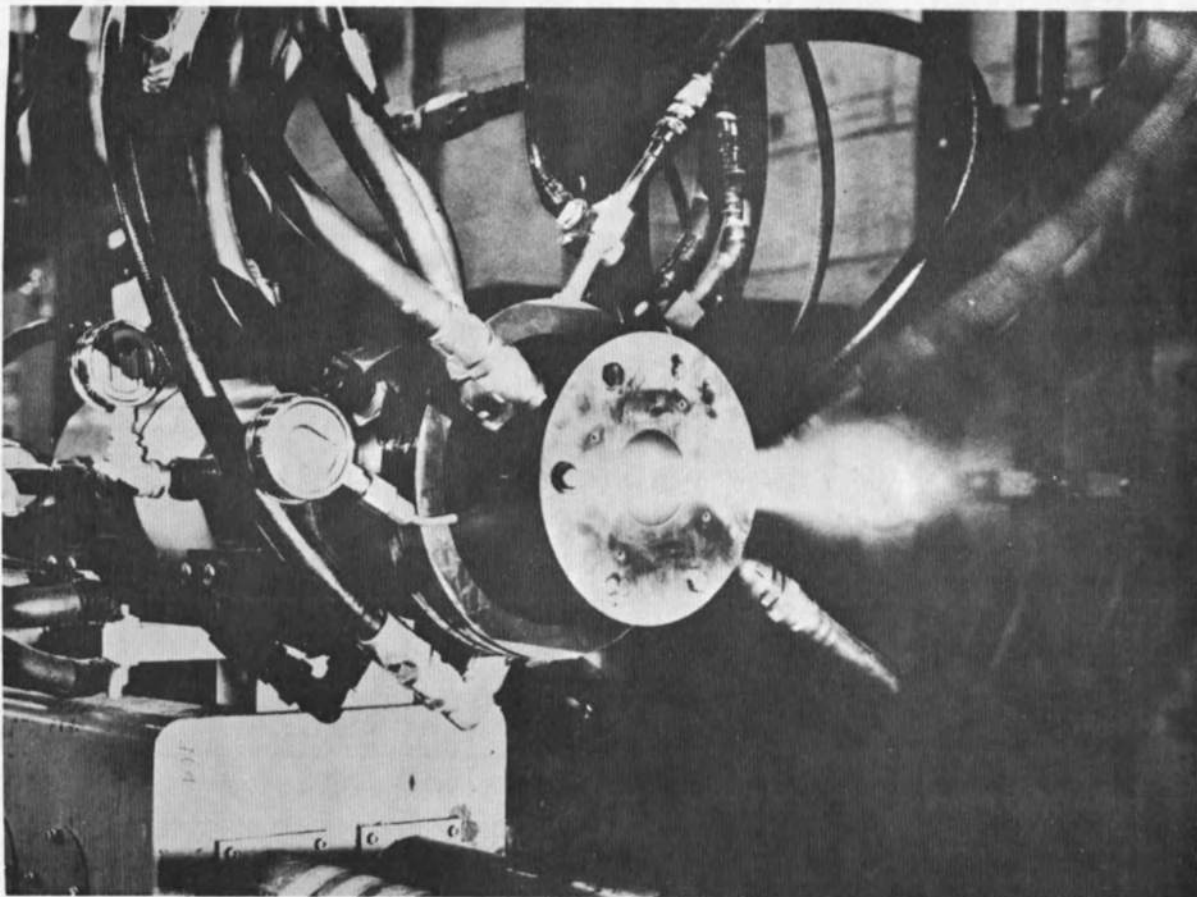


Fig. 123 2000 Kilowatt Arc Heater Test Setup



**Fig. 124    2000 Kilowatt Arc Heater in Operation**

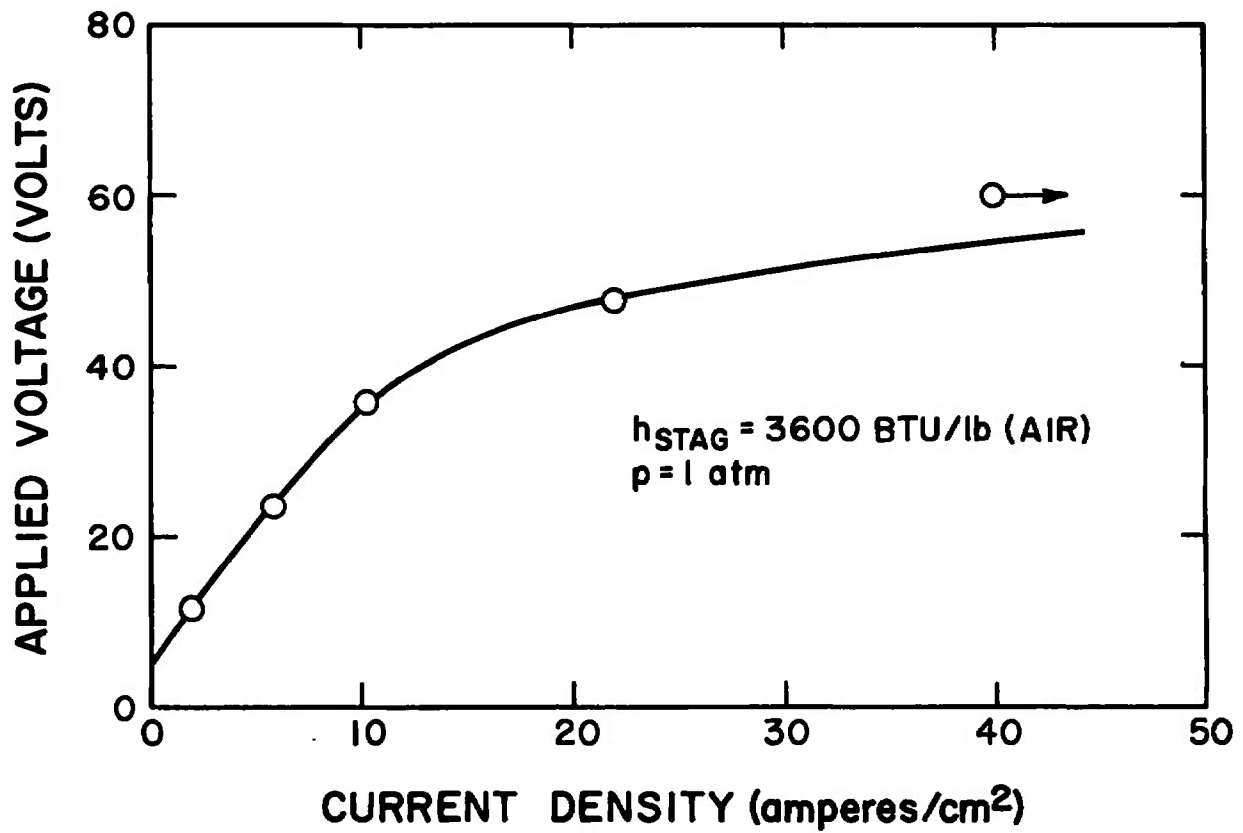


Fig. 125 Typical Electrode Characteristics as Determined in 2000 Kilowatt Arc Heater Test Rig

## REFERENCES

1. Cann, G. L., et al, "Magnetogasdynamic Accelerator Techniques", Arnold Engineering Development Center AEDC-TDR-62-145, July 1962
2. Ring, L., "General Considerations of MHD Acceleration for Aerodynamic Testing" Proceedings at the AGARD Fluid Dynamics Panel Meetings Rhode-St-Genese, Belgium, Sept. 21-23, 1964
3. Louis, J. F., Lothrop J. and Brogan T. R., "Fluid Dynamic Studies with a Magnetohydrodynamic Generator" Physics of Fluids, <sup>1</sup> Feb. 1964.
4. Louis, J. F., et al, "Detailed Theoretical and Experimental Study on a Large MHD Generator," AIAA Journal, vol 3, No. 8 (1965).
5. Mattsson, A., Ducharme, E., Govoni, E., Morrow, I., and Brogan, T., "Performance of a Self Excited MHD Generator." Avco Everett Research Laboratory Research Report 238, Oct. 1965, See Also Mech. Eng., Nov. 1966
6. Sonju, O., Teno, J., and DeNanno. L.. "MHD Generator Drive of Multiple Arc Heaters" Presented at the Ninth Symposium on Engineering Aspects of MHD, Tullahoma, Tenn, April 1968.
7. Rosa, R. J., Physical Principles of Magnetohydrodynamic Power Generation, Phy of Fluids 4, 182-194, Feb. 1961
8. Brogan, T., Powers, W., Liu, C., and Mattsson, A., "The Application of Matched MHD Generator-Accelerator Units to Hyper sonic Wind Tunnel Drive" as Ref. 2.
9. Louis, J., and Brogan, T., "Fluid Dynamics of MHD Generators", Proceedings of International Symposium on MHD Generation of Electric Power, Paris, July 1964
10. Teno, J., Liu, C., and Brogan, T. R., "Boundary Layers in MHD Generators," Proceedings of the 10th Symposium on the Engineering Aspects of MHD, Massachusetts Institute of Technology, March 26-28, 1969.
11. Teno, J., Brogan, T. R., and DiNanno, L., "Hall Configuration MHD Generator Studies," Proceedings of the International Symposium on MHD Electrical Power Generation, Salzburg, Austria, July, 1966.
12. Brogan, T. R. and Mitchell, C. E., "Two Dimensional Effects in Linear Hall Configuration MHD Generators," Proceedings of the 9th Symp. on the Engineering Aspects of MHD, Unit of Tennessee Space Institute, April 3-5, 1968.

13. Warga, J., "A Convergent Procedure for Solving the Thermochemical Equilibrium Problem," J. Soc. Indust. Appl. Math., Vol. II, No. 3, pp 594-606, Sept. 1963.
14. Frost, L. S., "Conductivity of Seeded Atmospheric Pressure Plasmas," J. Appl. Phys. 32 2029 (1961).
15. Schwitzer, S., and Mitchner, N., "Electrical Conduct of a Partially Ionized Gas in a Magnetic Field," Phys. Fluids 10 799 (1967).
16. McCune, J., "Transport Properties of Partially-Ionized Gases Using a Modified Frost's Mixture Rule," Avco Everett Research Laboratory, Amp. 201, 1966.
17. Souju, O. K., "Viscous Magnetohydrodynamic Flows," Stanford University Institute for Plasma Research SUIPR Report No. 245, 1968.
18. Johnson, P. W., "Sequenced Electrode Effects in MHD Flows with Hall Currents," Proceedings of the 9th Symposium on the Engineering Aspects of MHD, Univ. of Tennessee. Space Institute, April 3-5, 1968.
19. Fishman, J., "Instability of Hall MHD Generators to Magneto-Acoustic Waves," Proceedings of the 9th Symposium on the Engineering Aspects of MHD Univ. of Tennessee Space Institute, April 3-5, 1968.
20. Teno, J., Louis, J., Westra, L., and Brogan, T., "Long Duration Electrodes for MHD Generators", Proceedings of 8th Symposium on Engineering Aspects of MHD, Stanford, March 1967.
21. Teno, J., Brogan, T. R., Petty, S. W., Govoni, E. M., Windmueller, A. K., and Kannawin, W. I., "Studies with a Hall Configuration MHD Generator," Proceedings of the 10th Symposium on the Engineering Aspects of MHD, Massachusetts Institute of Technology, March 26-28, 1969.
22. Mattsson, A. & Brogan, T., "Self Excited MHD Generators" Proceedings of the Symp. on MHD Electrical Power Generation", Salzburg, Austria, July 1966, Published by IAEA, Vol. III, p. 665.
23. Mattsson, A., Ducharme, E., Morrow, I., Brogan, T., "Design and Performance of a Single Circuit Output Self Excited Faraday MHD Generator" Proceedings of the Eighth Symposium on Engineering Aspects of MHD, Stanford, March 1967.
24. Novack, M., and Brogan, T., "Water Cooled Insulating Walls for MHD Generators", Advanced Energy Conversion Journal, ASME Paper 63-WA-348, Nov. 1963. Also, Advanced Energy Conversion Journal, 5, 95-102 (1965)



25. Gruschwitz, E., Ing. Arch., 2, 321, (1931).
26. Ross, D., "Evaluation of the Momentum Integral Equation for Turbulent Boundary Layers," J. of the Aero. Sciences, 20, 1953.
27. Thompson, B. C. G., "A Critical Review of Existing Methods for Calculating the Turbulent Boundary Layer," AIAA J., 3, 1965, p. 746-47.
28. Rotta, J. C., "Recent Developments in Calculation Methods for Turbulent Boundary Layers with Pressure Gradients and Heat Transfer," ASME Paper No. 66-APM-F.
29. Garner, H. C., "The Development of Turbulent Boundary Layers," ARC of Britain R&M 2133 (1944).
30. Head, M. R., "Entrainment in the Turbulent Boundary Layer," ARC of Britain R&M 3152 (1960).
31. Schlichting, H., "Boundary Layer Theory," New York: McGraw Hill, 1955.
32. Ludwig, H., and Tillman, W., "Investigation of the Wall Shearing Stress in Turbulent Boundary Layers," NACA TM 1285, 1950.
33. Teno, J., Brogan, T., DiNanno, L., "Hall Configuration MHD Generator Studies," Proceedings of the Symp. on MHD Electrical Power Generation, Salzburg, Austria, July, 1966, Published by IAEA-ENEA, Vol. III, p. 603.
34. Mattsson, A., Ducharme, E., Govoni, E., Morrow, E., Brogan, T., "Performance of a Self-Excited MHD Generator," AERL RR 238, October 1965. See also Mech Engr., Nov. 1966.
35. Mattsson, A., and Brogan, T., "Self-Excited MHD Generators," Proceedings of the Symp. on MHD Electrical Power Generation, Salzburg, Austria, July, 1966, Published by IAEA-ENEA, Vol. III, p. 665.
36. Kerrebrock, J. L., AIAA J. 4, 1938 (1966).
37. Sherman, A., Phys. Fluids 9, 1782 (1966).
38. Fishman, F. J., "End Effects in Magnetohydrodynamic Channel Flow," Avco Everett Research Laboratory Research Report 78, (1959).
39. Sutton, G. W., Hurwitz, H., and Poritsky, H., Trans. AIEE, Commun. and Electron, 801, 687 (1962)

40. Velikhov, E. P., "Hall Instability of Current-Carrying Slightly-Ionized Plasmas," Proceedings Symposium on Magnetoplasmodynamic Electrical Power Generation, Newcastle upon Tyne, Great Britain, 1962, pp. 135-136.
41. McCune, J. E., "Wave Growth and Instability in Partially Ionized Gases," Proceedings International Symposium on Magnetohydrodynamic Electrical Power Generation, Paris, 1964, pp. 523-538.
42. Locke, E. V. and McCune, J. E., "Growth Rates for Axial Magneto-Acoustic Waves in a Hall Generator," AIAA Journal, Vol. 4, 1966, pp. 1748-1751.
43. Powers, W. L. and Dicks, J. B., "Transient Wave Growth in Magneto-gasdynamic Generator," AIAA Journal, Vol. 6, 1968, pp. 1007-1012.
44. McCune, J. E., "Linear Theory of an MHD Oscillator," Advanced Energy Conversion, Vol. 5, 1965, pp. 221-240.
45. Teno, J., Brogan, T. R., and DiNanno, L. R., "Hall Configuration MHD Generator Studies," Electricity from MHD, Vol. 3, International Atomic Energy Agency, Vienna, 1966, pp. 603-614.
46. Klepeis, J. E. and Olin, J. G., "Experimental Studies with an Arc-Driven Hall MHD Generator with Strong MHD Interaction," Proceedings of Ninth Symposium on Engineering Aspects of Magnetohydrodynamics, University of Tennessee Space Institute, Tullahoma, Tennessee, 1968, pp. 99-100.
47. Rosa, R. J., "The Hall and Ion Slip Effects in a Non-Uniform Gas," Phys. Fluids, Vol. 5, 1962, pp. 1081-1090.

UNCLASSIFIED

Security Classification

## DOCUMENT CONTROL DATA - R &amp; D

(Security classification of title, body of abstract and indexing annotation must be entered when the overall report is classified)

## 1. ORIGINATING ACTIVITY (Corporate author)

AVCO Everett Research Laboratory  
2385 Revere Beach Parkway  
Everett, Massachusetts

## 2a. REPORT SECURITY CLASSIFICATION

UNCLASSIFIED

## 2b. GROUP

N/A

## 3. REPORT TITLE

RESEARCH STUDIES AND THE DEVELOPMENT OF MHD GENERATORS  
AND ACCELERATORS

## 4. DESCRIPTIVE NOTES (Type of report and inclusive dates)

Final Report - August 21, 1963 to December 1969

## 5. AUTHOR(S) (First name, middle initial, last name)

Teno, J., Brogan, T. R.\*, Petty, S. W., et al.

\*Consultant

## 6. REPORT DATE

January 1970

## 7a. TOTAL NO. OF PAGES

290

## 7b. NO. OF REFS

47

## 8a. CONTRACT OR GRANT NO.

AF40(600)-1043

b. PROJECT NO. 7778

## 9a. ORIGINATOR'S REPORT NUMBER(S)

AEDC-TR-70-14

c. Task 11

d. Program Element 62410034

## 9b. OTHER REPORT NO(S) (Any other numbers that may be assigned this report)

N/A

## 10. DISTRIBUTION STATEMENT

This document is subject to special export controls and each transmittal to foreign governments or foreign nationals may be made only with prior approval of Arnold Engineering Development Center

## 11. SUPPLEMENTARY NOTES

(AETS), Arnold Air Force Station,  
Tennessee 37389.  
Available in DDC

## 12. SPONSORING MILITARY ACTIVITY

Arnold Engineering Development  
Center, Air Force Systems Command,  
Arnold AF Station, Tenn. 37389

## 13. ABSTRACT

This report presents the results of the LORHO Pilot Program undertaken to evaluate the potentiality of MHD generator-accelerator units for hypersonic wind tunnel drive. Basic features of matched MHD generator-accelerators are discussed, including especially operating voltage as related to gas conductivity, electric and magnetic field strength, and accelerator discharge stagnation pressure. These conditions lead to the choice of a high-voltage single-circuit output Hall configuration MHD generator coupled to a diagonally connected MHD accelerator fed with gas from a separately driven arc heater. A power level of 20,000 KW was chosen for the LORHO Pilot. Design details of the generator and accelerator are given, along with a detailed description of generator performance and the comparison of that performance with analysis. The generator delivered a maximum output of 18,000 KW and provided a convincing demonstration of the utility of MHD for the present application. The accelerator has not been operated. Methods of uprating the performance of the MHD generator to levels as high as 100,000 KW output are discussed. A brief description of the over-all LORHO Pilot facility is provided.

This document is subject to special export controls and each transmittal to foreign governments or foreign nationals may be made only with prior approval of Arnold Engineering Development Center (AETS), Arnold Air Force Station, Tennessee 37389.

14. KEY WORDS	LINK A		LINK B		LINK C	
	ROLE	WT	ROLE	WT	ROLE	WT
magnetohydrodynamic generator electric power generation plasma accelerators hypersonic wind tunnels						